2

MICROREFLECTANCE AND ELLIPSOMETRIC STUDIES ON THE POLISHED SURFACES OF SOME MINERALS

A thesis submitted in partial fulfilment
of the regulations of the Council for
National Academic Awards for the degree
of Doctor of Philosophy.

by

Karen J. Reeson (BSc.)

Sponsoring Establishment

Department of Metallurgy and Materials Science
Sir John Cass School of Science and Technology
City of London Polytechnic
Whitechapel High Street
London E1

Collaborating Establishment

Department of Mineralogy
The Natural History Museum
British Museum
South Kensington
London SW7

1987

CORRECTIONS

CONTENTS

1.2.1 Associations not Association
2.4 Absorption not Absorbtion
3.2 Techniques not Techiques
7.3.3 Data not Date

GLOSSARY

Eighth line down propagation constant not propergation constant.

CHAPTER 1

pg 19 et al. of Bither et al. should be underlined
pg 21 Capital T not small t fourth line from bottom
pg 22 Schlegal and Wachter 1975 not 197
pg 26 1.5.3 third line down should read the only optical data are those not is that.
pg 28 Tetrahedra not tetrahera
pg 29 Fourth line down should read Low and Weger [1960] not Low and Werger [1960].
pg 29 Second paragraph should begin Marfunin, Platanov and Fedorov not Platanov and Marfunin.
pg 32 Tenth line down Pattrick [1978] not Patrick [1978].
pg 33 Fig 1.16 b. ● instead of to
pg 36 Tenth line down where a increases not were a increases.
pg 36 Tenth line down 10.49 instead of 10.94.
pg 36 Eighteenth line down Kalbskopf [1977] not Kalbakopf [1977].
pg 37 Second paragraph tenth line down lead in copper sites should read atypical not typical
pg 37 Second paragraph seventh line down Guimaraes not Guirnaraes.
pg 49 Second paragraph seventh line down on the optical properties instead of of

CHAPTER 2

pg 54 i, j and k in equation 2.3 should be in bold type
pg 56 Fig 2.2 Θ not ϕ.
pg 57 equation 2.6 should be written $\sqrt{\frac{\varepsilon_1 \mu_1}{\varepsilon_0 \mu_0}}$
pg 57 First paragraph last sentance should read The ratio of the square root of the complex wavenumbers...
pg 57 Equation 2.9 should read $\alpha = (\mu\ell)^{1/2}\omega$
pg 57 Equation 2.10 should read $\beta = (\mu\sigma\omega)^{1/2}$
pg 57 Equations 2.9 and 2.10 μ not u
pg 58 2.1.4 heading i should read orientation and other terms need, not a orientation term needs.

pg 58 2.1.4 μ missing fifth line down heading ii.
pg 60 Equation 2.18 should be written with $\left(\frac{1+R}{1-R}\right)$ not $\left(\frac{1-R}{1+R}\right)$

pg 60 Equation 2.19 should be written $R(n_{calc}+1)^2-(n_{calc}-1)^2$ not $R(n_{calc}+1)^2+(n_{calc}-1)^2$

pg 65 k=0 not k 0;n[calc]=$\pm\infty$,k[calc] not n[calc]=$\pm\infty$k[calc]
pg 68 Large X not x equation 2.39
pg 69 Large Y,Large Z at start of equations 2.40 and 2.41
pg 71 Small y ,small z at start of equations third line down this equation should be labelled 2.45
pg 71 useful not usefull seventh line down paragraph 2.
pg 71 Subscript λ missing from D_λ last line paragraph 2 and first line i
pg 72 Fig 2.8 after Atkin and Harvey [1979]

CHAPTER 3

pg 81 3.1.3 first line down system not systyem.
pg 87 3.1.7.2 sixth line down should read insertion of the not insertion fo the.

CHAPTER 5

pg 121 5.2.2 eighth line down should read and/or not and or.
pg 125 Seventh line down should read at 30° incidence not 30°C incidence.
pg 125 Seventh line down = sign missing after $\frac{d}{R_u}$

CHAPTER 6

pg 152 6.6.1 fourth line down should read perceptible anisotropy not perceptable anisoptropy.
pg 158 Atomic ratios for safflorite should be Co=0.43,Fe=0.55 Ni=0.02,As=1.58,S=0.08. Formula should read $[Co_{0.43}\ Fe_{0.55}\ Ni_{0.02}\ ]As_{1.58}\ S_{0.08}$
pg 159 Correct formula for safflorite as above.
pg 162 Cleavage not clevage.
pg 167 6.8.1 fourth line down anisotropy not anisoptropy.
pg 167 6.8.1 eighth line down should read also exibited ; this is displayed not also exibited this is displayed.
pg 172 Atomic ratios for tetrahedrite should be Cu=10.18,Zn=1.91 As=1.19,Sb=2.95.Formula should be $[Cu_{10.18}\ Ag_{0.28}\ ][Zn_{1.91}\ Fe_{0.14}\ ][As_{1.19}\ Sb_{2.95}\ ]S_{12.85}$
pg 173 Correct formula for tetrahedrite as above
pg 179 L_α not M_α for Sn
pg 188 Remove the from end of line 6 first paragraph.

CHAPTER 7

pg 195 calculated reflectance values in table 7.1 400 nm 90.00 instead of 89.24 , 86.70 instead of 87.57, 88.90 instead of 89.67. 420nm 89.81 instead of 89.94, 90.46 instead of 90.65. 600nm 730 instead of 720. 700nm 89.68 instead of 88.51
pg 196 Bottom of page after of should be calculation which...

pg 197 7.3.3 fifth line down should read table 7.2 come from not table 7.2 comes from.
pg 197 Change using to uses
pg 201 6. should be 1978 not 1977
pg 202 Remove heading 7.
pg 203 End of paragraph 1 reference Bowie,Simpson and Auld [1978]
pg 206 Third paragraph sixth line should read microphotometric not microphotmetric.
pg 206 Third paragraph seventh line should read n and k [section 7.3.2] not n and k section 7.3.2.
pg 212 Formula for safflorite wrong see above for correct formula
pg 213 Third line for getter read accumulate.
pg 217 7.7.2 first line should read Fig. 6.18 not Fig. 5.18
pg 225 Formula for tetrahedrite wrong see above for correct formula
pg 232 Third line down should read Calas and Cottrant not Callas and Cottrant.
pg 232 7.9.4 third line down should read Calas andCottrant not Callas and Cottrant.
pg 234 Third line down should read Calas and Cottrant not Callas and Cottrant.
pg 235 7.10.2 should read Fig 6.30 not Fig 5.30.
pg 242 Second line down should read henryite, where contrary not henryite. Where contrary.

CONCLUSIONS

pg 243 Second paragraph ninth line down should read when the data are analysed not when the data is analysed.
pg 244 Second paragraph eighth line should begin In ellipsometry
pg 245 Eighth line insert near infront of normal

REFERENCES

pg 246 Atanasov [1975] not [1985]
pg 247 Cvech and Hak in wrong order should come after Criddle
pg 247 Wilkinson not Wilkenson
pg 247 Cottrant not Cottrand
pg 248 ref 18 should read Hallimond,A.F. [1970] The Polarising Microscope,Vickers Instruments Ltd. York 3 rd Edition.
pg 248 ref 16 no hyphons should read Cooke,Troughton and Simms York 2 nd edition.
pg 248 ref 27 should be CNAA not CNAFI

ACKNOWLEDGEMENTS

I would like to thank Peter Embrey and Errol Roberts for the support and help they have given during this project. I am also deeply indebted to Alan Criddle and Chris Stanley, at the Natural History Museum, for their tolerance, patience and their help in making experimental measurements and also for providing mineral specimens, stimulating debate and criticism. Thanks are also due to Dr R. King at the National Physical Laboratory for providing a calibrated evaporated aluminium slice and for making measurements on platinum iridium alloys provided by Johnson-Matthey Limited. I would like to thank the staff of the Mineralogy Department, Natural History Museum for making me so welcome, and the technical staff at City of London Polytechnic for their assistance. Thanks are also due to Rose Turner and Patsy Standbridge for converting my illegible scrawl into a neatly typed script. Finally, my thanks to my long suffering husband Stephen for his help and encouragement and for always being there when I needed him.

Microreflectance and ellipsometric studies on the polished surfaces of some minerals.

K.J.Reeson

ABSTRACT

The optical properties of a series of ore minerals are assessed using microscope photometry and ellipsometry. Results from both methods are compared and any discrepancies in the data are interpreted within the experimental and instrumental constraints of the two techniques. The errors involved in the calculation of reflectance and the optical constants n and k are also considered. A new type of microphotometric error known as the Standard-Specimen-Reflectance-Difference-Phenomenon (SSRDP) is investigated, its possible causes are discussed and tables evaluated for its correction.

The results of this study are compared with those of other workers and differences between the measurements are discussed within the context of electronic, structural and impurity ion considerations. Where possible, spectral maxima are assigned to electronic and/or excitonic transitions and ideas are advanced to rationalise some of the observed reflectance dispersions.

The use of spectroscopic ellipsometry in this investigation makes it possible to assess the effects of air-formed or other contaminant films. The influence of specimen preparation on the optical characteristics is discussed and the importance of using 'real surfaces' in order to make possible the geological and commercial application of this study is emphasised.

CONTENTS

GLOSSARY

A	Movement of analyser prism from its pre-set fiducial (degrees)
D_λ	Dominant Wavelength
E	Electric Field Vector
H	Magnetic Field Vector
k	Absorption coefficient
K^2	Propagation constant
n	Refractive index
N	Refractive index of surrounding media
P	Movement of polariser prism from its pre-set fiducial (degrees)
Pe%	Excitation Purity
R	Reflectance measured in air
im_R	Reflectance measured in oil
R_N	Normal reflectance
x,y,z	CIE colour coordinates
Y	Luminance
Δ	Relative phase shift
ϵ	Dielectric constant
ϵ_1	Real part of the dielectric constant
ϵ_2	Imaginary part of dielectric constant
θ	Angle of incidence
λ	Wavelength
μ	Magnetic permeability
ρ	Reflectivity factor
σ	Conductivity
ψ	Relative amplitude change
∇^2	Laplacian vector operator

Abbreviations

C.I.E.	Le Commision International de l'Eclairage
CLP	City of London Polytechnic
DVM	Digital Volt Meter
ELL	Ellipsometric value
I.A.D.	Illuminator Aperture Diaphragm
I.F.S.	Illuminator Field Stop
MP	Microphotometric value
N.A.	Numerical Aperture
NHM	Natural History Museum
NPL	National Physical Laboratory
Ph.F.S.	Photometer Field Stop
SSRDP	Standard Specimen Reflectance Difference Phenomenon

INTRODUCTION AND AIMS

The main aim of this study is to compare the optical techniques of microscope photometry and ellipsometry and to assess their usefulness or otherwise to the diagnostic study of metalliferous minerals. Although ellipsometry has been used for many years in corrosion studies and materials science it has found little application in mineralogy. Microscope photometry, however, has long been used as one of the principal techniques in the study of opaque minerals. Microscopy photometry has the disadvantage, however, that in certain circumstances the ill-conditioning of the equations used in the derivation of the optical constants n (refractive index) and k (absorption coefficient) can yield imaginary or erroneous solutions. Ellipsometrically derived n and k values do not suffer from the same problem, and it is desirable to know if they can be used as independent measurements with which to compare the microphotometric results. To this end a series of minerals were selected (in co-operation with the Natural History Museum, South Kensington) for ellipsometric and microphotometric evaluation. As the ellipsometer used in this study required a minimum isotropic, homogeneous surface area of 1 cm^2 the number of minerals available for study was obviously limited. This is also the reason why many of the specimens have no reasonable locality information as it would have been imprudent to cut up some of the better specimens on the off chance that they would yield an area suitable for ellipsometric measurement.

The study of electronic processes is pertinent to any discussion of the properties of chalcogenides, arsenides and oxides as, being almost exclusively semiconductors, their properties are readily influenced by dopant impurities and non-stoichiometry. For this reason these phenomena are treated in some depth and where possible features in the reflectance profiles such as spectral maxima are assigned to known or postulated electronic transitions. The structure of each mineral is also considered as, for a comprehensive treatment, it is necessary to understand the contributions of each anion and cation 'group'. The effects upon the reflectivity and various other physical properties of anionic and cationic changes have been studied by a number of workers (Burns and Vaughan,

1970; Bither et al. 1968; Vaughan and Craig, 1978). These studies serve to illustrate how the careful implementation of chemical theories can be used to explain experimental observations. In addition, these theories provide a comprehensive background to some of the factors influencing chalcogenide chemistry and for this reason are a good starting point from which to commence this study.

CHAPTER ONE
LITERATURE SURVEY

1.1 Factors Influencing the Reflectivity of Ore Minerals

The properties of the group of first row transition metal sulphides which adopt the pyrite structure (FeS_2, CoS_2, NiS_2, CuS_2, ZnS_2) have been investigated by Burns and Vaughan, 1970; Vaughan and Craig, 1978; Tossell, Vaughan and Burdett, 1981. Progressing along the series a systematic change in the reflectance and the electrical and magnetic properties is observed. These phenomena can be explained in terms of the localised versus delocalised behaviour of the electrons in the predominantly cationic 3d type orbitals (Tossell *et al*. 1981). The electrons in the non-bonding t_{2g} orbitals are localised on the cation. Overlap of metal $d^2(e_g)sp^3$ hybrid orbitals with sulphur sp^3 hybrids leads to the formation of doubly-degenerate anti-bonding e_g^* orbitals which, unlike the t_{2g} orbitals, are delocalised. Going across the pyrite disulphide series ($FeS_2(t_{2g}^6 e_g^0)$; $CoS_2(t_{2g}^6 e_g^1)$; $NiS_2(t_{2g}^6 e^2_g)$; CuS_2 $(t_{2g}^6 e_g^3)$; ZnS_2 $(t_{2g}^6 e_g^4)$) the number of electrons occupying the e_g^* level increases, and because of the anti-bonding nature of this orbital, the metal-sulphur bond becomes longer so destabilising the structure. This also accounts for the increase in the unit-cell edge *a* across the series, which parallels the decrease in reflectivity. The reasons for this drop in reflectance have been examined by a number of authors. Burns and Vaughan (1970) have postulated a decrease in π bonding between the metal $3dt_{2g}$ orbitals and vacant t_{2g} type 3d orbitals on sulphur and related it to a decrease in reflectivity. However, as the presence of such bonding has yet to be positively identified, and as Kjekshus and Nicholson (1971) have found no evidence of π back-bonding, this explanation is unsatisfactory. Vaughan and Craig (1978) have calculated the effective number of free electrons per unit volume and found this to be roughly proportional to the number of vacant e_g^* levels into which t_{2g} electrons can be excited. They therefore propose that electrons excited by visible light into e_g^* orbitals become delocalised through the nature of the covalent bonding between the metal and sulphur ligands.

In the preceding discussion it can be seen that changing the

cation in an isostructural group of minerals can alter the reflectivity. Frequently the same is true when the anion is changed. The efficiency of covalent bonding increases with size and hence the polarizability of the anions. When going down a group such as S, Se and Te the delocalisation of the e_g^* orbitals increases as does the strength of the anion-cation bond. Fig. 1.1 shows the increasing reflectance of the group of isostructural minerals $CuTe_2 > CuSe_2 > CuS_2$. A similar trend in reflectivity is seen in the isomorphous lead minerals, galena (PbS (R = 38.1 %)), clausthalite (PbSe (R = 50.1 %)) and altaite (PbTe (R = 65.5%)).

1.2 Chalcosine (Copper Sulphide)

1.2.1 Occurrence and Associations

Chalcosine is an economically important ore of copper, and is frequently found in association with cuprite and native copper. The mineral is most commonly found in zones of secondary sulphide enrichment. Extremely fine aggregates of chalcosine can appear isotropic. Chalcosine also exhibits apparent isotropism when subjected to excessive pressure during polishing. Djurleite behaves differently from chalcosine during polishing, as individual grains of djurleite show many different shades of grey or blue. Continued polishing, however, ultimately results in a uniform colouration (Utenbogaardt and Burke, 1971).

1.2.2 The Copper-Sulphur System

The copper-sulphur system is very complex (Fig. 1.2) and has only been adequately described within the last 15 - 20 years (Roseboom, 1966; Cook, 1972; Potter, 1977). The economically important copper ore low chalcosine (Cu_2S) has been known for many years but the existence of a low temperature nearby phase $Cu_{1.94}S$ was not suspected until the X-ray studies of Djurle (1958). This phase was later established as a naturally occurring mineral species by Roseboom (1962) and Morimoto (1962), and appropriately named djurleite. In 1942 Buerger proposed that the mineral hitherto known to ore microscopists as blue isotropic chalcosine was in fact a separate mineral species which he named digenite. Later studies by Morimoto and Gyobu (1971) established that the mineral had the formula $Cu_{6.9}Fe_{0.1}S_4$ and that the presence of small quantities of iron

FIG 1.1

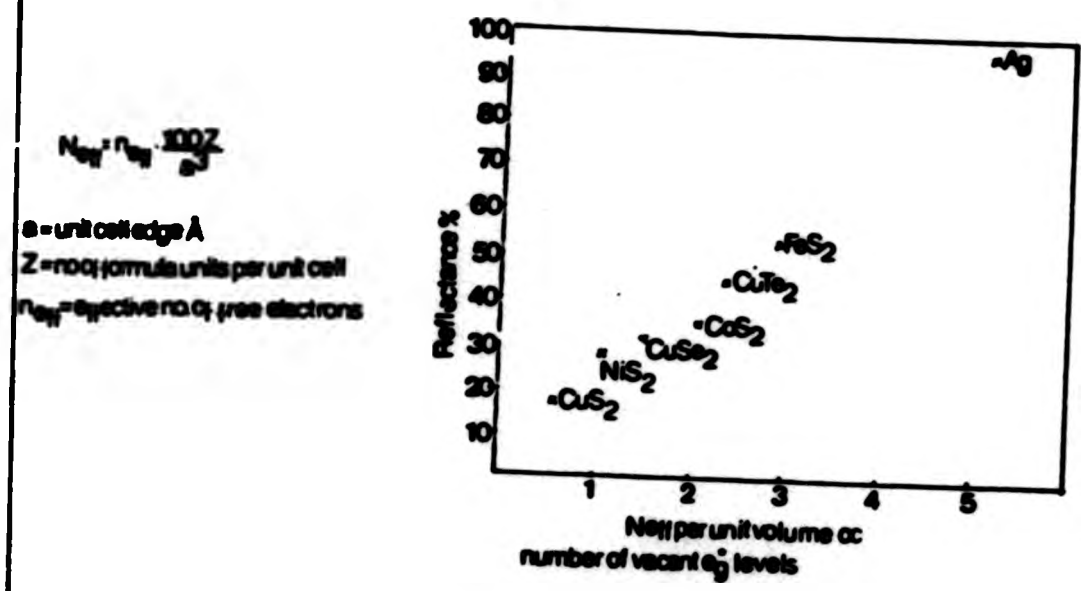

$N_{eff} = n_{eff} \cdot \frac{100Z}{a^3}$

a = unit cell edge Å

Z = no. of formula units per unit cell

n_{eff} = effective no. of free electrons

	FeS_2	CoS_2	NiS_2	CuS_2
Reflectance % at 496 nm	51·60	34·00	27·00	17·00
Unit cell edge a Å	5·42	5·53	5·69	5·79
M—S bond length Å	2·26	2·34	2·40	
no. of electrons in e_g^* band	0	1	2	3

After Burns and Vaughan 1970

Fig 1.1 Change in reflectivity, bond length and unit cell edge with increasing number of electrons in anti-bonding e_g^* level.

FIG 1.2

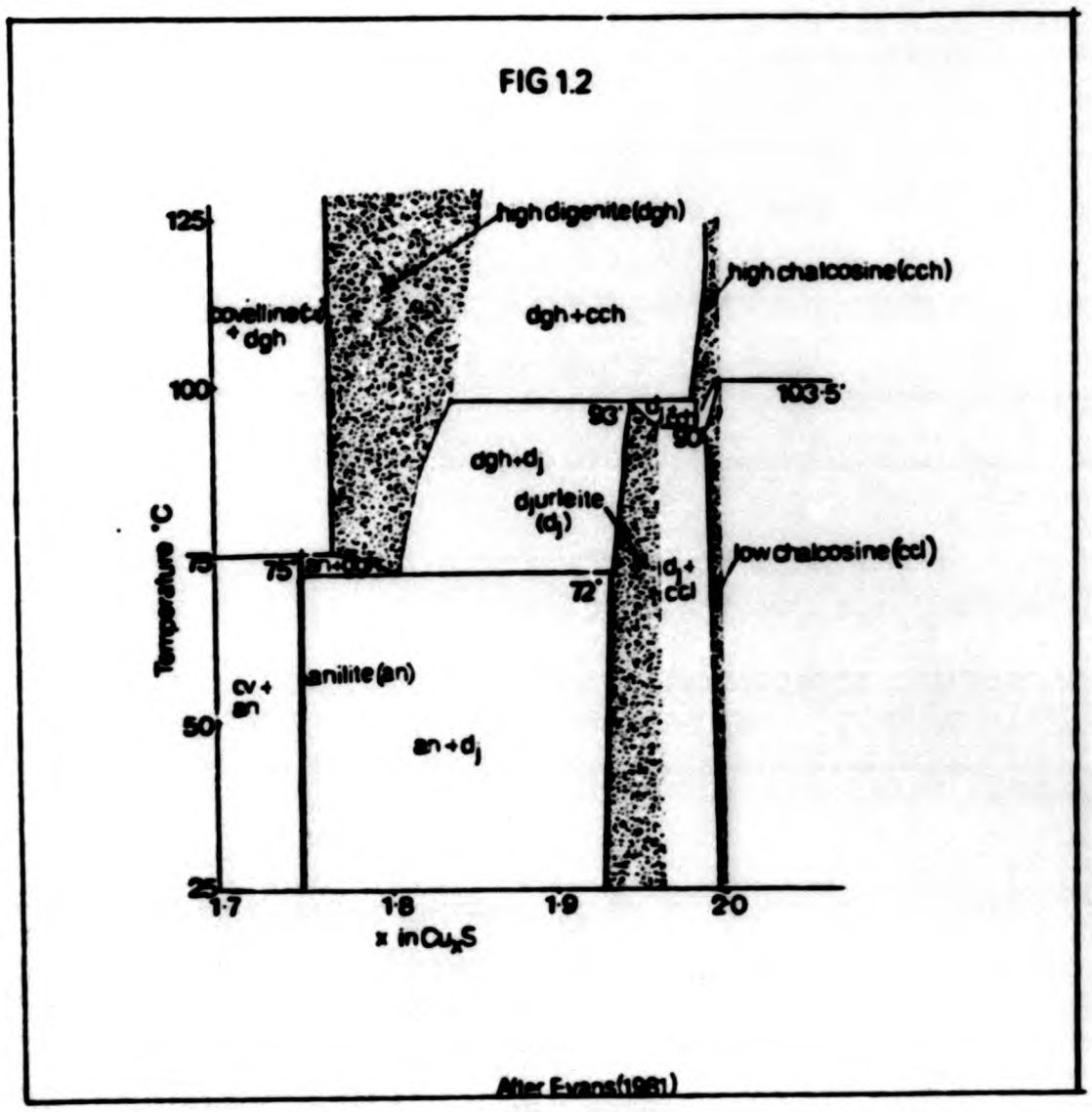

Fig 1.2 Phase diagram for the Cu-S system, in the low temperature region near Cu_2S. Dotted areas indicate single phases.

were necessary to stabilise the structure. More recently another copper sulphide, in which the copper to sulphur ratio is greater than unity, has been identified by Koto and Morimoto (1970) and named anilite, it has the formula Cu_7S_4.

Potter (1977) established that the range of homogeneity for low chalcosine is very small (Cu_xS, x = 1.997 - 2.000 $\pm$ 0.002), while that for djurleite is much wider (x = 1.934 - 1.965 $\pm$ 0.002). Low chalcosine and djurleite are physically difficult to distinguish and probably occur naturally with equal frequency. Thus many samples found in collections labelled chalcosine may actually be djurleite or intergrowths of low chalcosine and djurleite.

1.2.3 Structure of Chalcosine

The structure of low chalcosine is complex and was originally described as orthorhombic (Buerger and Buerger, 1944). Evans (1979, 1981) has now shown it to be monoclinic (Fig. 1.3), the pseudo orthorhombic appearance being due to extensive twinning. The unit cell, space group $P2_1/C$, has a = 15.246(4) Å, b = 11.884(2) Å, c = 13.494(3) Å, β = 116.35(1)° and contains 48 Cu_2S units. Of the 24 different copper atoms, eight are located in the sulphur layers occupying 2/3 of the available triangular sites. The remaining copper atoms are arranged between the layers mostly in triangular sites, although some of these are highly distorted. For one copper atom the distortion out of the triangular plane is so great that it appears to be in a distorted tetrahedral environment. Two copper atoms show a tendency towards two fold linear coordination. It is worth mentioning here that both a high temperature and a high pressure form of chalcosine are known. The high temperature form has a hexagonal structure, with 2 Cu_2S per unit cell, in which the copper atoms are highly disordered and randomly distributed between the available triangular, tetrahedral and linear sites. The high pressure form has a tetragonal structure (Janosi, 1964), which is surprisingly simple with only one type of copper atom in regular triangular coordination with sulphur (Fig. 1.4.).

FIG 1.3

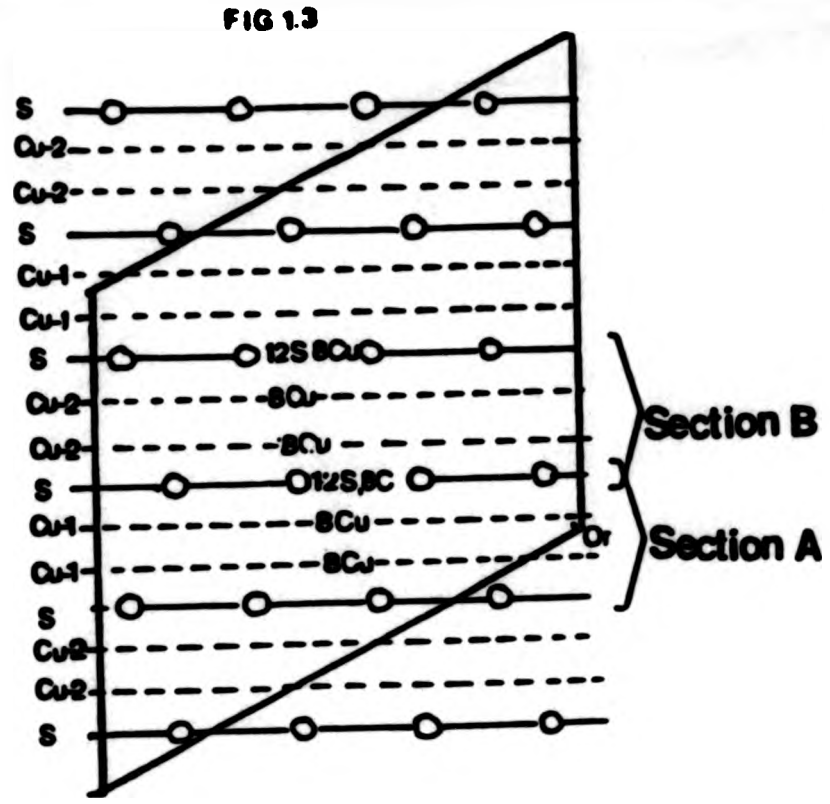

Fig 1.3a Distribution of atoms in low chalcosine shown schematically as viewed along the b axis

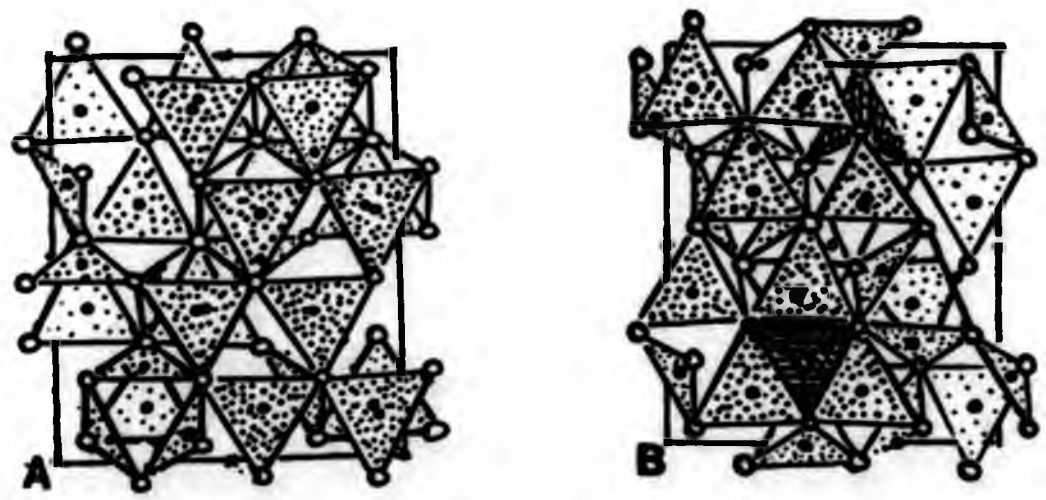

Fig 1.3b Projected sections A & B of the low chalcosine structure in which CuS_3 groups are shown as shaded triangles, distorted CuS_4 groups are shown as line hatched tetrahedra.

After Evans,1979

FIG 1.4

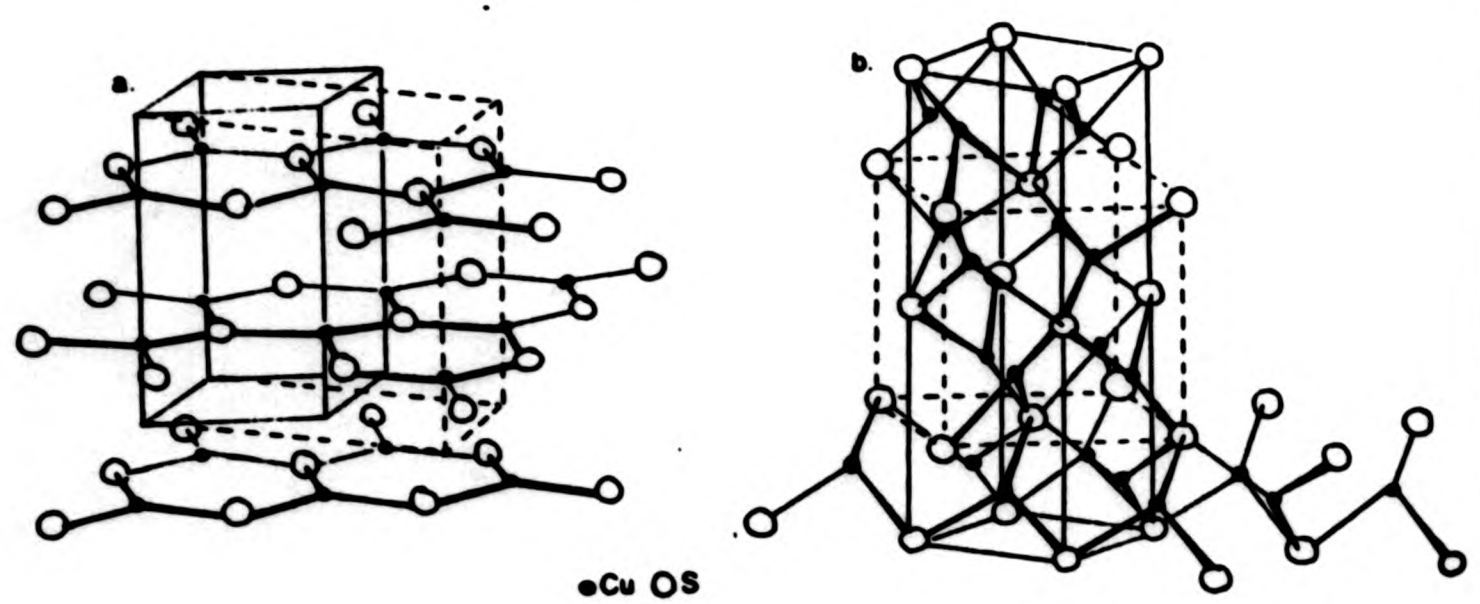

After Evans (1979, 1981)

Fig 1.4 High temperature and pressure phases of chalcosine,

a. Partial structure of high temperature phase (high chalcosine). Dashed lines show orthohexagonal unit cell

b. Structure of tetragonal, high pressure chalcosine. Dashed lines show the cubic unit of the close packed sulphur framework

1.2.4 Structure of Djurleite

Due to intensive twinning, djurleite, like low chalcosine, was originally thought to be orthorhombic (Djurle, 1958; Roseboom, 1962; Morimoto; 1962), but Evans (1979, 1981) has now shown it to be monoclinic (Fig. 1.5.) with a space group $P2_1/n$. The unit cell has dimensions of a = 26.897(6) Å, b = 15.745(3) Å, c = 13.565(3) Å, β= 90.13(3)° and contains eight $Cu_{31}S_{16}$ formula units. Of the sixty two different copper atoms, fifty two have triangular coordination, which in some cases is slightly distorted; nine have highly distorted tetrahedral coordination and one has unique linear two fold coordination. Two types of sulphur layer exist, compared to only one in low chalcosine.

1.2.5 Structure of Anilite

Anilite, as mentioned previously, has been described by Koto and Morimoto (1970). The unit cell is orthorhombic with space group Pnma (Fig. 1.6.) and dimensions a = 7.89 Å, b = 7.84 Å, c = 11.01 Å and 16 $Cu_{1.75}S$ formula units. Of the twenty eight different copper atoms twenty are in distorted triangular coordination while eight lie at the centre of distorted tetrahedra.

1.2.6 Optical and Electronic Properties

Folmer and Jellinek (1980) have used X-ray photoelectron spectroscopy to show that in chalcosine the copper is univalent (d^{10}) and diamagnetic. The oxidation state of the sulphur is -2. They also indicated that electrical conduction is via positive holes located in the sulphur 3p valence band.

Shuey (1975) postulates that the conduction band in low chalcosine is derived primarily from the copper 4s level, while the valence band is basically a mixture of copper 3d and sulphur 3p states. A significant degree of delocalisation is indicated by the high electronic mobility of the mineral. Unfortunately, to date, no comprehensive band structure has been published for low chalcosine or djurleite, this is probably due to the complexity of the structure.

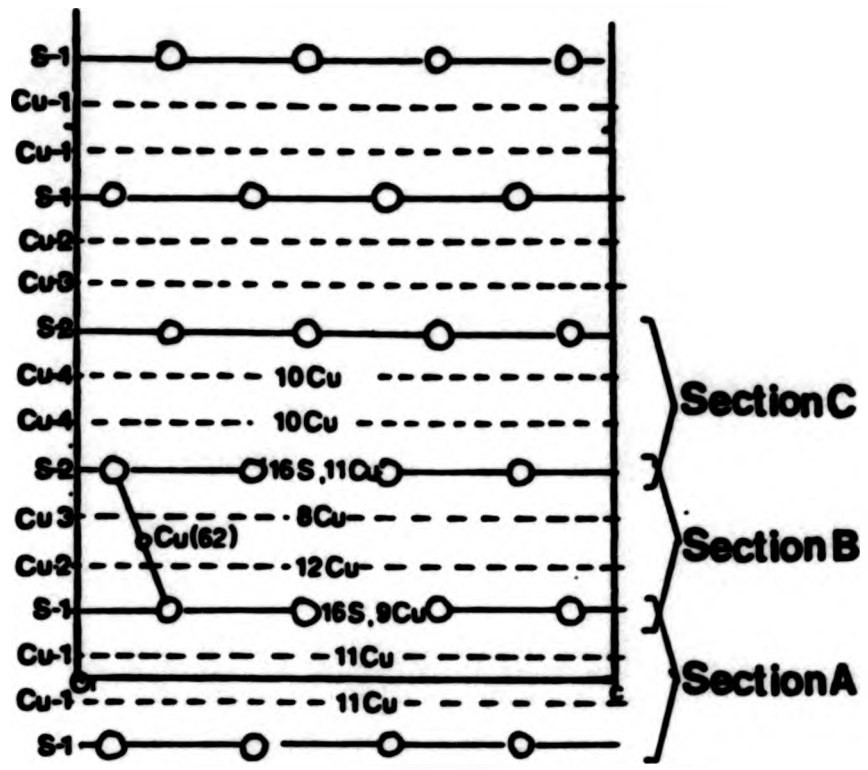

Fig 1.5a Distribution of atoms in djurleite shown schematically as viewed along the b axis.

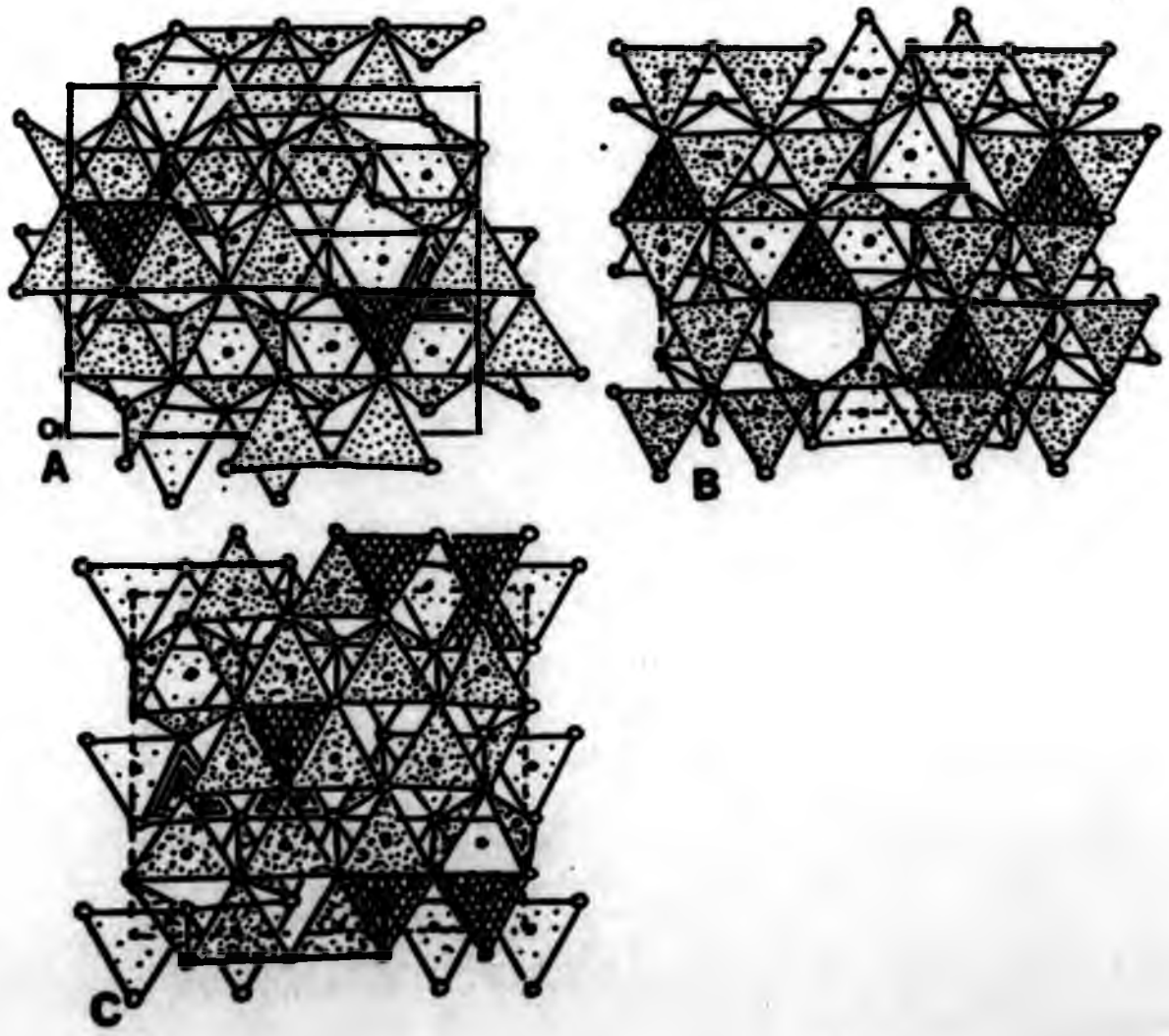

Fig 1.5b Projected section A,B & C of the djurleite structure in which CuS_3 groups are shown as shaded triangles, distorted CuS_4 groups are shown as line hatched tetrahedra.

after Evans 1979

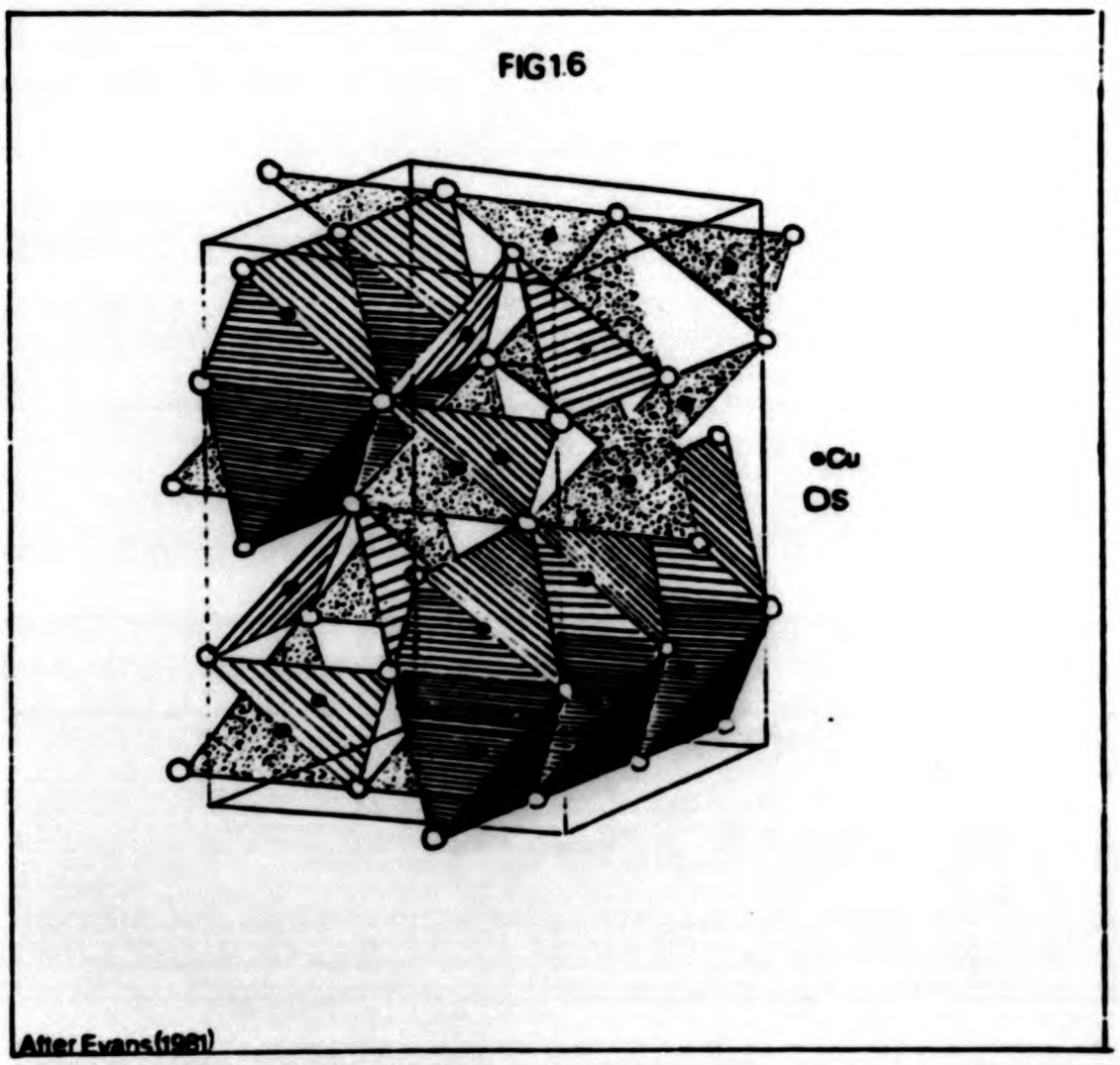

Fig 1.6 Crystal structure of anilite showing CuS_3 triangles and CuS_4 tetrahedra.

Eisenmann (1952) and later Abdullaev et al. (1968) have shown that interband transitions, manifested by an increase in absorption, commence at 1.8 eV and continue into the ultra-violet. These interband transitions are essentially independent of crystallographic orientation (Mulder, 1973). In the near infra-red, however, some weak absorption features are detectable which are polarisation dependent. These occur at 1.1 eV for light vibrating perpendicular to the c axis and at 1.4 eV for light vibrating parallel to the c axis. Marshall and Mitra (1965) have attributed these features to 'interband transitions' with electron and hole states at different points in the Brillouin zone. Mulder (1973) has suggested that the difference in energy between these polarisation dependent transitions arises from the fact that the valence band edge is predominantly S 3p rather than Cu 3d in character, with the wave function lobes perpendicular to the c axis.

1.3 Galena (Lead Sulphide)

1.3.1 Occurrence and Associations

The name galena comes from the Latin for lead ore. It is found following the bedding planes of some sedimentary rocks, in limestone replacement deposits, in hydrothermal veins and in pegmatites.

Crystals of galena are often in the form of cubes modified by octahedra. The perfect cubic cleavage is nearly always visible, and triangular pits along the cleavage lines are common. Twinning, in the form of contact or penetration twins is known though a zoned texture is not usual. Mosaic defects are common.

1.3.2 Structure of Galena

Galena has the simple halite (NaCl) structure, in which the anions are cubic close packed in planes parallel to [111]. Both the anions and the cations show regular six fold octahedral coordination, with the MX_6 octahedra sharing all twelve edges with adjacent octahedra (Fig. 1.7). Isostructural minerals include clausthalite (PbSe), altaite (PbTe) alabandine (α MnS) and oldhamite (CoS). The clear preference of galena (and clausthalite and altaite) for the high symmetry halite (NaCl)

FIG 1.7

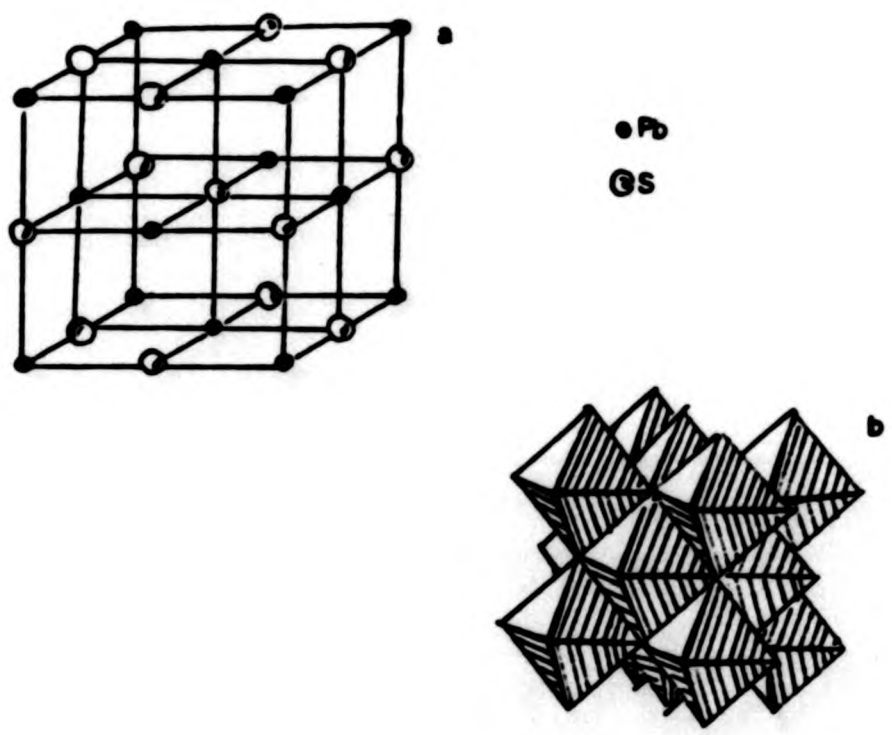

After Vaughan and Craig 1978

Fig 1.7 : a.Structure of galena
b.Arrangement of coordination polyhedra in galena.

structure can be understood in terms of the general trend towards 'metallic' structures going down a group (Adams 1974), although in this case the 'inert pair' does not exert a stereochemical effect. The bonding in lead sulphide can be described in terms of the overlap of the two 6p electrons on lead and the four 3p electrons on sulphur. Since the p-band is partially filled, metallic behaviour would be expected. In some respects PbS is best described as an intermetallic compound. Its electronic conductivity is, however, in the semi-conductor range due to the strong localisation of electrons on sulphur.

1.3.3 Optical and Electronic Properties

Galena can be either a n- or p-type semiconductor depending on whether the metal or the sulphur is in excess. Most natural galenas exhibit the metal-rich n-type semiconductivity, although Shuey (1975) has observed sulphur-rich p-type semiconductivity in galena from silver-rich hydrothermal deposits and limestone-zinc-lead 'Mississippi Valley type' deposits. Galena is opaque at wavelengths beyond the fundamental absorption edge, but at long wavelengths (less than 0.4 eV) it is transparent. The optical properties of lead chalcogenides have been extensively studied (Cardonna and Greenaway, 1964; Schoolar and Dixon, 1965; Dalven, 1969; Vaughan and Craig, 1978; Vendrell-Saz, Karup-Moller and Lopez Soler, 1978). Cardonna and Greenaway (1964) have examined the spectral reflectivity of galena, clausthalite and altaite over an energy range of 0 - 25 eV. They observed six peaks designated E_1 - E_6 which can be attributed to the following transitions (Fig. 1.8):

i) E_1,E_2 and E_3: transitions between the sulphur 3p non-bonding type orbitals and the conduction band.

ii) E_4, E_5 and E_6: transitions between the lead 6s-sulphur 3p bonding orbitals, and the sulphur 3s non-bonding orbitals into the conduction band.

As galena does not readily accommodate foreign ions in its structure, there is little in the literature relating to this phenomenon. Dalven, (1969) has reported the presence of donor and acceptor levels in galena due to bismuth and silver impurities. In clausthalite

FIG 1.8

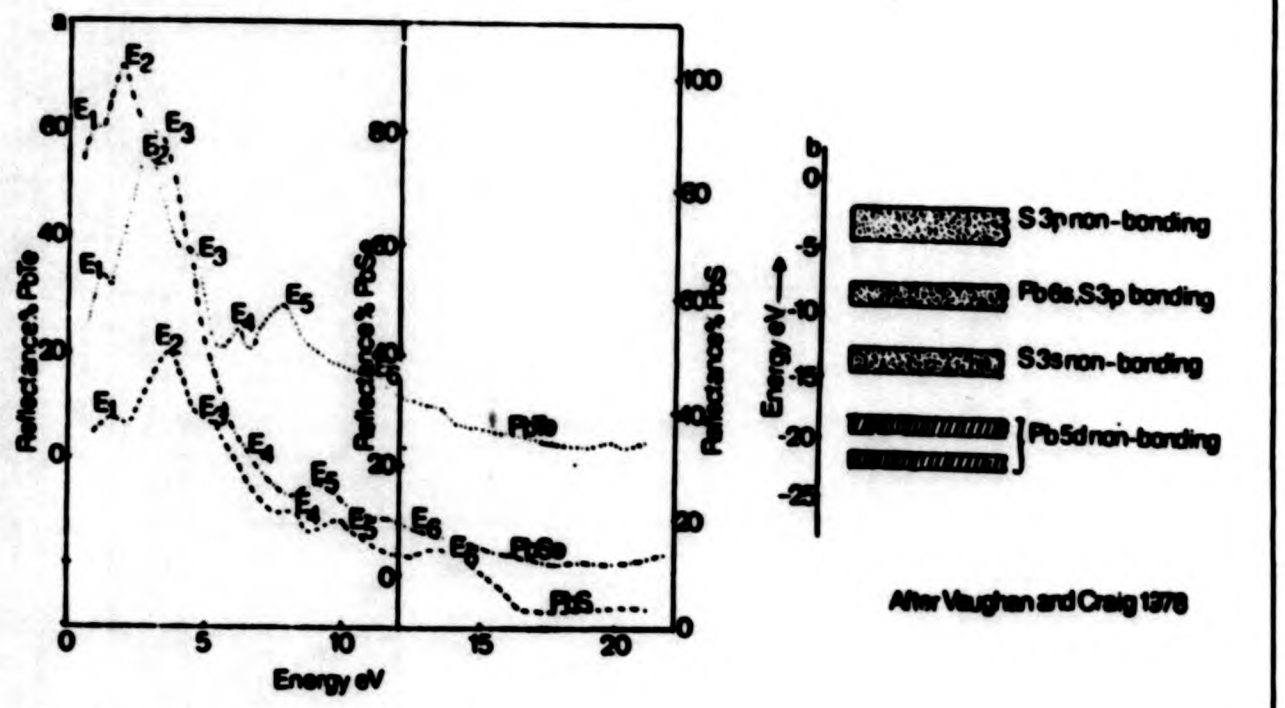

Fig 1.8 a. Reflectance dispersion curves for altaite(PbTe), clausthalite(PbSe), and galena at room temperature.

b. Simple band structure for galena.

and altaite more exotic elements such as gadolinium and bromine are responsible for the presence of donor levels. The presence of such donor and acceptor levels are known to influence the conductivity from which it can be deduced that they will also have an effect on the reflectivity.

1.4 Pyrite (Iron II Sulphide)

1.4.1 Occurrence and Associations

The name pyrite is derived from the greek 'pyr' meaning fire, and alludes to the fact that the mineral produces sparks when struck. Pyrite is one of the most widely distributed of the sulphide minerals, occurring in a variety of environments. In igneous rocks it occurs as an accessory mineral and in segregations. It is particularly prevalent in sedimentary rocks formed under stagnant anaerobic conditions, such as coals and black shales. It is also found in contact metamorphic zones. In slates it frequently forms well shaped cubic crystals. Pyrite is also commonly found in hydrothermal veins, and replacement deposits.

Crystals of pyrite are usually cubes, pyritohedra, octahedra or combinations of these forms. The cubes often show striations produced by oscillatory growth. The cleavage is poor and parallel to [100], [311] and [111] . Twinning is rare but when it does occur it appears as the iron-cross twin. Zoning is common and may be revealed by differences in colour and hardness.

1.4.2 Structure of Pyrite

Pyrite was one of the first minerals to be examined by X-ray diffraction techniques (Bragg, 1913). The lattice has cubic symmetry and is a derivative of the halite (NaCl) structure. The iron atoms form a face-centred-cubic array with the mid-point of covalently bonded S_2 dumb bells occupying the position of Cl^- in the NaCl structure, Fig. 1.9. Each sulphur atom is coordinated in a distorted tetrahedron to three iron atoms and one sulphur atom (in the S_2 unit). These S_2^{2-} pairs are aligned with the four distinct body diagonals of the cubic lattice. The iron cation is coordinated to six sulphur atoms. The sulphur octahedron is compressed along the trigonal axis and shares corners with neighbouring

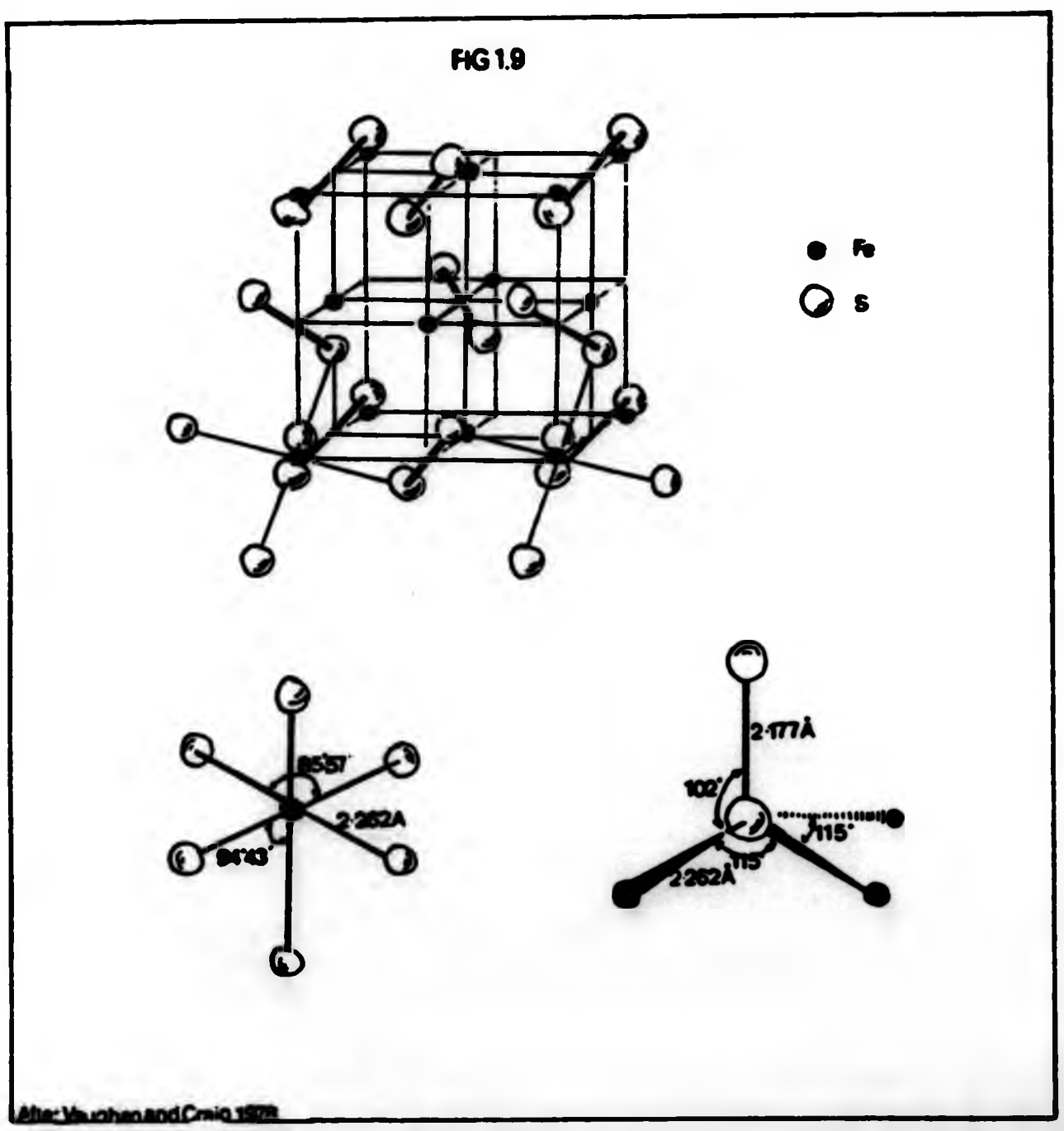

Fig 1.9 Structure of pyrite showing distorted octahedral co-ordination about iron, arrangement of S_2^{2-} dumb-bells and distorted tetrahedral co-ordination about sulphur.

octahedra. The pyrite structure is an important 'structure type' especially in chalcogenide mineralogy and is adopted by the following minerals:

Cattierite (CoS_2)
Vaesite (NiS_2)
Hauerite (MnS_2)
Trogtalite ($CoSe_2$)
Cobaltite (CoAsS)
Gersdorffite (NiAsS)
Ullmannite (NiSbS)
Penroseite ($NiSe_2$)

The bonding in pyrite is essentially covalent. The tetrahedral coordination of each sulphur atom is achieved by the hybridisation of the 3s and 3p orbitals to form sp^3 hybrids (Bither et al, 1968; Burns and Vaughan, 1970). One of the four sp^3 hybrids is involved in bonding with a sp^3 hybrid orbital from another sulphur ion (to form the S_2^{2-} pair). The remaining three are used in bonding with three d^2sp^3 hybrid orbitals from the cations. The d^2sp^3 hybrids are formed by the hybridisation of the 4s, 4p and $3d_{eg}$ orbitals of the iron, the remaining three $3d_{t2g}$ orbitals are assumed to be non-bonding (Bither et al, 1968). Burns and Vaughan (1970) have speculated that π bonding may occur between the filled non-bonding $3dt_{2g}$ orbitals of iron and the vacant $3dt_{2g}$ type orbitals of sulphur. This would increase the energy separation between t_{2g} and e_g orbitals ($\Delta_{cov-\pi} > \Delta_{cov-\sigma}$ Fig. 1.10). At the moment however, the presence of such bonding is uncertain, and Kjekshus and Nicholson (1971) found no evidence of π back-bonding. The iron in pyrite from Mossbauer, and magnetic studies has been shown to be low spin iron II (Benoit, 1955; Bither et al, 1968; Miyahara and Teranishi, 1968; Vaughan 1971) i.e., all six d electrons are spin-paired in the non-bonding t_{2g} orbitals. The molecular-orbital diagram shown in Figure 1.10 shows the splitting of the 3d levels under the influence of an octahedral ligand field. However, due to the trigonal distortion of the sulphur octahedron, the site symmetry of Fe^{2+} (l.s.) is reduced from O_h to S_6 lifting the degeneracy of the e_g^* and t_{2g} levels.

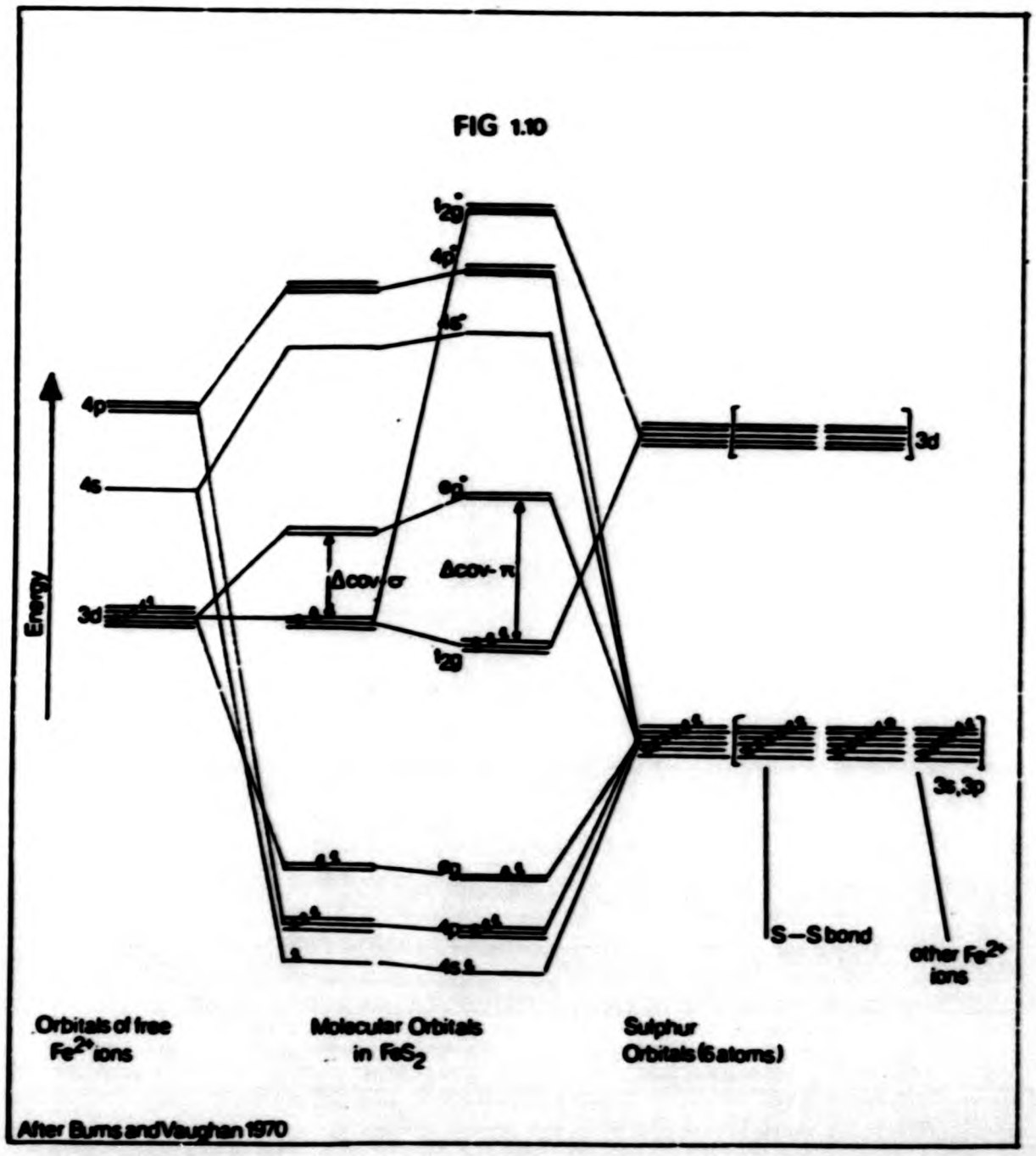

Fig 1.10 Molecular orbital energy level diagram for pyrite.

1.4.3 Optical and Electronic Properties

The infra-red reflectivity of pyrite has been measured by Verble and Wallis (1964) who identified four phonon lines (group theory predicts five). Schlegal and Wachter (1975) claim five lines although one of these is extremely weak. The reflectivity curves for pyrite in the visible and near ultra-violet have been considered by a number of workers (Bither et al. 1968; Schlegal and Wachter, 1975; Burns and Vaughan, 1970). Vaughan and Craig (1976) have shown that the absorption maximum is located at 1.7 eV (730 nm) indicating that the reflectivity of pyrite is greater in visible red light than in visible blue, which accounts for the yellow colour of the mineral. It must, however be remembered that beyond the absorption maximum, in the near infra-red, the reflectance of pyrite drops sharply and the mineral is relatively transparent. Schlegal and Wachter (1976) have assigned the peaks in the reflectance spectrum:

1. The peak at 2 eV is due to an inter-band transition between t_{2g}(n.b.) $\longrightarrow$ e_g^*. This peak is expected to be a doublet due to the non-degeneracy of the e_g^* levels.

2. The smaller peak at 3.9 eV is due to inter-band transitions (Fig. 1.11) from states of largely sulphur 3p character into the e_g^* state.

Cobalt, nickel, copper and gold are known to substitute for Fe^{2+} in pyrite (Uytenbogaardt and Burke (1971)). Up to eight weight percent arsenic can substitute for sulphur, and is most frequently found in 'melnikovite pyrite'. The reflectance of pyrite decreases as the concentration of impurity ions such as $Co^{2+}(d^7)$, $Ni^{2+}(d^8)$ and $Cu^{2+}(d^9)$ increases, the effect being most marked for Cu^{2+} substitution. This is caused by electrons entering the anti-bonding e_g^* orbitals, Vaughan and Craig (1978) have shown that reflectance in pyrite type minerals is proportional to the number of unoccupied e_g^* levels (Section 1.2). The decrease in reflectivity is paralleled by an increase in the size of the unit cell edge caused by the sulphur ligands being repelled outwards by the electrons now occupying the d_z2 and $d_x2_{-y}2$ orbitals. The presence of nickel impurity ions will introduce a small amount of splitting

FIG 1.11

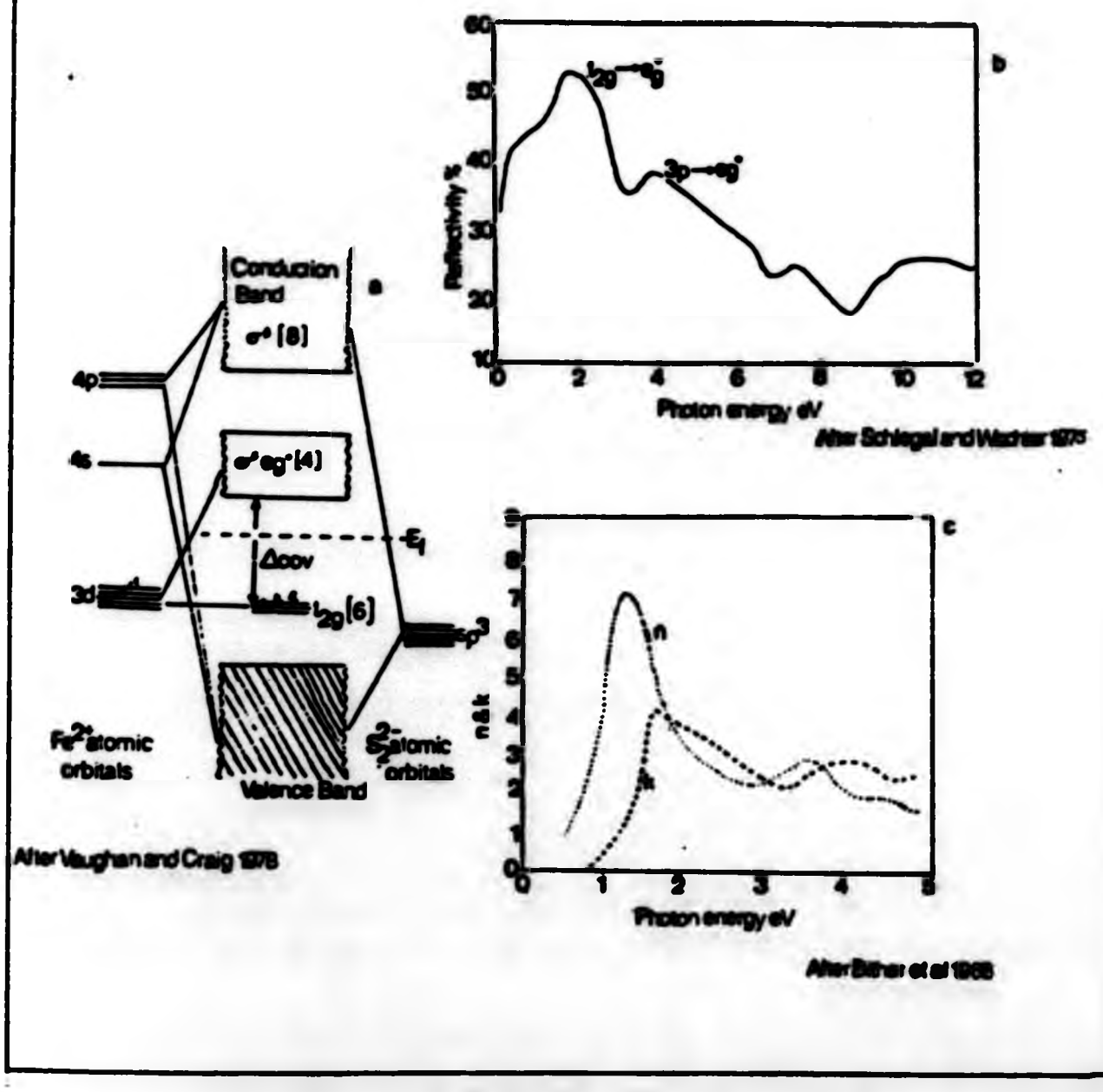

Fig 1.11 *a. Schematic energy band diagram for pyrite. E_f fermi level, numbers in brackets refer to number of electrons allowed in each band, per molecule.*

b. Reflectance dispersion curve for pyrite showing the electronic transitions responsible for the positions of certain peaks.

c. n & k dispersion curves for pyrite.

in the optical spectrum which is due to Jahn-Teller coupling which lifts the degeneracy of the d_z2 and $d_x2_{-y}2$ states.

1.5 Skutterudite (Cobalt, Nickel, Iron Arsenide)

1.5.1 Occurrence and Associations

Skutterudite derives its name from the locality of Skutterud (Sweden). The names smaltite, and chloanthite have been applied in the past to isometric nickel and cobalt diarsenides respectively. These names should not be used as nickel and cobalt diarsenides do not exist (Roseboom, 1962). Skutterudite occurs in veins where it can be intergrown with nickeline or bismuth. Nickel-rich skutterudites are most frequently found in association with silver, while cobalt-rich ones prefer association with bismuth. Crystals of skutterudite are usually cubes, octahedra, pyritohedra or combinations of these forms. Twinning is not observed. The cleavage is cubic and octahedral, and is rare in cobaltian skutterudites; zoning may also occur.

1.5.2 Structure of Skutterudite

Nickel (1970) has discussed the structure and bonding in skutterudites in terms of ligand-field theory. The structure for the pure $CoAs_3$ end member is unusual and is constructed of square planar arsenic groups octahedrally coordinated about the cation. Tossell (1983) views this structure as a distorted ReO_3 lattice, "in which the non-metal atoms on the four parallel edges of the unit cell are displaced into the cell to form a square planar group", (Fig. 1.12). Tossell suggested, using electron counting, that such a distortion is only favoured if the A_4 unit (in this case As_4) possesses 22 to 24 valence electrons.

Pleass and Heyding (1962) have shown that $CoAs_3$ is diamagnetic, indicating that the cobalt is trivalent and low spin i.e. all six d-electrons are spin paired in the t_{2g} level. This model is consistent with the bonding scheme proposed by Nickel (1970) whereby the cation forms electron pair bonds with the six nearest neighbour arsenic atoms (Fig. 1.12). The solid solution field for skutterudite (Fig. 1.13) extends from the pure cobalt end-member to the opposite side of the

Fig 1.12 a. *Structure of skutterudite showing square planar rings octahedrally co-ordinated about cobalt.*

b. *Distortion of ReO_3 structure to form square planar As_4 rings*

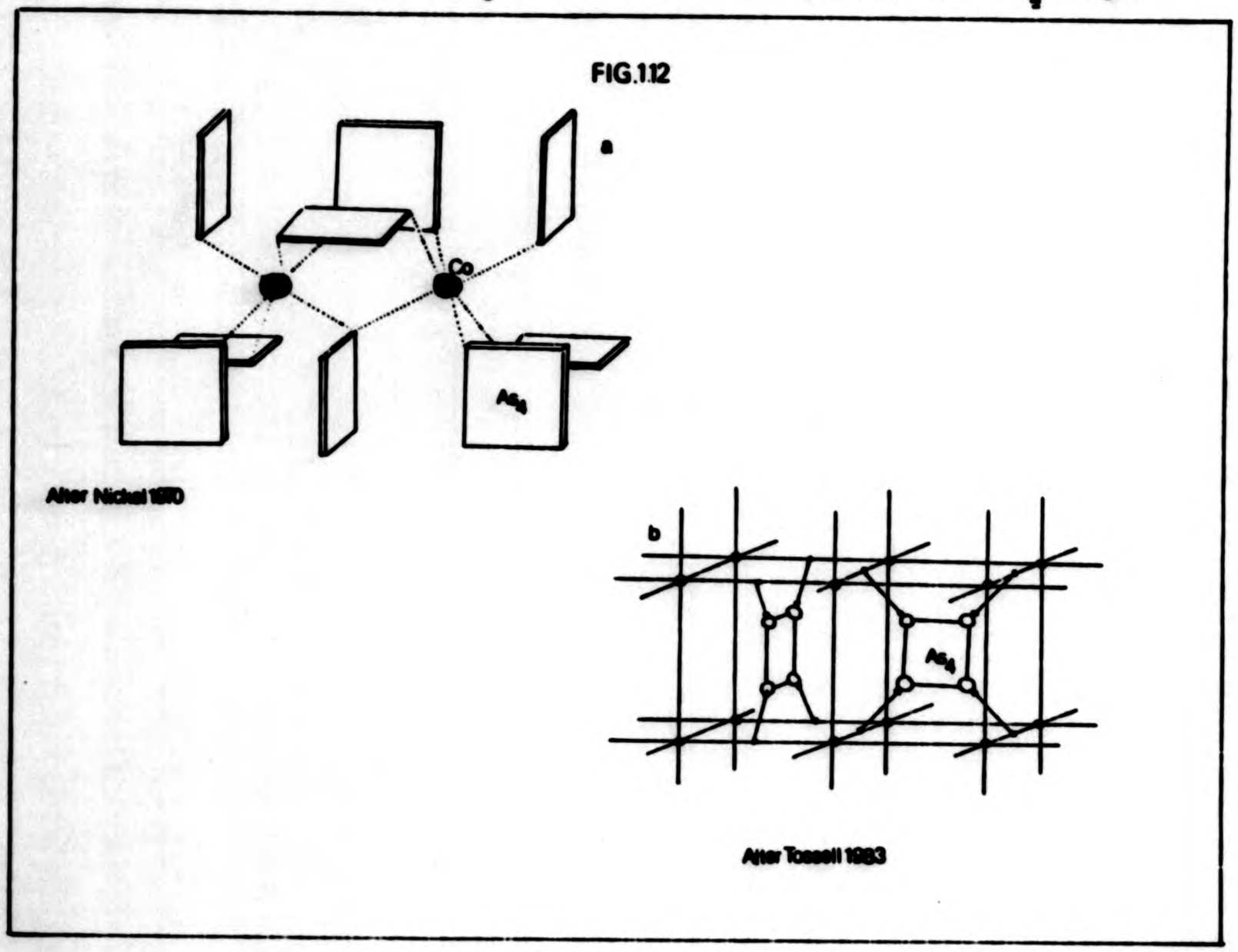

FIG 1.13

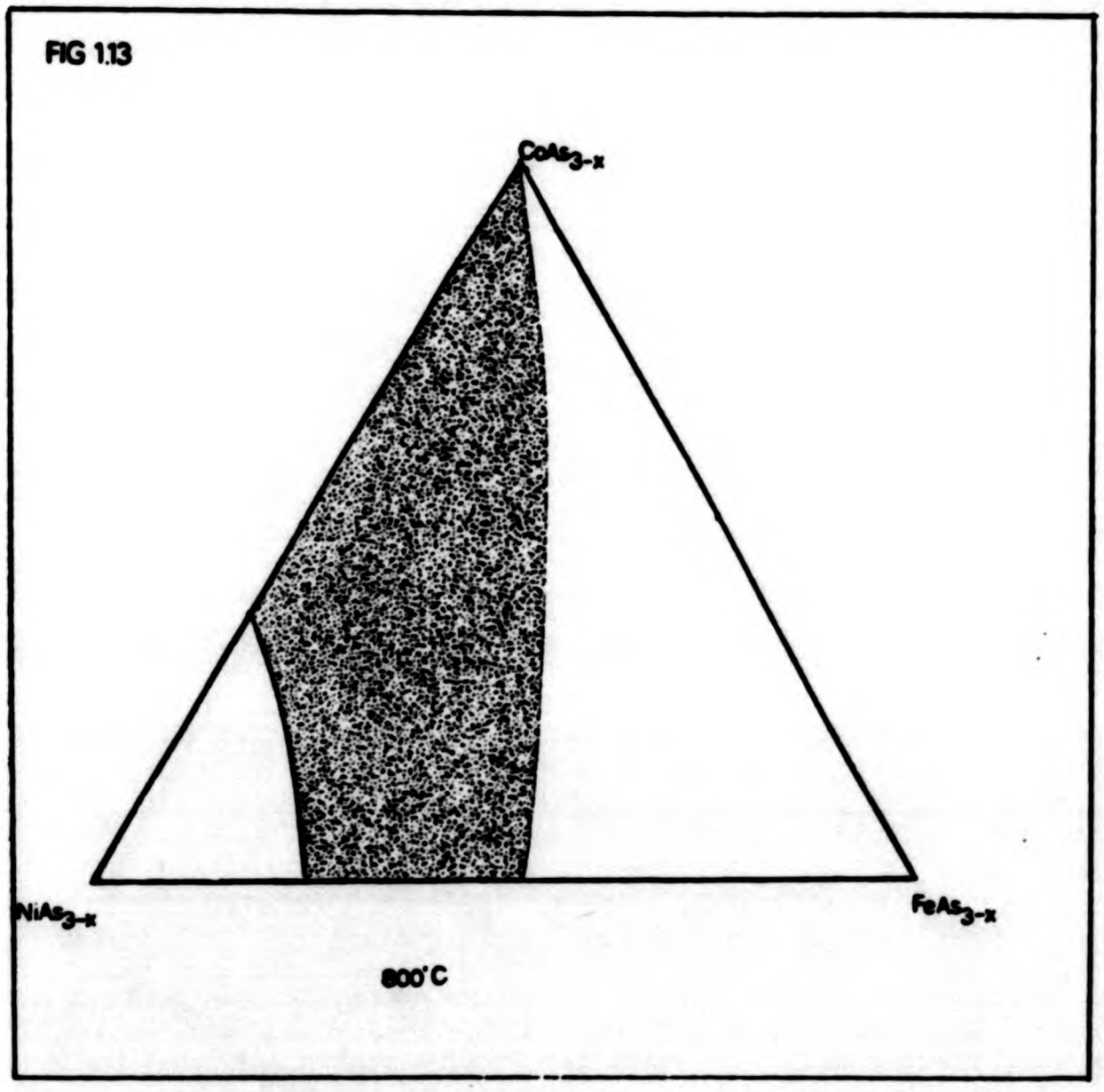

Fig 1.13 Phase diagram for skutterudite, shaded area delineates the compositionally stable region at 800°C

ternary diagram. This indicates that only coupled replacement of cobalt by nickel and iron can occur. Nickel (1970) has postulated that to maintain the t_{2g}^6 configuration the iron must be divalent while the nickel must be tetravalent:

$$2Co^{3+}(t_{2g}^6) \longrightarrow Fe^{2+}(t_{2g}^6) + Ni^{4+}(t_{2g}^6)$$

In this conclusion Nickel has neglected to mention that the Ni (IV) species is highly oxidising and would be unstable in the skutterudite lattice, Ni^{2+} therefore seems a far more likely choice (see chapter 7). The presence of Ni^{2+} as opposed to Ni^{4+} would also seem to explain the characteristic arsenic deficiency in skutterudites. In order to maintain charge neutrality some arsenic atoms must be missing. Thus the greater the substitution of nickel and iron for cobalt the higher will be the arsenic deficit.

1.5.3 Optical and Electronic Properties

Few data can be found in the literature relating to the optical and electronic properties of skutterudite. The only optical data are those found in the International Mineralogical Association, Commission on Ore Microscopy (IMA, COM) data file. To date no band structure has been calculated for the mineral. This is probably because of its wide solid solution field and the complexities involved when dealing with a multiple cationic situation. It is known that skutterudite is diamagnetic (Pleass and Heyding, 1962) and its high reflectance seems to suggest a narrow band gap.

1.6 Sphalerite (Zinc Sulphide)

1.6.1 Occurrence and Associations

The name sphalerite is derived from Greek, meaning treacherous, and refers to its great variability of appearance in hand specimens. Sphalerite is also often referred to as zinc-blende and is the most common and widespread zinc mineral. The mineral is often found in hydrothermal deposits in association with galena and other medium temperature minerals.

It may also be found in limestone replacement bodies in association with pyrite and magnetite. Crystals of sphalerite are commonly tetrahedral or rhombdodecahedral and are often distorted with curved faces. The cleavage, parallel to [110] is perfect rhombdodecahedral.

1.6.2 Structure of Sphalerite

Like pyrite (FeS_2), sphalerite was one of the early structure types investigated by Bragg (1913). the structure (Fig. 1.14) consists of a face-centred-cubic (f.c.c.) array of sulphur atoms in which half the tetrahedral sites are occupied by zinc atoms. The arrangement of the occupied sites is such that the structure can also be viewed as two interpenetrating f.c.c. lattices, one of sulphur and the other of zinc. Each zinc atom is coordinated to four sulphur atoms in a regular tetrahedron, and each sulphur atom lies at the centre of a regular tetrahedron of zinc atoms. The zinc blende structure is an important type structure and is adopted by hawleyite (CdS), metacinnabarite (HgS), tiemannite (HgSe), coloradoite (HgTe), and stilleite (ZnSe). When carbon replaces all the zinc and sulphur atoms the diamond structure is obtained.

The tetrahedral coordination of both sulphur and zinc suggests the involvement of sp^3 hybrids (hybridised 3s and 3p orbitals in the former and 4s and 4p orbitals in the latter) in the formation of σ bonds. The d electrons of zinc can be effectively regarded as core electrons, i.e., they play no part in bonding.

1.6.3 Optical and Electronic Properties

Pure sphalerite is a diamagnetic semi-conductor with a large band gap (3.65 eV), the absorption edge is located in the near ultra-violet at 340 nm hence the pure mineral is transparent and colourless. Naturally occuring sphalerites, however, are rarely without colour because the sphalerite lattice has a pronounced tendency to incorporate foreign ions in its structure. As iron is the most common substituent for zinc its effects have been extensively studied (Nickel, 1965; Low and Werger, 1960; Barton and Tolumin, 1963; Marfunin, Platanov and Fedorov, 1968; Manning, 1967; Vaughan and Tossell, 1980; Velasco, Pesquera and Autefage, 1981). Increasing iron concentration causes the

FIG 1.14

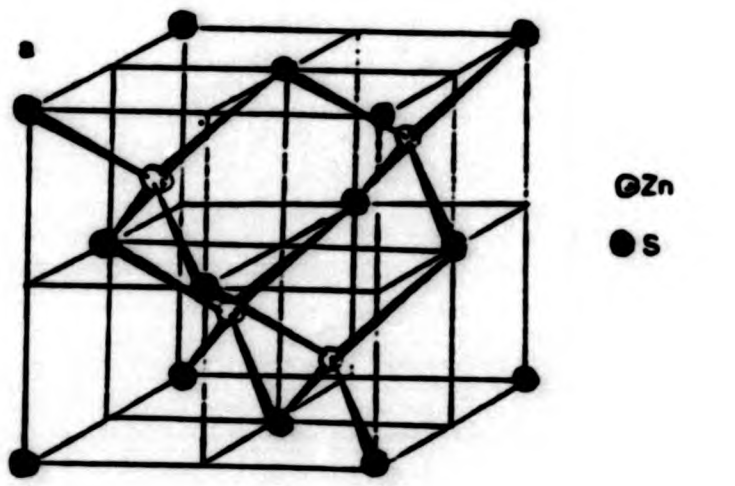

After Vaughan and Craig 1978

Fig 1.14 a. Structure of sphalerite.
b. Linkage of ZnS_4 tetrahedra in sphalerite.

colour of natural sphalerites to change from light yellow (low Fe content) to almost opaque dark browns and black (high Fe content). The absorption band in the infra-red at 3500 cm^{-1} (3,000 nm) has been attributed to Fe^{2+} in tetrahedral sites by Low and We ger, (1960) and is thought to be the single spin allowed $3d\ e_2 \rightarrow 3d\ t_2$ ($^5E_2 \rightarrow {}^5T_2$) transition. Marfunin, Platanov and Fedorov (1968) have observed a similar transition, but have reported it as a triplet not a singlet, they ascribed this splitting to Jahn-Teller coupling. This interpretation is somewhat surprising as Jahn-Teller effects are usually only seen in octahedral complexes. Mossbauer data (Vaughan and Craig, 1978) do not substantiate this finding, nor does it support Manning's (1967) hypothesis of trivalent iron in octahedral sites. The effects of iron substitution upon reflectance have been investigated by Velasco, Pesquera and Autefage (1981) who have found a nonlinear increase in reflectivity with increasing iron concentration.

Marfunin, Platanov and Fedorov (1968) have looked at the colours and absorption spectra of a large number of naturally occurring sphalerites, from various localities, and have identified several distinct features which they attribute to (Fig. 1.15):

i) Fundamental absorption edge; the position of which is defined by the energy required to promote an electron from the valence band into the conduction band. It is the most intense feature in the spectrum.

ii) Crystal field spectra; these features are mainly attributable to substitution by Mn^{2+}, Fe^{2+}, Co^{2+} and Ni^{2+} into the tetrahedral zinc sites. This gives rise to spin-allowed and weaker spin-forbidden 3d intra-band transitions. It is partly because of these crystal field effects that sphalerite has been so extensively studied as they provide a rare opportunity to study transition metal ions in tetrahedral coordination with sulphur.

iii) Charge-Transfer spectra; these are caused by the same cations as the crystal-field phenomena, and occur in the ultra-violet and visible blue region of the spectrum superimposed on the

FIG 1.15

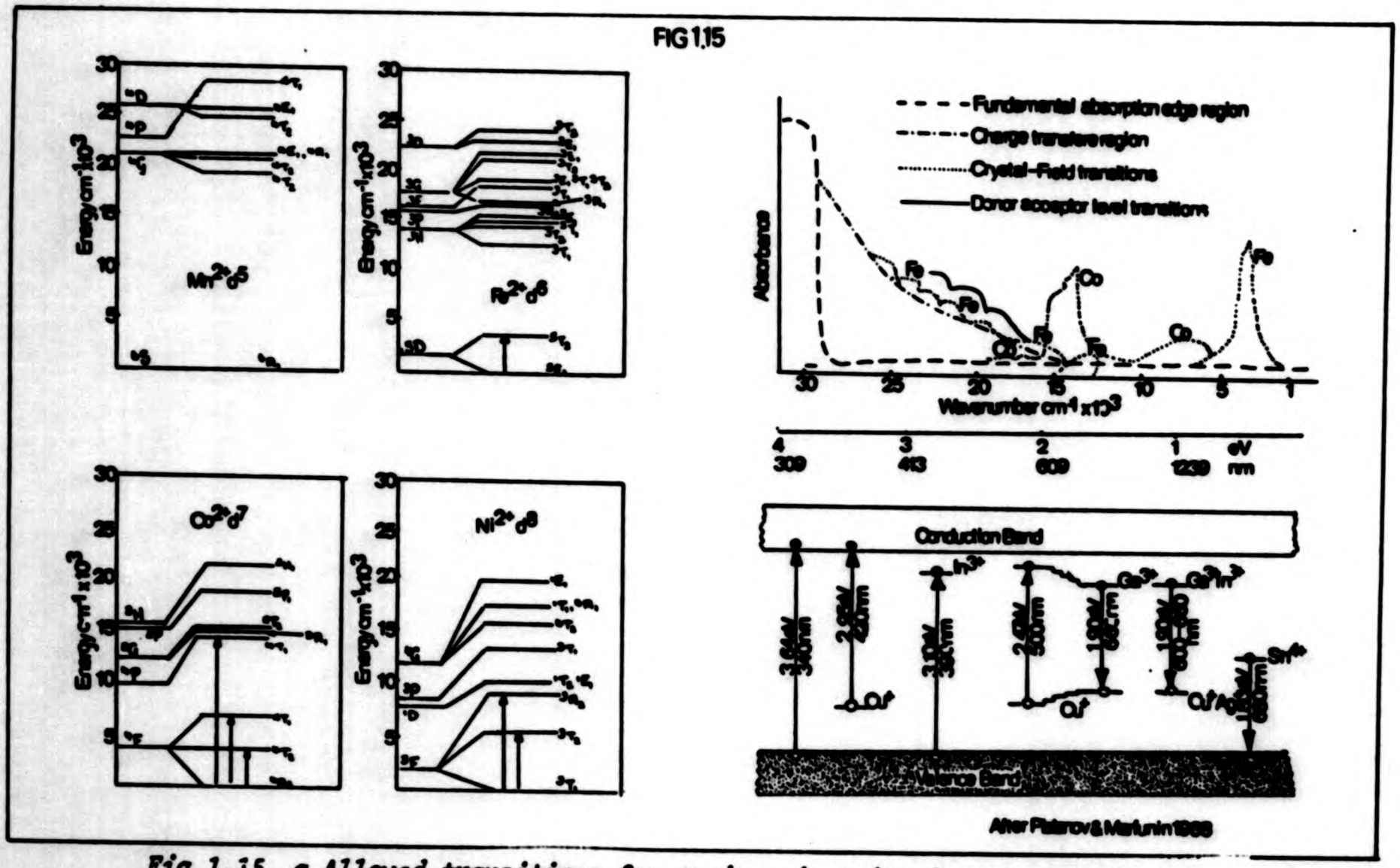

Fig 1.15 *a. Allowed transitions for various impurity ions in sphalerite.*

b. Composite diagram of the the electronic absorption spectrum for natural sphalerites.

c. Position of donor and acceptor levels in the band gap of ZnS.

broad intense absorption band. The mechanism of the charge-transfer is thought to be via the photoionization of the impurity ions promoting an electron from the localised d level into the conduction band i.e. $Fe^{2+} \longrightarrow Fe^{3+} + e^-$.

iv) Spectra due to extrinsic semi-conduction caused by the participation of donor and acceptor levels due to the presence of small amounts of univalent Cu^+, Ag^+, trivalent In^{3+}, Ga^{3+}, As^{3+}, Sb^{3+} and quadrivalent Sn^{4+} ions . The colours of naturally occurring sphalerite are principally affected by the amount of Fe^{2+} present in the lattice (see above), however, when the iron content is less than 1 atomic percent, small amounts of cobalt produce bluish-green colours, and the presence of donor and acceptor ions M^+, M^{3+} and M^{4+} causes orange-red colouration.

1.7 Tetrahedrite - Tennantite (Fahlore)

1.7.1 Occurrence and Associations

Minerals in the tetrahedrite-tennantite (Fahlore) solid solution series occur principally in hydrothermal veins, although tennantite has been found in metasomatic limestone deposits. The names freibergite, schwatzite, and annivite refer respectively to the silver, mercury and bismuth rich varieties of tetrahedrite.

Crystals of fahlore minerals are commonly tetrahedral, hence the name tetrahedrite. No cleavage is usually apparent and twinning is in the form of contact or penetration twins on the tetrahedron. A zonal texture is common and may be revealed by etching.

1.7.2 Structure of Tetrahedrite and Tennantite

A structure for tetrahedrite was first postulated by Machatschki (1928), based on the formula Cu_3SbS_3. Improved methods of chemical analysis led Pauling and Newman (1934) to suggest that the formula was actually $Cu_{12}Sb_4S_{13}$, and proposed a structure based on a derivative of the sphalerite lattice. This structure was refined in 1964 by Wuensch, who also proposed the general formula $X_{12}Z_4S_{13}$, for members of the

tennantite (Z = As) - tetrahedrite (Z = Sb) solid solution series where the cation X = Cu but could be substituted by up to 16% of Zn, Fe, Ag, Hg, Pb, Ni and Co. The results of more recent research have revised this formula to $A_{10}B_2C_4D_{13}$ where:

A = Cu, Ag;
B = Cu, Fe, Zn, Hg, Cd, Pb;
C = Sb, As, Bi, Te;
D = S, Se;

(Springer, 1969; Johan and Kvacek, 1971; Charlat and Levy, 1974; Patrick, 1978; Cvech and Hak, 1979; Sandecki and Amcoff, 1981; Basu et al, 1981).

The basic structure of tetrahedrite, described by Wuensch (1964) is as follows: considering first the coordination of the copper and antimony atoms about sulphur (Fig. 1.16), two observations can be made;

i. Six Cu(2) are octahedrally co-ordinated about S(2) at 2.234 Å to form a regular octahedron.

ii. Each S(1) is tetrahedrally co-ordinated, to two Cu(1) at 2.342 Å, one Cu(2) at 2.272 Å and one Sb at 2.446 Å to form a distorted tetrahedron.

The linkage of the regular octahedra and distorted tetrahedra is indicated in Fig. 1.16 in which a quarter of the unit cell is shown. The antimony atoms are located on those corners of the tetrahedra which lie closest to the octahedron. A void exists in the structure at the site where a sulphur atom is missing from a complete sphalerite arrangement, seen in Figure 1.16 at the left hand corner of the cell.

Considering the co-ordination of sulphur atoms about copper and antimony reveals several features about the structure which are obscured in the sphalerite analogy (Fig. 1.17).

i) Four S(1) atoms are co-ordinated about each Cu(1) to form a slightly distorted tetrahedron, the Cu(1)-S(1) bond length is 2.342 Å

FIG 1.16

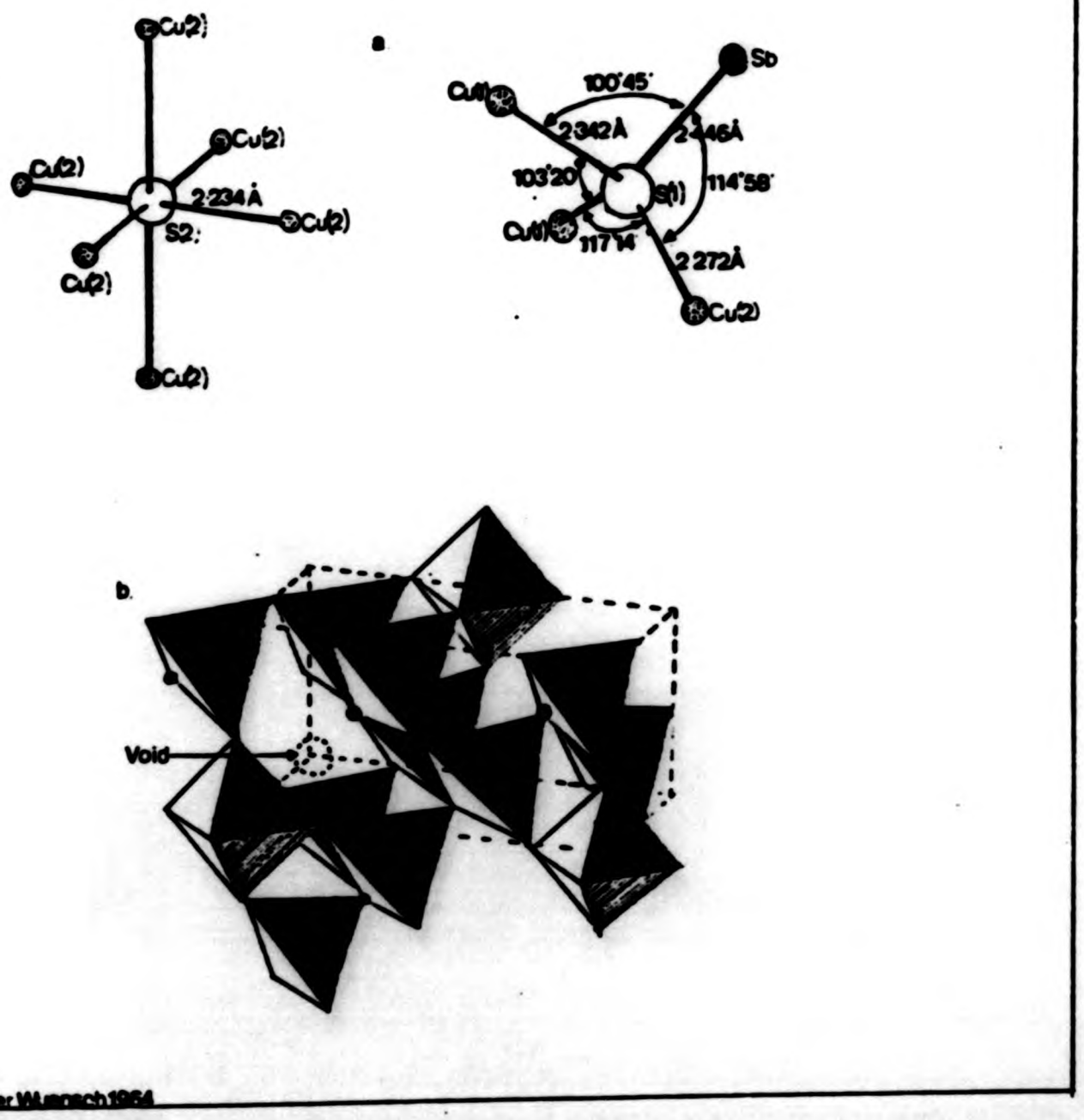

After Wuensch 1964

Fig 1.16 Co-ordination and linkage of polyhedra formed by metal atom co-ordination to sulphur in tetrahedrite.

a. Co-ordination polyhedra.

b. Linkage of SCu_6 and SCu_3Sb polyhedra ● represent positions of Sb atoms, all other vertices represent Cu atom positions.

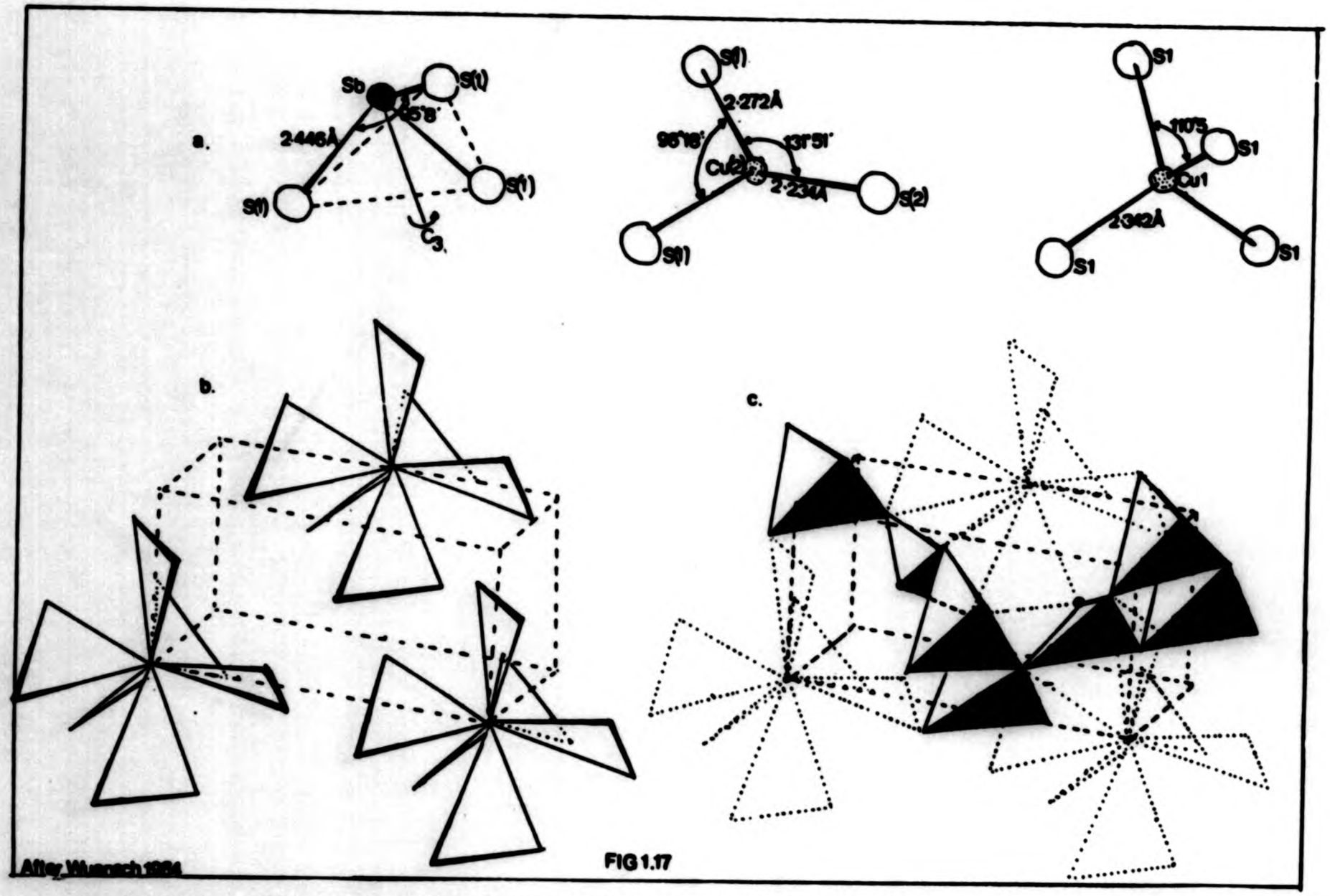

Fig 1.17 Co-ordination and linkage of polyhedra formed by sulphur atom co-ordination to metal atoms in tetrahedrite.

a. Co-ordination polyhedra

b. Arrangement of "spinners", composed of six CuS_3 triangles sharing a corner.

c. Linkage of SbS_3 pyramids and CuS_4 tetrahedra.

ii) Cu(2) is trigonally co-ordinated to two S(2) at 2.272 Å and one S(2) at 2.234 Å, this group is planar as it lies entirely within the <110> symmetry plane of the cell.

iii) Three S(1) atoms are located about a C_3 axis, at 2.446 Å from Sb, which forms the apex of the pyramid.

These polyhedra are linked in a complex manner. Six CuS_3 triangles share a corner at the origin, Fig. 1.17, to form a six bladed 'spinner' (Wuensch, 1964). As these triangles lie on the [110] symmetry planes of the cell there are four locations on the spinner where the corners of the three triangles are in close proximity. The base of the SbS_3 pyramid links these corners. Correspondingly there are four locations on the spinner where the corners of the triangles are widely separated, here the Sb atom at the apex of the SbS_3 pyramid associated with a neighbouring spinner sits snugly.

The co-ordination of antimony suggests the reason for the formation of such a structure. The disposition of the three short bonds in tetrahedrite suggests that the $4p^3$ electrons on antimony are involved in the formation of strong bonds. The failure of antimony to form a fourth bond with another sulphur atom accounts for the void in the structure. It is therefore misleading to describe the tetrahedrite structure as a sphalerite derivative, where different metal atoms have been substituted (as in chalcopyrite, $CuFeS_2$).

Minerals in the tetrahedrite-tennantite series have a pronounced tendency to incorporate foreign cations in their lattices (Springer, 1969), and are therefore sensitive indicators of the physico-chemical environment during ore deposition. Common cation substituents are zinc, iron and silver. Riley (1974) has predicted the possible existence of a totally substituted tetrahedrite, composition $Ag_{10}(Fe,Zn)_2Sb_4S_{13}$. However, up to now no tetrahedrite in which all the univalent copper has been substituted by silver has been found. The concentration of silver in fahlore minerals makes them important silver ores, (Miller and Craig, 1983). Various workers namely Hall (1972); Atanasov (1975); Basu *et al.* (1981); Sandecki and Amcoff (1981); Miller and Craig (1983) have remarked on the significant antiparallelism between several of the substituting elements e.g. As/Sb,

As/Ag and Fe/Zn/Hg. In most cases this phenomenon can be explained by structural considerations.

The unit cell edge a is a sensitive parameter to changing composition. Across the series tennantite to tetrahedrite a increases with increasing antimony content from 10.168 Å in pure tennantite (Maske and Skinner, 1970) to 10.319 Å in pure tetrahedrite (Hall, 1972). Hall (1972) has shown that substitution by zinc, iron and silver results in the same increase in the unit cell edge (+0.0093 Å per 1.0 atomic percent Cu substituted). This, however, is not true for Hg substitution, where a increases more rapidly (a = 10.49 Å at 19 wt% Hg, (Bernard, 1958). This could be why the largest unit cell edge a = 10.64(1) Å so far reported (Atanasov, 1975) is for an argentian-mercurian tetrahedrite. Because of their economic importance freibergites (silver rich tetrahedrites) have been extensively studied. Petruk (1971) and Riley (1974) have shown that there is a uniform expansion of the lattice with increasing silver content up to 20 wt%, after which further increase in silver causes the lattice to contract. Kalbskopf (1977) showed that silver will preferentially enter the triangular planar Cu(2) sites and only when all these sites have been substituted will it be forced to enter the tetrahedral Cu(1) sites. Riley, (1974) suggested two possible explanations for the lattice contraction of silver-rich tetrahedrite:

i) The Ag-S bond being more covalent than the Cu-S bond.

ii) Different stacking sequence.

It is likely that both these factors are playing a part in reducing the size of the unit cell. However, as the Ag^{+} ion is larger than the Cu^{+} ion it seems likely that at a given silver concentration, lattice restructuring will occur.

In the Garpenberg-Moira deposit of central Sweden, Sandecki and Amcoff (1981) have noticed that when a tetrahedrite grain is adjacent to an arsenopyrite grain the silver content of the former is dramatically reduced, even when native silver is present in the assemblage. From this they conclude that a high concentration of arsenic has a more profound

effect on the structure than does silver, i.e. arsenic can readily enter the $(As, Sb)^{3+}$ site , while silver has a greater reluctance to enter the $(Cu,Ag)^{+}$ position if arsenic is already present in the structure. This could explain the antipathy between the two elements whereby As^{3+} compresses the structure so prohibiting the entry of Ag^{+}.

A number of references to plumbian fahlore minerals can be found in the literature (Hoffmann, 1895; Guimaraes, 1934; Nash, 1975; Bishop, Criddle and Clark, 1977; Basu et al. 1981) the two earliest of which are now regarded with some skepticism, as minerals from the same localities have been found to be associated with galena and jamesonite, which due to the lack of modern instrumental techniques could not be positively identified at the time. The presence of lead does not seem to significantly alter the unit cell dimensions (Bishop et al. 1977). As three-fold-planar coordination (Cu(1) site) and four-fold-tetragonal coordination (Cu(2) site) are typical for Pb^{II}, Basu et al. (1981) have suggested that lead enters the three-fold pyramidal site normally occupied by As and Sb. This supposition is backed up by the fact that in several lead sulphantimonides lead and antimony are reported to occupy the same positions in the crystal structure eg, zinckenite (Lebas and Lebihan, 1976; boulangerite Petrova, 1978).

1.7.3 Optical and Electronic Properties

The reflectance dispersion curves for the fahlore minerals (Figs. 1.18, 1.19, 1.20) show substantial variations with composition. Hall (1974) has synthesised a variety of tetrahedrites in order to determine the effects of iron, silver and zinc on their optical properties, i.e.;

i) Substitution of copper by zinc caused an increase in reflectivity which was essentially linear with increasing zinc content, it also caused the peak at 580 nm to become more pronounced, Fig. 1.18.

ii) Substitution of silver for copper caused a slight decrease in reflectance and a straightening of the curve in the 580 nm region, Fig. 1.19.

FIG 1.18

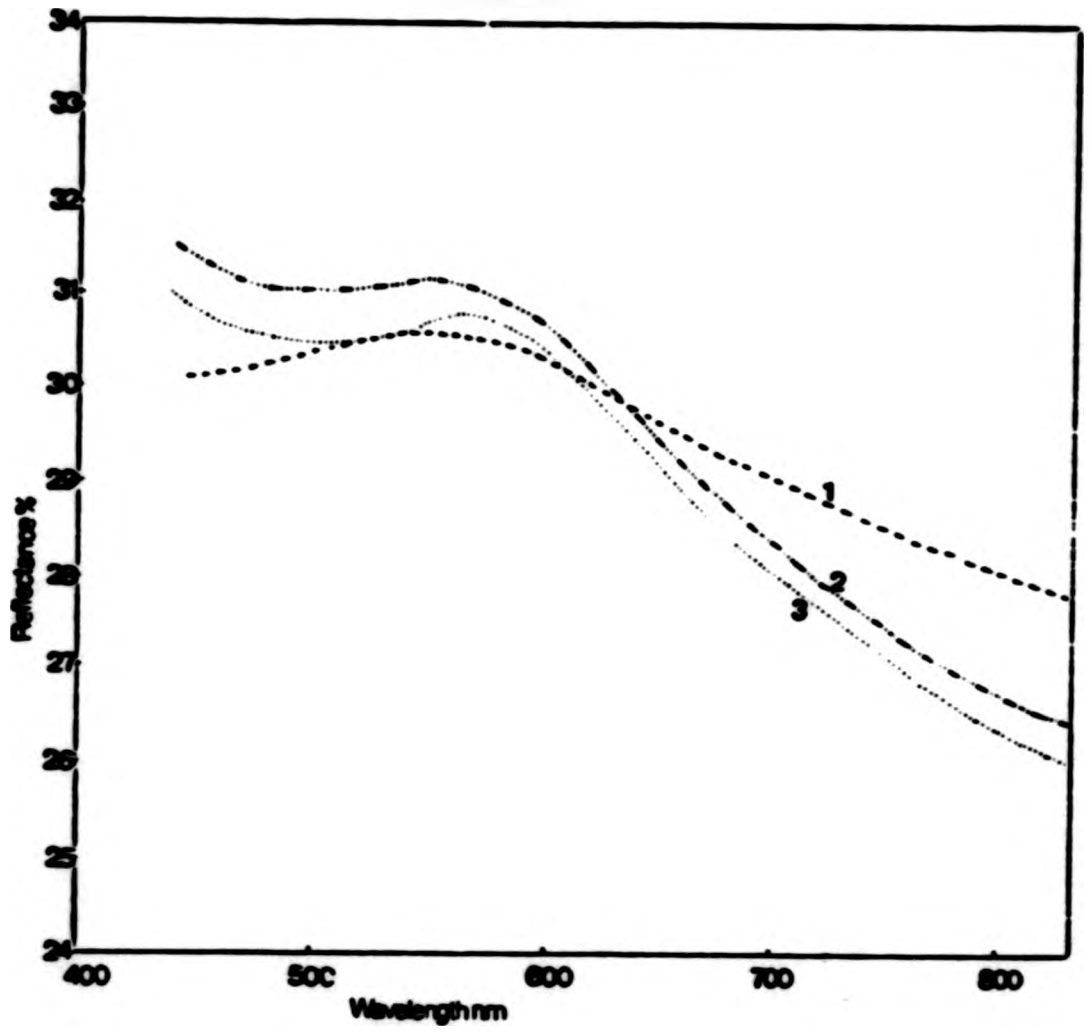

Zn/ Fe/Hg

1=$(Cu_{0.95}Ag_{0.05})(Cu_{0.25}Zn_{0.25}Fe_{1.45}Hg_{0.05})(Sb_{2.00}As_{1.00})S_{7}$

2=$(Cu_{0.97}Ag_{0.03})(Cu_{0.12}Zn_{0.00}Fe_{0.65}Hg_{0.23})(Sb_{2.02}As_{1.00})S_{7}$

3=$(Cu_{0.95}Ag_{0.05})(Cu_{0.00}Zn_{0.22}Fe_{0.00}Hg_{0.97})(Sb_{2.00}As_{1.00})S_{7}$

Charlat and Levy(1976)

Fig 1.18 Reflectance dispersion curves showing effects of Zn/Fe/Hg substitution.

Fig 1.19 Reflectance dispersion curves of substituted fahlore minerals, showing effects of silver, zinc and iron substitution.

FIG 1.19

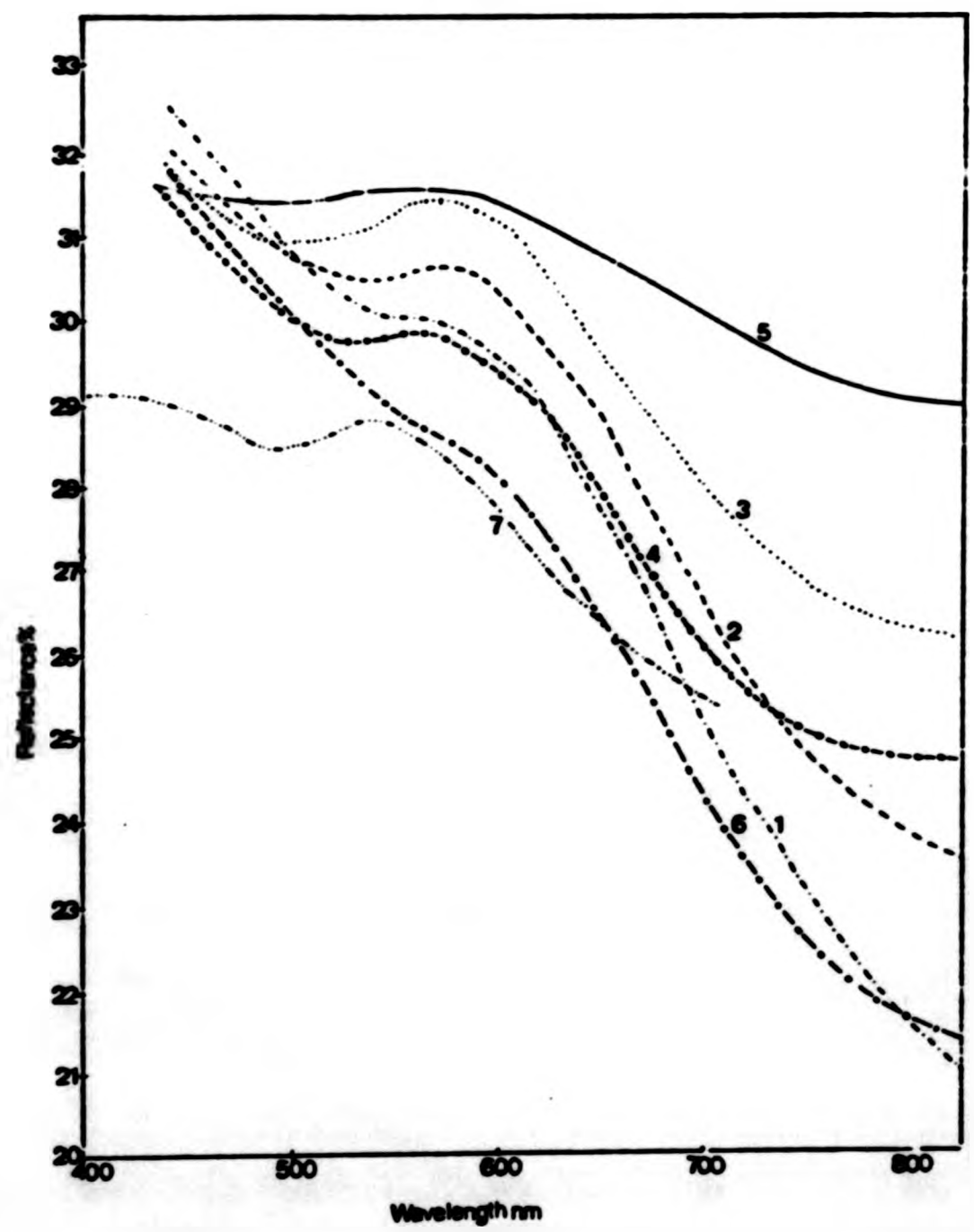

1=$Cu_{4.2}Sb_4S_{13}$

2=$Cu_{3.1}Zn_{1.1}Sb_4S_{13}$

3=$Cu_{4.0}Zn_2Sb_4S_{13}$

4=$Cu_{3.1}Ni_{1.1}Sb_4S_{13}$

5=$Cu_{4.0}Ni_2Sb_4S_{13}$

6=$Cu_{3.1}Ag_{1.1}Sb_4S_{13}$

7=$Cu_{4.0}Ag_{0.3}Zn_{0.5}Fe_{0.3}Pb_{0.1}As_{2.0}Sb_{1.8}S_{13.7}$

Hall, Cervelle and Levy (1974) synthetic substituted tetrahedrites

Bishop, Criddle, and Clarke (1977) Plumbian tennantite from Sark.

FIG 1.20

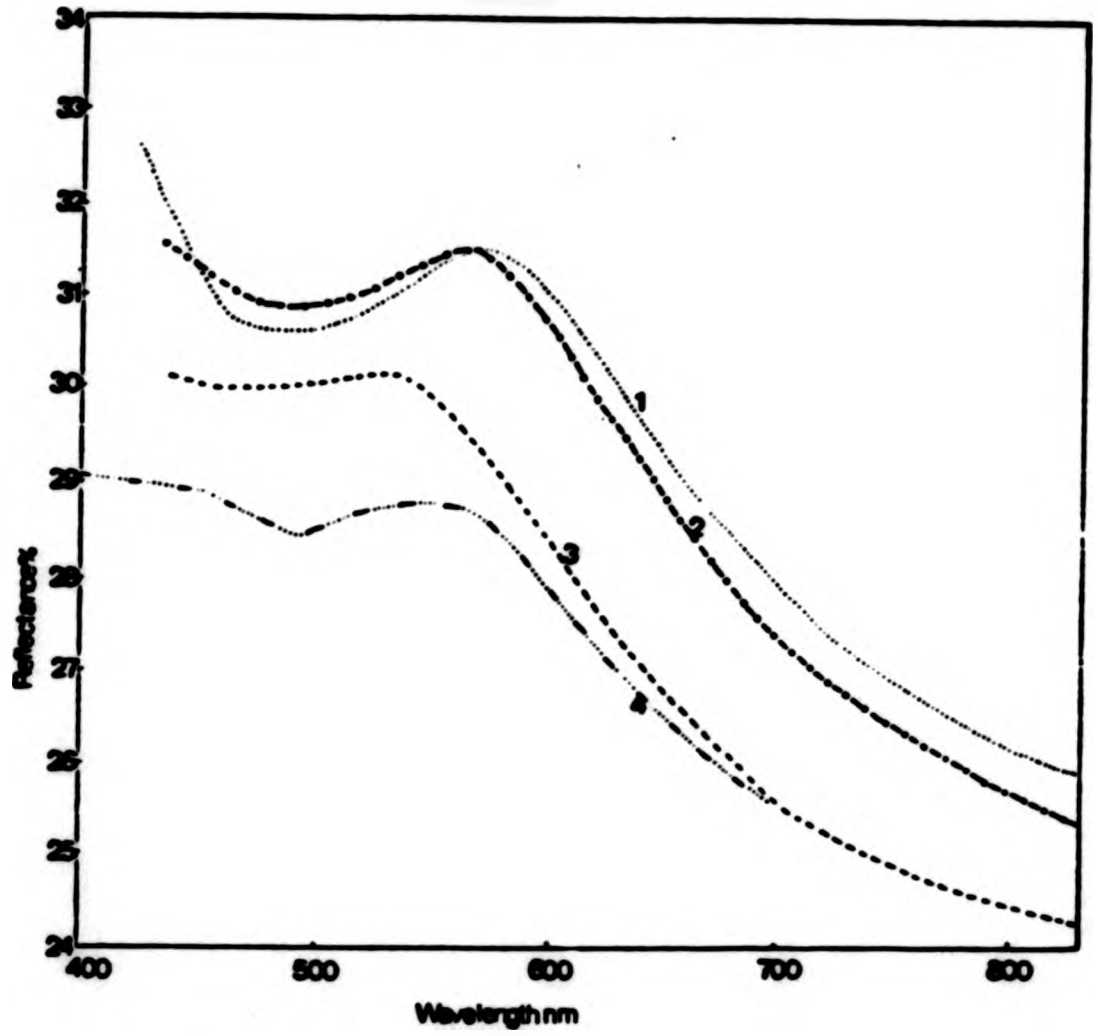

As/Sb/Pb

1. $(Cu_{0.94}Ag_{0.06})(Cu_{0.91}Zn_{1.62}Fe_{0.27})(Sb_{2.04}As_{0.06})S_{12.70}$
2. $(Cu_{0.91}Ag_{0.09})(Cu_{0.67}Zn_{1.70}Fe_{0.14})(Sb_{2.47}As_{0.53})S_{13}$ Charlat and Levy (1976)
3. $Cu_{1.0}(Cu_{0.52}Zn_{1.61}Fe_{0.10})(Sb_{0.10}As_{2.00})S_{13}$
4. $(Cu_{1.01}Ag_{0.99}Zn_{0.98}Fe_{0.99}Pb_{0.03})(Sb_{1.44}As_{2.56})S_{13.1}$ Bishop, Criddle and Clarke (1977)

Fig 1.20 Reflectance dispersion curves showing effects of As/Sb/Pb substitution.

Charlat and Levy (1976) investigated the optical properties of a large number of naturally occurring tetrahedrites and tennantites, their results are similar to those of Hall (1974), however they also looked at two types of substitution not covered by Hall,

i) Substitution of antimony by arsenic (Fig. 1.20) led to a decrease in reflectivity throughout the spectrum, this decrease was essentially linear with increasing arsenic content.

ii) Substitution of iron and/or zinc by mercury (Fig. 1.18) caused a small decrease in reflectance which was proportional to the amount of mercury present.

Bishop et al.(1977) have looked at the optical properties of a plumbian tennantite (Fig. 1.20) where lead substitution has a marked effect on the optical properties. In this tennantite the ratio of antimony to arsenic was 1:1.184 so the reflectance would be expected to be higher than that for pure tennantite (curve 3, Fig. 1.20), however the reverse was true, the effect being most marked at short-wavelengths. To explain the previous phenomena fahlore minerals may be regarded qualitatively as narrow-gap semi-conductors, the increase in reflectivity at wavelengths shorter than 600 nm, marks the area where the energy of the incident light is sufficient to promote an electron from the valence band into the conduction band. The changes in the optical properties due to substitution are caused by the varying role of the d electrons in chemical bonding causing the positions of some of the bands to fluctuate.

The computed chromatic parameters for a series of naturally occuring fahlores have been discussed by Chikhaovi and Levy, (1982). They have shown that these minerals, in particular tetrahedrites, are almost colourless. The intensity of the colouration (expressed in terms of excitation purity P_e%) was found to increase proportionally with arsenic content, the presence of which was also responsible for the green tinge in tennantites (λ_D= 485 - 495 nm). The copper associated with the divalent metals (Fe, Zn, Hg) as distinct from that associated with the silver was also responsible for the green colouration (λ_D= 475 - 485 nm) suggesting that it is also divalent i.e. Cu^{2+}. This confirms the results of earlier studies, where the presence of two types of copper

ion co-existing in the fahlore structure had been suggested, (Charlat and Levy, (1976)). The other divalent metals iron, zinc and mercury were not observed to have any effect on the colour. The luminance Y was found to increase with increasing antimony content but was reduced with the presence of silver and divalent copper.

1.8 Cassiterite (Tin IV oxide)

1.8.1 Occurrence and Associations

Cassiterite is the most common tin mineral and is the principal ore of the metal. It typically occurs in high temperature hydrothermal veins and pegmatites located within them. Due to the stability and weight of the mineral it is also found as rounded pebbles in alluvial deposits (stream tine). Cassiterite occurs as coarse grained pyramidal or short prismatic crystals which are often zoned. Twinning is very common and the cleavage which is prismatic is occasionally visible.

1.8.2 Structure of Cassiterite

Cassiterite (SnO_2) adopts the tetragonal rutile structure, with space group D_{4h}^{14}. The unit cell contains two SnO_2 formula units and has dimensions a = b = 4.737 Å and c = 3.185 Å (Wells, 1962). Each tin atom lies at the centre of a regular octahedron of oxygen atoms and each oxygen lies at the centre of an equilateral triangle of tin atoms, (Fig. 1.21). The almost regular triangular planar co-ordination of oxygen, indicates the involvement of sp^2 hybrids in its bonding with the highly charged Sn^{4+} species.

1.8.3 Optical and Electronic Properties

Pure cassiterite is rarely found in nature, as ferric iron (Fe^{3+}) is usually present as well as small amounts of tantalum, niobium and vanadium. Because spectral features due to Sn^{4+} occur only in the ultra-violet, it is the presence of impurity ions which accounts for the reddish brown to black colours of naturally occurring cassiterites. The colour is due to strong coupling between the electronic levels of the impurity ion (usually Fe^{3+}) and the cassiterite lattice via charge-transfer processes.

Fig 1.21 a.Structure of cassiterite

b.Overall view of the structure emphasising the arrangement of octahedral chains.

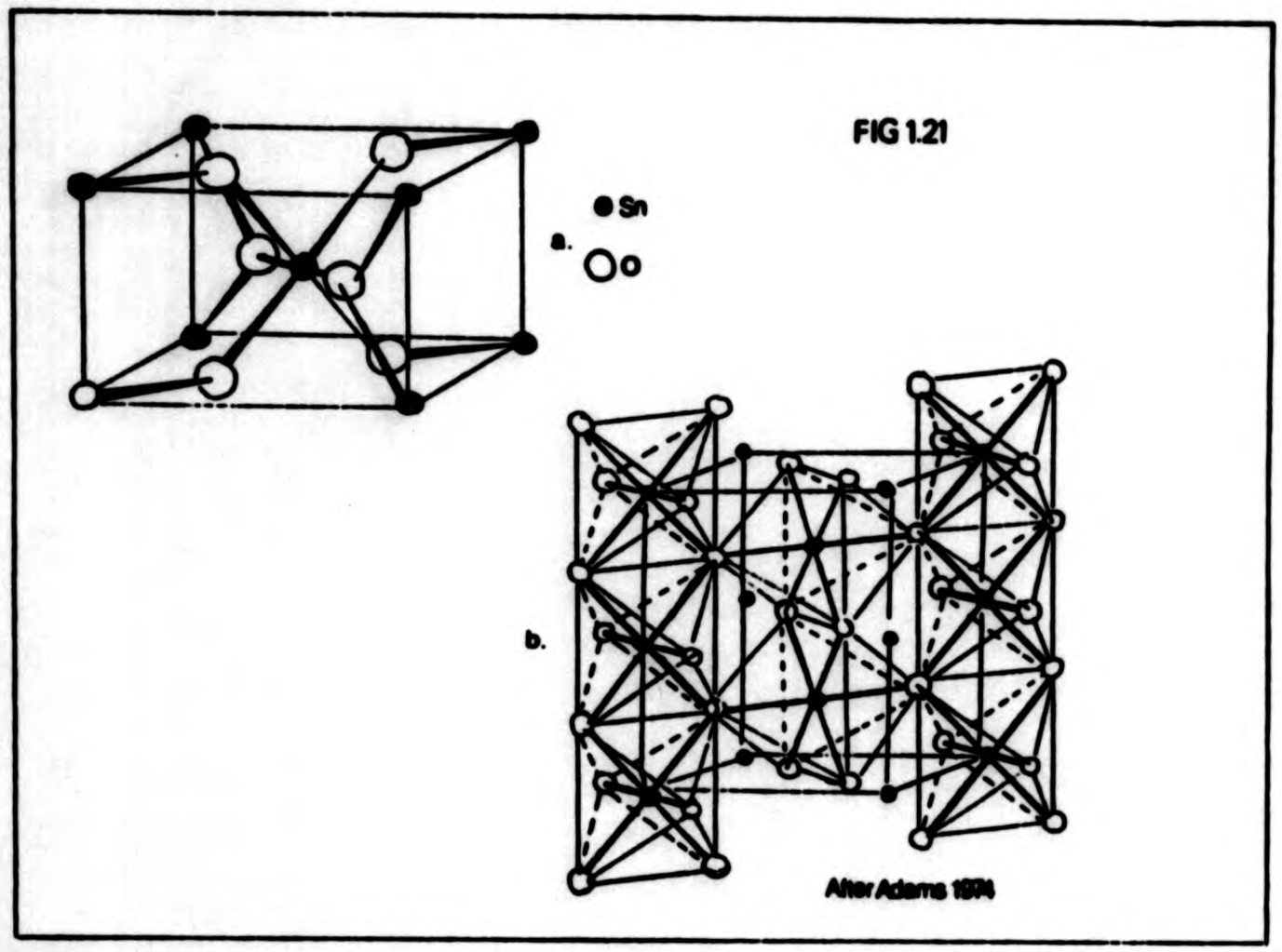

Calas and Cottrant (1982) have examined a number of naturally occurring cassiterites from Brittany (France) using both electron-paramagnetic resonance (EPR) and optical absorption techniques. Their EPR studies showed that the Fe^{3+} impurity ion can exist in up to four different types of sites, of which two are substitutional and highly distorted. Fig. 1.22 shows the optical absorption spectrum for vibrations parallel and perpendicular to the optic axis c for a single crystal of cassiterite. The position of the fundamental absorption edge (Jarzebaki and Marton 1976) is dependent upon the crystal orientation and is located at 3.5 eV (350 nm) and 3.93 eV (315 nm) for vibrations parallel and perpendicular to the optic axis respectively. Apart from the charge-transfer peak the only feature of note in the visible spectrum is the absorption band located at 450 nm. Calas and Cottrant (1982) have tentatively ascribed this structure to a spin-forbidden interband transition from the ground state ^6S to the doubly degenerate quartet states ^4E, $^4A_1$ of the octahedrally co-ordinated impurity Fe^{3+}. Unlike the charge-transfer spectrum which is most intense for vibrations perpendicular to the optic axis the iron transition is most apparent for vibrations parallel to the c axis, this is thought to be because the impurity Fe^{3+} occupies chains of octahedral sites parallel to the c axis.

Cassiterite is generally believed to be an n-type semiconductor with a large band gap. The nature of the defect structure of pure SnO_2 has not yet been satisfactorily elucidated. Both doubly ionized oxygen vacancies and interstitial ions have been proposed (Jarzebaki and Marton, 1976). An exciton series similar to that of cuprite has been observed in the low temperature spectrum of cassiterite. These peaks are seen between 340 and 345 nm as a series of narrow lines. No excitonic peaks have been observed in the visible or infra-red regions of the spectrum. The weak ferromagnetism often encountered in natural cassiterites is thought by Callas and Cottrant (1982) to be due to finely divided iron oxides, or vanadium (IV) impurity ions.

After Calas and Cotrant (1982)

FIG 1.22

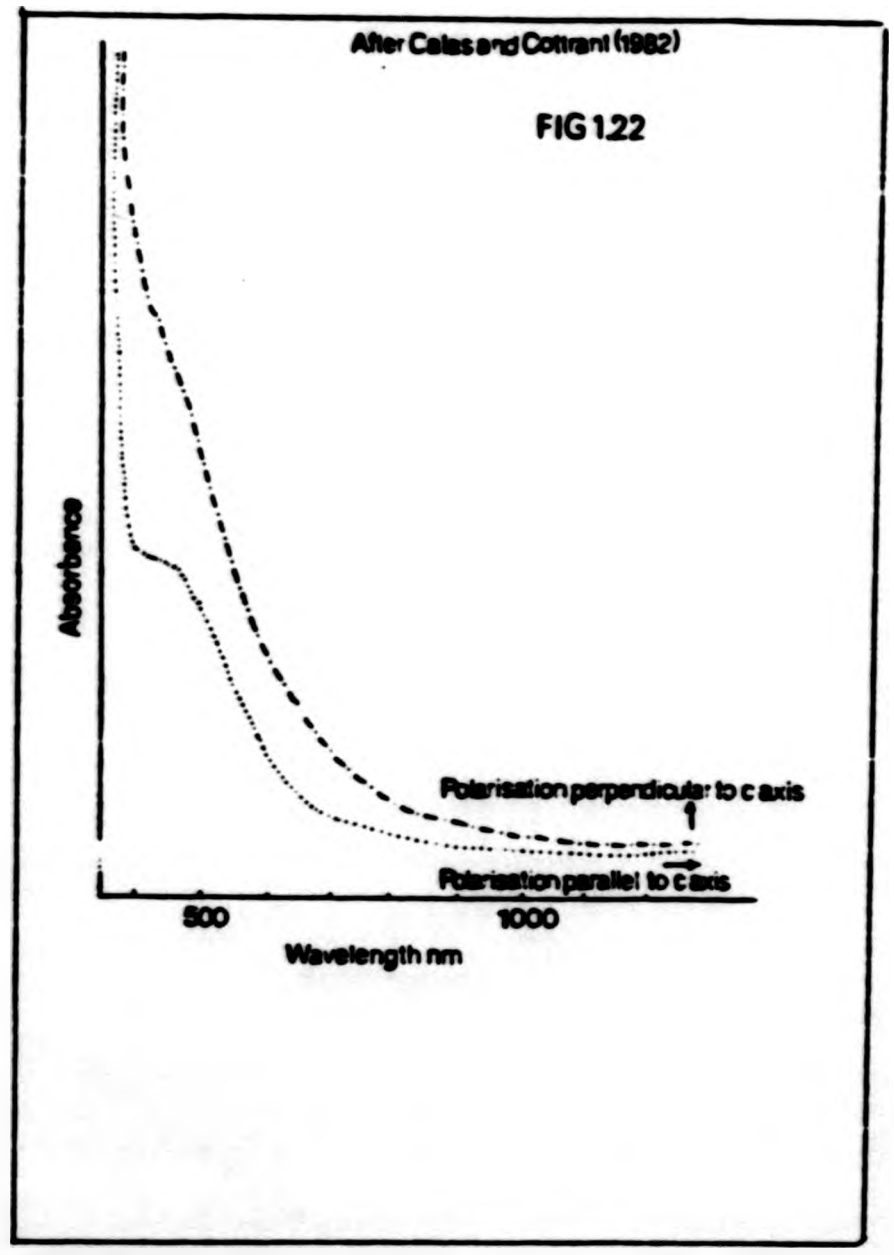

Fig 1.22 Optical absorption spectrum for a cassiterite from Brittany, for vibrations parallel and perpendicular to the optic axis C.

1.9 Cuprite (Copper I oxide)

1.9.1 Occurrence and Association

The name cuprite is derived from the latin cuprum meaning copper. Cuprite is usually formed as a secondary mineral in the oxidised zone of copper deposits. Crystals of cuprite are usually octahedral, cubic or rhombdodecahedral. When the mineral is in the form of fine hair like growths it is known as chalcotrichite. The cleavage when visible is parallel to [111]; no twinning is apparent.

1.9.2 Structure of Cuprite

The structure of cuprite is unusual, and consists of two interpenetrating cristobalite type lattices with no primary bonds between them. The length of the Cu-O-Cu unit gives rise to a very open structure in which there is room to accommodate two such lattices, (Fig. 1.23, Wells, 1962). In cuprite the oxygen is sp^3 hybridised and lies at the centre of a regular tetrahedron of copper atoms, each of which is linearly co-ordinated to two nearest neighbour oxygen atoms. Ag_2O is isostructural with cuprite, while $Zn(CN)_2$ and $Cd(CN)_2$ adopt the anti-cuprite structure in which the metal atom is in tetrahedral co-ordination.

1.9.3 Optical and Electronic Properties

The optical spectrum of cuprite in the visible region (especially at low temperature) is extremely complex. Much of this complexity is due to the presence of excitonic species, the manifestations of which were first observed, independently, by Gross and Karryev (1952) in Leningrad, and Hayashi in Japan (1952). Nikitine (1966) subsequently confirmed these results. The excitonic transitions can be split into four sequences, of which the 'hydrogen-like' yellow and green series are best viewed in the low temperature absorption spectrum while the blue and violet series are so placed as to be best investigated by reflectance techniques.

Brahms and Nikitine (1965) have undertaken a detailed examination

FIG 1.23

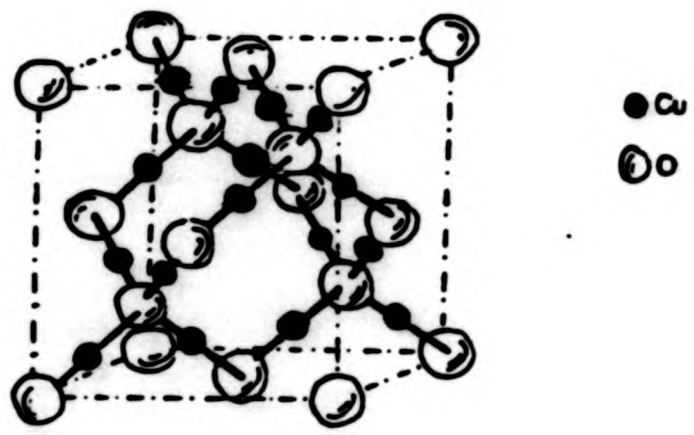

Fig 1.23 Structure of cuprite, actual structure consists of two inter-penetrating lattices like that above with no bonds between them.

of the spectrum between 2.5 and 6.5 eV (496 - 190 nm) and have used the methods described by Elliot (1961) to ascribe transitions to the peaks found therein. They managed to identify two exciton series within this range; the violet at 2.71 eV (457.5 nm) and the blue at 2.58 eV (480.6 nm). They also considered the peak lying at 3.67 eV (337.8 nm) to be excitonic in origin. Gross and Kuang-yin (1961) attributed the two peaks at 4.33 eV (286 nm) and 4.74 eV (262 nm) to be excitonic. Two of the main features of the reflectance spectrum are the maxima located at 4.27 eV (190 nm) and 3.44 eV (360 nm) which are thought to be caused by direct interband transitions between the non-degenerate copper 3d band and the conduction band (Shestatskii et al. 1969; Gross et al. 1962; Dahl, 1966; Roberts and Rastall, 1978). Gross et al. (1962) suggest these transitions are excitonic in nature. After 500 nm the reflectivity of cuprite decreases rapidly as k approaches zero, so that in the red and infra-red region of the spectrum cuprite can be regarded as a transparent mineral. Cuprite is a p-type semiconductor with a band gap of 2.38 eV (Zhilich and Makarov, 1960). At high temperature (>300°C) cuprite exhibits 'self activated' conduction, the amount of which increases with temperature.

1.10 Surface Condition of Polished Ore Minerals

1.10.1 Introduction

Nearly all samples prepared in air for optical examination (Chapter 3) are subject to some surface contamination which can originate from a variety of sources, for example;

i. During the polishing process diamond grit, lubricants and water can collect in surface irregularities (cracks, holes, pores etc.).

ii. After the final cleaning process a thin film of acetone, or other cleaning solvents, may be adsorbed on the surface of the specimen.

iii. A thin film of adsorbed atmospheric oxygen will always be present on the surface of the specimen.

iv. After polishing a tarnish film may develop, the type and rate of formation of which is dependent on the material type (see 1.10.3).

Of the above, (i) and (ii) can to some extent be avoided if ultrasonic and careful cleaning methods are employed. (iii) can only be eliminated if the sample is prepared, and always kept, under vacuum, which for practical purposes is impossible. The film of adsorbed oxygen is stable, very thin, and forms instantaneously after polishing and so to all intents and purposes cannot be avoided. As most workers observe 'real surfaces', and as the effect of the adsorbed oxygen layer on the optical properties is negligible with respect to other errors (Chapter 4), it is usually ignored.

1.10.2 Polish Damage

Undistorted specular reflectance measurements require a surface which is flat and from which surface artefacts have been reduced below the wavelength of visible light. Apart from those samples which have perfectly cleaved crystal surfaces all samples require some surface preparation before optical measurements can be made. Mechanical polishing is the most frequently adopted technique because of the ease of control it affords.

All forms of mechanical polishing introduce some surface damage, and hence the surface has different optical properties from the bulk material. Several steps can, however, be undertaken to minimise the extent of this damage, the most important of which is to make sure that at every stage of the polishing sequence the scratches from the previous stage are entirely removed. Preliminary grinding is also very important and without great care the polished surface will not be suitable for reflectance measurements. Surface damage is greatly increased (especially in softer materials) if too much pressure is applied to the surface during polishing. This results in a 'smeared' surface, the optical properties of which are totally unrepresentative of either the 'normal unsmeared' surface or the bulk material, Criddle (1983).

Cervelle, Levy and Pinet (1975) have measured the optical

properties of sphalerite using:

i. The prism method to determine the refractive index.

ii. Microphotometry on two cleavage flakes.

iii. Microphotometry on two polished specimens.

They have found (Fig. 1.24) that the reflectance in air of the two cleavage lamellae is slightly lower than the theoretical values calculated from the n values obtained by the prism method and that the reflectance of the two mechanically polished specimens is lower still. The results in oil are slightly different; again the reflectance of the polished specimens is below that of the theoretical values, but the reflectance of the cleavage lamellae between 400 and 500 nm lie slightly above or slightly below the calculated values. Cervelle et al. account for the difference in reflectivity between the two cleavage flakes (which is seen in oil but not in air) to haphazardly orientated terraces which resulted when the flakes were separated. Piller and Von Gehlen (1964) showed that reflectance measurements in oil are influenced more by light scattering effects than those in air. Cervelle et al. (1975) also concluded that the polishing process gives rise to a systematic error leading to a decrease in reflectivity in both air and oil, but were unable to explain this phenomenon.

Ohlidal (1974) investigated the effects of surface damage on silicon by ellipsometry and has concluded that the damage layer extends to a depth of 1 mm so that no undamaged silicon is 'seen' by the light. The derived optical constants showed considerable scatter, which he concluded was due to the irreproducibility of surfaces by mechanical polishing processes. This finding seems to be at odds with much of the published data especially when it is remembered that ellipsometrically derived n and k values are not subject to the errors inherent in the microphotometric calculations. Thus it can only be presumed that polishing procedures have advanced sufficiently since 1974 to make the situation described by Ohlidal no longer apparent.

As nearly all reflectance measurements found in the literature

FIG 1.24

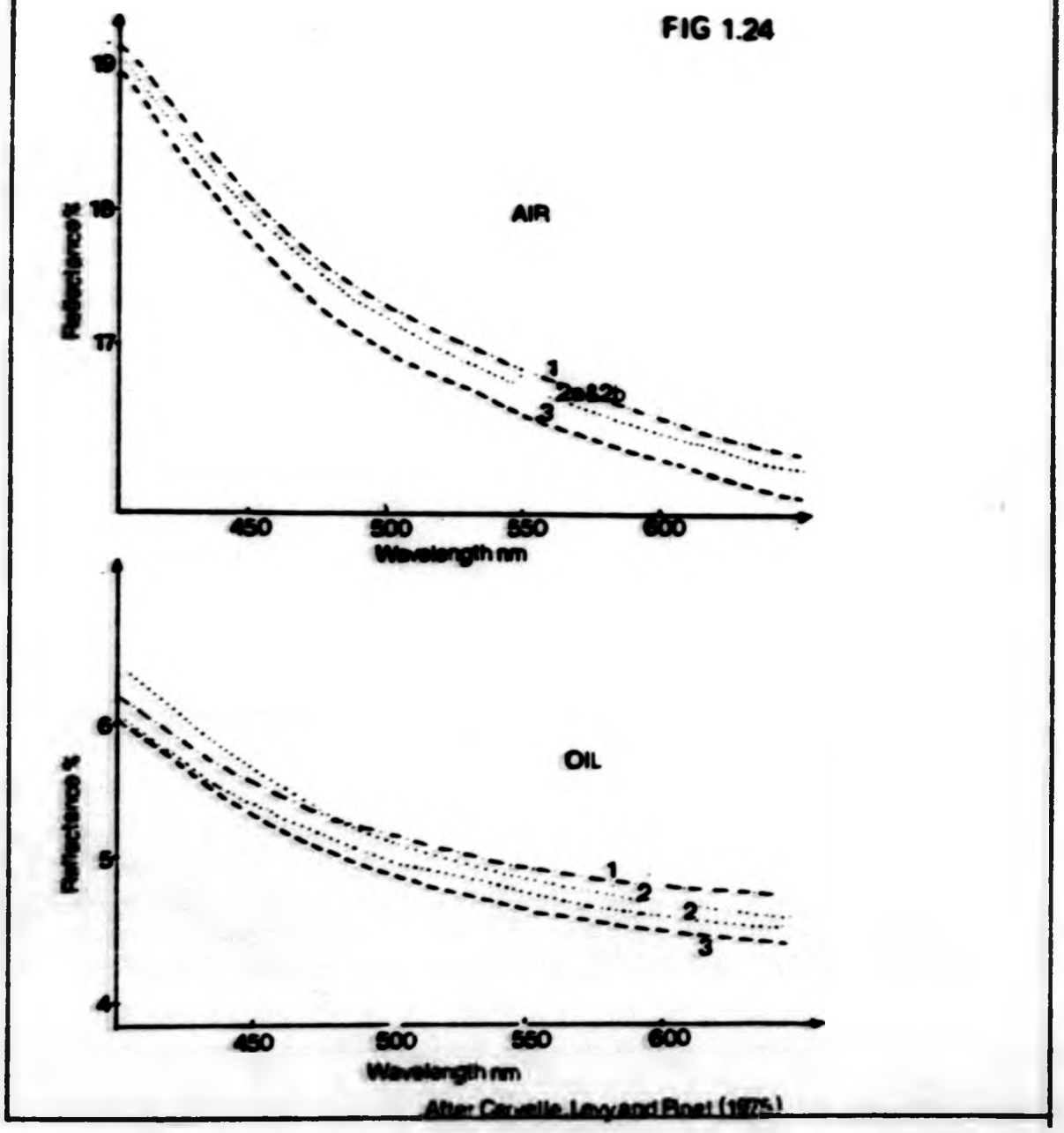

Fig 1.24 Reflectance dispersion of sphalerite in air and oil immersion
1.Theoretical values calculated from prism method
2.Microphotometric measurements on two cleavage lamellae a & b.
3.Microphotometric measurements on a polished section.

are made on mechanically polished surfaces and provided that the researcher appreciates the errors involved, i.e. that the derived optical constants are indicative of the surface and not the bulk it is quite proper for measurements made on various minerals to be compared and discussed.

1.10.3 Tarnishing

The phenomenon of mineral tarnishing especially in sulphides has long been recognised. The rate of tarnishing not only differs between different mineral species, but can also vary, for a given mineral, from different localities. Even within a single polished specimen different grains of the same mineral can tarnish quite differently. Thorpe *et al.* (1976) first reported the possible correlation between the rapid tarnishing of chalcopyrite specimens and high silver content. Chen and Petruk (1978) observed a similar phenomenon in chalcopyrites. They found that in chalcopyrites where the silver content was less than 0.1 wt% the tarnish film was light golden brown in colour, whereas in chalcopyrite with a high silver content (>3.8 wt%) the film was coloured blue or purple. Chen *et al.* (1980) showed that when chalcopyrite is in contact with silver bearing minerals, especially native silver, rapid tarnishing occurs. They proposed that the silver diffuses onto the surface of the chalcopyrite where it reacts with sulphur to form acanthite Ag_2S. A detailed X-ray examination of the surface film on chalcopyrite revealed it to be acanthite.

Chen *et al.* (1980) also studied a rapidly tarnishing tennantite specimen. The mechanism by which tennantite tarnishes seems to be more complex and to indicate metal-sulphide diffusion, arising from the partial decomposition of the tennantite;

$$Cu_{12}(As,Sb)_4S_{13} \longrightarrow xCu_2S + Cu_{12-2x}(As,Sb)_4S_{13-x}$$

As the volume of the tarnish product is small the tennantite phase remaining differs only slightly from the original. The tarnish film (from X-ray examination) appears to be either silver bearing chalcosine or silver bearing digenite of which the latter is only present in the early stages of film formation being eventually replaced by chalcosine. As in chalcopyrite, the presence of silver aids tarnish film formation

which Chen et al. (1980) attribute to its enhancing the rate of surface diffusion of Cu_xS. The tarnishing rate is also dependent upon the environment. The optimum conditions are ones in which the air is warm and moist. It should be noted that not all tennantites undergo rapid tarnishing, as composition and environment seem to play a key role in this phenomenon. The presence of even thin tarnish films can have a profound effect on the optical properties as illustrated in the case of henryite where not only did the reflectance change, but so did the dispersion (Criddle et al. 1983). For this reason samples should be buffed using γAl_2O_3 or MgO before making measurements (Stanley 1983).

CHAPTER TWO
THEORY

2.1 Maxwell's Equations

2.1.1 The Wave Equation

The interaction of electromagnetic radiation with matter was first mathematically quantified by J.C. Maxwell. Today Maxwell's theories and their results are enshrined in the literature. Less frequently considered are the conditions under which Maxwell's original equations strictly apply, namely an isotropic homogeneous medium in which there are no free charges ie. ε the dielectric constant and μ the magnetic permeability are invariant. Under these conditions Maxwell's equations may be used to describe the changes which occur in the electric (E) and magnetic (H) field vectors during a series of magnetic and electrical events. Using Maxwell's fundamental equations the wave equations (2.1 and 2.2) can be derived.

$$\nabla^2 E = \mu\varepsilon \ddot{E} - \mu\sigma \dot{E} \qquad 2.1$$

$$\nabla^2 H = \mu\varepsilon \ddot{H} - \mu\sigma \dot{H} \qquad 2.2$$

where ∇^2 = Laplacian vector operator
ε = Dielectric constant
μ = magnetic permeability
σ = conductivity

. and .. refer to the first and second differentials respectively.

The Laplacian ∇^2 is a convenient way to express the divergence of the gradient (div. grad) as a single differential operation. ∇^2 involves differentiation with respect to more than one variable and like grad, div and curl it makes no reference to any particular co-ordinate system and in order to solve a specific problem ∇^2 must be expressed in terms of x, y, z etc. appropriate to that problem. For any vector F:

$$\nabla^2 F = i\ \nabla^2 F_x + j\ \nabla^2 F_y + k\ \nabla^2 F_z \qquad 2.3$$

The two terms $\mu\epsilon\dot{\vec{E}}$ and $-\mu\sigma\vec{E}$ can be viewed as the expression for the electric component of a plane oscillating wave and the expression for the impedance i.e. the effect by which the wave is damped.

The wave equation (2.1) can be simplified for monochromatic radiation of angular frequency ω.

$$\nabla^2 E = -K_\nu^2 E \qquad 2.4$$

where

$$K_\nu^2 = \mu_\nu \epsilon_\nu \omega^2 \pm \mu_\nu \sigma_\nu \omega i \qquad 2.5$$

K_ν^2 is referred to as the propagation constant (also known as the complex wave number) and has dimensions of cm^{-1}, its magnitude is dependent upon the material through which the wave is propagating, represented by ν . The wave equation is equally applicable to the magnetic field vector H. Thus in a homogeneous isotropic medium, the wave can be viewed as two mutually perpendicular transverse oscillations which are plane polarised and in phase with each other (Fig. 2.1). Note the currents induced by the magnetic field vector (H) are perpendicular to H and so aligned with those of the electric field vector (E).

As long as K_ν^2 remains a constant, ie. the wave remains in the same homogeneous isotropic medium, energy loss will occur only by absorption. If, however, the wave enters a second medium in which the physical properties are different, reflection and refraction will occur at the interface of the two media (Fig. 2.2).

2.1.2 Dielectric Media

If the second medium is a transparent dielectric and the first medium is air, Snells law will apply:

Fig 2.1 Distribution of electric and magnetic vectors in a plane polarised monochromatic wave.

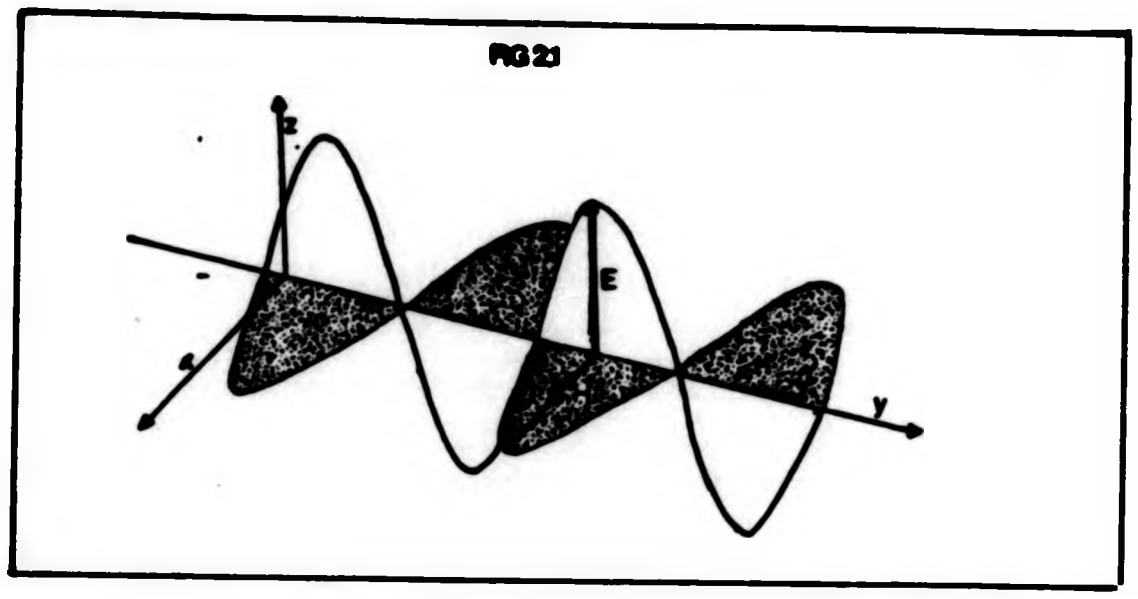

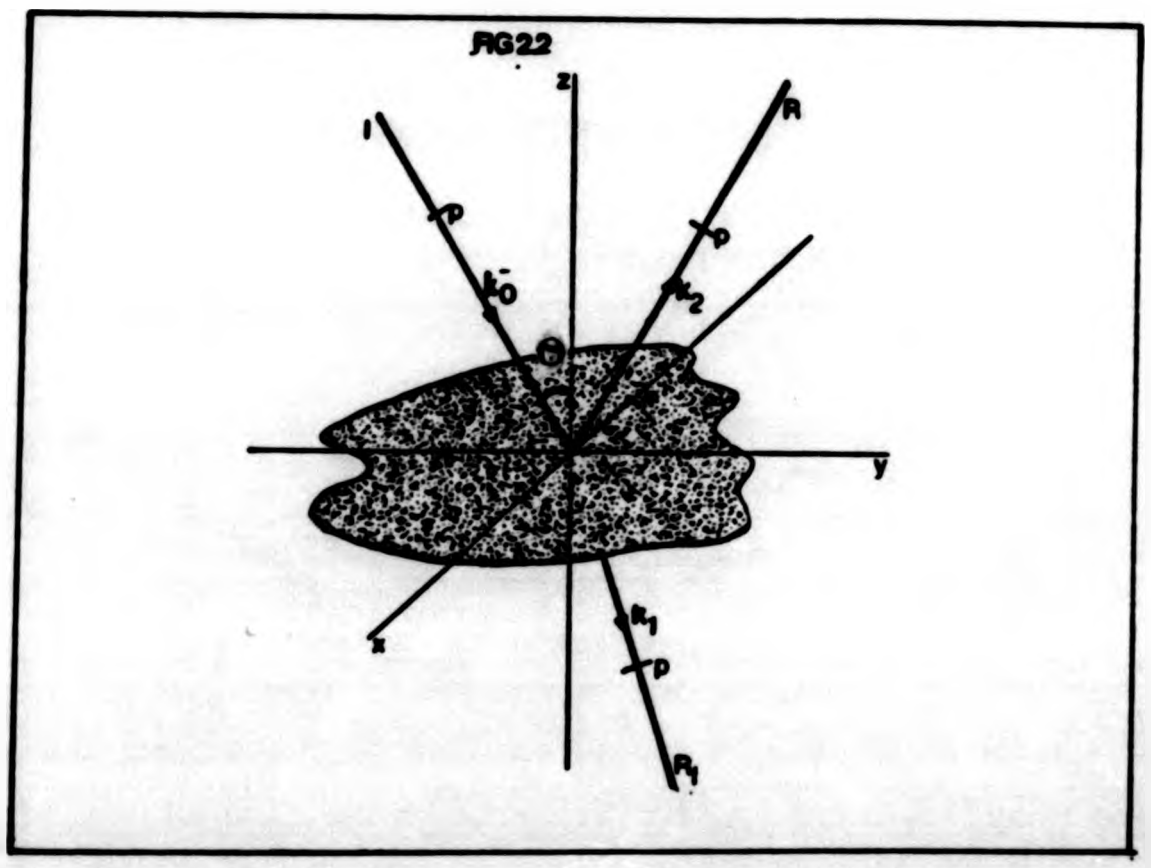

Fig 2.2 Reflection and refraction at the interface between two media which have different physical properties.

$$\frac{\sin \Theta_0}{\sin \Theta_1} = \frac{K_1}{K_0} = \sqrt{\frac{\varepsilon_1 \mu_1}{\varepsilon_0 \mu_0}} = n_{01} \qquad 2.6$$

Where the subscript 0 denotes the first medium and 1 denotes the second, Θ_0 is the angle of incidence and Θ_1 is the angle of refraction. The ratio of the complex wavenumbers represents the index of refraction.

2.1.3 Conducting Media

If, however, the second medium is an electrical conductor, the refracted ray will only penetrate for a short distance. There will be an induced current and hence absorption in addition to reflection. Because the propagation direction of the refracting medium is now complex, the angle of refraction Θ_1 is replaced by a complex relationship containing two angles ($\psi + \chi i$), one for the wave front of constant phase and the other for the wavefront of constant amplitude. As the reflected ray is in the same medium as the incident ray they are distinguished by the subscripts 0 and 2. From equation 2.5 the complex wavenumber for both media (air subscript 0 and the electrical conductor subscript 2) may be derived:

$$K_2^2 = \mu_2 \varepsilon_2 \omega^2 + \mu_2 \sigma_2 \omega i \quad \text{or} \quad K_2 = \alpha_2 + i \beta_2 \qquad 2.7$$

$$K_0^2 = \mu_0 \varepsilon_0 \omega^2 \quad \text{or} \quad K_0 = \alpha_0 = \omega(\mu_0 \varepsilon_0)^{\frac{1}{2}} \qquad 2.8$$

$$\text{where } \alpha = \{\mu \varepsilon\}^{\frac{1}{2}} \omega \qquad 2.9$$

$$\text{and} \quad \beta = \{\mu \sigma \omega\}^{\frac{1}{2}} \qquad 2.10$$

Snell's law still applies in the formal sense and may be written:

$$\frac{\sin \Theta_0}{\sin(\psi + \chi i)} = \frac{K_2}{K_0} = \frac{\alpha_2}{\alpha_0} + \frac{\beta_2 i}{\alpha_0} \qquad 2.11$$

$$\frac{\sin \Theta_0}{\sin(\psi + \chi_1)} = N = n + ik \qquad 2.12$$

where N = the complex index of refraction
n = the refractive index
k = the absorption coefficient

2.1.4 Limitations of Maxwell's Equations

It must be noted that in microscope photometry the expression n + ik is used for the complex index N, while in ellipsometry the convention is to use a negative sign. Either is correct as long as the same sign convention is used throughout.

It is appropriate here to mention the assumptions limiting the applications of the above equations.

i) They assume that the absorbing medium is isotropic. Since, however, most materials are anisotropic, it would seem that for them orientation and other terms need to be introduced. This leads to very complex mathematics to eliminate the tensor.

ii) At optical frequencies, ε and the electrical charge density ρ are not uniform with space and time, and so an extension to Maxwell's equations called diffusion theory must be applied. At optical frequencies, providing the material studied is not ferromagnetic, the contribution due to μ can be effectively ignored, as the ratio $\frac{\mu_2}{\mu_0} = 1$

iii) Many recent ellipsometers use coherent laser light, thus the equations used will need modification to accommodate this fact.

2.2 Reflection

2.2.1 Fresnel Reflection Intensity Formulae

From Snell's law the Fresnel reflection intensity formulae can

be derived (Mowat and Muller, 1966; Holl, 1963):

$$R_s = \frac{\left(\frac{q}{a_0} - \cos\Theta_0\right)^2 + \left(\frac{p}{a_2}\right)^2}{\left(\frac{q}{a_0} + \cos\Theta_0\right)^2 + \left(\frac{p}{a_2}\right)^2} \qquad 2.13$$

$$R_p = \frac{\left[\left\{\left(\frac{\alpha_2}{\alpha_0}\right)^2 - \left(\frac{\beta_2}{\alpha_0}\right)^2\right\}\cos\Theta_0 - \frac{q}{\alpha_0}\right]^2 + \left[2\frac{\alpha_2}{\alpha_0}\cdot\frac{\beta_2}{\alpha_0}\cos\Theta_0 - \frac{p}{\alpha_0}\right]^2}{\left[\left\{\left(\frac{\alpha_2}{\alpha_0}\right)^2 - \left(\frac{\beta_2}{\alpha_0}\right)^2\right\}\cos\Theta_0 + \frac{q}{\alpha_0}\right]^2 + \left[2\frac{\alpha_2}{\alpha_0}\cdot\frac{\beta_2}{\alpha_0}\cos\Theta_0 + \frac{p}{\alpha_0}\right]^2} \qquad 2.14$$

where p and q are functions of α, β and Θ_0

2.2.2 Normal Incidence

For measurements made at normal incidence the situation is much simpler as:

$$R_s = R_p = R_N \qquad 2.15$$

and the above equations reduce to:

$$R_N = \frac{(n - N)^2 + k^2}{(n + N)^2 + k^2} \qquad 2.16$$

where N is the refractive index of the surrounding non-absorbing medium.

If measurements are made in air the equation simplifies still further, as N now approximates to 1.

$$R = \frac{(n - 1)^2 + k^2}{(n + 1)^2 + k^2} \qquad 2.17$$

2.2.3 Determination of n and k by Two Media Reflection Method

Equations 2.16 and 2.17 form the basis of a method pioneered by Konigsberger (1913) for determining the optical constants of absorbing materials by measuring their reflectivities in two different immersion media (usually air and oil and designated R and im_R respectively). Solving equations 2.16 and 2.17 gives rise to expressions for n and k, these are often referred to as the Konigsberger equations.

$$n_{(calc)} = \frac{\frac{1}{2}(N^2 - 1)}{N\left(\frac{1+im_R}{1-im_R}\right) - \left(\frac{1+R}{1-R}\right)} \qquad 2.18$$

$$k_{(calc)} = \sqrt{\left(\frac{R(n_{calc}+1)^2 - (n_{calc}-1)^2}{1-R}\right)} \qquad 2.19$$

Equation 2.16 can be rearranged to the form (Embrey and Criddle, 1978):

$$n^2 + k^2 - 2nN\left(\frac{1 + im_R}{1 - im_R}\right) + N^2 = 0 \qquad 2.20$$

and

$$\left(n - N\left(\frac{1 + im_R}{1 - im_R}\right)\right)^2 + k^2 = \frac{4N^2\, im_R}{(1 - im_R)^2} \qquad 2.21$$

A comparison of equation 2.20 with that of a circle $(x^2 + y^2 - 2gx + c = 0)$, shows that equation 2.18 is that of a family of circles centred on the x or n axis, the radii of which are given by:

$$\text{radius air} = \frac{2\sqrt{im_R}}{(1 - R)} \qquad 2.22$$

$$\text{radius oil} = \frac{2N\sqrt{im_R}}{(1 - im_R)} \qquad 2.23$$

Embrey and Criddle (1978) have shown that the distance from the origin of the air and oil curve centres (designated a and h respectively) can be expressed as:

$$a = \left(\frac{1 + R}{1 - R}\right) \qquad 2.24$$

$$h = N\left(\frac{1 + im_R}{1 - im_R}\right) \qquad 2.25$$

N.B. R and im_R should be expressed in decimal rather than percentage form.

It is now apparent that the denominator in equation 2.18 is equal to the distance between the centres of the air and oil curves, so that equation 2.18 and 2.19 can be simplified to the forms:

$$n_{calc} = \frac{\frac{1}{2}(N^2 - 1)}{(h - a)} \qquad 2.26$$

$$k_{calc} = \sqrt{\left\{\frac{(N^2 a - h)}{(h - a)}\right\} - \left\{\frac{\frac{1}{2}(N^2 - 1)}{(h - a)}\right\}^2} \qquad 2.27$$

2.2.4 Errors in Determining n and k by Two Media Reflection Method

2.2.4.1 n/k Diagram

As stated previously equation 2.20 describes a family of circles, however the only part relevant to this discussion is the portion which falls in the quadrant where both n and k are positive. It is clear that for any set of n and k values for a given value of N there will be only one point where the R, im_R curves intersect, the converse is however, rarely true (Fig. 2.3). When the R and im_R curves do not intersect the solution will be imaginary. Even if intersection does occur, to give real values of n and k, these will not necessarily be without error.

Piller and Von Gehlen (1964) and Galopin and Henry (1972) have pointed out that if two curves intersect at a low angle, then n and

FIG 23

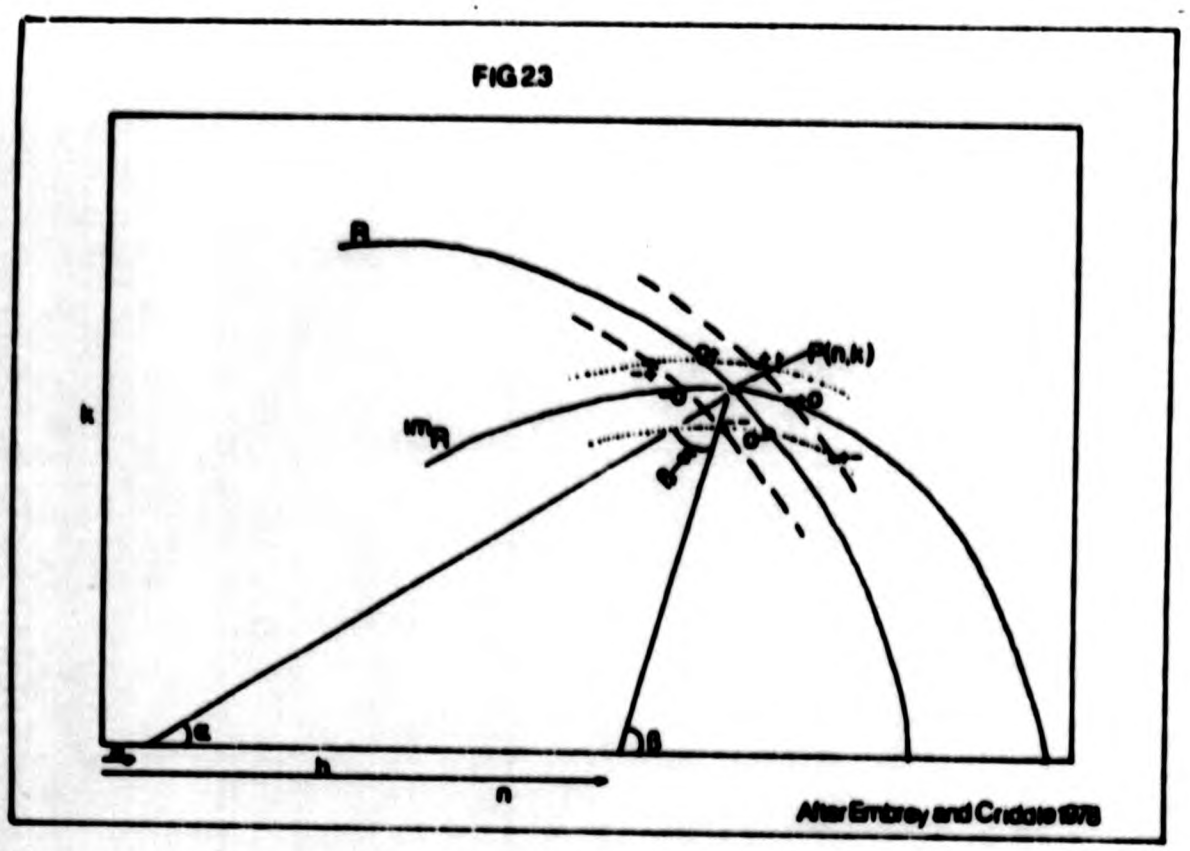

Fig 2.3. The position of a point P(n,k) at the intersection of the true reflectance curves R and ^{im}R. The intersection angle is the acute angle β-α and a and h are the distances of the centres of the true curves from the origin. A derived point P'(n',k') lies in the region bounded by arcs of curves for which the measured reflectances are in error; limiting points are labelled (+o),(++) etc.

k are more likely to be in error. They have suggested that an attainable relative accuracy of 1% in measuring R and im_R is desirable. Embrey and Criddle (1978) have shown graphically that this corresponds to an intersection angle of 5°. They have suggested that the intersection angle ($\beta - \alpha$) (Fig. 2.3) can be calculated from measured reflectances by the following equation:

$$\frac{R + im_R - 2\sqrt{(R\ im_R)}\ \cos(\beta - \alpha)}{(1 - R)(1 - im_R)} = \frac{(N - 1)^2}{4N} \qquad 2.28$$

In Fig. 2.4 contours of constant intersection angle for the air and oil reflectance curves are shown. The shaded area is where the values of n and k can be determined with some confidence. Outside this region caution should be exercised when discussing the results.

2.2.4.2 R/im_R "Cigar" Diagram

While the n/k diagram is useful in a qualitative sense, the R/im_R diagram is more useful quantitatively, as it can be used to determine n and k directly from measured reflectances. Fig. 2.5 shows the R/im_R diagram drawn for N = 1.515 (Embrey and Criddle, 1978), and shows contours of constant absorption coefficient. The boundary k = 0 demarks the real from the imaginary regions. Curves of constant n radiate from R = im_R = 100% and cut the "cigar" at intervals, those outside the k = 0 boundary having no real physical meaning. The line $n = \pm\infty$ marks a transition after which n is negative. An examination of Fig. 2.5 shows that at high reflectances the contours become crowded, and if n and k are to be accurately determined graphically, this portion should be enlarged (Fig. 2.6). It can thus be seen that at higher reflectances, a small error in the determination of R and/or im_R can radically alter the derived n and k values. The worst combination is when R is measured too high and im_R too low.

2.2.5 Ellipsometric Determination of Reflectance and the Optical Constants

The preceding discussion is applicable to methods where reflectance is measured directly. In ellipsometry reflectance is one of

FIG 24

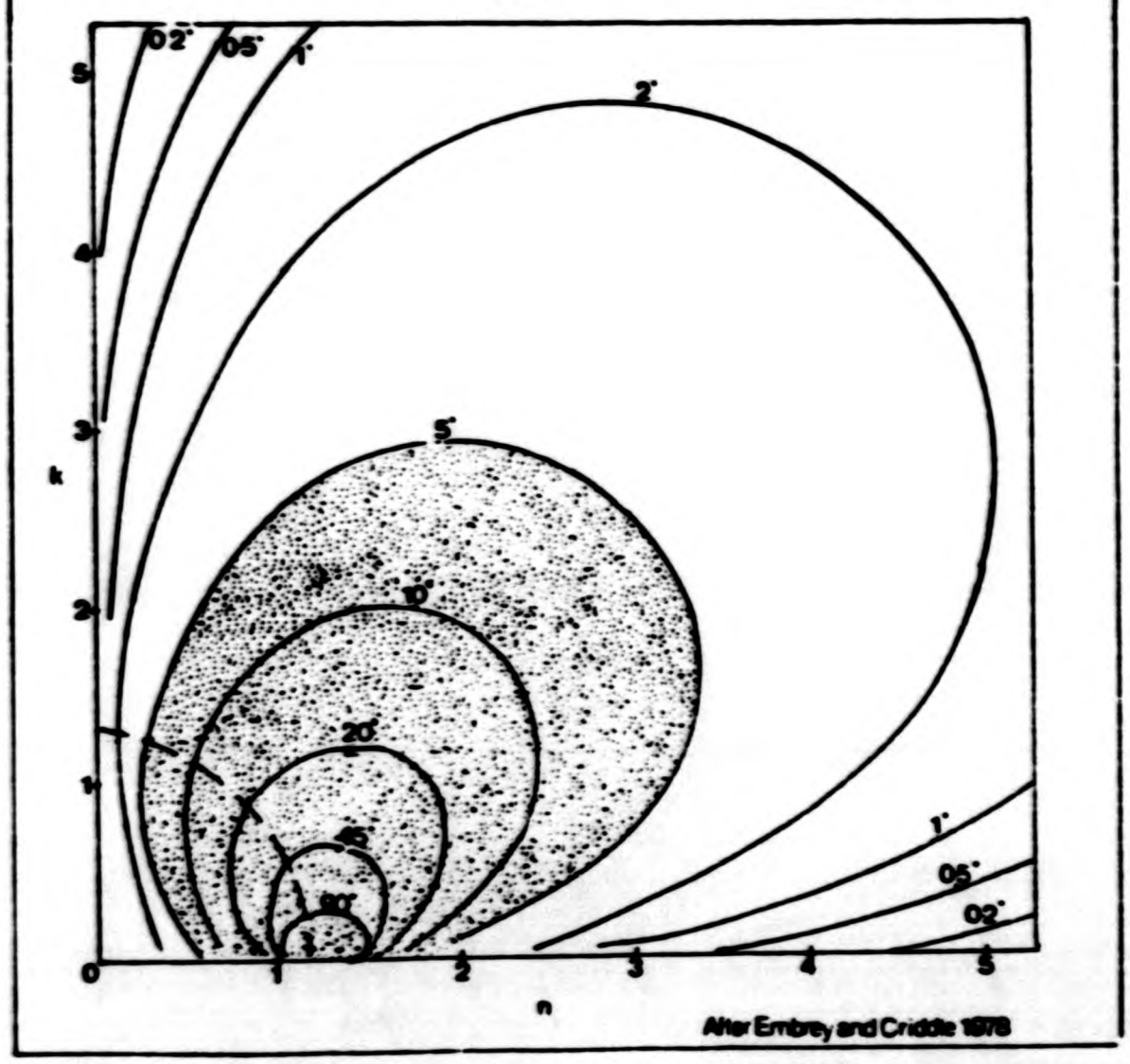

Fig 2.4. Contours of constant intersection angle of the reflection curves for air and oil (N=1.515).

Fig 2.5. The R/ ^{im}R cigar diagram drawn for N=1.515. The field of real values of n and k lies inside the k-0 contour. Above the cigar and between it and the curve n(calc)= ±∞;k(calc) is complex and n (calc) negative.

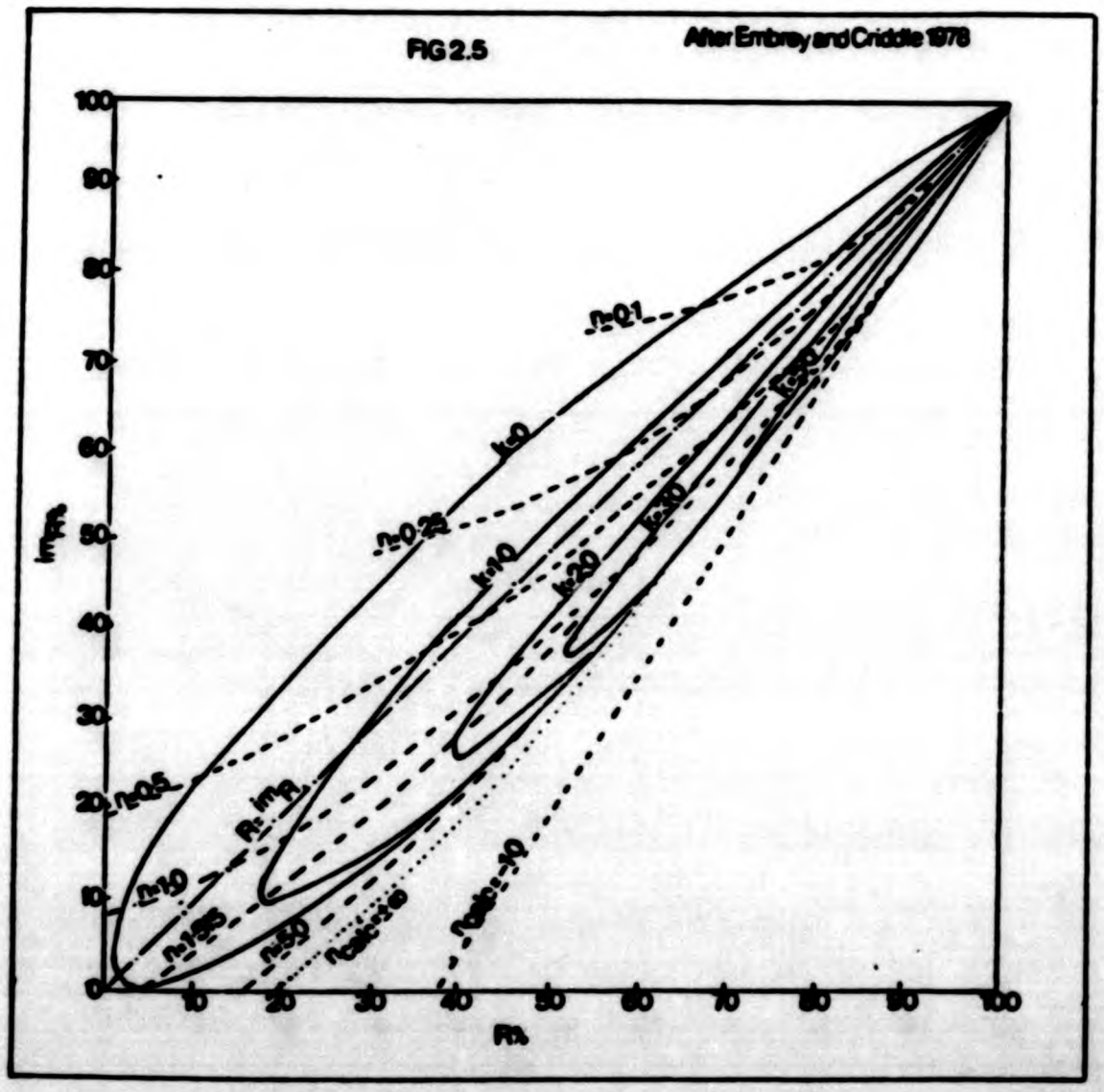

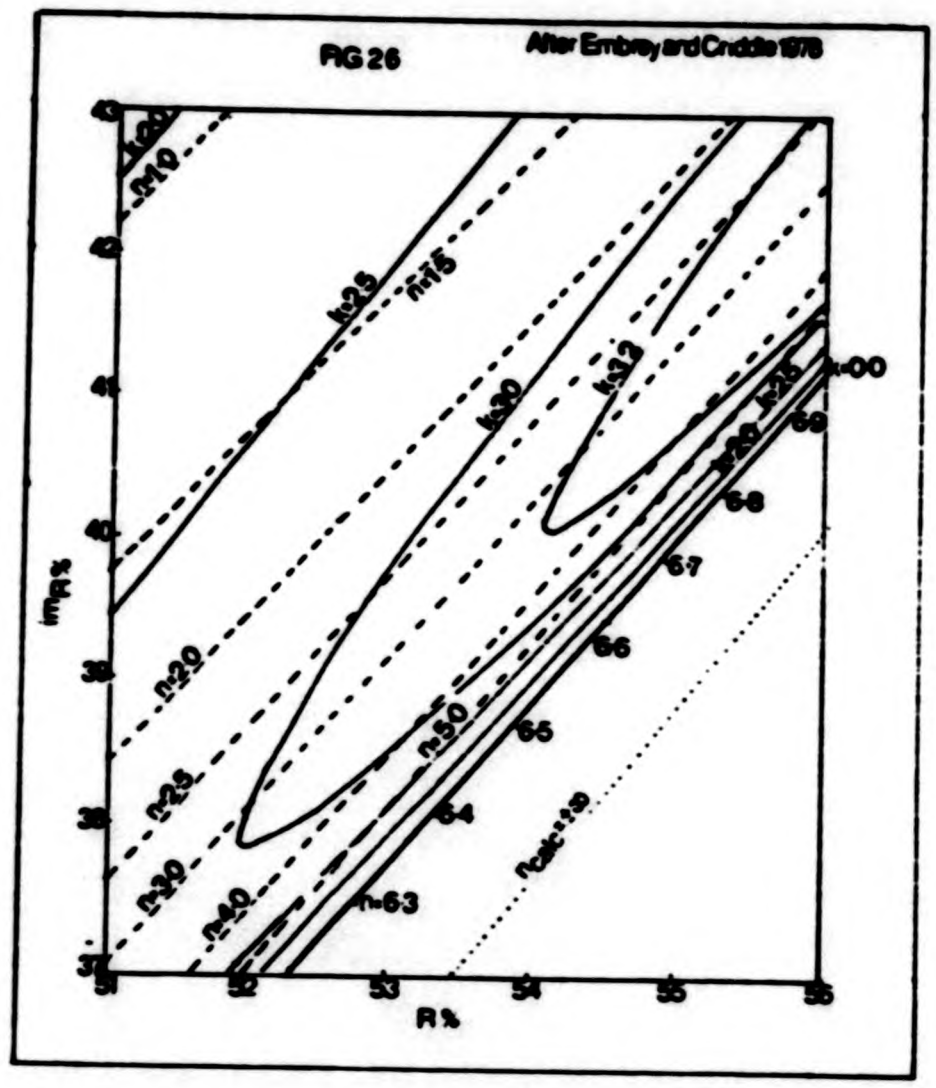

Fig 2.6. An enlarged portion of the $R/^{im}_{R}$ cigar diagram for N=1.515.

the last parameters to be derived using already calculated normal n and k values substituted into equation 2.16. Here the actual measured quantities are the angular displacements of the analyser and polariser prisms from their fiducial positions, denoted as A and P. A and P can be simply related to Δ the relative phase-shift and Ψ the relative amplitude-change, only if a perfect retarder is employed, that is one which induces a phase shift of exactly 90°. If this is not the case a correction factor must be applied. Measurements were made in two zones so that a compensator file could be collected:

$$\Psi = 45 - A \qquad 2.29$$

$$\Delta = \frac{P}{2} \qquad 2.30$$

Muller (1967) has derived the refractive index n and the absorption coefficient k as follows:

$$n = N\left[\tfrac{1}{2}(+\{G^2 - E^2 + \sin^2\Theta\} + \sqrt{(G^2 - E^2 + \sin^2\Theta)^2 + 4G^2E^2}\,\right]^{\frac{1}{2}} \qquad 2.31$$

$$k = N\left[\tfrac{1}{2}(-\{G^2 - E^2 + \sin^2\Theta\} + \sqrt{(G^2 - E^2 + \sin^2\Theta)^2 + 4G^2E^2}\,\right]^{\frac{1}{2}} \qquad 2.32$$

where,

$$G = \frac{\sin\Theta\tan\Theta\cos 2\Psi}{1 + 2\sin\Psi\cos\Theta} \qquad 2.33$$

$$E = \frac{\sin\Theta\tan\Theta\sin 2\Psi\sin\Delta}{1 + 2\sin\Psi\cos\Delta} \qquad 2.34$$

The real and imaginary parts of the dielectric constant can also be calculated from Δ and Ψ as follows:

$$\varepsilon_1 = N^2\sin^2\Theta\left[\frac{1 + \tan\Theta\{\cos^2 2\Psi - \sin^2 2\Psi\sin\Delta\}}{\{1 + \sin 2\Psi\cos\Delta\}^2}\right] \qquad 2.35$$

$$\varepsilon_2 = 2N^2 \sin^2\Theta \tan^2\Theta \left[\frac{\sin 2\psi \cos 2\psi \sin\Delta}{\{1 + \sin 2\psi \cos\Delta\}^2}\right] \qquad 2.36$$

$$\text{As } \varepsilon_1 = n^2 - k^2 \qquad 2.37$$

$$\text{and } \varepsilon_2 = 2nk \qquad 2.38$$

The normal reflectance R_N can be calculated by substitution of n and k in equation 2.16.

2.3 Colour

2.3.1 Introduction

The observed colour of an ore mineral in reflected light is an obvious diagnostic property. Colour is, however, a very subjective property and hence it is very difficult to describe accurately. In 1931 a quantitative method for determining colour was devised by Le Commission Internationale de l'Eclairage (C.I.E.). Only since the introduction of suitable photomultipliers has it become possible to apply this system to the study of ore minerals in reflected light.

2.3.2 Determination of CIE Colour Values

The colour values, x, y, z and Y can be calculated from a set of reflectance values by first obtaining the 'tristimulus' values X, Y and Z which are defined as (Piller 1977):

$$X = \frac{1}{K} \int_{\lambda=b}^{\lambda=a} (\bar{x}\lambda . S\lambda) . R\lambda \, . d\lambda \qquad 2.39$$

$$Y = \frac{1}{K}\int_{-b}^{-a} (\bar{y}\lambda . S\lambda) . R\lambda . d\lambda \qquad 2.40$$

$$Z = \frac{1}{K}\int_{-b}^{-a} (\bar{z}\lambda . S\lambda) R\lambda . d\lambda \qquad 2.41$$

where $x\lambda, y\lambda, z\lambda$ = tristimulus values for red, green and blue light respectively (Fig. 2.7)

$S\lambda$ = relative spectral wavelength of light source used

$R\lambda$ = reflectance

a,b = limits of reflectance measurements, typically a = 700, b = 400 (nm)

K = normalising constant

The integrals are complicated, but good approximations to X, Y and Z can be made by the following summations:

$$X = \frac{1}{K}\sum_{-b}^{-a} (\bar{x}\lambda . S\lambda) . R\lambda . \Delta\lambda \qquad 2.42$$

$$Y = \frac{1}{K}\sum_{-b}^{-a} (\bar{y}\lambda . S\lambda) . R\lambda . \Delta\lambda \qquad 2.43$$

FIG 27

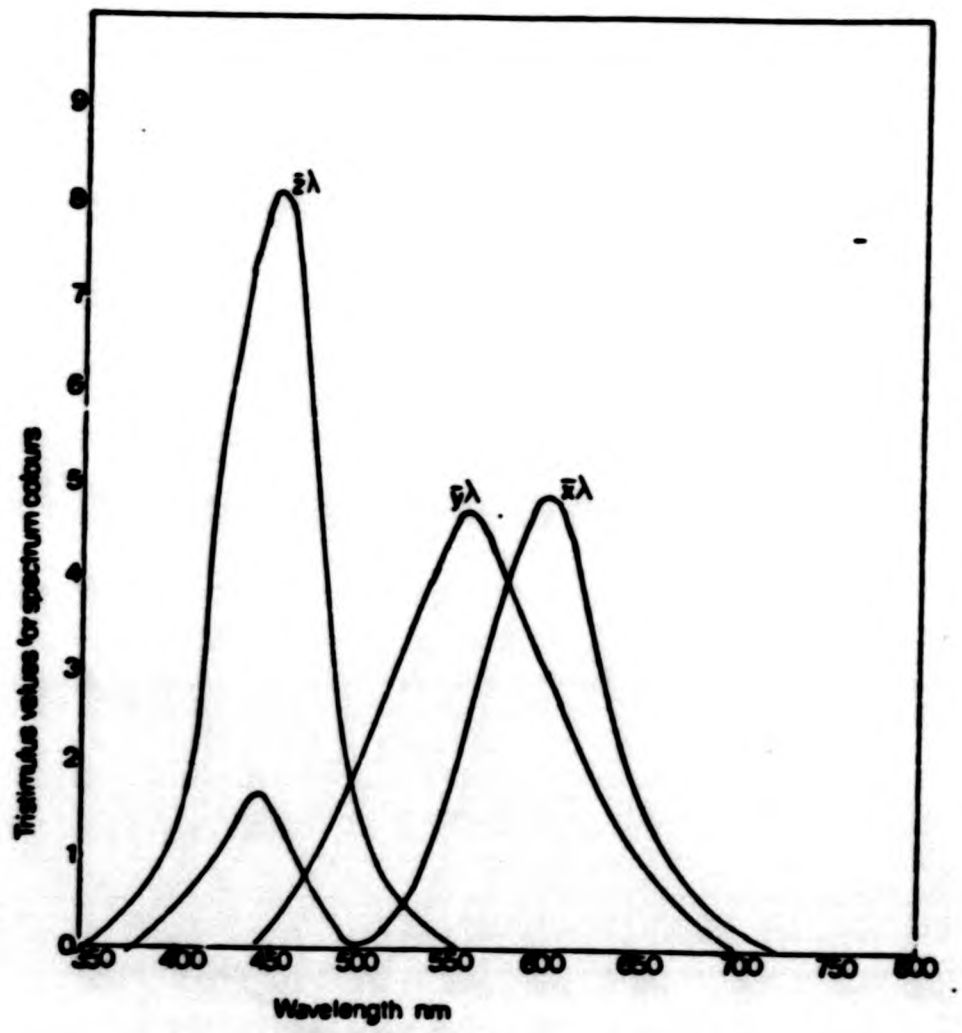

Fig 2.7. xλ,yλ and zλ, tristimulus values for red, green and and blue light.

$$Z = \frac{1}{K}\sum_{\lambda=b}^{\lambda=a}(z_\lambda . S_\lambda)R_\lambda \Delta\lambda \qquad 2.44$$

The chromaticity coordinates x, y and z are calculated from:

$$x = \frac{X}{X+Y+Z}, \quad y = \frac{Y}{X+Y+Z}, \quad z = \frac{Z}{X+Y+Z} \qquad 2.45$$

The sum $x + y + z = 1$

The brightness (or luminance) of a mineral is given by the tristimulus value Y (which must be divided by 100 if reflectance percentages are used). The chromaticity coordinates can now be plotted on a CIE chromaticity diagram (Fig. 2.8). Although chromaticity coordinates can be used to accurately locate a colour on a CIE chromaticity diagram, they do not allow the easy visualisation of that colour. For this reason other values can be derived which often prove more useful . These are the Helmholtz values, dominant wavelength D_λ and excitation purity Pe%, D_λ and Pe% can be derived graphically in Fig. 2.8:

i) D_λ is the point of intersection T on the spectral locus of a line drawn from the light source (in this case C) through R (the point defined by coordinates x, y and z).

ii) Pe% is expressed as a percentage of the distance CR divided by CT.

If the co-ordinates (x, y) place the object in the purple region, point P, then D_λ has the negative value of the complementary wavelength and Pe% is CP as a percentage of CS.

FIG2.8

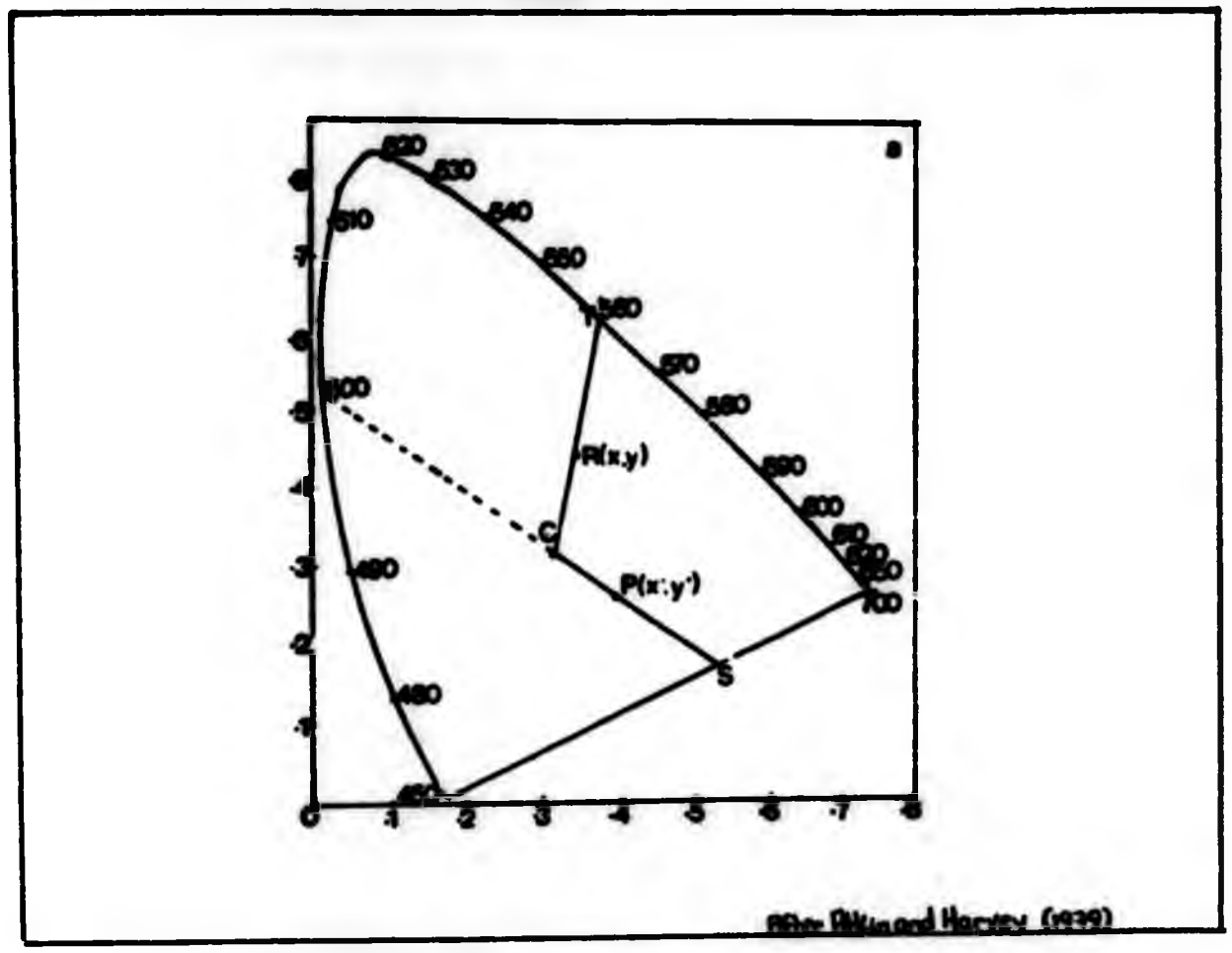

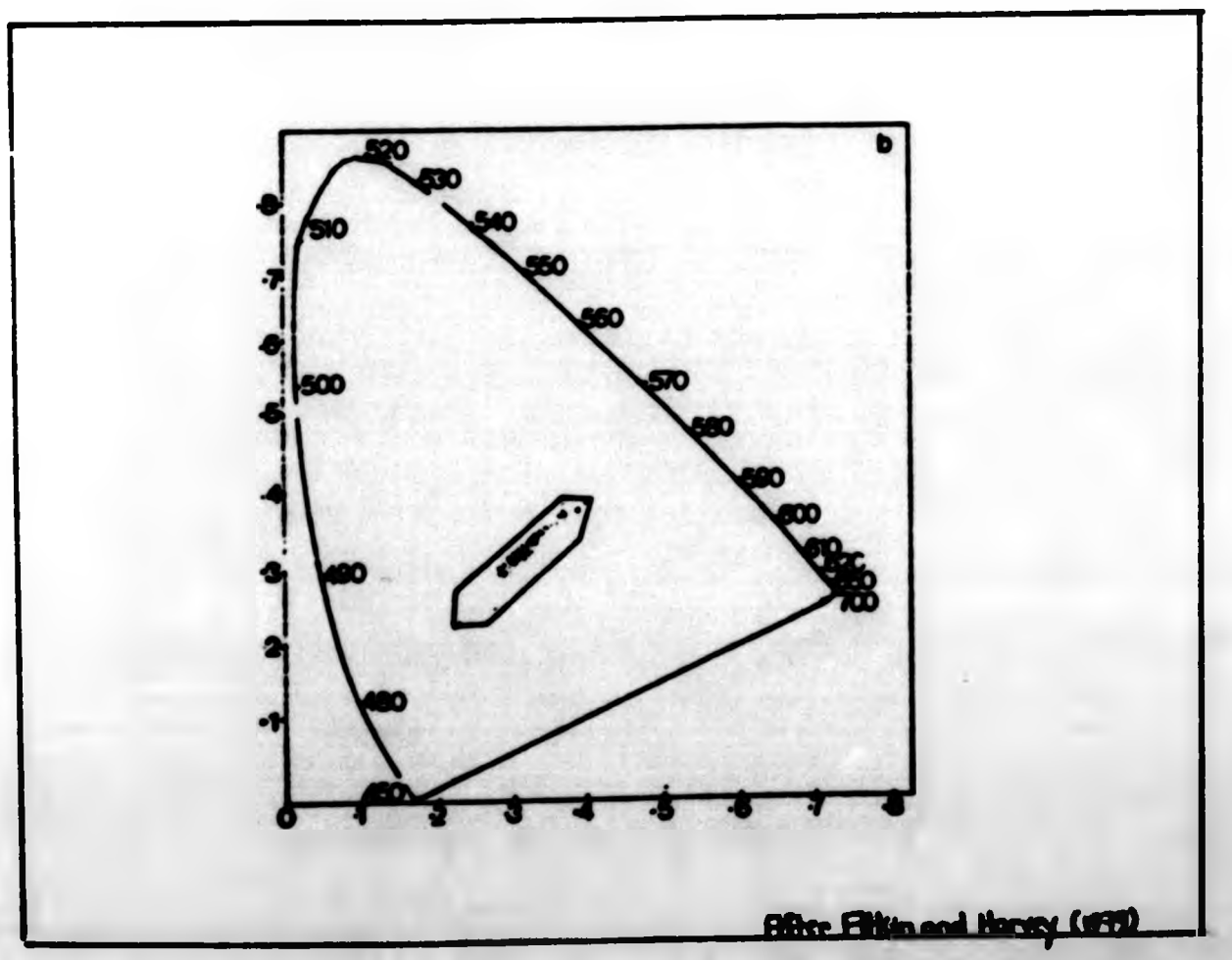

Fig 2.8. a, Graphical determination of dominant wavelength λ_D and excitation purity Pe%.

b. Position of most minerals on the CIE chromaticity

2.4 Absorption Processes

2.4.1 Introduction

Several kinds of absorption processes can occur when light interacts with a crystal lattice namely:

i) Direct electronic transitions which involve the absorption of a photon in order to promote an electron from the valence band into the conduction band. Such transitions give rise to the fundamental absorption edge of the material and help to determine its colour. In direct electronic transitions only the energy of the electron changes, the wave vector $\vec{K}$ remains unchanged.

ii) Indirect electronic transitions involve both the absorption of a photon and a phonon in order to promote an electron from the valence band into the conduction band. In this case both the energy and the wave vector of the electron changes, Fig. 2.9.

iii) Excitons are bound electron positive hole pairs. These occur when the electron excited by the incident photon has insufficient energy to escape the influence of the positive hole it leaves behind, and so exists in a stable state with that hole. The electron and hole are held together by their mutual coulombic attraction. The allowed exciton states lie within the forbidden energy gap of the host material and give rise to intense absorption bands close to the fundamental absorption edge (Fig. 2.10). An exciton is capable of diffusing throughout the host material, and is able to transfer energy without a net change in charge.

iv) The presence of foreign ions within a host lattice can give rise to electronic transitions, which occur via the photoionization of the impurity ion, so creating free electrons and positive holes. This phenomenon occurs principally in medium to large band-gap semi-conductors, and is only seen in narrow band-gap materials at very low temperatures.

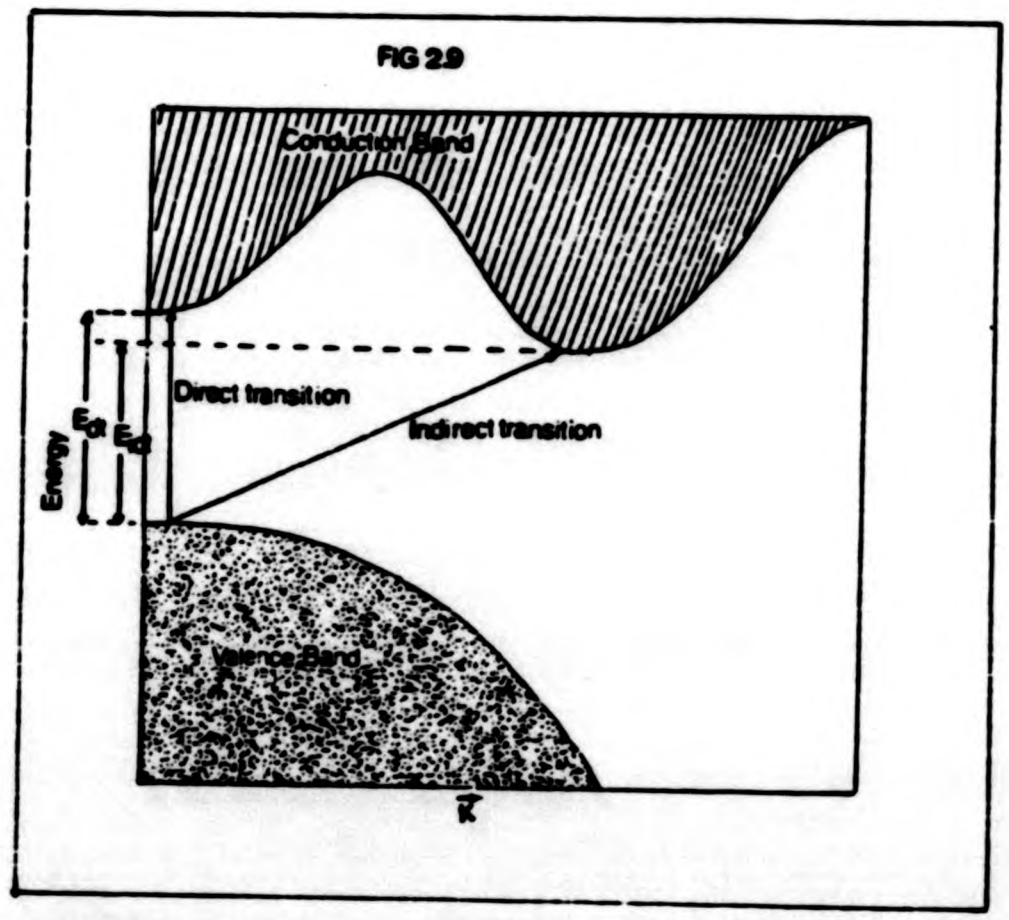

Fig 2.9. Direct and indirect interband transitions

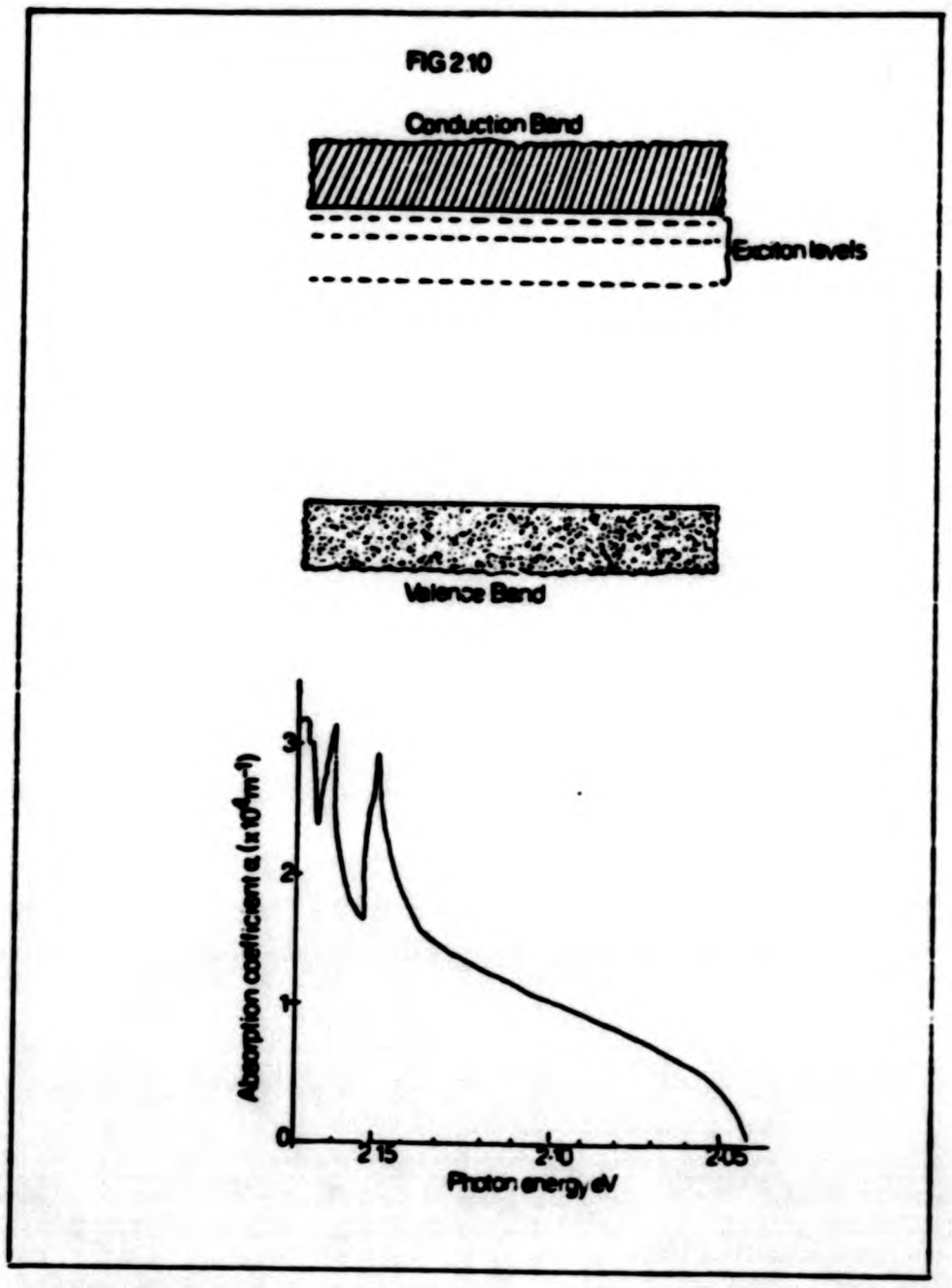

Fig 2.10. Exciton levels in the forbidden energy gap. Excitonic transitions give rise to intense absorptions in the region of the fundamental absorption edge.

2.4.2 Selection Rules

The selection rules which pertain to electronic transitions can be derived from quantum mechanics. They determine the probability of transitions occurring between certain spectroscopic states, and the relative intensity of the absorption bands so produced.

2.4.2.1 Spin Multiplicity Selection Rule

In the free ion, transitions which involve a change in the number of unpaired electrons are forbidden. Thus the spin-multiplicity selection rule maintains that transitions can only occur between states of the same spin multiplicity i.e. if the ground state is a quartet transitions may only occur to other quartet states. Due to spin-orbit coupling some formally spin forbidden transitions can occur, albeit weakly. For example, in octahedrally coordinated d^5 ions, where there are no spin allowed transitions some weak transitions do occur between the sextet $^6A_{1g}$ ground state and various higher quartet states.

2.4.2.2 Laporte Selection Rule

This selection rule specifies that transitions within a single quantum 'shell' are strictly forbidden, for example d ⟷ d transitions. As electronic transitions take place through the interaction of electromagnetic radiation with a component of the dipole moment of the absorbing system, transitions can thus only result when the expression $\langle n/\mu_r/m \rangle$ transforms as a totally symmetric species. Where n is the ground state, m is the final state and μ_r is the operator. For centro-symmetric groups such as O_h the p orbitals have antisymmetric u labels, the d orbitals symmetric g labels, and the operator transforms as T_{1u}; so, for example:

i) p ⟶ p transitions $\langle n/\mu_r/m \rangle$ ⟶ u x u x u ⟶ u
which is an antisymmetric species and therefore the transition is forbidden.

ii) p ⟶ d transitions $\langle n/\mu_r/m \rangle$ ⟶ u x u x g ⟶ g
which is a totally symmetric species and therefore the transition is allowed.

iii) d ⟶ d transitions $\langle n/\mu_r/m \rangle \longrightarrow g \times u \times g \longrightarrow u$
which is an antisymmetric species and therefore the transition is forbidden.

There are two mechanisms by which transitions can occur which are formally forbidden by the Laporte selection rule. If the ion occupies an environment in which there is no centre of symmetry i, then a certain amount of mixing of the p and d orbitals can occur, and so transitions can take place between levels of mixed p and d character. This kind of mixing is not possible if the ion is within a centrosymmetric environment such as O_h and it is here that the second type of mechanism may occur. Here the forbidden nature of the d $t_{2g} \longrightarrow e_g$ transition (which tranforms to the antisymmetric u species) can be eliminated, if the symmetry of the molecule is destroyed by vibration. Such vibration (Fig. 2.11) removes the centre of the symmetry of the complex and therefore removes the g and u classification of the orbitals so that d ⟶ d transitions can occur. These vibration dependent types of d⟶d transitions are referred to as vibronic. In practice vibronic transitions give rise to very weak features in the absorption spectrum.

Forbidden and indirect transitions are only apparent in those regions of the spectrum which are not dominated by direct allowed transitions.

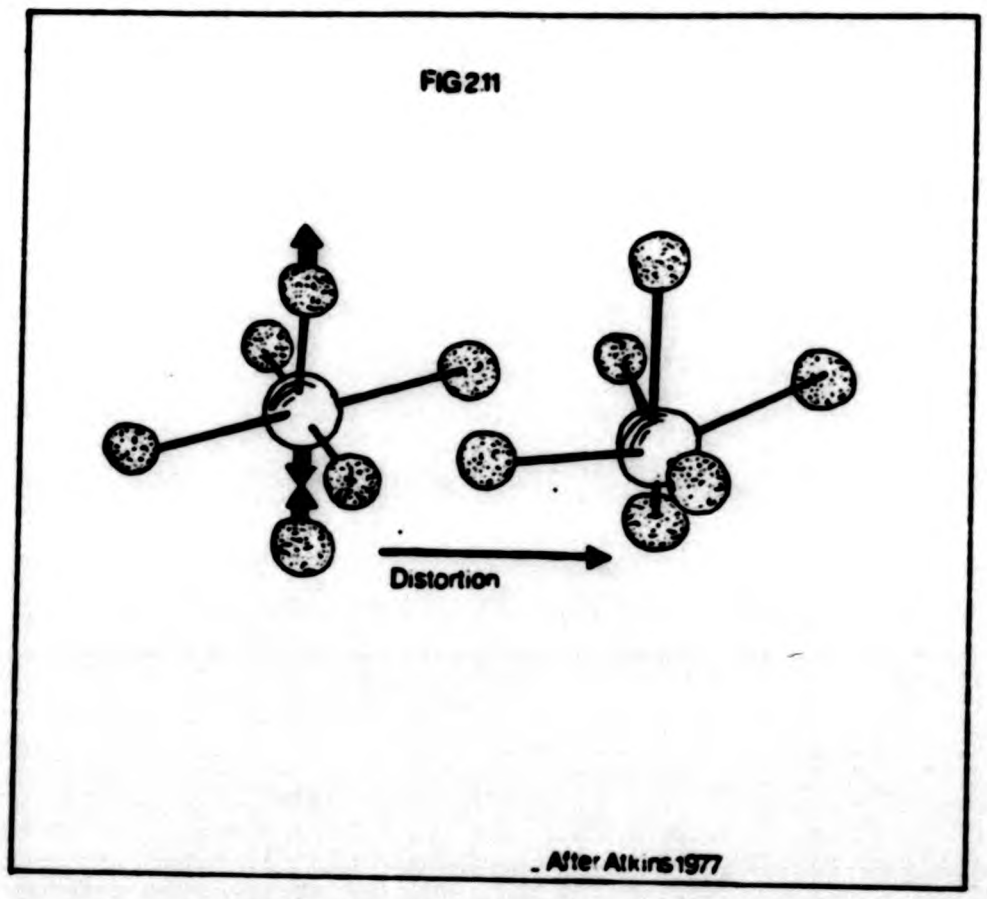

Fig 2.11. A vibronic transition in an octahedral complex.

CHAPTER THREE
APPARATUS AND EXPERIMENTAL MEASUREMENT

3.1 Microscope Photometer - Description of Apparatus

3.1.1 Introduction

The modules which constitute the basis of the Zeiss MPM03 microscope photometer are shown in Fig. 3.1. In the following sections a brief description of their properties, functions, and any corrections which need to be applied are given for each part of each module. For a much more detailed account of microphotometric instrumentation and measurement the reader is referred to Piller (1977).

3.1.2 Lamp

There are two main types of lamp used in microscope-photometry, incandescent filament lamps and high pressure gas discharge lamps. The microscope photometer used in this study utilises an incandescent flat-wire-coil tungsten-filament lamp which emits a continuous spectrum in the infra-red and visible. For precision photometry the lamp must be supplied with a highly stabilised d.c. current, in which the a.c. component has been reduced to a minimum so as to prevent fluctuations in the measured readings. The precision of the measurements can also be affected by 'flicker'. This arises from uneven fluctuations at the different surface elements of the lamp. Flicker can be kept to a minimum by always ensuring that the lamp has been given sufficient time to warm up (fifteen minutes) before starting measurements.

The lamp should also be watched for any signs of ageing, manifested by a darkened appearance and a gradual decrease in radiance, caused by the deposition of evaporated metal on the inside of the bulb. Modern filament lamps use a halogen atmosphere to slow down the ageing process. However, these types of lamp are very sensitive to the input voltage, which if slightly too high will cause the destruction of the lamp. Correct positioning of the lamp is essential; this is accomplished conoscopically so that the image of the filament is centred and as bright and uniform as possible.

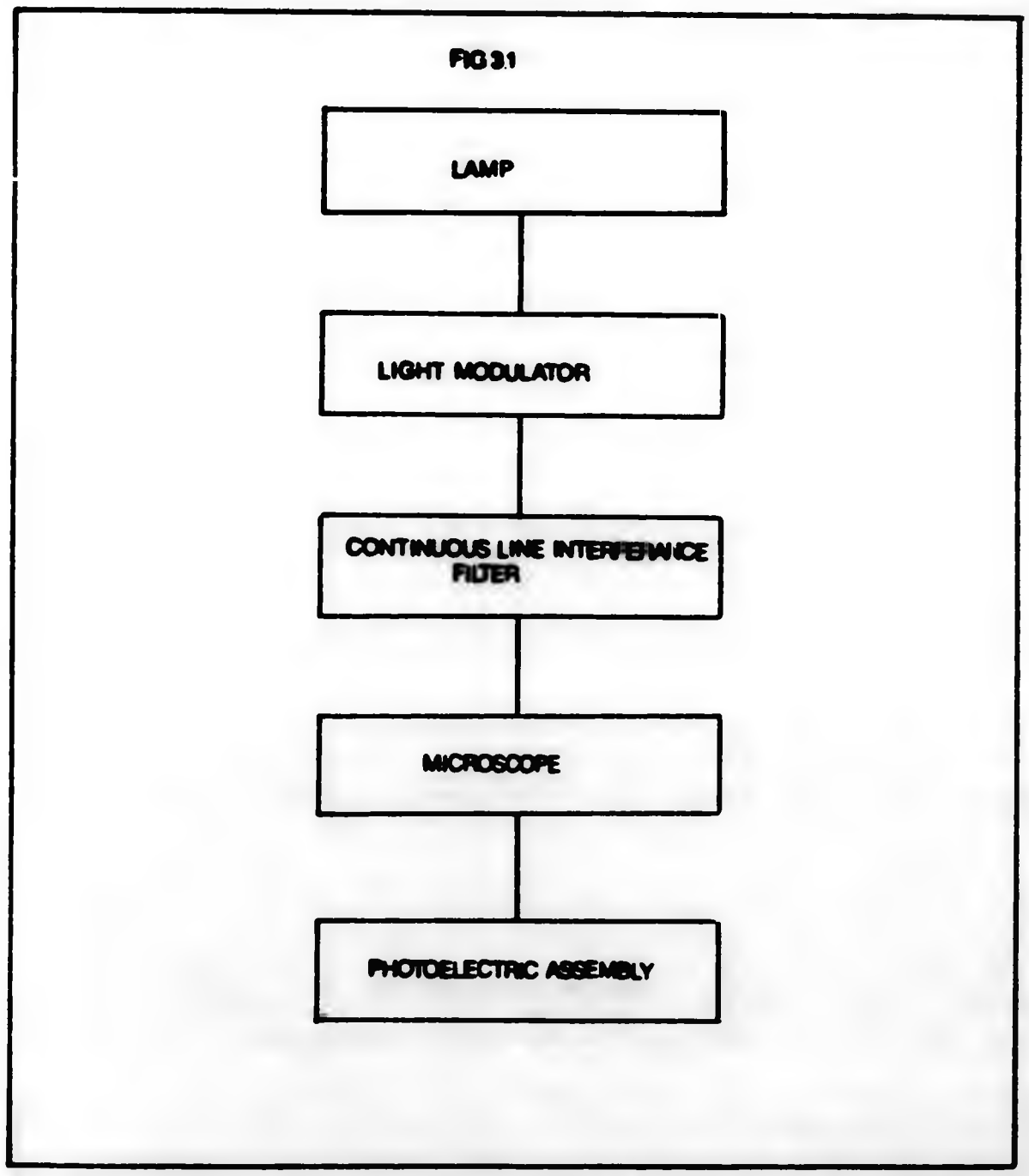

Fig 3.1 Modules which constitute the basis of the Zeiss MPM03 microscope photometer.

3.1.3 Modulation

In an unmodulated syst em, the dark current from the photo-detector (section 3.1.8) and any extraneous light entering the system, will produce a background value superimposed on the measured value from the specimen. However, if the incident light is modulated with a certain frequency and phase, then only the modulated light reflected from the specimen will be accepted by the measuring system. The dark current of the photo detector, and the current due to extraneous light, being unmodulated, are ignored by the detector. Modulation also to some extent suppresses photo current noise. This is particularly advantageous in photomultipliers with a low to moderate gain. Modulation is achieved by means of a rapidly rotating chopper synchronised with the measuring system so that only modulated light is detected.

3.1.4 Monochromator

The Monochromator utilised by the microscope-photometer in this study was of the continuous interference filter type with a band width of 12 nm. This type of interference filter works by transmission. It consists of a glass substrate upon which successive layers of low reflective dielectric and higher reflective materials have been deposited. The greater the number of layers the higher the transmittance and the wider the pass band. For quantitative work a narrow band monochromator is essential, so the number of layers has to be limited.

The measured results can be influenced by the presence of 'false light' in the monochromator. This is light extended over a wavelength range outside the characteristic pass band, which can be defined by:

$$\text{False light portion} = \frac{I_f}{I(\lambda)} \times 100\ \%$$ (Piller, 1977) 3.1

I_f = intensity of light having wavelengths outside the pass band

$I(\lambda)$ = intensity of light having wavelengths within the pass band

λ = central wavelength

Piller (1977) has shown that false light can originate from a variety of sources, namely:

i) Heterochromatic stray light: This is light which gets through the interference filter in an irregular manner, and because of its wide spectral range appears white. It arises from imperfect glass surfaces, metal mounts, dust and cement within the device which reflect, scatter and transmit the light. Due to the method of manufacture, no interference filter is completely free of holes, so care should be taken when choosing an interference filter to ensure there are as few holes as possible. Care should also be taken to maintain a dust free environment within the device.

ii) Fluorescence: This phenomenon arises when the glass and/or the cement show distinct fluorescence, the intensity of which is particularly apparent at short wavelengths. For this reason the monochromator should be fitted with high quality glass and cement which do not exhibit fluorescent behaviour.

iii) Harmonic Spectral bands: These are bands containing light of regular multiples or sub multiples of the wavelengths within the regular band.

3.1.5 Polariser

As many reflected light phenomena viewed under crossed polars are due to small rotations and ellipticities, it is vital that such effects are not introduced within the microscope itself. A faulty or imperfectly set polariser renders the microscope unusable for the observation of such effects. For this reason the vibration direction of the polariser must lie in or perpendicular to the symmetry plane of the reflector (section 3.1.7). In practice the polariser is usually set with

its vibration direction E-W to allow the maximum intensity of light to reach the detector.

3.1.6 Objectives

Microscope objectives can be characterised by the following properties:

i) Magnification number which lies in the range 1 - 25.

ii) Numerical aperture defined as:

$$N \sin \theta = (N.A.) \qquad 3.2$$

where:

N = refractive index of the medium

θ = angle of incidence on stage object (or half angle of cone)

iii) The nature of the corrections for various types of aberrations shown in Fig. 3.2.

3.1.7 Reflectors

The purpose of the reflector is to deflect the incident horizontal beam downwards onto the specimen on the stage. There are three main types of reflector:

3.1.7.1 Gauss Mirror Reflector

The front surface of the reflector (Fig. 3.3) is coated with a film to increase reflection downwards, while the back surface is bloomed to minimise such reflection. After reflection by the sample, the reflected beam travels upwards towards the reflector, where a considerable amount of the returning light is lost by:

i) Being reflected back towards the lamp.

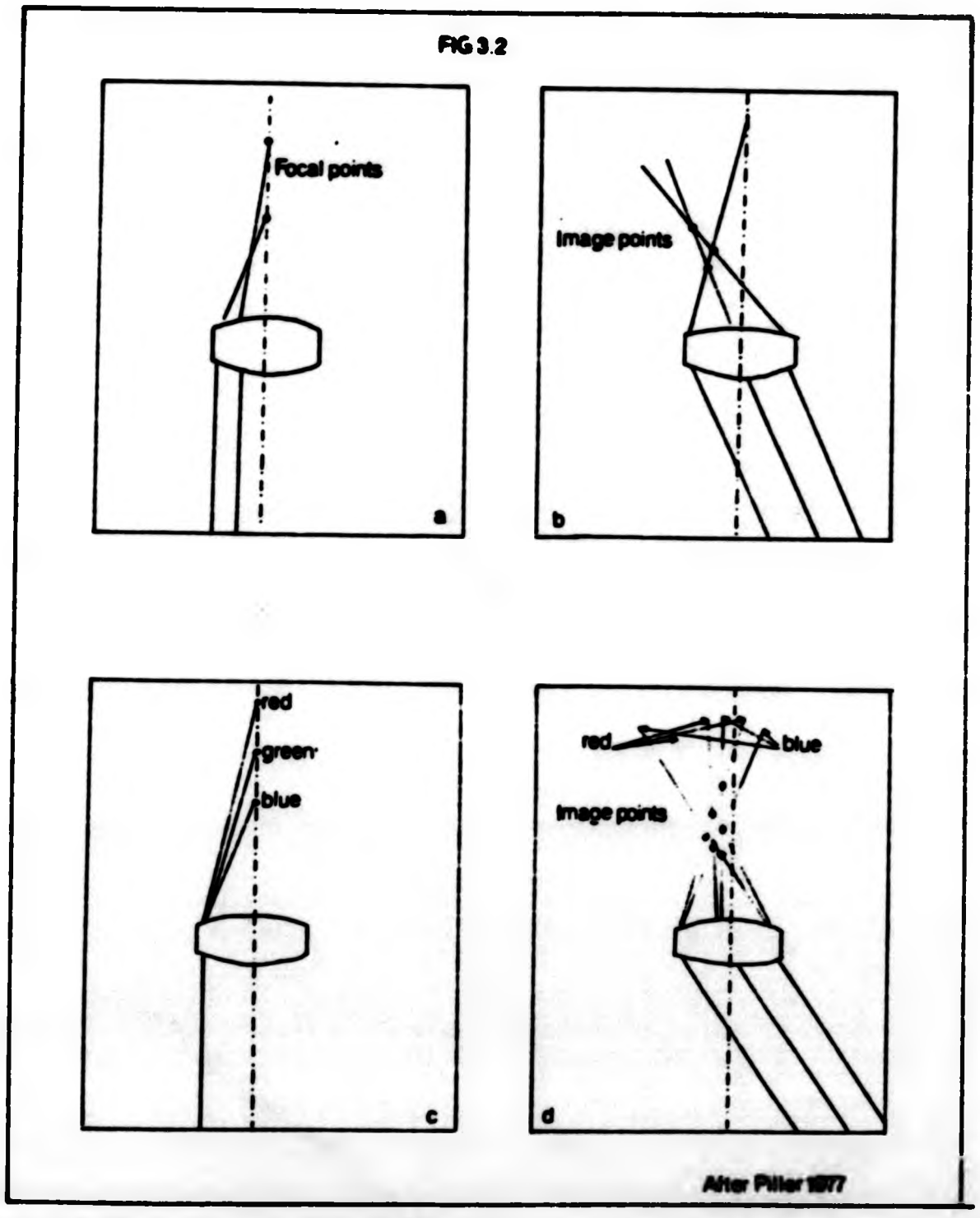

Fig 3.2 Basic lens aberrations,

a. Spherical aberration, along the axis, the image of a point appears blurred.

b. Asymmetrical aberration, normal to the axis, the image of an off axial point appears as a comet shaped blur.

c. Chromatic aberration, along the axis, the image of a white point in the axis appears with different colouration for different focussing positions of the lens.

d. Chromatic aberration, normal to the axis, the image of an off axial point appears blurred and shows different colouration for different focussing positions of the lens.

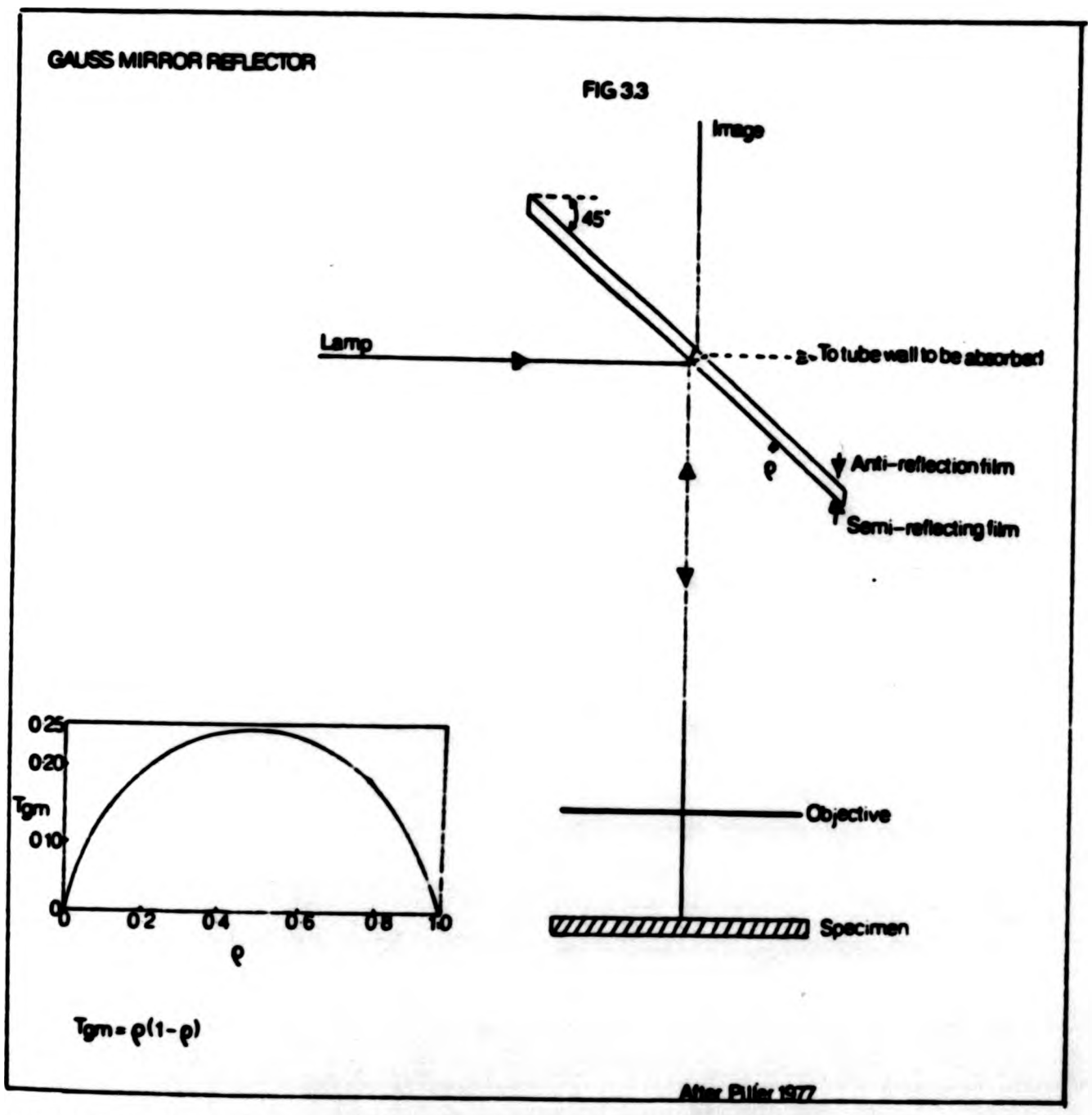

Fig3.3 Path of the axial ray in a Gauss mirror reflector.

ii) Being absorbed by the front-surface-film.

The efficiency of the reflector can be thus expressed by the total transmittance (T_{gm}) given by:

$$T_{gm} = \frac{\text{Intensity of light leaving Gauss mirror in the direction of the image}}{\text{Intensity of the light arriving from the lamp}} \qquad 3.3$$

If the reflection from the back of the Gauss mirror, the absorption of the glass and the interactions of the beam with the medium outside the Gauss mirror are negligible then:

$$T_{gm} = \varrho(1 - \varrho) \qquad 3.4$$

Where ϱ is the reflectivity of the front face of the glass plate for a given angle of incidence.

The Fresnel formulae for linearly polarised light at oblique incidence (Chapter 2) are:

$$R_s = \frac{\sin^2(\theta_0 - \theta_1)}{\sin^2(\theta_0 + \theta_1)} \qquad R_p = \frac{\tan^2(\theta_0 - \theta_1)}{\tan^2(\theta_0 + \theta_1)} \qquad 3.5$$

Where θ_0 = angle of incidence
and θ_1 = angle of refraction

The reflectance of the s-component is always greater than the p-component so consequently:

i) On illumination with natural light the Gauss mirror exhibits certain polarising properties.

ii) For linearly polarised light, the transmittance of the reflector is greater if the vibration direction of the polariser is set E-W than if it is set N-S. This is because in the former case

it is the s component which is effective whereas in the latter it is the p.

iii) Hallimond (1953) has shown that vibration directions of light waves not lying in either of the principal planes are rotated by the glass plate, such that when observed under crossed polars, the image reflected from an isotropic surface has a dark band running vertically across it. Only within this band are the rotation effects negligible and thus only within this area should reflectance measurements be made.

3.1.7.2 Smith Reflector

The dark band effect of the Gauss mirror reflector can be substantially reduced by using the design shown in Fig. 3.4 (Smith, 1964) where a mirror is used to reduce the angle of incidence on the glass plate by half to 22.5°. This greatly reduces the rotation effect on the plane of polarisation of the light, see above. Consequently, the whole field of view appears dark upon insertion of the analyser. As the mirror is not a perfect reflector there is a loss of some 10 % in transmittance compared to the Gauss mirror reflector, but this is acceptable in view of the advantages described above. Assuming that the reflection from the back of the glass plate, the interaction of the beam with the medium outside the glass plate, and the absorption of the glass are negligible, then the transmittance T_{sm} is:

$$T_{sm} = \varrho\, \varrho_m (1 - \varrho) \qquad 3.6$$

where:

ϱ = reflectance of front face of glass plate for actual angle of incidence on the glass plate.

ϱ_m = reflectance of mirror for the actual angle of incidence on the mirror

SMITH REFLECTOR

FIG 3.4

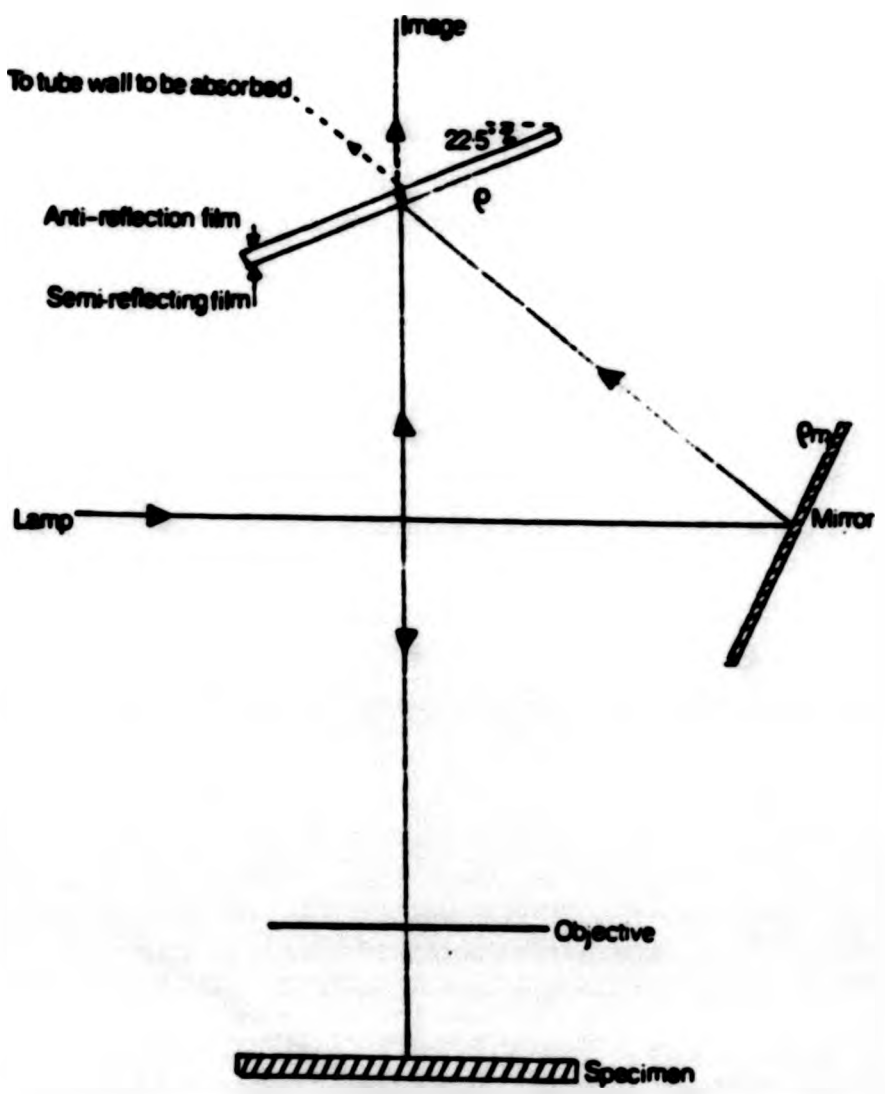

$T_{em} = \rho_m \rho (1-\rho)$

After Piller 1977

Fig 3.4. Path of the axial ray in a Smith reflector.

3.1.7.3 Berek Prism Reflector

The Berek or trapezium prism (Berek, 1936) achieves an almost entirely dark field under crossed polars, reflecting a uniform state of polarisation across the field of view. In the prism the light undergoes a set of three internal reflections, at each of which a phase retardation of the reflected ray with respect to the incident ray is introduced, Fig. 3.5. However, this phase retardation is not the same for both p and s components, resulting in a phase difference between them. The magnitude of this phase-shift is dependent upon the refractive index of the glass used to construct the prism. For a refractive index of 1.74 it is approximately 60°, thus three reflections introduce a phase-lag of 180°. Consequently a linearly polarised beam incident on the prism at any given azimuth will be rotated through 180° so that on leaving the prism it will still be linearly polarised.

The transmittance of the prism reflector (T_{pr}) is much greater than the two reflectors described previously, as very little light is lost during the internal reflections.

$$T_{pr} = \frac{\text{Intensity of light leaving prism in the direction of the objective}}{\text{Intensity of light arriving from the lamp}} \qquad 3.7$$

If the effects due to reflection at the entrance and exit faces of the prism, and absorption by the glass are negligible the transmittance is determined by the reflectance from each of the prism faces as:

$$T_{pr} = \varrho^3 \qquad 3.8$$

(because Total Internal Reflection (T.I.R) $\varrho = 1$) assuming N of glass = 1.74

The prism reflector does have the disadvantage that it can only occupy half the aperture area of the objective, the other half being required to accommodate the returning reflected rays from the specimen. The other disadvantage of the prism is that the light beam falling on the specimen is oblique causing shadowing. This disadvantage is compensated

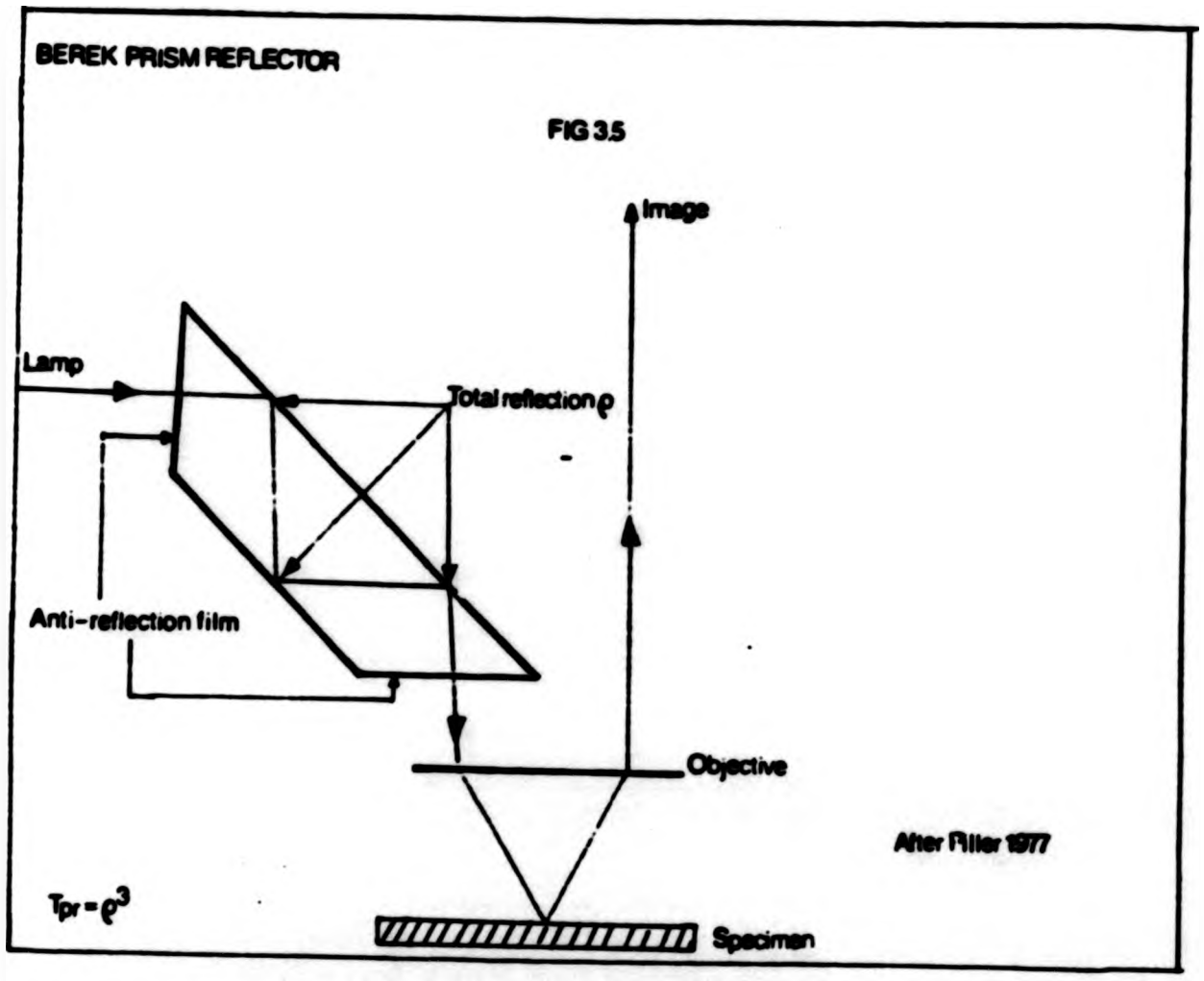

Fig 3.5 Path of the axial ray in a Berek prism reflector.

for by the reduction in glare (due to reflections at glass surfaces). The prism prevents light arising from these sources from reaching the image.

3.1.8 Photoelectric Assembly

The technical design of the photomultiplier tube is shown in Fig. 3.6. The photo-detector used in this study was of the S20 type where the prefix S is an internationally agreed symbol for photomultiplier tubes and the number denotes the type of photocathode material and the spectral response of the tube (Fig. 3.7). In the S20 photomultiplier the photocathode is made up of a mixture of the alkali metals, Na, K, Cs and Sb and has a useful spectral range of 320 - 790 nm.

The dark current mentioned in section 3.1.3 is a permanent d.c. current caused mainly by thermionic emission from the cathode and its neighbouring electrodes. The degree of dark current is dependent upon the temperature and the thermal work function of the cathode. However, in this study the dark current can effectively be ignored because the light is modulated.

Apart from the dark current the photodetector is also susceptible to other types of electrical noise which can originate from any of the following:

i) Lamp flicker (section 3.1.2).

ii) Disturbance of the light train by vibrations of a mechanical origin.

iii) Fluctuations in the electric supply.

iv) Photomultiplier noise.

Photomultiplier noise arises from fluctuations in the photon input, and the dark current, and from other electrical emissions within the photomultiplier tube. Every effort is made to keep all types of noise to a minimum and so increase the precision of the measured values.

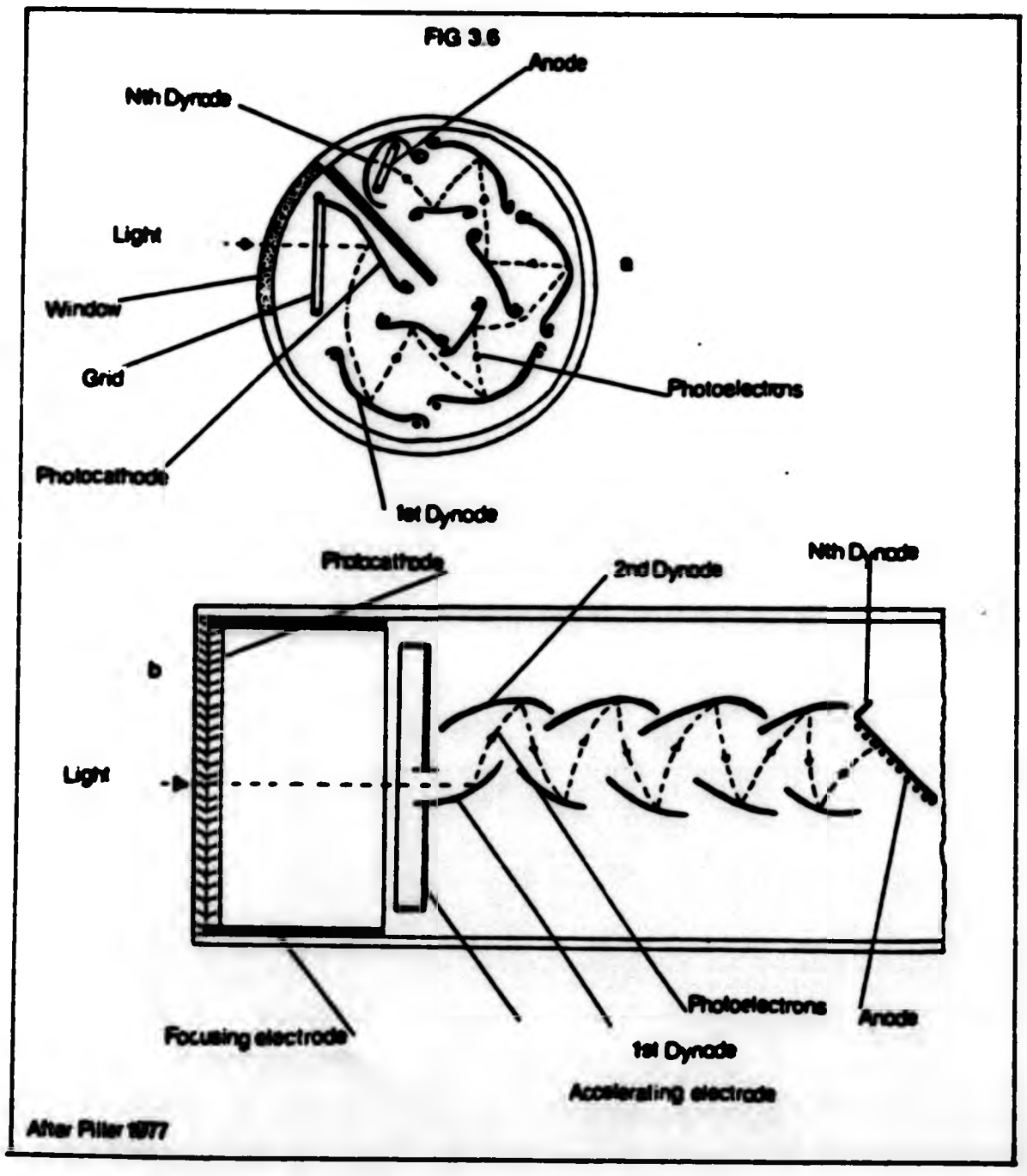

Fig 3.6 Design of photomultiplier tubes,

a. Side window tube: The light falls from the side on a reflecting cathode, the number of dynodes is usually limited to nine.

b. End window tube: The light falls from the front on a semi-transparent cathode, the number of dynodes being upto fourteen.

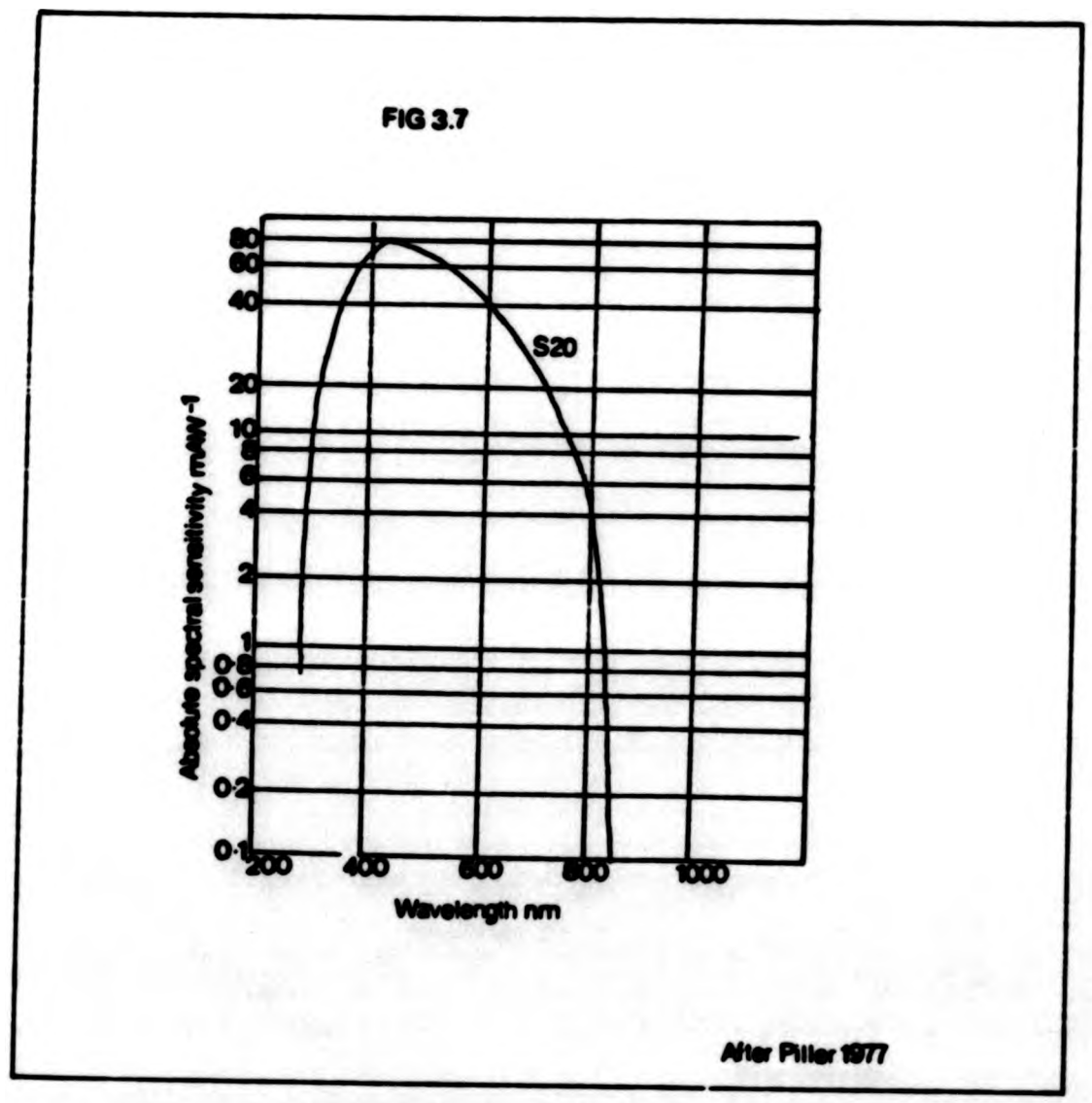

Fig 3.7 Absolute spectral sensitivity of the S20-type photocathode.

The final measurements are achieved by a set of electric modules which convert the photometer response into a digital readout, Fig. 3.8.

3.2 Microscope Photometer Measurement Techniques

3.2.1 Measurement Procedure

The main components of the equipment used in this study have already been described, section 3.1, a brief account of the equipment can also be found in Clark and Criddle (1982). The following procedure is adopted when making a series of measurements:

The microscope-photometer is switched on and left for approximately thirty minutes in order to allow the lamp and electronics to stabilise. During this time the standard and specimen can be cleaned.

Careful cleaning of samples is essential, as the presence of surface impurities and films can radically alter the measured values. If the surfaces of the samples are coated with oil (from previous measurements) or other impurities, they can be removed by the use of a detergent solution and soft tissue, (which should be kept in a box because atmospheric dust can scratch soft samples) followed by careful cleaning with alcohol and then acetone. Care is taken to avoid the contact of acetone with the mounting resin, which is soluble in it.

The specimen and standard are then placed on a Lanham specimen-changer stage (section 3.2.2), where, after a suitable area has been chosen for measurement, the two are levelled. Careful levelling of specimen and standard within the same focal plane is essential (c.f. errors Chapter 4) if accurate results are to be obtained. Levelness is tested for by means of the image of the illuminator aperture diaphram (I.A.D.) as reflected by the specimen (or standard) and formed in the back focal plane of the objective. This is observed conoscopically using a low magnification objective (x 4), with the I.A.D. closed down (usually to 2) to give a sharp image. Upon rotation of the stage if the image of the I.A.D. is seen to move then the sample is not level, this situation can be remedied by adjustment of the three fine screws, so that stage rotation causes no movement of the image.

FIG 3.8

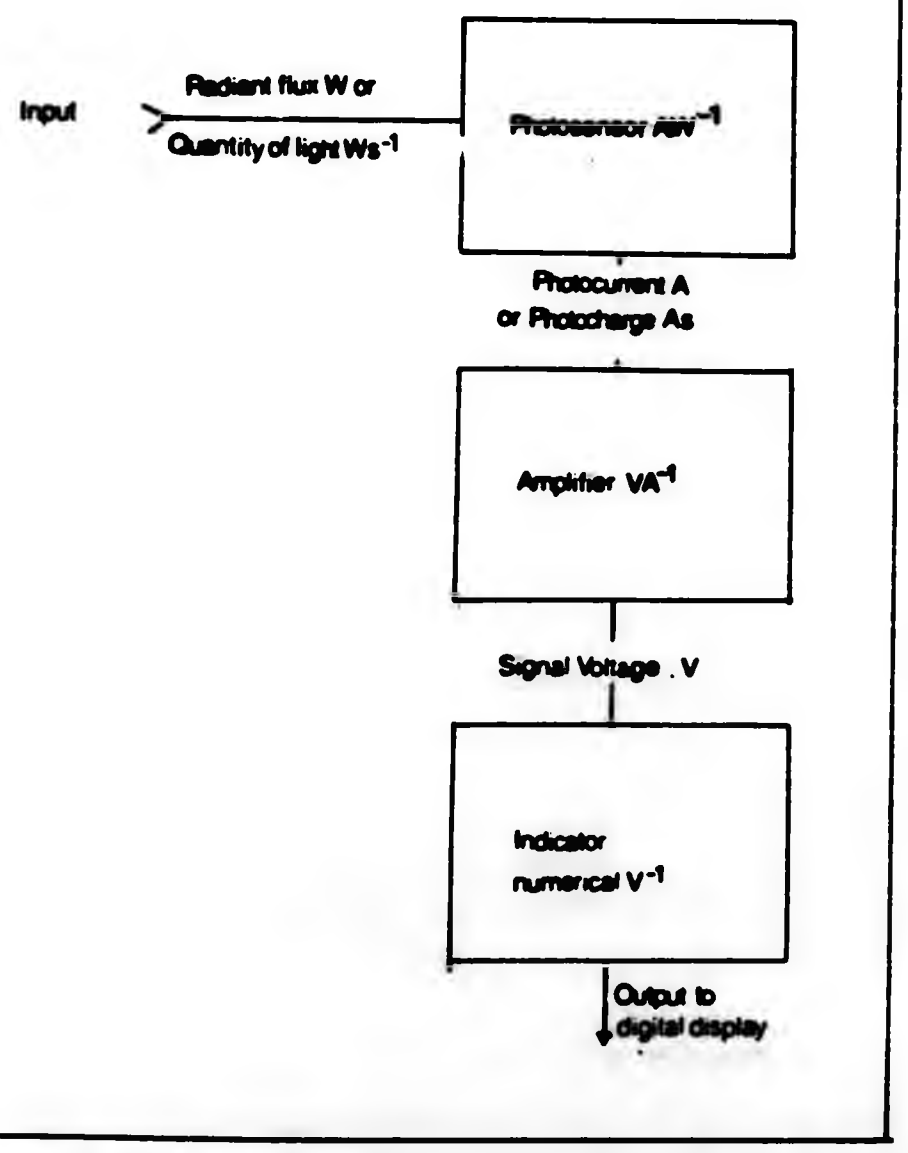

Fig 3.8 Basic photoelectric assembly.

When both specimen and standard have been successfully levelled, a higher powered objective can be used, (usually x 16) and the surface of the specimen brought into sharp focus. The appropriate photometer-field-stop (Ph.F.S.) is selected and centred on the cross wires. (Slight re-focussing of the specimen may be necessary after insertion of the photometer-stop). The illuminator-field-stop (I.F.S.) is then selected, this should be approximately twice the apparent diameter of the photometer stop. The reason for having the measured area well inside the illuminated area is to prevent any diffraction effects from the edge of the latter passing into the photometer. The stop is then centred on the cross wires.

Next, the appropriate sensitivity range is chosen for the photometer, this is done by selecting the sample with the highest reflectance, driving the interference filter to 550 nm (the region of maximum sensitivity) and then adjusting the digital voltmeter (DVM), which was zeroed at the start of the experiment, to read approximately 1800 (arbitary units). This ensures that both specimen and standard will fall within the same range, the interference filter is then driven back to the 400 nm start position.

After inserting the correct programme into the H.P. 9830 desk top computer, measurement can commence. The programme used requires alternate measurements of specimen and standard (fifteen of each) to be made in air, and then, after refocussing, the same procedure to be repeated in oil. Each set of specimen-standard readings takes approximately two minutes, but can be made faster or slower, by altering the step rate of the interference filter. However, two minutes is found to be the optimum, as any faster reduces the precision of the readings, and any slower increases the time taken to complete the experiment without a significant improvement in precision. After each set of specimen-standard measurements the focus is checked for drift and if necessary adjusted.

The preceding discussion is true for isotropic minerals, however, when anisotropic minerals are being measured, the specimen must be measured at the positions of extinction (found by inserting the analyser) which should approximate to the maximum and minimum in the DVM readings, the

measuring sequence being:

i) Measurement of specimen in maximum position.

ii) Measurement of standard.

iii) Measurement of specimen in minimum position.

The programme analyses the results, discarding the two highest and two lowest of the fifteen sets of readings in air and oil and then prints out the average and standard deviation of the remaining measurements.

3.2.2 Lanham Specimen-Changer Stage

The Lanham specimen-changer stage, Fig. 3.9, enables both specimen and standard to be positioned and levelled at the beginning of an experiment and interchanged by means of a precision base-slide. Specimen and standard are brought into exactly the same plane focus by the following procedure:

i) The specimen is brought into approximately the same focal plane as the standard by rotating the work table of the specimen holder up or down on a screw thread,

ii) With the slide at the end of its travel on the specimen side, the area to be measured is selected and centred by movement of the holder. This holder has a magnetic base plate to facilitate measurement, the specimen is then carefully levelled,

iii) The slide is drawn to the other end position and the standard is carefully levelled, and by means of a screw-controlled inclined plane is brought into exactly the same position of focus as the specimen. The movement of the rising slide is very fine and the slight lateral displacement produced is of little consequence as the standard has a relatively large homogeneous surface area.

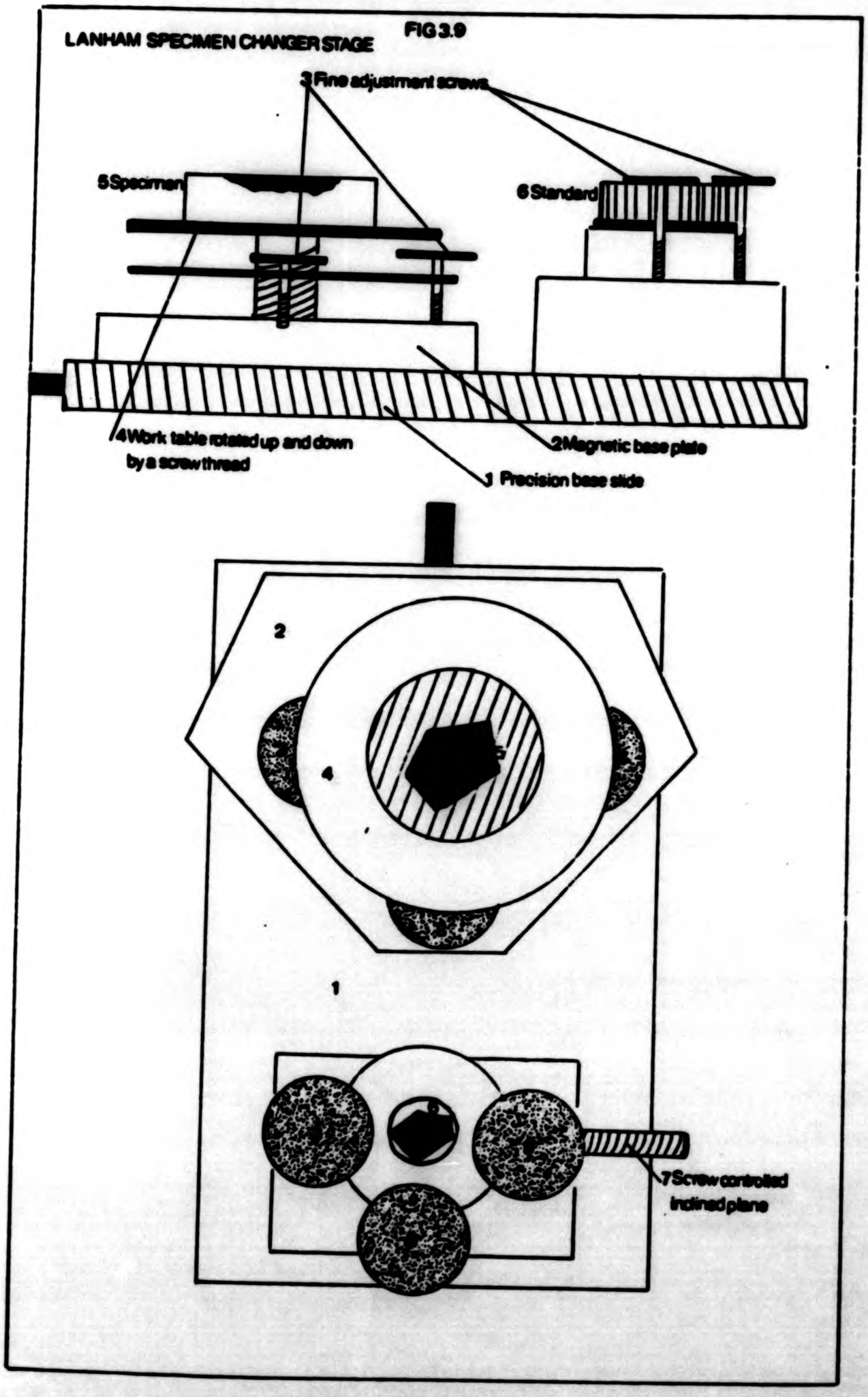

Fig 3.9 Lanham specimen-changer stage.

Interchange of specimen and standard is achieved by moving the slide from one end position to the other; when this is done smoothly neither of the polished surfaces should move, so the area being examined will remain the same.

3.2.3 Standards

"The procurement of material standards of suitable quality is a major limitation of the art" (Clarke, 1972) and considerable energies have been devoted to this problem (Hallimond, 1970; Galopin and Henry, 1972; Piller, 1974, 1977; Embrey and Criddle, 1978). The main difficulty in finding suitable reflectance standards stems from the criteria which must be fulfilled before a material is acceptable, namely:

i) The material must be chemically and physically stable both internally and externally, i.e. it must not corrode or tarnish or show any signs of lattice restructuring with time. The latter is the reason why vacuum deposited surfaces are unsuitable. It must also be capable of taking and retaining a good polish.

ii) The surface must be perfectly flat over an area of at least 0.5 cm^2 (Piller, 1977) as this is the area required for primary calibration in a standards laboratory.

iii) The material must be perfectly isotropic.

iv) The standard must have an absorption sufficient to prevent the return of light scattered from the base, and free from any internal reflections, which involves the absence of sub-surface cleavages and cracks.

At present there are only four standards officially recognised by COM IMA (Commission on Ore Microscopy of the International Mineralogical Association), these are:

1) Single homogeneous crystal of tungsten-titanium-carbide (WTiC) with the (0001) basal face polished; mean reflectance of 47 % in air,

ii) Silicon; mean reflectance 45% in air,

iii) Single crystal black silicon-carbide (SiC) with basal face 0001 polished; mean reflectance 20 % in air.

iv) Dark neutral glass: mean reflectance in air of 4 %.

Piller (1977) has suggested that liquid surfaces could be used as reference standards in the ultra-violet and near infra-red. There is a large gap in reflectance between the two most commonly used standards in ore mineralogy, namely SiC and WTiC of some 20 %. There are also, to date, no accepted standards for higher reflectances although synthetic sperrylite (PtAs) with a mean reflectivity of 54 % has been considered Criddle (1984) the problem here is to persuade a commercial organisation of its economic viability.

The situation is, however, much worse for oil reflectance standards. With the exception of SiC these are all derivative standards, calibrated by computation from the air reflectance and the refractive index of immersion oil assuming zero absorption.

3.3. Ellipsometer - Description of Apparatus

3.3.1 Introduction

The construction and operation of the ellipsometer used in this study have been described by Roberts and Meadows,1974; Meadows,1975; Clarke, 1980 and Rastall, 1980. As technology has advanced so the ellipsometer has been modified, and in the following discussion these changes will be concentrated on, and their effects on the results obtained.

3.3.2 Ellipsometer Layout

The light source (1), Fig. 3.10, originally used was a Hytek mercury arc lamp, which produced a line spectrum of sufficient intensity to enable readings to be taken at 366, 435.8, 564.1 and 577.1 nm. the light source currently in use is an AEG Osram high pressure xenon arc, which allows continuous readings to be made over a spectral range from

FIG 3.10

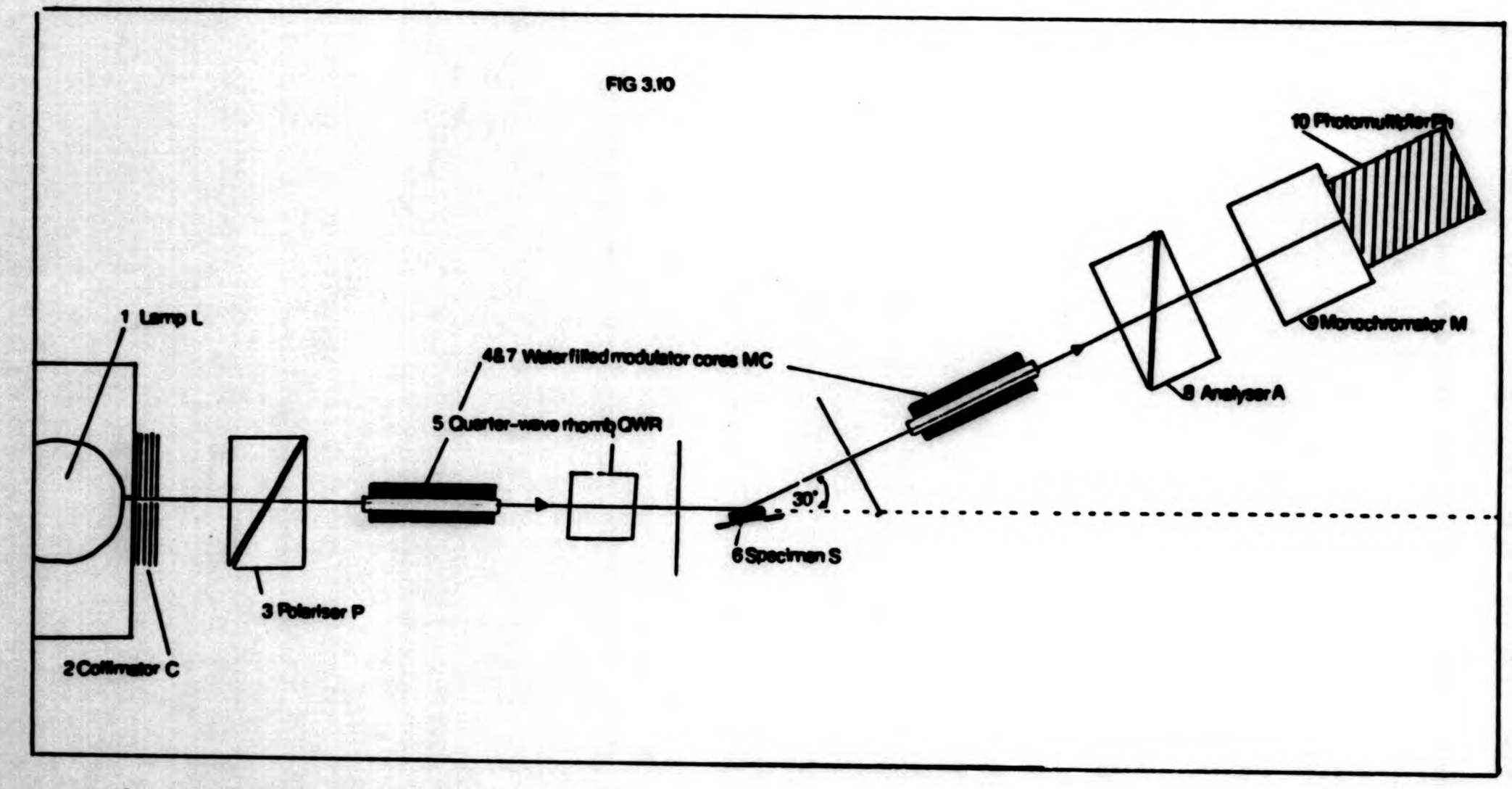

Fig 3.10 Basic ellipsometer layout.

the near infra-red to the near ultra-violet. Clarke (1980) observed that while changing lamps led to some reduction in the absolute resolution of the analyser and polariser azimuths, this was more than compensated for by the increased spectral range.

The xenon arc lamp is operated from an 80V, 30A d.c. supply, the a.c. component of which has been smoothed to minimise cathodic erosion. The lamp housing is water cooled to avoid temperature fluctuations during an experiment; the cooling is also enhanced by the passage of air over the lamp, which provides a means for the removal of the large quantities of ozone produced. A filter containing successive layers of activated charcoal removes most of the ozone before the air is returned to the atmosphere.

The beam is collimated (2) and limited by a succession of stops to a beam diameter of approximately 2 mm before entering the polariser prism (3) which is of a Glan-Foucault air-gap type and mounted on a servo goniometer. The light, now plane polarised, travels to the first of two Faraday modulator cores (4) and (7).

The Faraday effect is the rotation of the plane of polarisation of a transmitted light beam by an applied longditudinal magnetic field. The effect of a magnetic field on the absorption bands of the core material is to produce a splitting, or Zeeman effect, such that at any particular wavelength there are two effective refractive indices. Of these one is peculiar to right-handed circularly polarised light, and the other is to left-handed, so that the two components travel at different velocities through the core. A phase lag is thus induced, and on recombination of the left and right handed components, a rotation in the plane of polarisation is observed, the magnitude of which is dependent on the path length and the difference between the two refractive indices. The magnitude of the dispersion is affected by the proximity of the absorption band, and thus, it is difficult to find a suitable modulating medium to cover the entire visible range.

For this reason the ellipsometer described by Clarke (1980) used silica cores to cover the ultra-violet and visible blue region of

the spectrum, and dense flint glass for the visible red region and infra-red. Liquid water cores are now used for the following reasons:

i) Solid cores had to be changed during the course of the experiment, necessitating a major realignment of the apparatus,

ii) It was advisable to allow the temperature to equilibrate for at least half an hour to minimise strain birefringence in the cores.

None of the above is readily apparent using liquid cores. The cores themselves are constructed from glass tubing 1.5 cm in diameter and 40 cm long, the ends of which are parallel. Quartz windows are attached to either end. Strain birefringence is minimised by using an adhesive which does not contract upon setting. Using water cores does lead to a loss of sensitivity in the infra-red due to the magnetically induced birefringence of water being less than that of solid core materials, and the decreased modulation of the second core.

After passing through the first modulator, the beam enters the compensator, an achromatic quarter-wave rhomb (5) (King and Downs, 1969) coated with a thin film of magnesium fluoride, calibrated by The National Physical Laboratory, Teddington. The original calibration gave the retardation as within 0.1° of 90° over the complete visible range but the tolerance may have increased over the ensuing years (King, 1983). Due to the sensitivity of the quarter-wave rhomb to vibration it is situated on the rigid incident rather than the mobile reflection arm. The elliptically polarised light passes through an iris stop and onto the reflecting surface of the sample (6); the reflected light being linearly polarised. After passing through a further stop the light enters a second modulator core (7), which is similar in construction to the first but operated at a frequency of 1500 Hz compared to 1200 Hz in the previous case. The beam, now doubly-modulated, enters the analyser (8) which is identical to the polariser, after which it proceeds to a Spex-Minimate monochromator (9) and then to a photomultiplier tube (10).

Two photomultipliers were used for most experiments, the most sensitive being an EMI tube which was used between 300 - 600 nm, a less sensitive RCA tube was used between 580 - 750 nm. Although a

the spectrum, and dense flint glass for the visible red region and infra-red. Liquid water cores are now used for the following reasons:

i) Solid cores had to be changed during the course of the experiment, necessitating a major realignment of the apparatus,

ii) It was advisable to allow the temperature to equilibrate for at least half an hour to minimise strain birefringence in the cores.

None of the above is readily apparent using liquid cores. The cores themselves are constructed from glass tubing 1.5 cm in diameter and 40 cm long, the ends of which are parallel. Quartz windows are attached to either end. Strain birefringence is minimised by using an adhesive which does not contract upon setting. Using water cores does lead to a loss of sensitivity in the infra-red due to the magnetically induced birefringence of water being less than that of solid core materials, and the decreased modulation of the second core.

After passing through the first modulator, the beam enters the compensator, an achromatic quarter-wave rhomb (5) (King and Downs, 1969) coated with a thin film of magnesium fluoride, calibrated by The National Physical Laboratory, Teddington. The original calibration gave the retardation as within 0.1° of 90° over the complete visible range but the tolerance may have increased over the ensuing years (King, 1983).
Due to the sensitivity of the quarter-wave rhomb to vibration it is situated on the rigid incident rather than the mobile reflection arm.
The elliptically polarised light passes through an iris stop and onto the reflecting surface of the sample (6); the reflected light being linearly polarised. After passing through a further stop the light enters a second modulator core (7), which is similar in construction to the first but operated at a frequency of 1500 Hz compared to 1200 Hz in the previous case. The beam, now doubly-modulated, enters the analyser (8) which is identical to the polariser, after which it proceeds to a Spex-Minimate monochromator (9) and then to a photomultiplier tube (10).

Two photomultipliers were used for most experiments, the most sensitive being an EMI tube which was used between 300 - 600 nm, a less sensitive RCA tube was used between 580 - 750 nm. Although a

300 - 750 nm photomulitplier was available, this was considered less sensitive, and less accurate and thus unsuitable for making accurate measurements; the two photomultiplier method was preferred.

Extraneous noise was minimised by encasing the photomultiplier in a series of black silk cloths and employing only d.c. lighting during the course of an experiment.

3.4 Ellipsometer: Measurement Techniques

3.4.1 Alignment

The accuracy of the ellipsometer for a given reflecting surface is limited by the reproducibility, measurement of angle or incidence and of the null positions of the analyser and polariser prisms. Complete realignment of the ellipsometer should be undertaken at least every six months if exact and accurate results are required. A detailed account of both optical and electronic realignment is given by Hunt (1984).

The operational procedure for making a set of ellipsometric measurements is as follows:

Thirty minutes should elapse after switching on to enable the lamp and electronics to warm up.

The modulating cores are refilled with water, and repositioned. Due to slight imperfections in the construction of the cores, i.e. the ends are not quite parallel, they must be adjusted so as to enable the light to pass down their central axis. This position was defined previously in the straight through position by placing a mirror at the end of the reflection arm (the photomultiplier and monochromator having been removed) and the cores rotated such that the incident and reflected rays travelled along the same path, i.e. throught the centre of the cores. The mirror was then removed and the spot where the light struck the wall marked. This means that when the marked spot and light spot are coincident the cores are correctly positioned.

While still in the straight-through position, after replacing the monochromator and photomultiplier, the electronic alignment of the system can proceed, whereby the polariser is allowed to seek its null under servo control at 475 nm and adjusted back to its fiducial by means of the quarter wave rhomb.

Optical alignment is undertaken after removing the photomultiplier and monochromator and setting the instrument to manual control. The reflection arm is rotated by means of air bearings to the required angle of incidence (usually 75°) which is measured by a vernier sliding on a fixed scale. Greater accuracy is achieved by supplementing this with a dial gauge enabling the angle of incidence to be set at 75° within tolerance limits of $\pm$ 0.01° (Rastall 1980).

The sample is attached to the back plate by means of sellotape and a magnet. Sellotape is preferred to plasticine (Rastall, 1980) as it holds the sample rigid whereas plasticine tends to 'flow', especially during warm weather, so that the area of orientation of the sample is not constant during the experiment. The back plate is kinematically controlled by three screws enabling rotation in all planes.

Fig. 3.11 shows the configuration of the ellipsometer for sample alignment, whereby light is reflected from the sample along the reflection arm and onto an alignment iris. The back plate screws are manipulated so that the light passes through the centre of the alignment iris, from which it strikes a plane mirror and is reflected onto the far wall of the laboratory. On the wall is a premarked spot, the position of which was determined by the previous optical realignment. Slight adjustment to the back plate screws are made until the light spot and the premarked spot are coincident, when this occurs the sample is optically aligned. After the alignment iris has been removed and the photomultiplier and monochromator replaced the ellipsometer is ready for use.

3.4.2 Measurement Procedure

Spectral scans were carried out in the range 300 - 700 nm, this is smaller than that quoted by Clarke (1980) and Rastall (1980) and is due, in part, to the changing of the core modulator medium from solid to

FIG 3.11

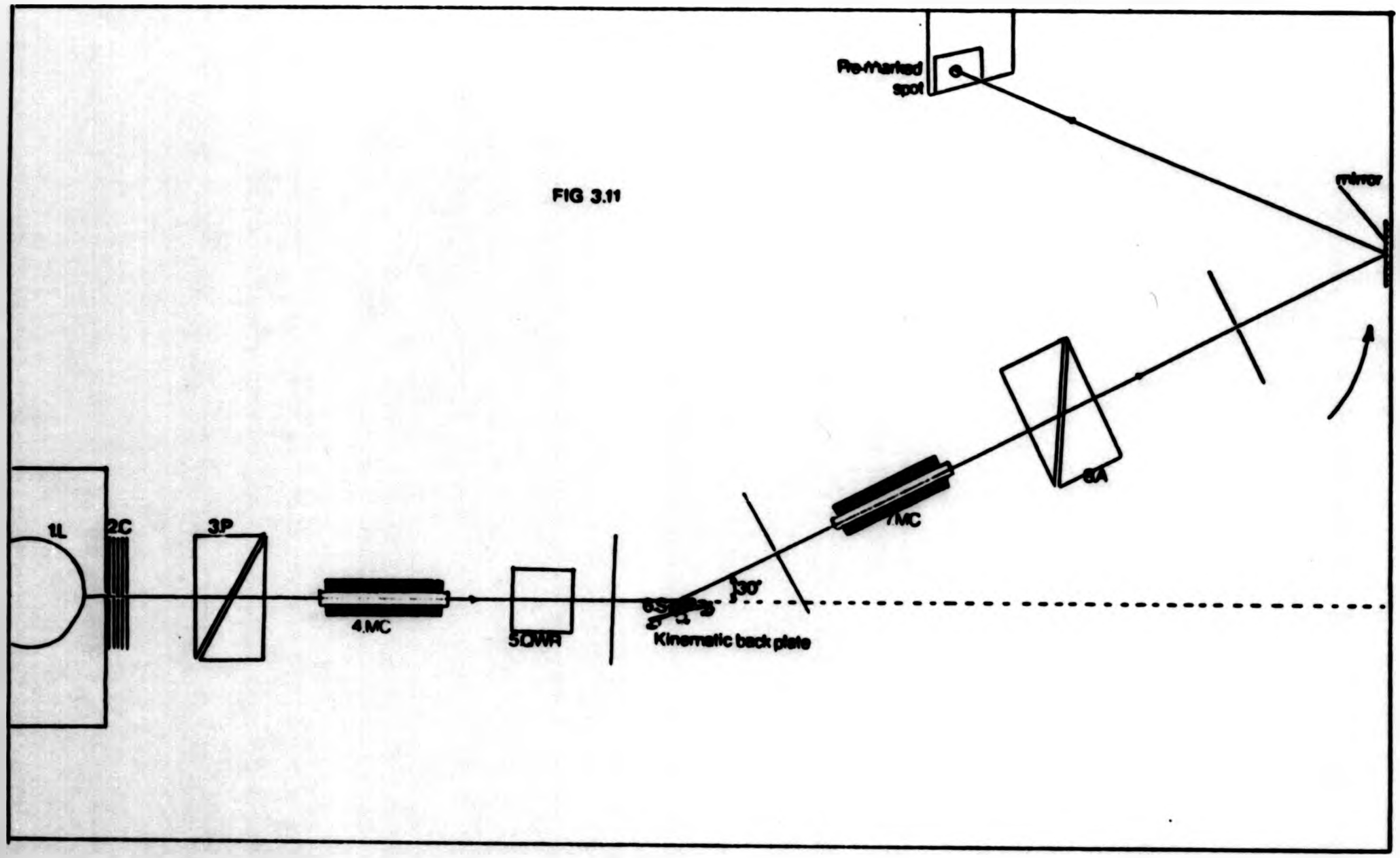

Fig 3.11 Alignment of specimen on ellipsometer.

liquid. Liquid water cores because of their lower Verdet constant produce a loss in sensitivity of the instrument at wavelengths greater than 620 nm. Despite this loss of sensitivity scans were continued up to 700 nm, in order to make the derived CIE colour co-ordinates meaningful. The measurement procedure was carried out as follows:

The monochromator is set to 300 nm, and the goniometers driven to the expected null position under manual control. Servo facilities were not used as this leads to a loss of 'steps' and consequently erroneous readings. This is due to the fact that the stepping motors are not designed to follow large changes in azimuth, where they are required to move rapidly, but small subtle changes to find an accurate null.

When the signal on the oscilloscope shows the characteristic near-null signal, servo driving can be employed, to achieve the first null positions which are recorded. The analyser and polariser azimuths are recorded at 10 nm intervals, after allowing the instrument to null.

At 600 nm the ellipsometer is switched over to manual control, and the extra high tension supply (EHT) turned down so that the photomultiplier can be changed. The EHT is then turned up to a higher value so as to compensate for the loss of sensitivity in both equipment and photomultiplier. The ellipsometer is then switched to servo and the scan continued. The ranges of the two photomultipliers are usually overlapped in the 560 - 600 nm region but the analyser and polariser readings are rarely very different.

Measurements are usually made in two quadrants for greater accuracy the zones chosen being 1 and 3, primarily because both analyser (A) and polariser (P) readings are positive in these quadrants and it is not necessary to move the quarter wave plate. The relationship between readings taken in zones 1 and 3 is given by:

$$A_1 = 90 - A_3 \qquad 3.9$$

$$P_1 = 90 + P_3 \qquad 3.10$$

After completing a scan in two zones, the reflection arm is

rotated on its air bearings back to the straight through position, the prisms driven back to their premarked fiducials and the instrument checked and corrected for drift.

The analyser and polariser readings are converted to reflectance n and k values on a DEC 10 computer using a suite of programmes designed by Clarke (1980).

3.5 Polishing

3.5.1 Polishing Procedure

Correct grinding and polishing of mineralogical specimens is extremely important, primarily because the equations used in Chapter 2 refer to specular rather than diffuse reflectance i.e. a surface on which all the artefacts have been reduced below the wavelength of visible light. The samples were mounted in Metaserv cold setting resin, special care was taken to remove any air bubbles that appeared, and the samples left overnight to harden. After removal of any excess plastic, the grinding and polishing procedure could commence. Successively finer silicon carbide-water slurries on glass were used to grind the samples which were thoroughly cleaned after each stage. After grinding on a 1200 silicon carbide-water mixture samples had a flat greyish matt appearance devoid of any bright scratch marks. Polishing was facilitated by the use of a suite of Kent mark 2 polishing machines, using 6, 3, 1 and 1/4 micron Hyprez diamond pastes on a six inch Engis PSU disc, with a water based lubricant. Each polishing stage took approximately one hour, depending on the hardness of the sample. Care was taken to avoid such effects as relief, 'comet tailing', and 'orange peeling' which would have detrimental effects on the ellipsometric and microphotometric results. After the 1/4 micron diamond polish, the sample was buffed using an alumina-water slurry on a 410 disc. The sample was now ready for ellipsometric or microphotometric measurements, buffing on alumina was also undertaken before the start of any experiment in order to remove tarnish films formed after polishing.

CHAPTER FOUR
ERRORS

4.1 Introduction

Without a full appreciation of the errors which might result during a series of microphotometric measurements a full understanding of the results cannot be achieved. Improvements in equipment design have eliminated some of the errors which were particularly prevalent in the past. Thus in the following discussion the lamp and photometer are assumed to be stable. The readings of the latter are also assumed to be linear (this is usually guaranteed by the manufacturer but should always be checked). The interference filter should also be checked to ensure that it is free from pin-holes.

Three types of error will be discussed here, those inherent in the apparatus, those caused by the operator, and those which are related to standard calibration or the effects of using such a standard in microscope photometry. The effects of reflectance errors on the derivation of the optical constants n and k have already been discussed in Chapter 2 section 2.2.4.

4.2 Focussing and Levelling Errors

4.2.1 Levelling Errors

A perfectly flat specimen, or standard, is a prerequisite for accurate photometric measurements, as a tilted surface will automatically produce an error. To minimise levelling errors the conoscopic levelling test (section 3.2.1) is employed using a low power objective. With a x3 objective a tilt angle of 0.08° can be detected, while the minimum tilt detectable with a x40 objective is 0.85° (fig. 4.1). This argument assumes that the eye can detect a shift of 0.1 mm in the image of the image aperture diaphram (I.A.D.) on the back focal plane of the objective.

4.2.2 Focussing Errors

Correct focussing of the specimen is obviously very important,

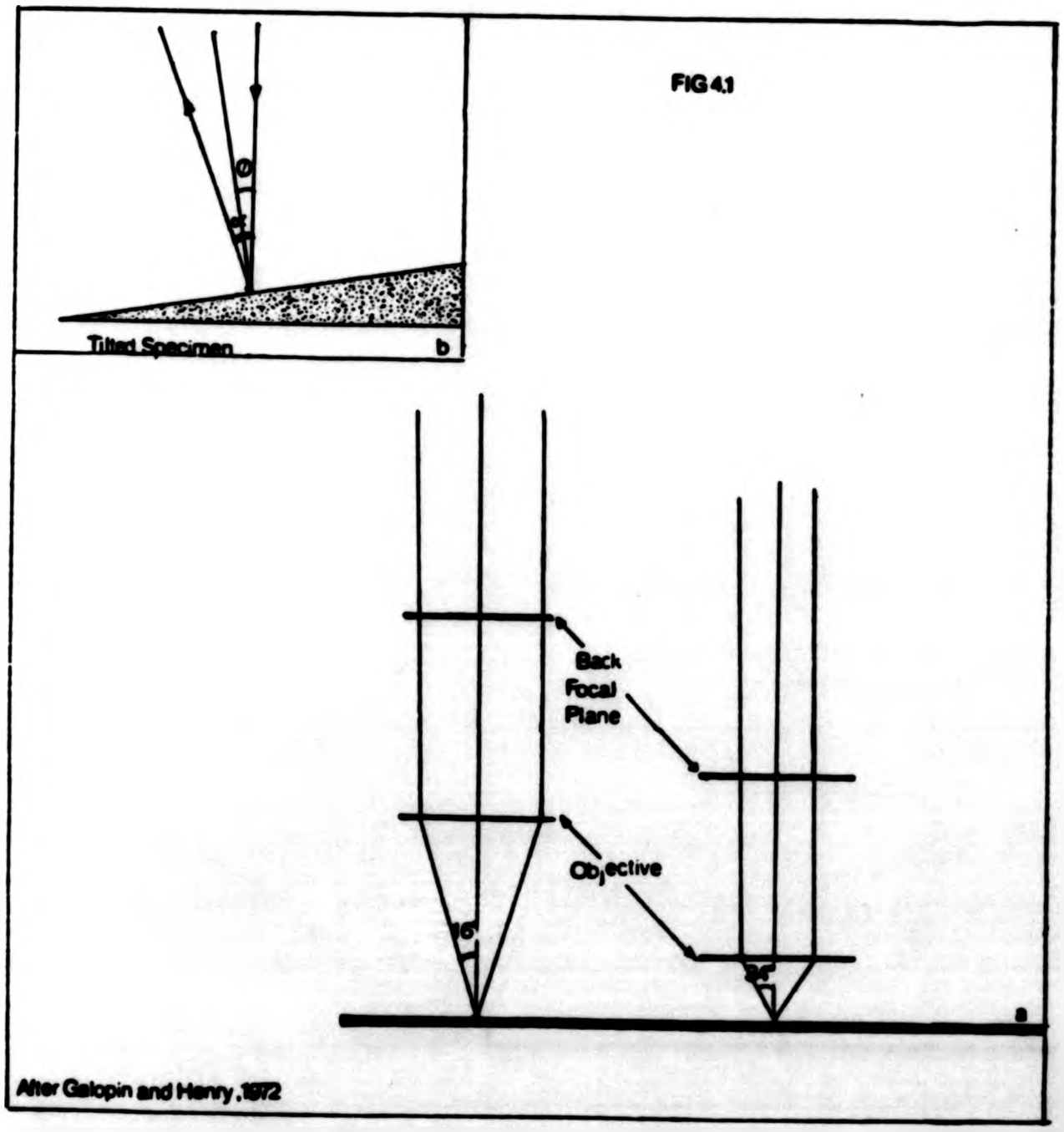

Fig 4.1. Angles involved in levelling the objective.

especially when care has been taken to avoid levelling errors. The change in height of a reflecting surface over which there is no perceptible diminution in the sharpness of the image is called the depth of focus. Over this range there is no change in the photometer reading, but outside it a small change in height will produce a dramatic change in the photometer reading. With a low powered objective there is a large depth of focus, but as the magnification increases the depth of focus decreases (Fig. 4.2).

4.3 Glare

4.3.1 Primary Glare

The phenomenon of glare sometimes referred to as the Schwartzchild-Villiger effect has been examined by a number of workers, (Naora, 1952; Galopin and Henry, 1972; Piller, 1977) and can be separated into primary and secondary components.

The first effect is caused by light from the back surface of the objective being reflected upwards before it has fallen on the specimen, Fig. 4.3. Most modern objectives are designed so as to reduce primary-glare to a minimum. To measure the amount of primary glare present in a system, under normal measuring conditions, a black box is placed over the front of the objective. This ensures that no light other than that reflected by the back surface of the objective reaches the photodetector. The reading on the DVM, C, is the correction factor which must be subtracted from all measurements to correct for the effect of primary glare

$$\frac{G_{sp} - C}{G_{st} - C} = \frac{R_{sp}}{R_{st}} \qquad 4.1$$

where,

G = DVM reading

R = reflectance

C = correction for primary glare

sp = specimen

st = standard

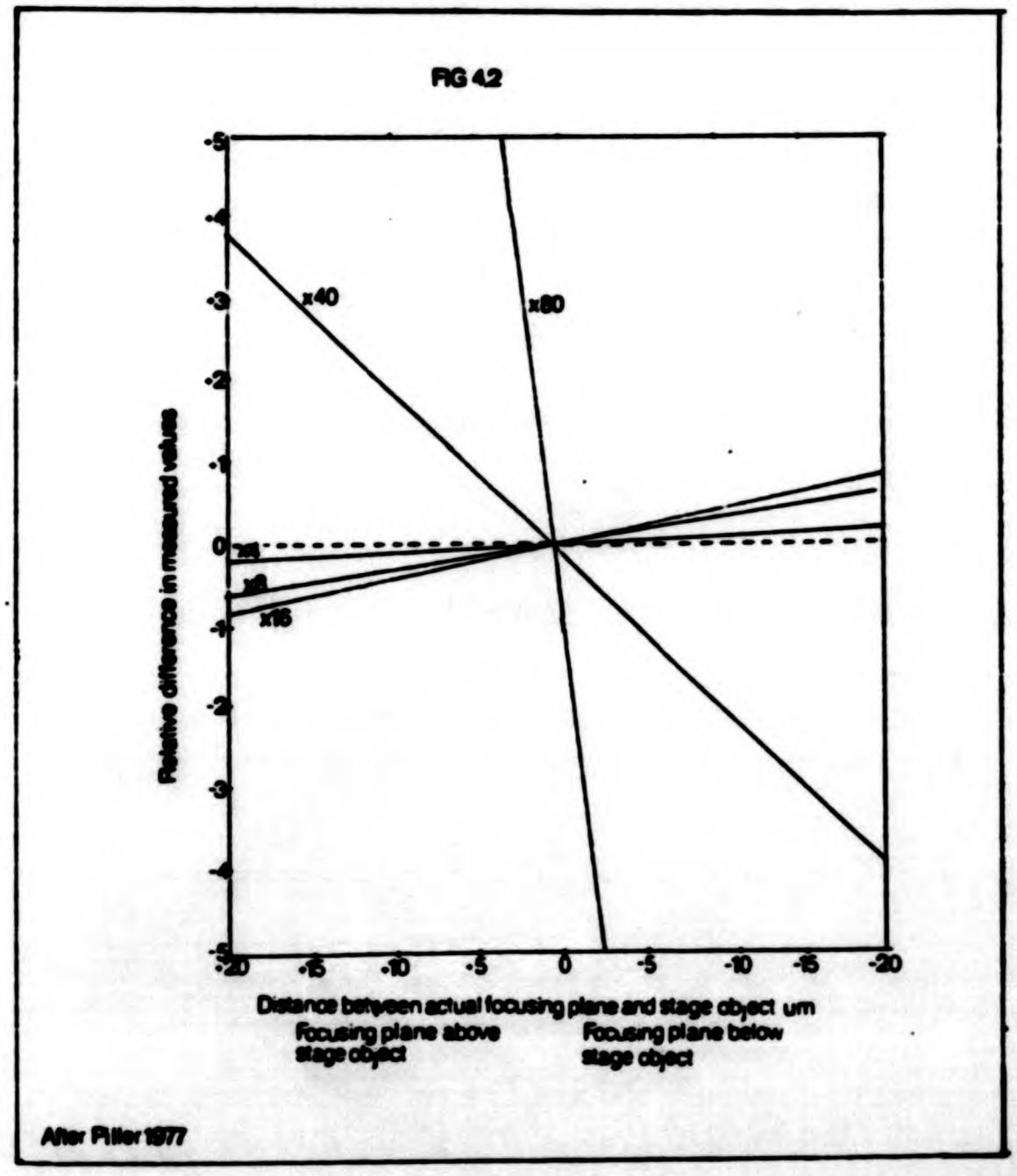

Fig 4.2. Experimentally determined values (Piller, 1977) of the relative differences in the measured results by varying the position of focus of the objective.

FIG 4.3

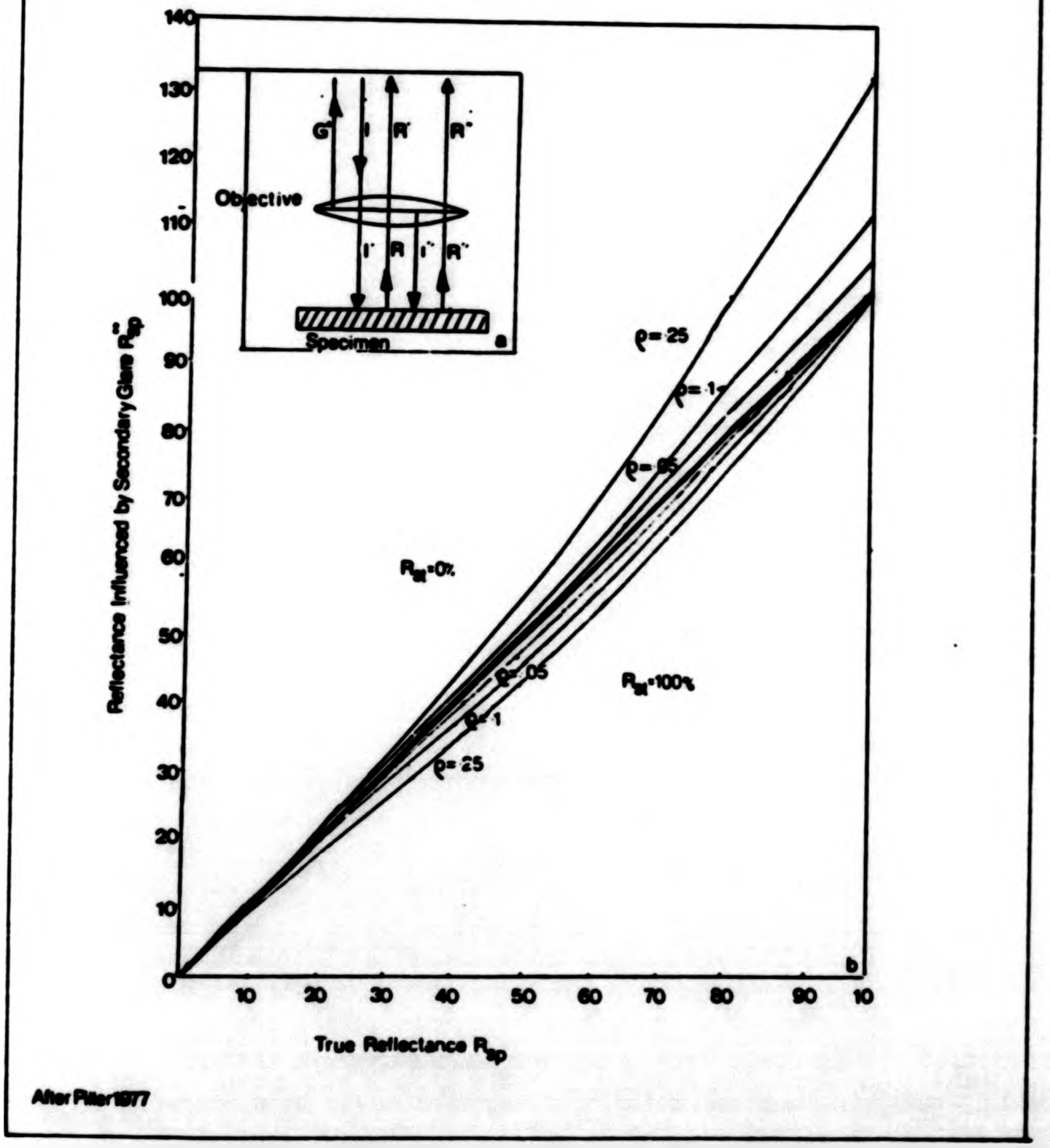

Fig 4.3 Errors due to secondary glare:

a, The incident beam I loses part G' by primary glare, the rest I' (defined as I-G') forms the primary component incident on the specimen, which reflects the beam R. This is partially re-reflected at the objective due to secondary glare, so there is a component I'' also incident on the specimen which is reflected as R'' and so on.

b, Influence of secondary glare for various reflectances of optics.

For the microscope photometer used in this study, a reading of zero was registered on the DVM when the black box test was used indicating that the system was free from primary glare.

4.3.2 Secondary Glare

Secondary glare is due to reflected light from the specimen being partially re-reflected down again by the objective (fig. 4.3). This effect is variable and is dependant upon the reflectivity of the material studied and so is not usually the same for specimen and standard. This means that the measured reflectance of the specimen is either too high or too low. The latter being true when the standard has the higher reflectance and the former when the specimen has the higher reflectance. This can be expressed by the following equation:

$$\frac{G_{sp}^{**}}{G_{st}^{**}} \cdot R_{st} = R_{sp}^{**} = R_{sp}\left[\frac{1 - \rho R_{st}}{1 - \rho R_{sp}}\right] \qquad 4.2$$

where

G = photometer reading
R = reflectance (expressed as a decimal)
sp = specimen
st = standard
** = secondary glare
ρ = reflectivity factor

Modern objectives are 'bloomed' at all air glass interfaces, to reduce reflectivity and hence primary and secondary glare to a minimum. It is not, however, always possible for this to be done equally well at all wavelengths, leading to a dispersion in the reflectivity factor ρ. In practice the lenses are bloomed so that ρ will be at a minimum in the middle of the spectrum, ie. by suppressing the yellow-greens with respect to the reds and blues. This produces a purplish colour from which the term blooming is derived.

The microscope can be calibrated to eliminate the effects of secondary glare at any given wavelength, by using a set of calibrated reflectance standards and using each in turn as a standard to measure the others. By plotting the calibrated reflectance values against the measured reflectance values, curves such as those in figs. 4.3 and 4.4 can be plotted.

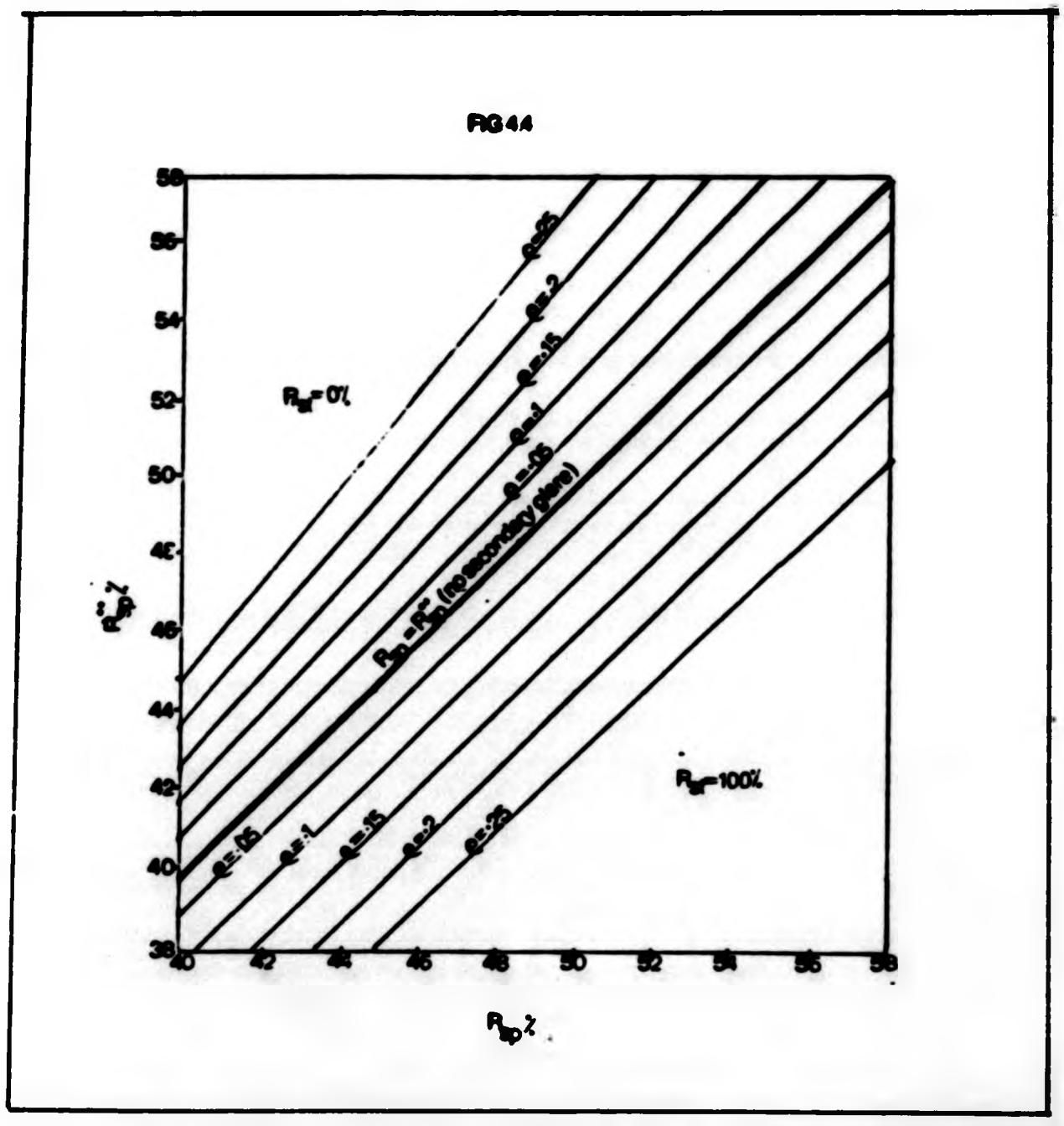

Fig 4.4 Magnification of a portion of fig 4.3 ,influence of secondary glare for various reflectances of optics.

CHAPTER FIVE

THE STANDARD SPECIMEN REFLECTANCE DIFFERENCE PHENOMENON (SSRDP) AND ITS CORRECTION

5.1 Identification of a New Type of Error

Fig. 5.1 shows the reflectance dispersion curves for evaporated aluminium using silicon-carbide and tungsten-titanium-carbide as the standards from which it is clear that something akin to secondary glare is occurring. The theory proposed by Piller (1977) maintains that primary glare is a precondition for secondary glare. In this study, however, a phenomenon similar to secondary glare was observed in the absence of primary. Moreover its magnitude was greatest in the middle of the spectrum where the blooming of the objectives would be expected to make it a minimum.

To try to locate the source of this error various steps were taken:

1. Changing to objectives of higher and lower magnification. This yielded no appreciable increase or decrease in the error. As these same objectives had been used in much earlier experiments where no errors were detectable, it seemed improbable that all had developed the same systematic error at the same time.

2. Changing the reflector (a full description of the various types of reflector can be found in section 3.1.7); the Gauss mirror reflector usually employed was replaced by:

   i) A new Gauss mirror reflector
   ii) A Smith reflector
   iii) A prism reflector

Fig. 5.2 shows the results obtained using these various reflectors, firstly, with the polariser in its normal position and then rotated through 90°. The rotation of the polariser had no significant effect on the results obtained using the Gauss mirror and Smith

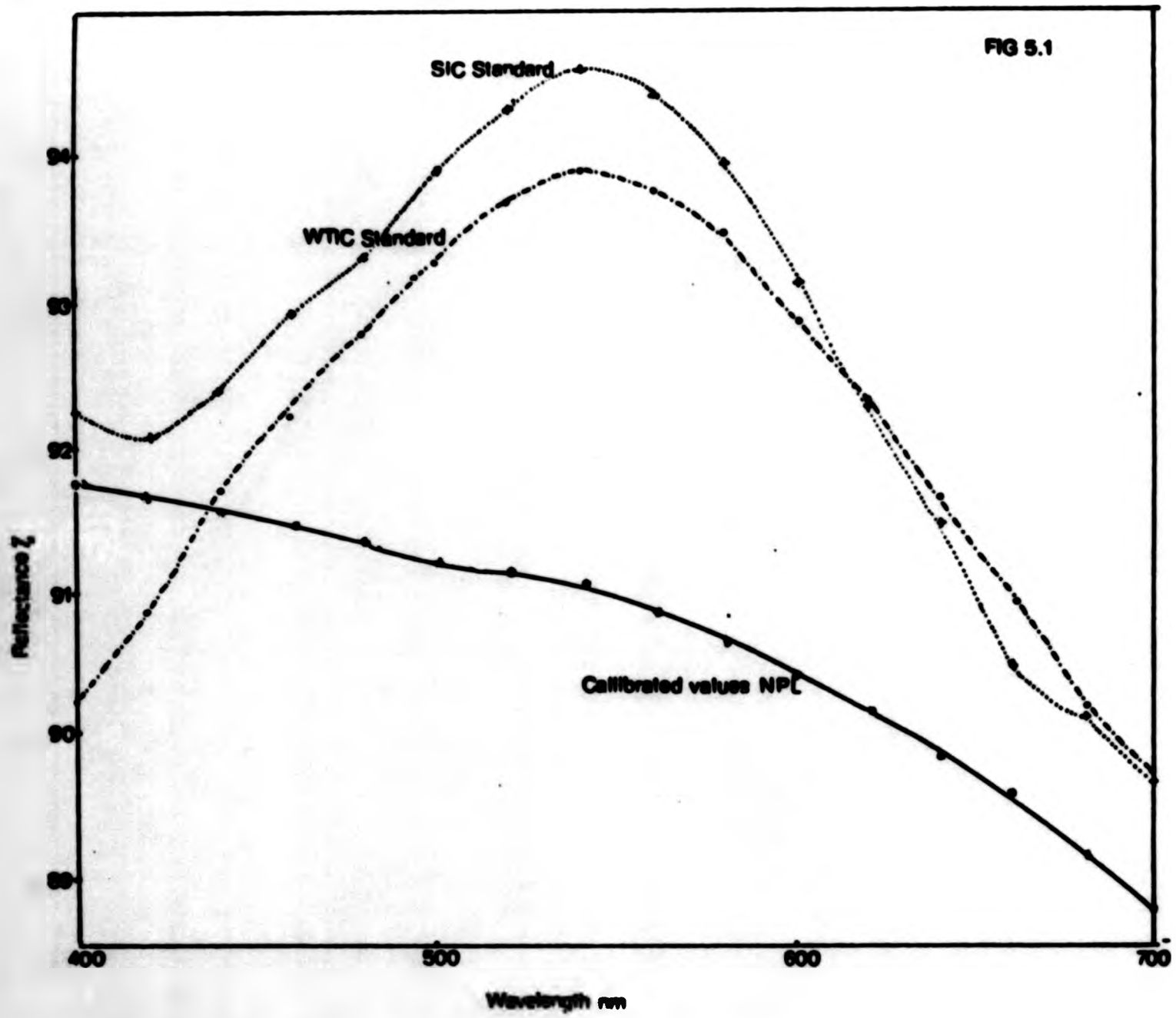

Fig 5.1 Effects of the Standard-Specimen-Reflectance-Difference Phenomenon (SSRDP) on the measured reflectance of aluminium using SiC and WTiC standards.

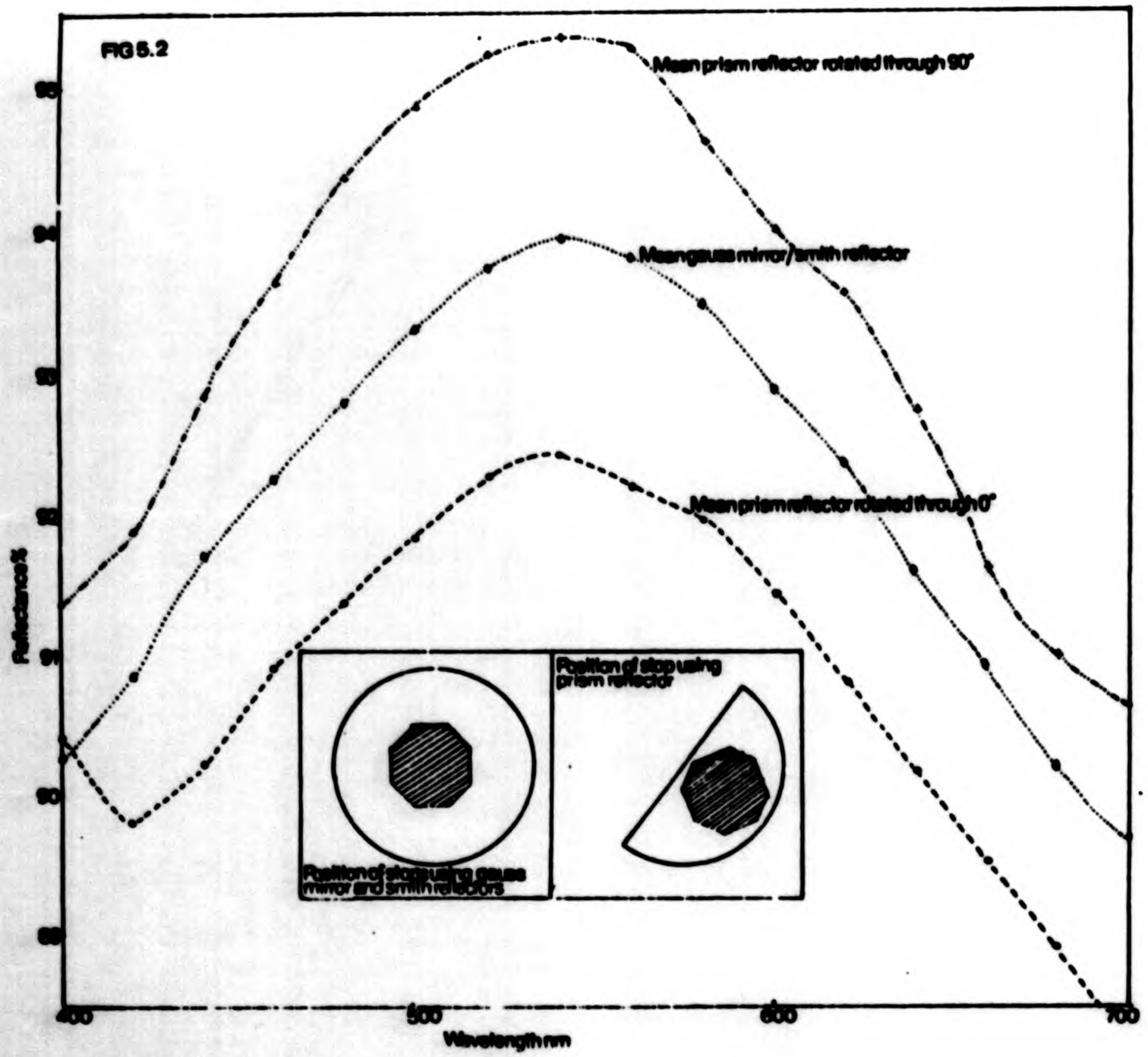

Fig 5.2 Effects on the reflectivity of aluminium using various types of reflector. Inset; position of stops with various types of reflector.

reflectors. As expected, however, the reflectance dispersion curves for the prism reflector display a maximum (polariser rotated through 90°) when the magnitude of the s component is greater than that of the p and a minimum (polariser in normal position) when the reverse is true. The mean of these two curves approximates to the reflectance dispersion given by the Gauss mirror and Smith reflectors.

3. The optimum conditions for operating the microscope with a minimum of secondary glare are given by Galopin and Henry (1972) and can be summarised thus:

The size of the stops used is dependent on the area to be measured. The I.F.S. should be chosen so that its diameter does not exceed half the surface area of the grain. The Ph.F.S. should have half the apparent diameter of the I.F.S., so that diffracted rays from the edge of the latter are not measured. When possible, low powered objectives should be used so that the incident beam falling on the specimen is at approximately normal incidence. If high N.A. objectives have to be used (ie. if the mineral grain to be measured is small) then the effective aperture angle can be reduced by closing down the I.A.D.

Any deviations from the above should lead to an increase in the secondary glare factor. To see if the phenomenon observed in this study was affected by the same factors the equipment was adjusted so as to increase the amount of any secondary glare present.

i) Opening the I.A.D. to its full extent caused the observed reflectance of WTiC using a SiC standard to increase by 0.1% at 550 nm.

ii) Using the largest available I.F.S. with the largest Ph.F.S. caused the observed reflectance of WTiC to increase by 0.3% at 550 nm using a SiC standard.

iii) As shown in above changing the objectives had no appreciable effect on the observed reflectance.

An examination of the photometer field stop showed that the light was not travelling exactly through the centre of it. To check that this had no effect upon the readings a photometer stop with a moveable diaphram was substituted. As there was no difference between the two sets of readings it was concluded that the slight defect in the photometer stop could be ignored.

5.2. The Standard Specimen Reflectance Difference Phenomenon (SSRDP)

5.2.1 Introduction

In the above discussion a systematic replacement of components within the microscope along with changing operating conditions was undertaken to try and locate the cause of the apparent 'secondary glare'. None of these changes, however, produced a significant variation in the measured readings. Which, in addition to the lack of primary glare and the fact that the phenomenon has its maximum, where blooming should make it a minimum, seems to indicate that this is not in fact true secondary glare.

5.2.2 Possible Causes of the Standard Specimen Reflectance Difference Phenomenon (SSRDP)

It is possible that the phenomenon hereafter referred to as the standard-specimen-reflectance difference phenomenon (SSRDP) could have its origin in the microphotometric assembly and it is interesting to note that the maximum in the SSRDP coincides with the maximum transmission of the microscope. This could be indicative of a defect either in the modulating system, or in the photodetector itself. Another possibility could be the occurrence of 'false light' in the monochromator via harmonic spectral bands and/or fluorescence. This is, however, unlikely as the monochromator was designed to minimise such phenomena.

Another source of microphotometric measurement error has been proposed by Embrey (1984). In microphotometry the normal reflectance of a mineral is calculated by the formula:

$$R_1 = R_2 \cdot \frac{G_1}{G_2} \qquad 5.1$$

$$\text{or} \quad R_2 = R_1 \cdot \frac{G_2}{G_1} \qquad 5.2$$

Assuming that either 1 or 2 is the standard then the 'normal' reflectance (R) is given by equations (5.1) and (5.2) where G is the photometer reading (a measure of the light intensity).

Due to the geometry of the optical train, the measured reflectance (R_{meas}) is the mean of R_p and R_s for a Gauss mirror, because the stop is symmetrical with respect to the back focal plane of the microscope objective (fig. 5.2).

$$R_{\substack{meas \\ Gauss \\ mirror}} = \frac{1}{2}(R_p + R_s) \qquad 5.3$$

Use of the Berek prism, however, can cause serious errors. Because the central axis of the illuminating beam of light is offset from the axis of the objective, the integrated s and p components are of unequal intensity. Correction can be made by either taking the mean of measurements made with the polariser in its two principal orientations (and thus doubling the labour involved in making a series of measurements) or by using a semi-circular illuminator with its straight edge close to the diameter of the objective stop.

Capdecomme (1938) was the first to show that for transparent media, provided that the angle of incidence is not too large:

$$\frac{(R_p + R_s)}{2} = R_N \qquad 5.4$$

Computation shows that this is also true for absorbing media (figs. 5.3 and 5.4). There is, however, a small departure from equality.

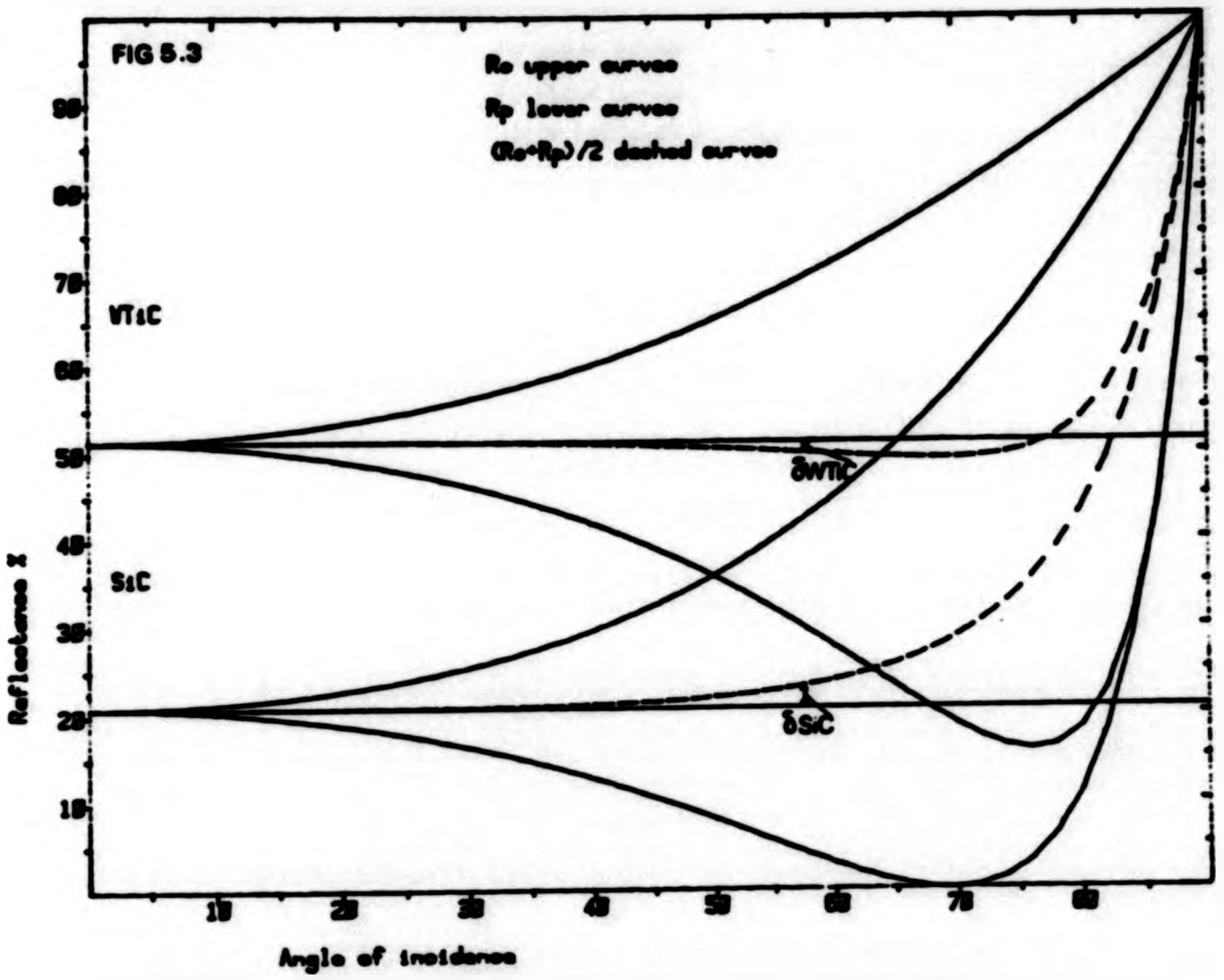

Fig 5.3 R_s, R_p and $(R_s+R_p)/2$ curves for WTiC and SiC.

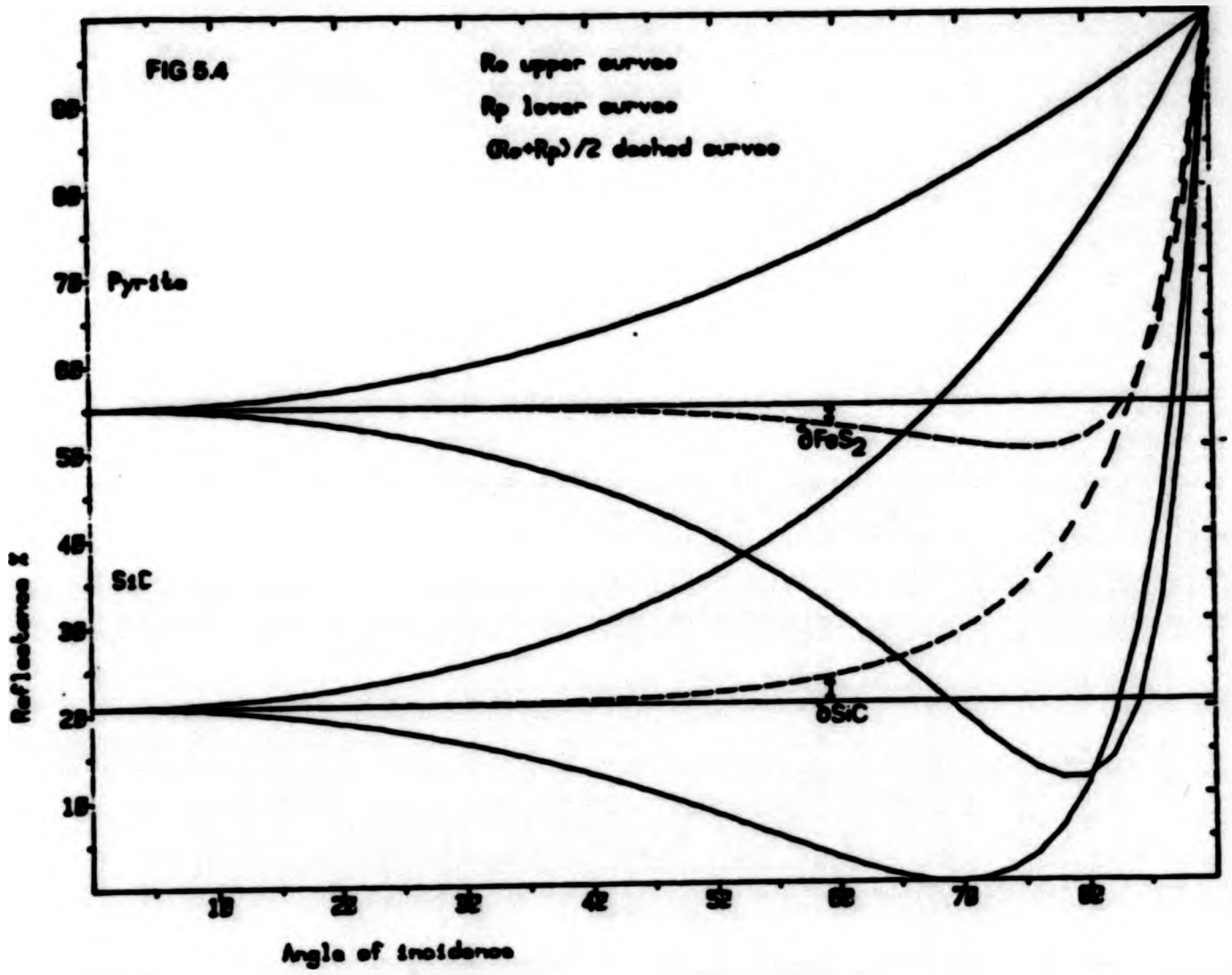

Fig 5.4 R_s, R_p and $(R_s+R_p)/2$ curves for FeS_2 and SiC.

If $\frac{(R_p + R_s)}{2} - R_N = \delta$, 5.5

then $\frac{G_1}{G_2} = \frac{R_{meas1}}{R_{meas2}} = \frac{(R_{N1} + \delta_1)}{(R_{N2} + \delta_2)}$ 5.6

Expanding the right hand side this becomes:

$$\frac{G_1}{G_2} = \frac{R_{N1}}{R_{N2}} \left(1 + \frac{\delta_1}{R_{N1}} - \frac{\delta_2}{R_{N2}} \ldots\ldots\right) \quad 5.7$$

Computations by Embrey (1984) show that $\frac{\delta_1}{R_{N1}}$ and $\frac{\delta_2}{R_{N2}}$ are rarely equal in magnitude and may differ in sign. Using the reflectance standards WTiC and SiC for illustration, at 30° incidence, $\frac{\delta}{R_N}$ = + 0.006 and - 0.002 respectively; so that:

$$\frac{G_{SiC}}{G_{WTiC}} = \frac{R_{NSiC}}{R_{NWTiC}} \quad (1 + 0.006 - 0.002), \quad 5.8$$

and the reflectance of WTiC measured against SiC will be too low (and vice versa). Fortunately, this error is usually small and can moreover be computed with sufficient accuracy from initial values of n and k.

As the origin of the SSRDP has yet to be positively established, even though it is likely to be attributable at least in part to the phenomena described above and as the values for δ_1 and δ_2 have yet to be incorporated into the microphotometric software a series of correction factors based on many sets of experimental results were calculated.

5.2.3 Correction for the Standard Specimen Reflectance Difference Phenomenon (SSRDP)

The correction procedure used is similar to that described in section 4.3.2. Due to the fact that the phenomenon does not show a uniform dispersion a different correction factor has to be applied at each wavelength. As there are no recognised reflectance standards for

reflectances greater than 47% (WTiC), microscopes are usually calibrated for high reflectances by extrapolation from curves such as those in fig. 4.3. In this case it was felt that higher reflectance calibration standards were desirable, this was achieved by using a vacuum deposited film of pure aluminium on glass (prepared and calibrated at the National Physical Laboratory, Teddington). An aluminium film could not be used as a working standard for normal reflectance measurements because of its fragility but it is suitable for the preparation of correction factors. The method for calculating the correction factors is as follows:

i) The mean of many sets of data R_{mmsp} is taken and the maximum (R_{+msp}) and minimum (R_{-msp}) data points calculated by respectively adding and subtracting two standard deviations (2SD). Values falling outside the range R_{+msp} to R_{-msp} are disregarded, and a new mean value can be calculated.

$$R_{mmsp} \pm 2.SD = R_{+msp}, R_{-msp} \qquad 5.9$$

This is displayed in fig. 5.5.

ii) From these values the calibrated spectral value of the specimen (R_{csp} when known) are subtracted.

$$R_{-msp} - R_{csp} \; , \; R_{+msp} - R_{csp} \qquad 5.10$$

iii) These values are then divided by the difference between the calibrated specimen and the calibrated standard. ie, $R_{csp} - R_{cst}$.

iv) Thus the correction formula is,

$$C^* = \frac{R_{-msp} - R_{csp}}{R_{csp} - R_{cst}} \; , \; \frac{R_{+msp} - R_{csp}}{R_{csp} - R_{cst}} \qquad 5.11$$

Correction factors C* for a series of calibrated standards and specimens, in this case other calibrated standards, can be found for both air and oil environments in table 5.1. These tables can be used to determine the extent of the deviation between real and measured reflectances

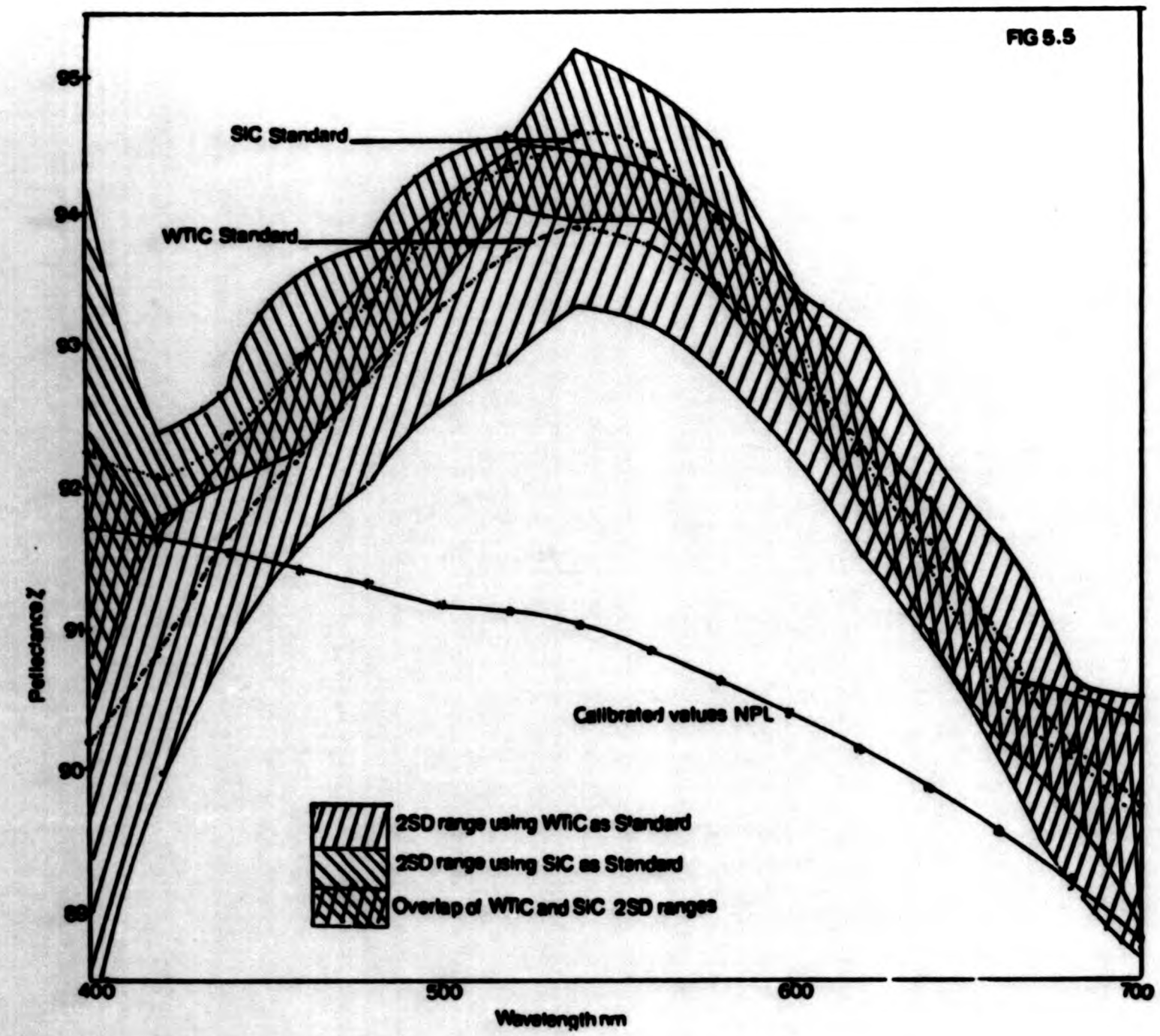

Fig 5.5 Mean reflectance values ± 2 standard deviations for aluminium using SiC and WTiC as standards.

Table 5.1 **Correction factors C* for a series of calibrated specimens and standards**

λ nm	WTiC measured using SiC standard	Al measured using WTiC standard	Al measured using SiC standard	SiC measured using WTiC standard	SiC measured in oil using WTiC standard	WTiC measured in oil using SiC standard
400	-0.0588,+0.1157	-0.0830,+0.0154	-0.0203,+0.0351	-0.0348,+0.0249	-0.0228,-0.0082	-0.0470,+0.1082
420	-0.0057,+0.0690	-0.0362,+0.0009	+0.0019,+0.0011	-0.0268,+0.0128	-0.0107,+0.0063	-0.0063,+0.0661
440	+0.0150,+0.0620	-0.0109,+0.0161	+0.0068,+0.0168	-0.0295,+0.0124	-0.0084,+0.0022	+0.0122,+0.0419
460	+0.0204,+0.0594	+0.0040,+0.0292	+0.0115,+0.0302	-0.0270,+0.0054	-0.0102,+0.0017	+0.0115,+0.0388
480	+0.0279,+0.0601	+0.0158,+0.0473	+0.0210,+0.0348	-0.0109,-0.0052	-0.0087,-0.0004	+0.0096,+0.0387
500	+0.0366,+0.0633	+0.0319,+0.0620	+0.0315,+0.0458	-0.0295,-0.0020	-0.0085,-0.0012	+0.0134,+0.0378
520	+0.0429,+0.0689	+0.0396,+0.0751	+0.0407,+0.0487	-0.0318,-0.0080	-0.0099,-0.0028	+0.0182,+0.0405
540	+0.0500,+0.0717	+0.0519,+0.0791	+0.0410,+0.0593	-0.0317,-0.0116	-0.0966,-0.0027	+0.0197,+0.0456
560	+0.0473,+0.0721	+0.0546,+0.0823	+0.0442,+0.0576	-0.0298,-0.0138	-0.0083,-0.0038	+0.0215,+0.0358
580	+0.0443,+0.0677	+0.0528,+0.0820	+0.0387,+0.0558	-0.0287,-0.0117	-0.0073,-0.0037	+0.0176,+0.0367
600	+0.0352,+0.0549	+0.0452,+0.0750	+0.0329,+0.0449	-0.0241,-0.0090	-0.0060,-0.0011	+0.0135,+0.0249
620	+0.0262,+0.0463	+0.0358,+0.0738	+0.0254,+0.0354	-0.0178,-0.0064	-0.0041,-0.0007	+0.0086,+0.0197
640	+0.0219,+0.0356	+0.0272,+0.0632	+0.0164,+0.0299	-0.0157,-0.0039	-0.0047, 0.0000	+0.0054,+0.0202
660	+0.0169,+0.0316	+0.0169,+0.0553	+0.0094,+0.0169	-0.0140,-0.0019	-0.0046, 0.0000	+0.0056,+0.0128
680	+0.0174,+0.0286	+0.0022,+0.0538	+0.0077,+0.0201	-0.0140,-0.0028	-0.0045, 0.0000	+0.0029,+0.0220
700	+0.0179,+0.0319	-0.0006,+0.0486	+0.0014,+0.0233	-0.0131,+0.0040	-0.0090,+0.0016	+0.0134,+0.0277

To choose the appropriate correction factor C* use the column of figures where the difference in reflectance between the calibrated specimen and standard approximates to the reflectance difference in the case under consideration.E.g. for pyrite (reflectance difference using WTiC standard at 560nm =6.06) use column 1.Reflectance of pyrite at 560nm=54.00% this is corrected by multiplying the relevent correction factor (+0.0473,+0.0721) by 6.06 to give values of 54.29 to 54.43 when added to the original pyrite value.

at any wavelength. This is done by subtracting the reflectance of the standard from the true reflectivity of the specimen and multiplying the result of the appropriate correction factor C*.

$$C^* (R_{csp} - R_{cst}) = A^* \qquad 5.12$$

When this result (A*) is added or subtracted to the real specimen value it should be within experimental error give the measured result:

$$R_{csp} \pm A^* = R_{msp} \qquad 5.13$$

Under normal circumstances, however, the true reflectivity of the mineral is rarely known. Under these conditions the measured value R_{msp} may be substituted for R_{csp} into equations 5.10 and 5.11 to give an approximation to the real value. It should always be remembered that this method is only an approximation, and that strictly speaking R_{csp} and not R_{msp} should be used in the above equations. This method of estimation, however, does seem to work quite well, as long as it is treated as an approximation and provided the difference in reflectivity between specimen and standard does not exceed 40%.

The SSRDP is found to vary in an essentially linear manner with increasing reflectivity difference between standard and specimen upto approximately 70%. After which its gradient becomes somewhat erratic. This could be a real phenomenon, but is more likely to be an artefact, caused by the disparity between the DVM readings. This is due to the fact that the same DVM range has to be used for a set of standard-specimen reflectance measurements. Thus when the reflectance difference between standard and specimen is large, the lower reflecting materials DVM response will be negligible when compared with that of the higher reflecting material ie there will be a loss in the number of significant figures for computation. This for obvious reasons leads to erroneous results.

CHAPTER SIX

RESULTS

6.1 Introduction

The results obtained for each mineral constitute the first part of the results section, and are displayed in the following manner:

i) Features such as the locality from which the mineral was obtained, its colour and surface characteristics when polished and the type of section used in anisotropic minerals are described in brief. Any data, such as slight anisotropy in 'isotropic' sections, which would affect the measured and derived optical characteristics are also noted. Also included in this subsection are details which pertain to the size, extent and nature of any mineral inclusions.

ii) The electron probe microanalysis of the mineral, (a brief account of the procedure used can be found in section 6.2).

iii) Comparison of the ellipsometric and microphotometric reflectance data. In the latter case the dispersion curves are shown for both air and oil immersion media, using the most appropriate standard.

iv) Comparison of the ellipsometric and microphotometric n and k dispersion curves.

v) The dispersion curves for the real ϵ_1 and imaginary ϵ_2 components of the dielectric constant. These are calculated from the ellipsometric data only. This is because of the errors inherent in calculating n and k from microphotometric measurements (section 2.2.4) which would be magnified if used to calculate ϵ_1 and ϵ_2.

vi) Tabular summary of the data for each mineral.

The next section of results deals with the study of some iridium-platinum alloys supplied by Johnson-Matthey, and compares the reflectivity

data obtained using a variety of methods, i.e:

i) Ellipsometry at The City of London Polytechnic (CLP).

ii) Microscope photometry at The Natural History Museum (NHM).

iii) Ellipsometry at The National Physical Laboratory (NPL).

iv) Ultra-violet and visible reflectometry at NPL.

It is pertinent here to mention that due to the nature of the water modulation cores used in the ellipsometer at CLP the precision of the measurements between 600 - 700 nm is not as great as those made between 300 - 600 nm.

6.2 Electron Probe Microanalysis

To ascertain the chemical composition and trace element concentrations all the minerals used in this study were analysed at the Natural History Museum using a Cambridge Instruments Microscan IX with an acceleration voltage of 20 kV, I am indebted to Dr C.J. Stanley for his help in carrying out this analysis. Several areas of each mineral were analysed to assess both the homogeneity of the specimen and the distribution of any trace elements. For most elements pure metal standards were used. However, a troilite standard was used for iron and sulphur and galena for lead. Oxygen was determined by difference.

The beam of electrons striking the specimen is approximately one to two microns in diameter and penetrates up to three microns below the specimen surface, leaving a burn mark measuring three to five microns in diameter.

All the analyses of the minerals in this study are corrected for X-ray absorption, fluorescence and atomic number differences. The formula of the mineral calculated from the data, together with the main X-ray lines used in the determination are also shown.

6.3 Chalcosine

6.3.1 Introduction

The sample of chalcosine (E720; BM 1964R, 385) comes from an unknown locality. A visual examination showed it to be dark silvery-blue in colour with a metallic lustre. As chalcosine and djurleite are monoclinic (Evans 1981) the mineral section polished at the Natural History Museum was expected to be anisotropic. Rotation of the specimen on the microscope stage, however, revealed no perceptible anisotropy, i.e. an unchanging reading on the DVM. This meant that the polished mineral section could be treated as isotropic.

The polished chalcosine surface (Fig. 6.1) is cut by several small localised inclusions some of which are branched. The surface also displays some porosity in the form of a rim of tiny pores extending part way around the edge of the specimen. Fine mixed veinlets of chalcopyrite and bornite with lesser amounts of covelline meander around the specimen edges and fractures. Despite the general presence of fractures, pores and veinlets, some areas of the specimen are free from them. These are the areas suitable for microphotometric and ellipsometric studies.

The chalcosine specimen was ground and polished in the usual manner (section 3.5), and buffed with magnesium oxide before the start of each set of measurements (for chalcosine, magnesium oxide proved a superior buffing medium to gamma-alumina). The chalcosine specimen showed extensive tarnishing after being left for several weeks. This was manifested by the formation of deep brown rims around the edges, with intermixed light brown and blue-grey patchy colouration on the main part of the specimen. This illustrates that the tarnish film is of sufficient thickness to form light interference effects. The tarnish film is easily removed by buffing with magnesium-oxide and shows the necessity of pre-measurement buffing.

6.3.2 Electron Probe Analysis

Several areas of the chalcosine specimen were examined using the electron probe microanalyser. The analysis showed that the centre of the specimen was fairly homogeneous and consisted solely of copper and

sulphur. Traces of arsenic (0.2 wt.%) were detectable around the rim. The results of the analysis are shown in table 6.1 together with the X-ray lines for each element used in the determination.

6.3.3. Reflectance, n, k, ϵ_1 and ϵ_2

The air and oil reflectance dispersion curves for chalcosine using ellipsometric and microphotometric techniques are displayed in fig. 6.2 , fig. 6.3 shows the n and k curves and fig. 6.4 the dispersion of the ellipsometrically derived ϵ_1 and ϵ_2 values. All these data together with the CIE colour coordinates for illuminants A, C and D_{65} are shown in table 6.2.

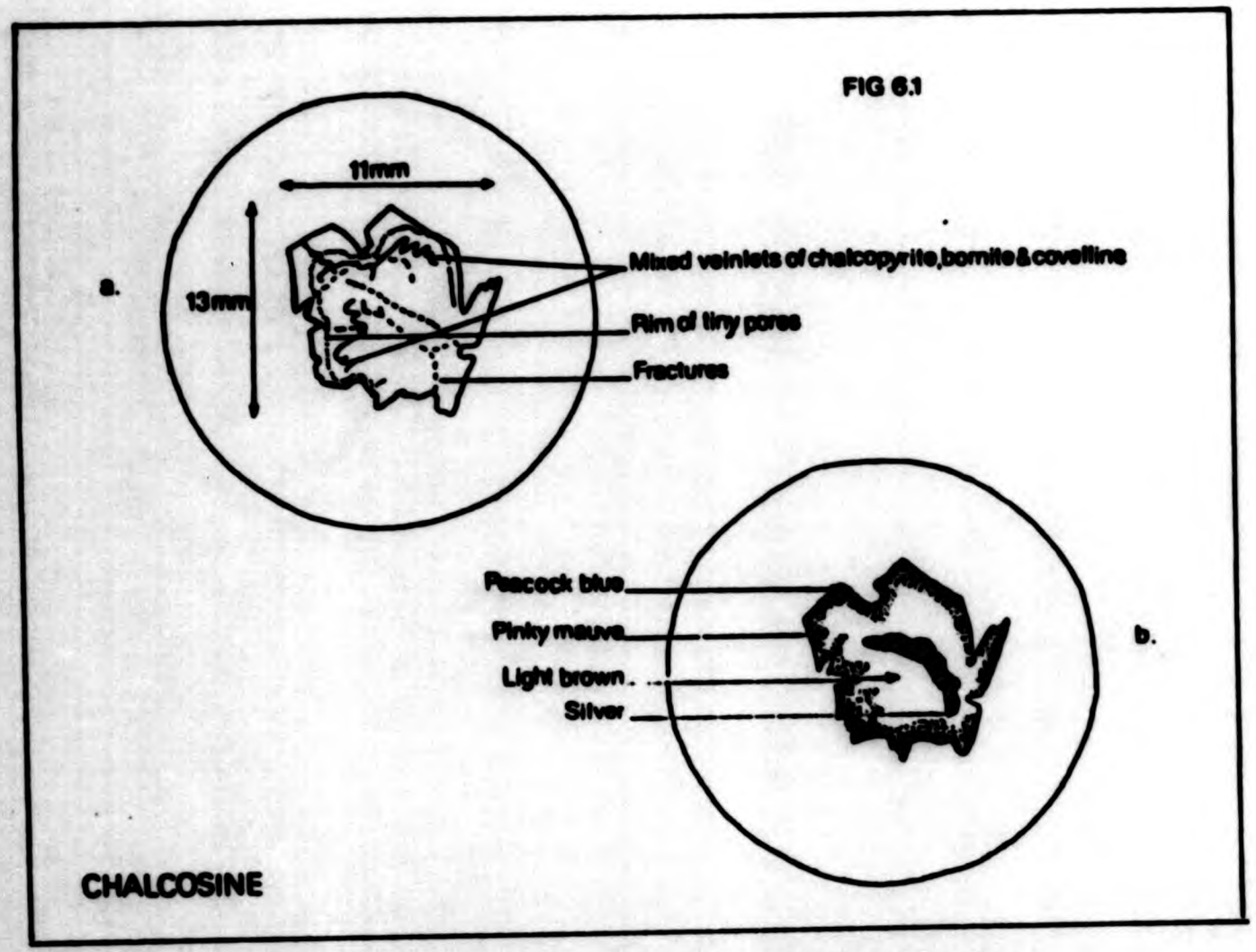

Fig 6.1 Chalcosine specimen a, directly after polishing
b, tarnish film after several weeks exposure to the atmosphere.

FIG 6.2

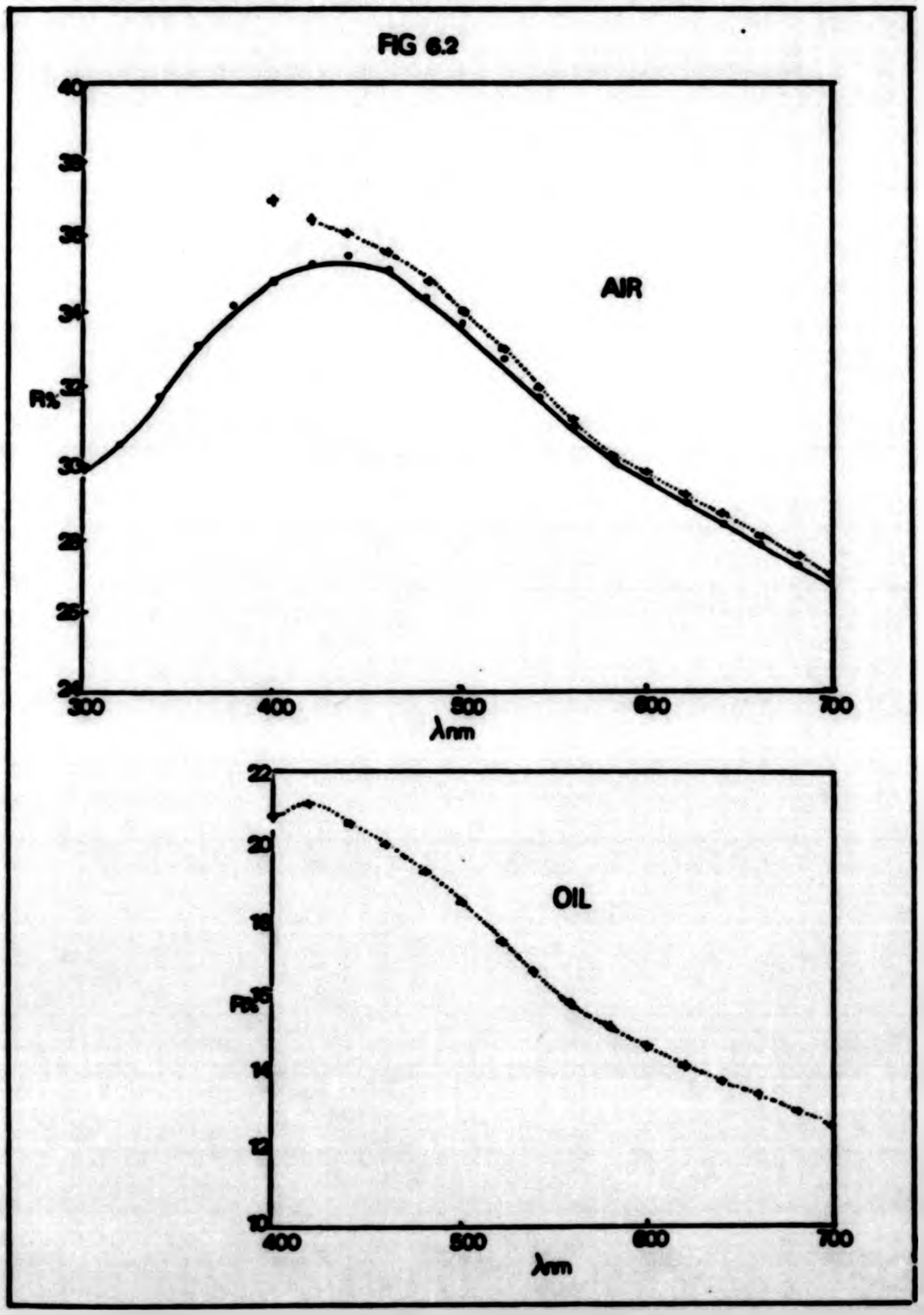

Fig 6.2 a, Comparison of microphotometric (·····) and ellipsometric (——) reflectance dispersion curves for chalcosine in air

b, Microphotometric reflectance dispersion curve for chalcosine in oil.

Fig 6.3 Comparison of microphotometric (·····) and ellipsometric (——) n and k values for chalcosine.

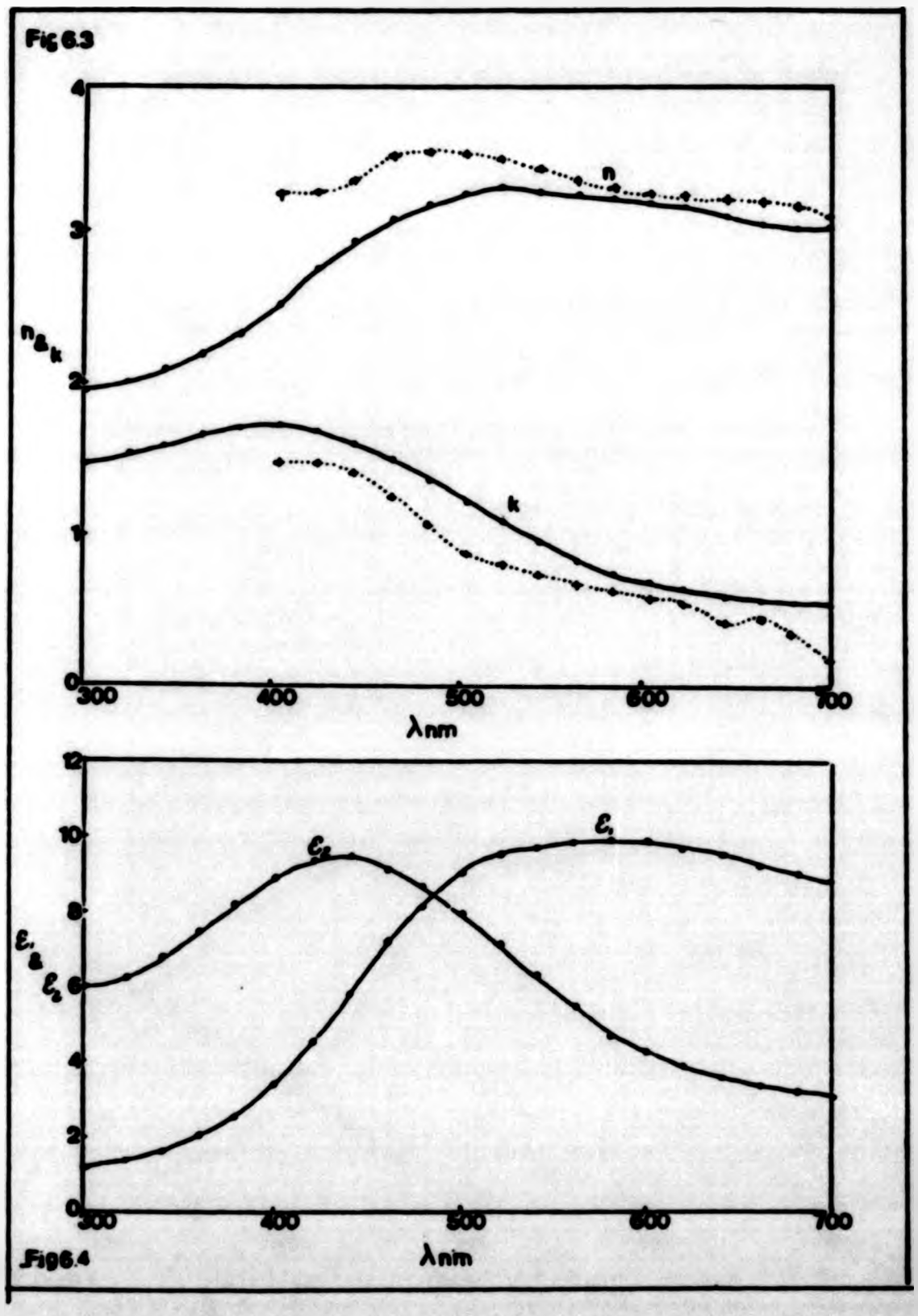

Fig 6.4 Ellipsometric ε_1 and ε_2 values for chalcosine.

Table 6.1 Electron Probe Analysis of Chalcosine

MINERAL NAME: Chalcosine			
ELEMENT	Wt%	ATOMIC RATIO'S	ELEMENT LINE
Cu	78.70	1.96	Cu Kα
S	20.20	1.00	S Kα
Total	98.90		
CALCULATED FORMULA: $Cu_{1.96}S_{1.00}$			
Formula based on $\Sigma S_{atoms}=1$			
TRACE ELEMENTS: Traces of arsenic around specimen edges			

Table 6.2 Summary of chalcosine data

MINERAL NAME:Chalcosine IDEAL FORMULA:Cu_2S LOCALITY:Unknown,BM.1964,R385,E720

CRYSTAL SYSTEM:Monoclinic,pseudo orthorhombic,no detectable anisotropy on this specimen.

X-RAY ANALYSIS:S=20.2wt% Cu=78.7wt%,traces of arsenic around rim upto 0.2wt% REAL FORMULA:$Cu_{1.965}S$

OPTICAL DATA:
Standard WTiC

Reflectance %

λ nm	ELL Air	MP Air	MP Oil	ELL n	MP n	ELL k	MP k	ELL ε_1	ELL ε_2
300	29.54			1.98		1.54		1.58	6.09
320	30.35			2.02		1.58		1.60	6.36
340	31.66			2.11		1.64		1.79	6.92
360	33.01			2.25		1.70		2.17	7.62
380	34.13			2.40		1.74		2.77	8.34
400	34.67	36.83	20.76	2.57	3.29	1.73	1.49	3.62	8.89
420	35.30	36.41	21.06	2.76	3.28	1.71	1.47	4.72	9.45
440	35.41	36.07	20.67	2.94	3.38	1.64	1.40	5.99	9.63
460	35.06	35.60	20.12	3.09	3.50	1.52	1.22	7.27	9.38
480	34.44	34.85	19.39	3.20	3.53	1.37	1.08	8.35	8.78
500	33.65	33.94	18.51	3.26	3.55	1.23	0.90	9.10	8.01
520	32.77	32.91	17.58	3.28	3.50	1.09	0.79	9.56	7.18
540	31.91	31.88	16.70	3.28	3.42	0.98	0.74	9.78	6.42
560	30.97	30.98	15.93	3.27	3.36	0.85	0.69	9.96	5.56
580	30.08	30.27	15.34	3.24	3.30	0.75	0.66	9.92	4.86
600	29.57	29.67	14.84	3.23	3.26	0.68	0.62	9.96	4.37
620	28.93	29.14	14.38	3.19	3.24	0.62	0.55	9.81	3.98
640	28.39	28.62	13.91	3.16	3.24	0.60	0.42	9.60	3.78
660	27.81	28.07	13.46	3.11	3.20	0.58	0.41	9.35	3.60
680	27.22	27.56	13.03	3.07	3.17	0.55	0.34	9.14	3.37
700	26.78	27.10	12.63	3.06	3.16	0.49	0.21	9.10	3.01

CIE Colour Co-ordinates

		MP Air	MP Oil
Illuminant C			
	x	0.2936	0.2830
	y	0.3018	0.2914
	z	0.4046	0.4256
Luminance	Y	31.33	16.33
	Pe%	7.63	12.67
	D_λ	479.4	478.7
Illuminant A			
	x	0.4313	0.4203
	y	0.4038	0.4002
	z	0.1649	0.1795
Luminance	Y	30.76	15.84
	Pe%	4.02	6.77
	D_λ	490.9	490.2
Illuminant D_{65}			
	x	0.2962	0.2857
	y	0.3151	0.3049
	z	0.3887	0.4094
Luminance	Y	31.35	16.35
	Pe%	7.34	12.22
	D_λ	480.6	479.9

OTHER DATA:Specimen contains small mixed veins of bornite,chalcopyrite, and covelline.

6.4 Galena

6.4.1 Introduction

A visual examination of the galena specimen, (E1001), shows it to be silver-grey in colour, possessing a metallic lustre, with a clearly defined perfect cubic cleavage (fig. 6.5). In reflected light the polished mineral surface appears perfectly isotropic, reflecting its cubic symmetry. Some difficulties were encountered during polishing, as the cleavage traces of the specimen acted as reservoirs for extraneous polishing grit and other foreign material. The situation was further exacerbated by the tendency of small parts of the specimen to flake off during ultra-sonic cleaning. Care was taken to select areas of the specimen as free of cleavage traces as possible for microphotometric and ellipsometric analysis.

Before measurements were made the sample was gently buffed with magnesium oxide, which in this case proved more suitable than gamma-alumina. Apart from the cleavage traces the specimen shows no other surface features and is devoid of any mineral inclusions. The surface shows no visual features attributable to tarnishing but probably in common with most minerals forms a thin, air-formed film immediately after polishing.

6.4.2 Electron Probe Analysis

Quantitative analysis of the galena specimen using galena, troilite, and pure bismuth standards revealed that the mineral was fairly homogeneous and consisted almost entirely of lead and sulphur, with traces of bismuth. The full analysis of the galena is displayed in table 6.3 together with the X-ray lines used and the formula of the mineral calculated from the data.

6.4.3 Reflectance, n, k, ϵ_1 and ϵ_2

In fig. 6.6 the ellipsometric and microphotometric reflectance dispersion curves are displayed in the latter case for both air and oil environments. Fig. 6.7 shows the derived values of n and k and fig. 6.8 is a plot of the ellipsometrically calculated ϵ_1 and ϵ_2 values. The

above data are summarised in table 6.4 together with CIE colour values for illuminants, C, A and D_{65}.

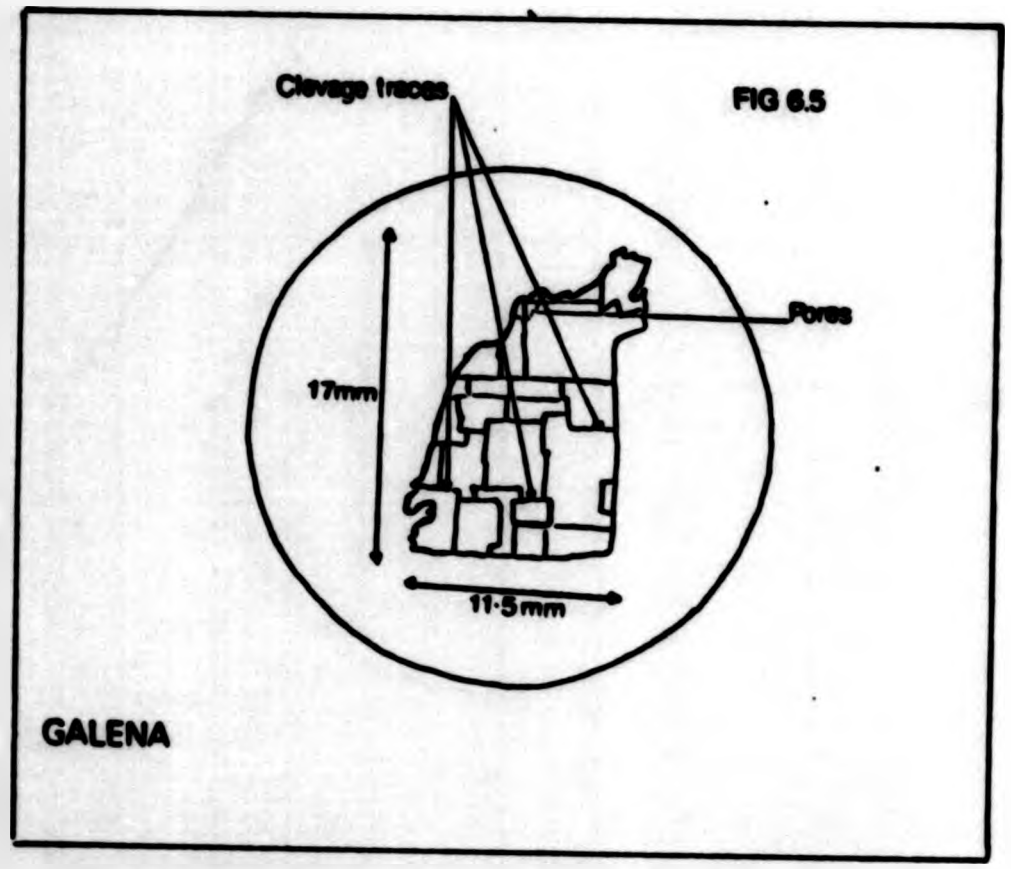

Fig 6.5 Galena specimen directly after polishing.

FIG 6.6

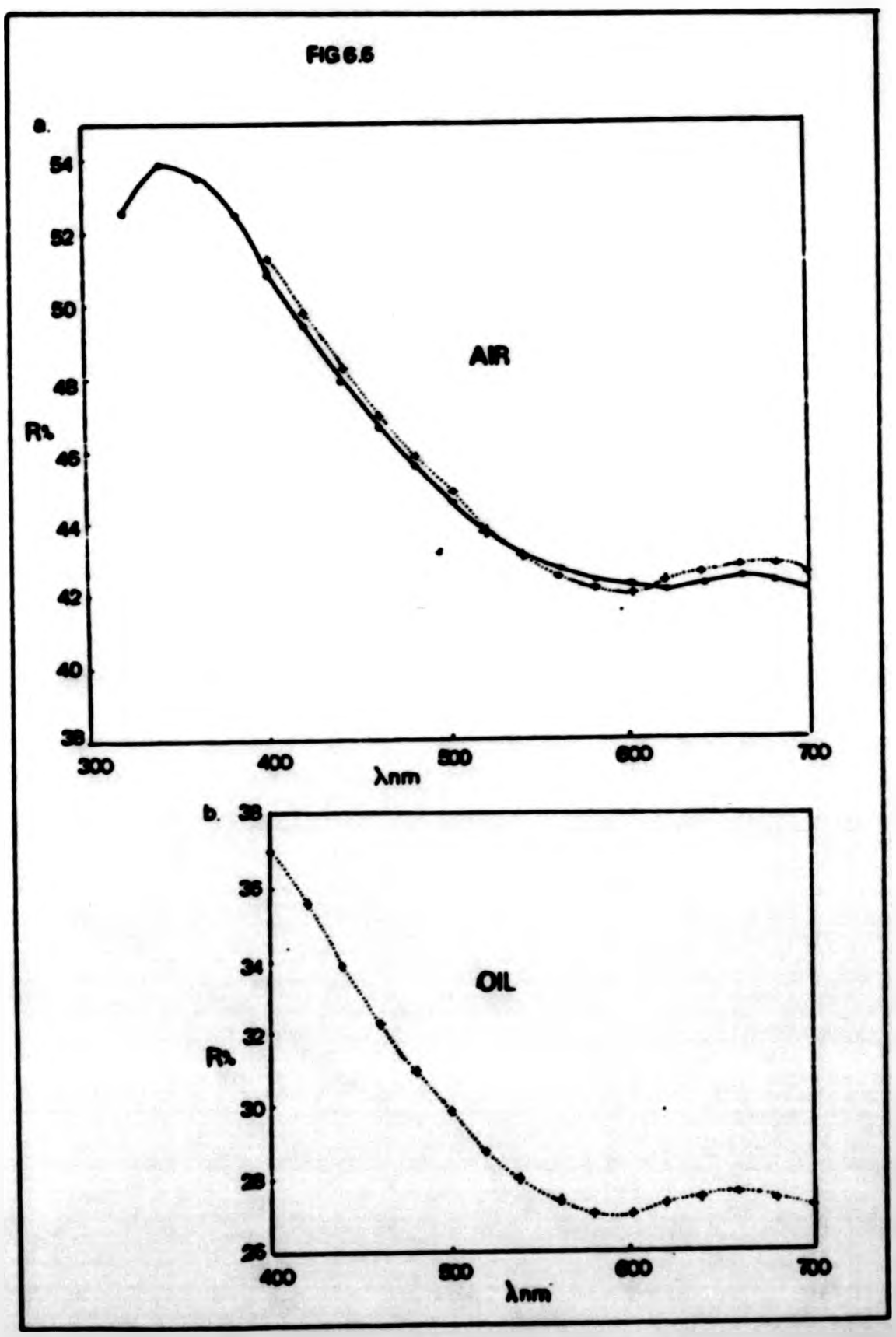

Fig 6.6 a, Comparison of microphotometric (·····) and ellipsometric (——) reflectance dispersion curves for galena in air

b, Microphotometric reflectance dispersion curve for galena in oil.

Fig 6.7 Comparison of microphotometric (·····) and ellipsometric (——) n and k values for galena.

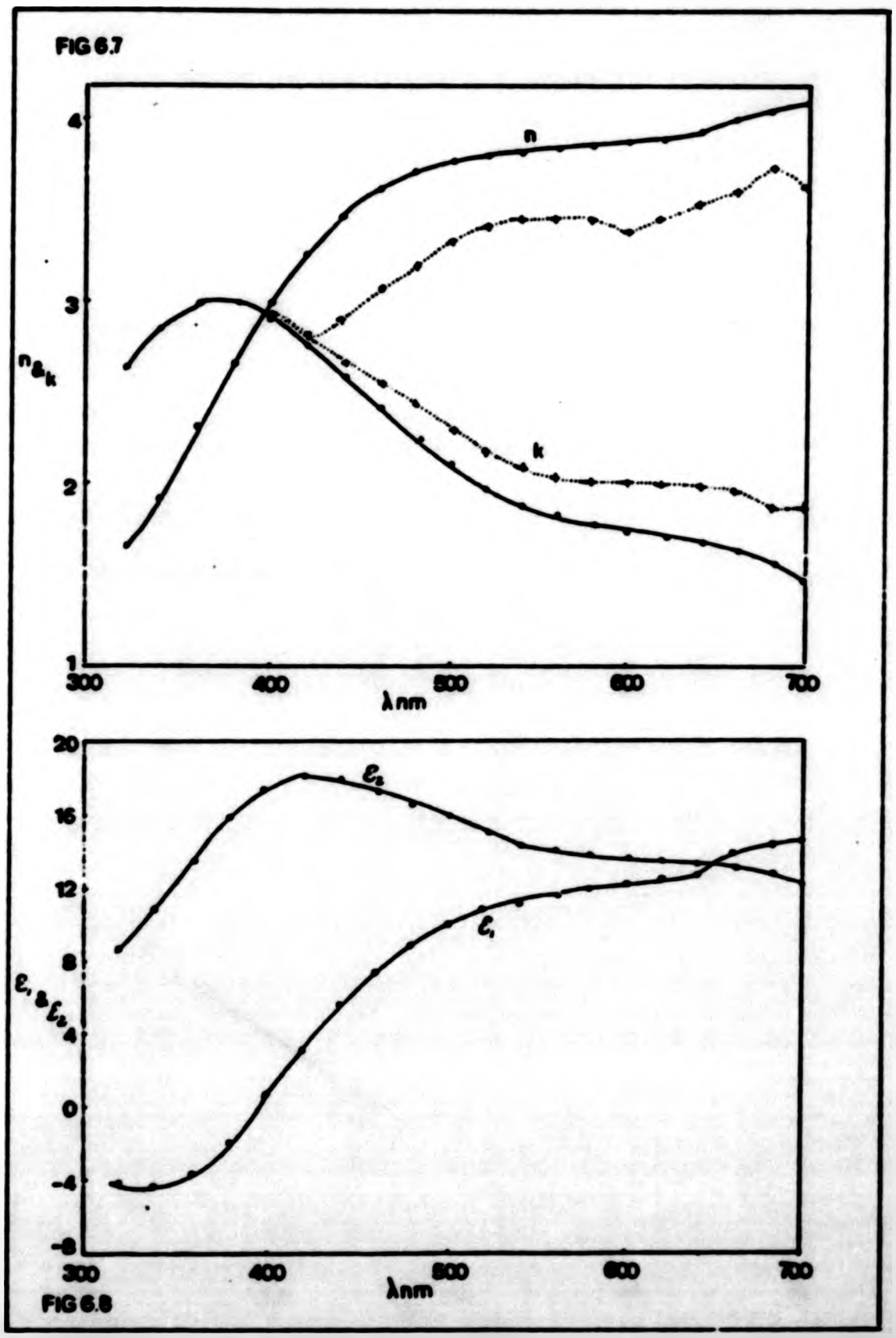

Fig 6.8 Ellipsometric ε_1 and ε_2 values for galena.

Table 6.3 Electron Probe Analysis of Galena

MINERAL NAME: Galena			
ELEMENT	Wt%	ATOMIC RATIO'S	ELEMENT LINE
Pb	86.18	1.04	Pb Ma
S	12.81	1.00	S Ka
Total	99.42		
CALCULATED FORMULA: $Pb_{1.04}S_{1.00}$			
Formula based on $\Sigma S_{atoms}=1$			
TRACE ELEMENTS: Bi=0.33wt%			

Table 6.4 Summary of galena data

MINERAL NAME:Galena IDEAL FORMULA:PbS LOCALITY:Unknown,E1004 CRYSTAL SYSTEM:Cubic,isotropic.

X-RAY ANALYSIS:Pb=86.18wt% S=12.81wt% trace bismuth 0.33wt%. REAL FORMULA: $Pb_{1.04}S$

OPTICAL DATA:
Standard:WTiC.

λ	Reflectance%								
	ELL Air	MP Air	MP Oil	ELL n	MP n	ELL k	MP k	ELL ϵ_1	ELL ϵ_2
300	49.89			1.53		2.41		-3.47	7.39
320	52.58			1.65		2.62		-4.17	8.66
340	53.86			1.91		2.84		-4.44	10.84
360	53.60			2.26		2.98		-3.74	13.48
380	52.51			2.65		3.00		-1.96	15.92
400	50.91	51.20	36.87	3.00	2.90	2.91	2.93	0.56	17.44
420	49.38	49.67	35.46	3.27	2.77	2.76	2.79	3.09	18.04
440	47.96	48.17	33.76	3.47	2.90	2.59	2.68	5.36	17.96
460	46.71	46.90	32.30	3.62	3.07	2.42	2.56	7.23	17.47
480	45.61	45.76	31.03	3.72	3.18	2.26	2.45	8.74	16.77
500	44.60	44.69	29.80	3.78	3.33	2.10	2.31	9.90	15.94
520	43.66	43.72	28.74	3.81	3.41	1.98	2.19	10.62	15.08
540	43.03	42.98	27.96	3.83	3.45	1.88	2.10	11.14	14.45
560	42.56	42.43	27.41	3.85	3.46	1.82	2.07	11.49	13.97
580	42.29	42.13	27.12	3.86	3.47	1.77	2.00	11.76	13.67
600	42.14	42.03	27.10	3.88	3.40	1.73	2.02	12.05	13.46
620	42.04	42.15	27.20	3.90	3.47	1.70	2.00	12.34	13.29
640	42.18	42.35	27.36	3.95	3.55	1.68	1.98	12.79	13.26
660	42.38	42.53	27.50	4.03	3.62	1.63	1.96	13.59	13.17
680	42.25	42.55	27.44	4.07	3.74	1.57	1.89	14.11	12.82
700	42.04	42.33	27.26	4.10	3.69	1.51	1.90	14.57	12.37

CIE Colour Co-ordinates

		MP Air	MP Oil	ELL Air
Illuminant C				
	x	0.3008	0.2952	0.3011
	y	0.3040	0.2959	0.3044
	z	0.3951	0.4090	0.3945
Luminance	Y	42.95	27.98	42.97
	Pe%	4.88	7.98	4.67
	D_λ	471.5	470.5	471.2
Illuminant A				
	x	0.4400	0.4355	
	y	0.4027	0.3989	
	z	0.1573	0.1656	
Luminance	Y	42.64	27.66	
	Pe%	2.05	3.34	
	D_λ	483.0	481.6	
Illuminant D_{65}				
	x	0.3036	0.2980	
	y	0.3171	0.3090	
	z	0.3793	0.3930	
Luminance	Y	42.94	27.97	
	Pe%	4.65	7.61	
	D_λ	472.8	471.9	

OTHER DATA:Perfect cubic cleavage clearly visible.

6.5 Pyrite

6.5.1 Introduction

A visual examination of the pyrite specimen (E1002) reveals it to be yellow-gold in colour with a metallic lustre. In reflected light the polished mineral surface appears perfectly isotropic reflecting the mineral's cubic symmetry. Apart from a few small localised fractures, the surface shows no other surface or sub-surface features, or any mineral inclusions fig. 6.9. When microphotometric and ellipsometric measurements were made, care was taken to avoid the surface fractures.

The pyrite specimen was ground and polished in the manner described in section 3.5 and before measurements were made the specimen was buffed with gamma-alumina. In addition to the air-formed film formed immediately after polishing, further surface tarnishing does occur on pyrite, dulling the lustre of the mineral and emphasising the need for pre-measurement buffing of the specimen.

6.5.2 Electron Probe Analysis

Quantitative microanalyses of several areas of the pyrite specimen were undertaken. Only slight variations in the major element concentrations were detected between the various sets of data indicating homogeneity in the specimen. The major constituents of the mineral were iron and sulphur, with cobalt and arsenic detectable in trace quantities. Table 6.5 shows the elemental analysis of the pyrite specimen, together with the X-ray lines usd in the determination and the formula of the mineral calculated from the data.

6.5.3 Reflectance, n, k, ϵ_1 and ϵ_2

The microphotometric air and oil reflectance curves are displayed in fig. 6.10, together with the ellipsometric data. Fig. 6.11 shows the dispersion of the derived n and k values for both techniques, and fig. 6.12 shows the ellipsometric ϵ_1 and ϵ_2 curves. All the above data are summarised in table 6.6, with the CIE colour coordinates using illuminants C, A and D_{65}.

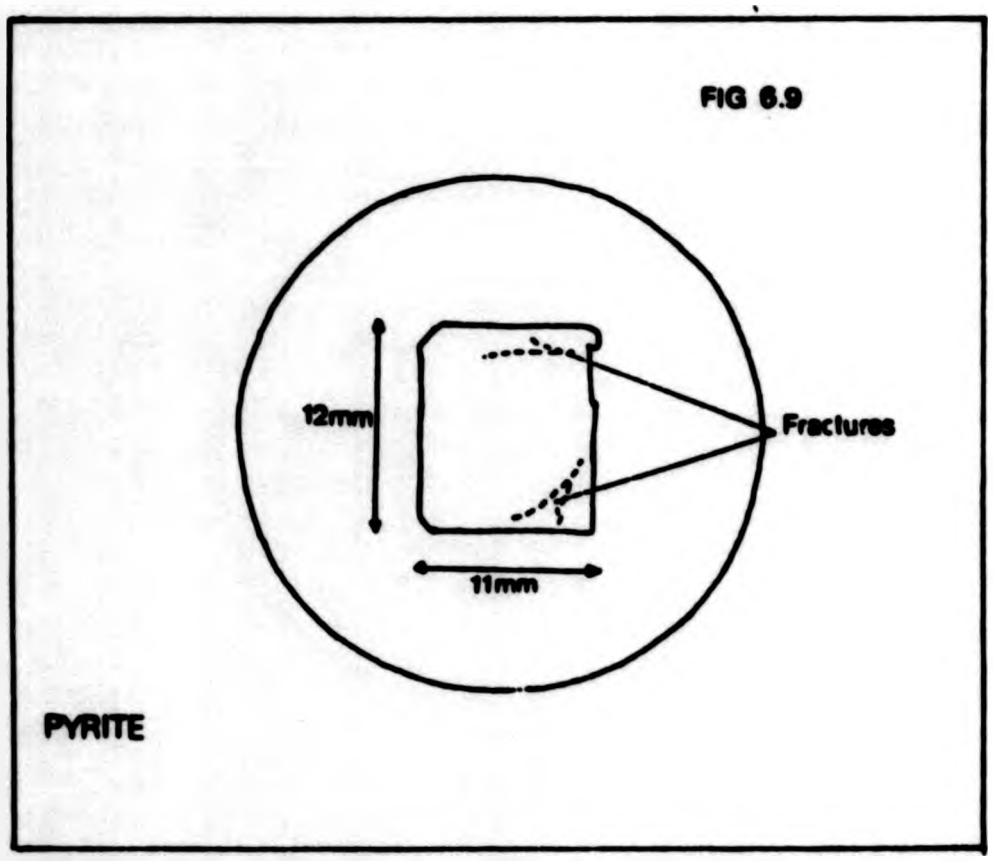

Fig 6.9 Pyrite specimen directly after polishing.

Fig 6.10 a, Comparison of microphotometric (·····) and ellipsometric (——) reflectance dispersion curves for pyrite in air.

b, Microphotometric reflectance dispersion curve for pyrite in oil.

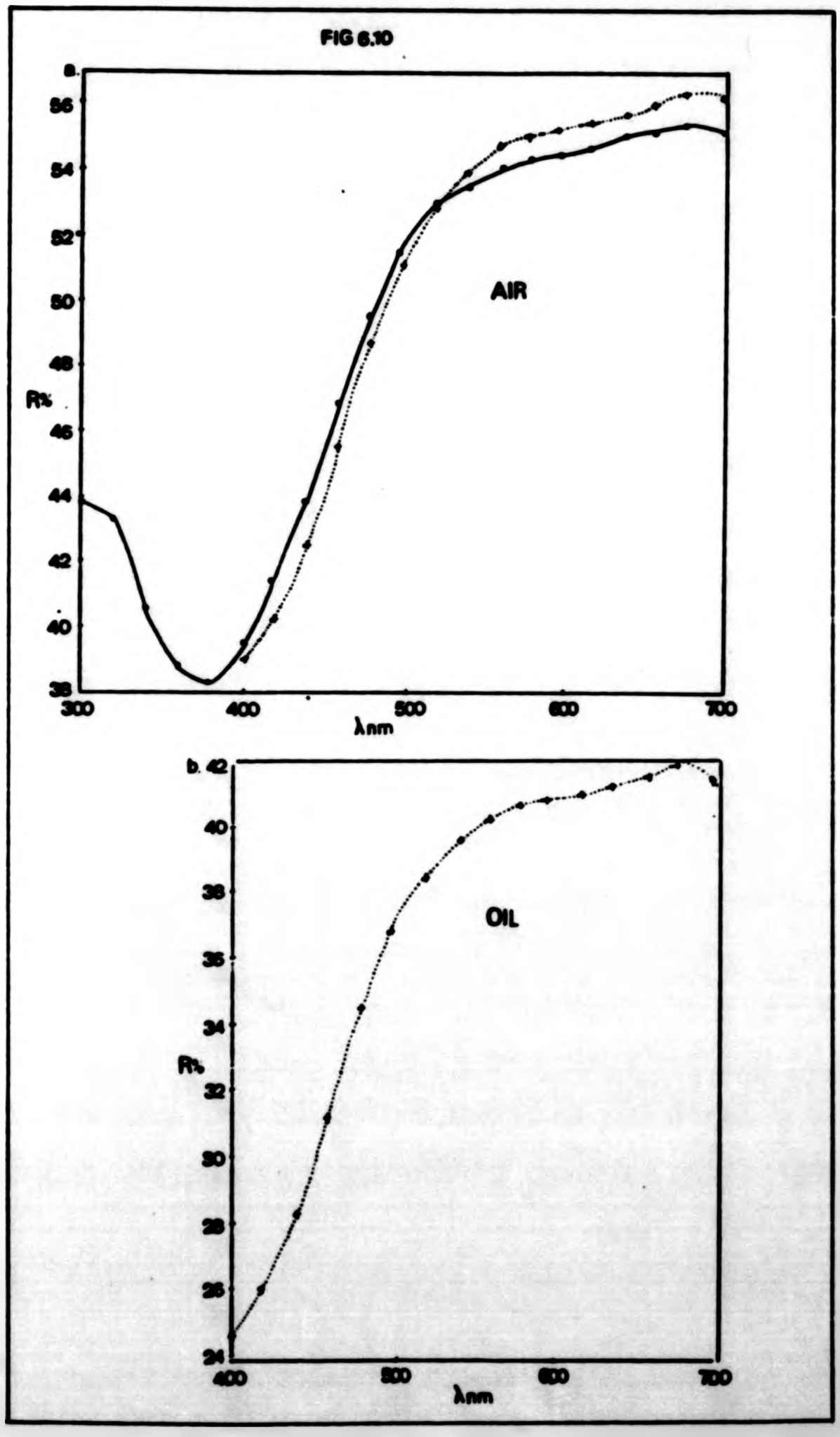

Fig 6.11 Comparison of microphotometric (·····) and ellipsometric (——) n and k values for pyrite.

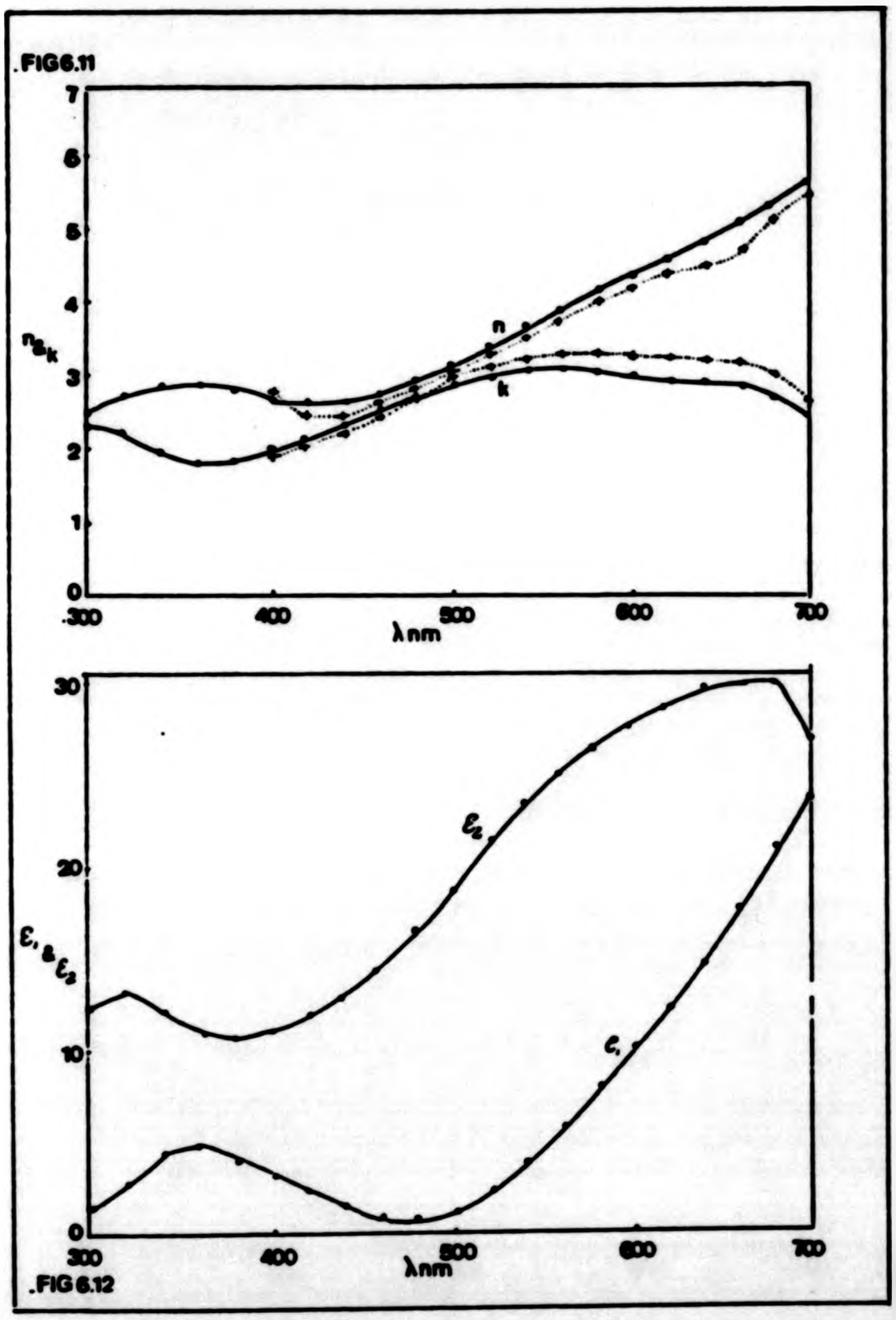

Fig 6.12 Ellipsometric ε_1 and ε_2 values for pyrite.

Table 6.5 Electron Probe Analysis of Pyrite

MINERAL NAME:Pyrite			
ELEMENT	Wt%	ATOMIC RATIO'S	ELEMENT LINE
Fe	47.87	1.05	Fe Ka
S	52.14	2.00	S Ka
Total	100.45		
CALCULATED FORMULA:$Fe_{1.05}S_2$ Formula calculated on $\Sigma S_{atoms}=2$			
TRACE ELEMENTS:Co=0.27wt% As=0.17wt%			

Table 6.6 Summary of pyrite data

MINERAL NAME:Pyrite IDEAL FORMULA:FeS_2. LOCALITY:Unknown,E1002 CRYSTAL SYSTEM:Cubic,isotropic

X-RAY ANALYSIS:Fe=47.87wt% S=52.14wt% trace cobalt 0.27wt% and arsenic 0.17wt% REAL FORMULA:$Fe_{1.05}S_{2.00}$

OPTICAL DATA:
Standard:WTiC

λ nm	Reflectance % ELL Air	MP Air	MP Oil	ELL n	MP n	ELL k	MP k	ELL c_1	ELL c_2
300	43.95			2.60		2.36		1.19	12.32
320	43.38			2.84		2.31		2.75	13.10
340	40.58			2.95		2.06		4.45	12.18
360	38.96			2.89		1.95		4.57	11.29
380	38.44			2.79		1.94		4.04	10.83
400	39.40	39.04	24.43	2.71	2.73	2.03	2.00	3.23	11.01
420	41.39	40.31	26.03	2.69	2.58	2.18	2.12	2.48	11.70
440	43.85	42.59	28.50	2.70	2.53	2.35	2.27	1.78	12.74
460	46.71	45.54	31.47	2.77	2.59	2.56	2.48	1.11	14.22
480	49.42	48.65	34.61	2.93	2.70	2.78	2.71	0.87	16.30
500	51.39	51.07	36.98	3.15	3.00	2.95	2.92	1.24	18.60
520	52.69	52.68	38.53	3.41	3.30	3.06	3.07	2.27	20.91
540	53.46	53.79	39.66	3.66	3.51	3.12	3.17	3.63	22.83
560	54.00	54.57	40.43	3.92	3.77	3.14	3.23	5.47	24.64
580	54.26	55.04	40.86	4.16	4.04	3.12	3.25	7.58	25.99
600	54.42	55.23	41.03	4.39	4.18	3.08	3.24	9.77	27.02
620	54.67	55.40	41.19	4.60	4.36	3.04	3.22	11.99	27.96
640	54.93	55.65	41.48	4.81	4.40	2.99	3.24	14.18	28.75
660	55.23	56.00	41.80	5.07	4.68	2.91	3.20	17.24	29.48
680	55.29	56.22	41.94	5.31	5.16	2.78	3.03	20.47	29.46
700	55.01	56.18	41.81	5.48	5.54	2.59	2.79	23.38	28.41

CIE Colour Co-ordinates

	MP Air	MP Oil	ELL Air
Illuminant C			
x	0.3266	0.3329	0.3234
y	0.3394	0.3484	0.3355
z	0.3340	0.3187	0.3411
Luminance Y	53.80	39.65	53.42
Pe%	10.62	14.72	8.77
D_λ	573.0	573.0	572.7
Illuminant A			
x	0.4589	0.4630	
y	0.4164	0.4195	
z	0.1247	0.1175	
Luminance Y	54.38	40.22	
Pe%	14.14	19.16	
D_λ	582.3	582.3	
Illuminant D_{65}			
x	0.3287	0.3349	
y	0.3516	0.3603	
z	0.3196	0.3048	
Luminance Y	53.78	39.64	
Pe%	10.83	14.98	
D_λ	572.4	572.4	

OTHER DATA:Specimen contains several small fractures.

6.6 Skutterudite

6.6.1 Introduction

A visual examination of the Skutterudite sample (E1003) reveals it to be a silvery-white mineral with a metallic lustre. The cubic symmetry of the mineral is confirmed by reflected light observations which show no perceptable aniso tropy. A large fracture through the centre of the specimen extends from one end to the other, fig. 6.13. There are also many other smaller localised fractures cutting the specimen surface.

Approximately two thirds of the polished mineral surface is unsuitable for making microphotometric and ellipsometric measurements, not only because it is highly fractured but also because the skutterudite is intimately intergrown with safflorite.

Apart from safflorite isolated inclusions of calcite and chalcopyrite are also present. Areas of the mineral do however exist where the surface is free from irregularities, intergrowths and inclusions and it was upon these areas that measurements were made.

The skutterudite specimen was ground and polished (section 3.5) and gently buffed with gamma-alumina before measurements were made. Skutterudite does show a small amount of surface tarnishing, manifested by a dulling of the mineral's lustre. This tarnishing is, however, small in comparison to that of the chalcopyrite inclusion, which after several weeks becomes a dull orange-red in colour.

6.6.2 Electron Probe Analysis

The electron probe microanalysis of the skutterudite sample showed it to be a cobaltian variety. Quantitative analyses were carried out on the pure skutterudite and the safflorite intergrowth.

The analyses of the skutterudite and safflorite are shown in Table 6.7 together with their calculated formulae, and the major element lines used in the determination.

6.6.3 Reflectance, n, k, ε_1 and ε_2

In fig. 6.14 the microphotometrically measured reflectance values are displayed for both air and oil environments. Also shown are the ellipsometric air reflectance values. Fig. 6.15 shows the derived n and k values for both techniques, and fig. 6.16 displays the dispersions of the ellipsometric ε_1 and ε_2 values. All the preceding results are displayed in table 6.8 with the CIE colour coordinates for illuminants C, A and D_{65}.

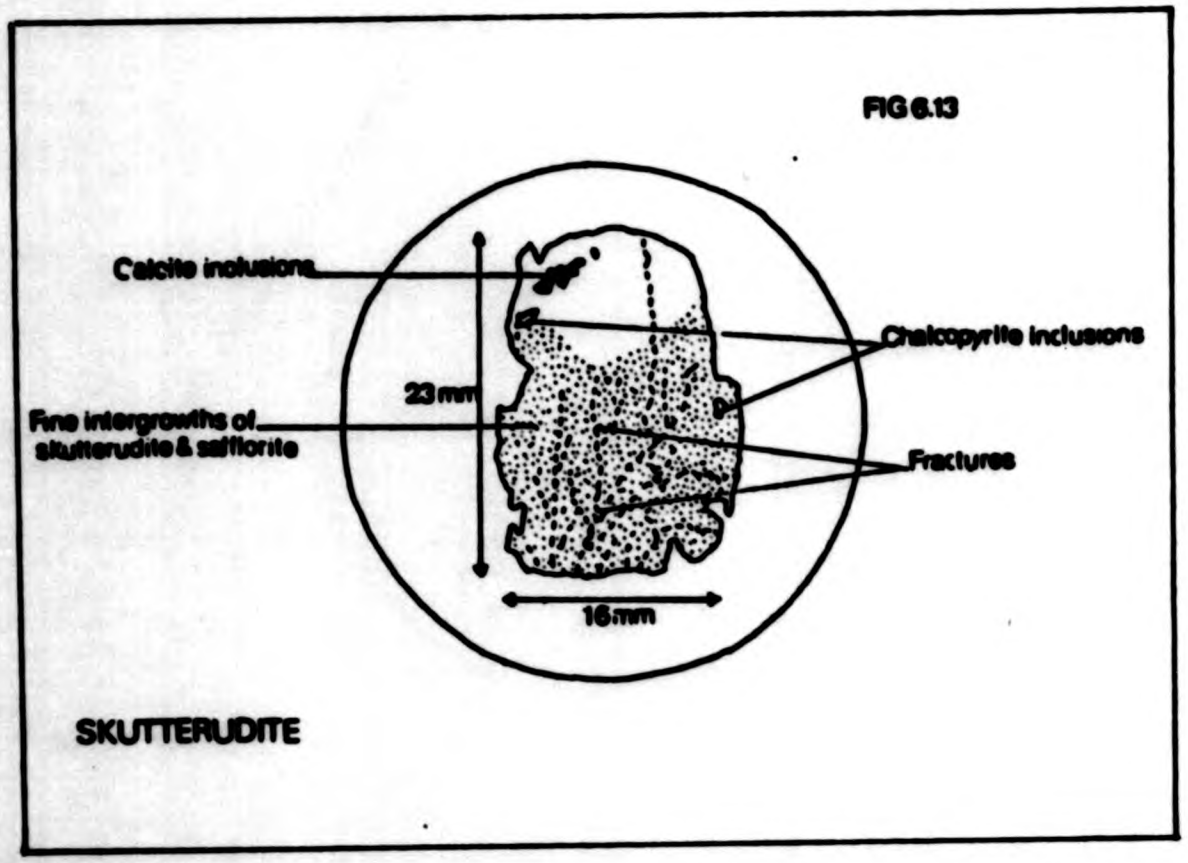

Fig 6.13 Skutterudite specimen directly after polishing.

FIG 6.14

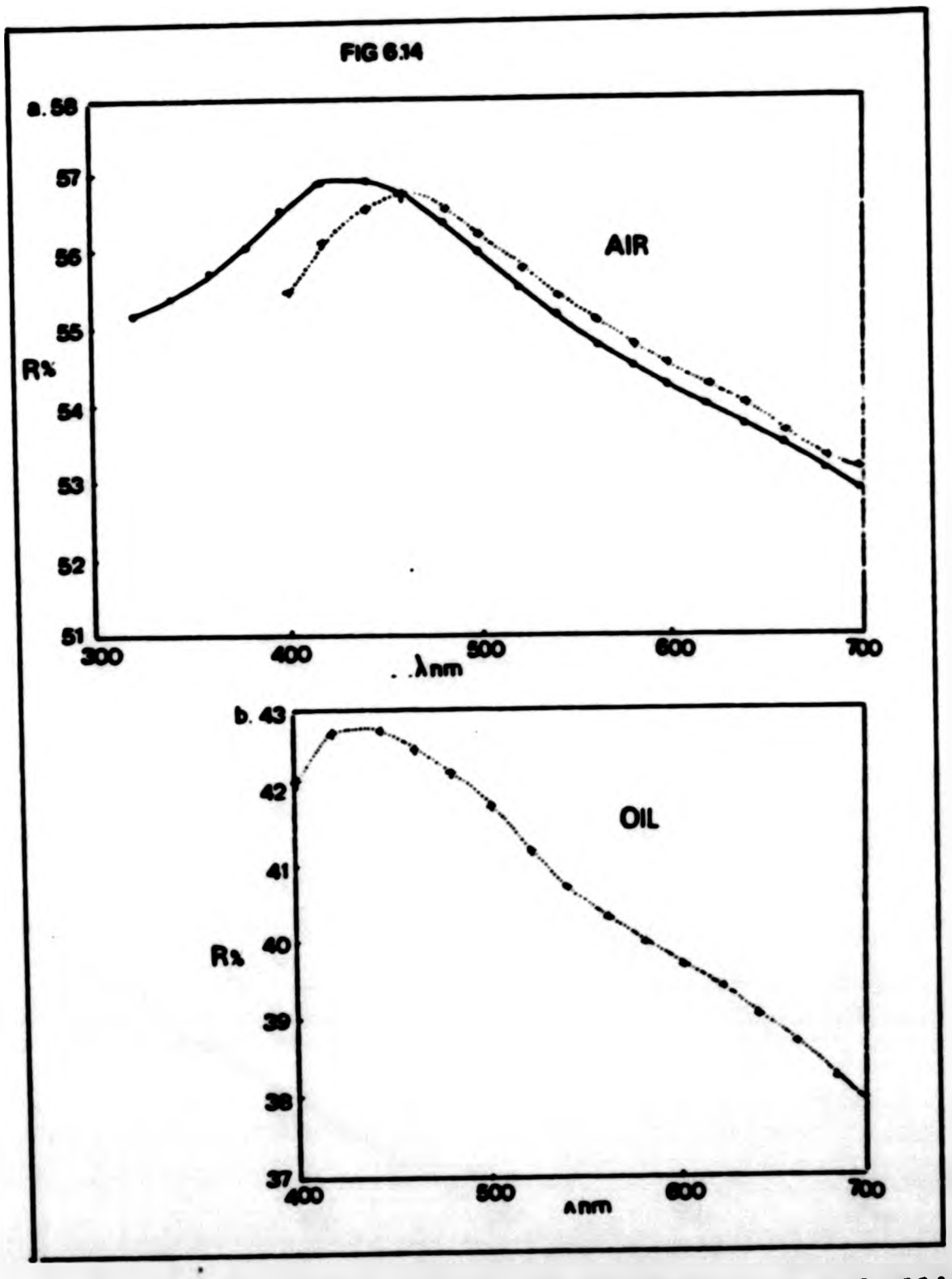

Fig 6.14 a, Comparison of microphotometric (.....) and ellipsometric (——) reflectance dispersion curves for skutterudite in air.

b, Microphotometric reflectance dispersion curve for skutterudite in oil.

FIG 6.15

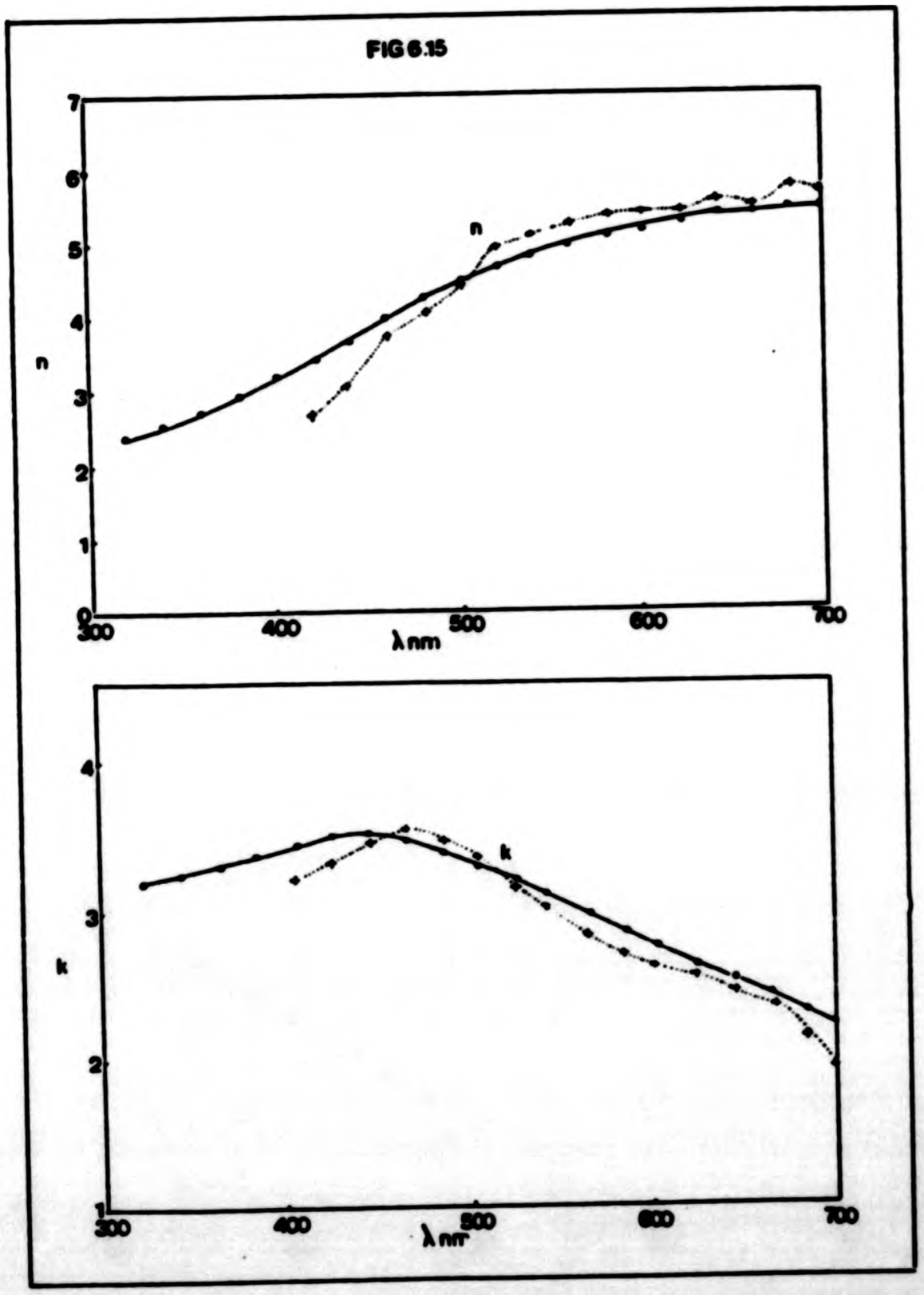

Fig 6.15 Comparison of microphotometric (·····) and ellipsometric (——) n and k values for sputtered ZnO.

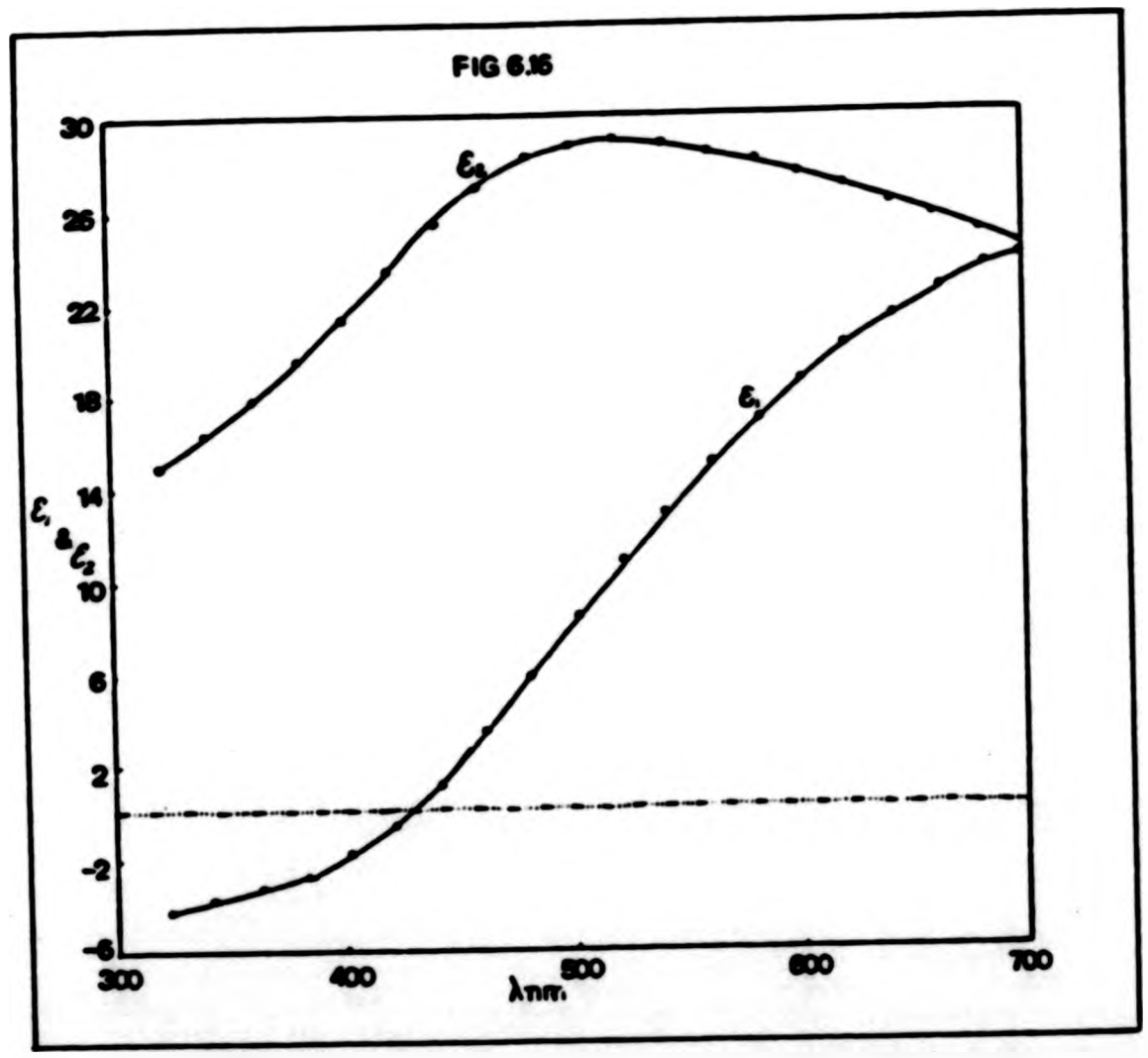

Fig 6.16 Ellipsometric ε_1 and ε_2 values for skutterudite.

Table 6.7 Electron Probe Analysis of Skutterudite and Safflorite

MINERAL NAME:Skutterudite				MINERAL NAME:Safflorite			
ELEMENT	Wt%	ATOMIC RATIO'S	ELEMENT. LINE	ELEMENT	Wt%	ATOMIC RATIO'S	ELEMENT LINE
Co	18.91	0.88	Co Kα	Co	14.47	0.43	Co Kα
Fe	1.90	0.09	Fe Kα	Fe	17.48	0.55	Fe Kα
Ni	0.53	0.02	Ni Kα	Ni	0.51	0.02	Ni Kα
As	78.20	2.87	As Kα	As	67.06	1.58	As Kα
S	0.49	0.04	S Kα	S	1.59	0.08	S Kα
Total	100.03			Total	100.63		
CALCULATED FORMULA: $(Co_{0.88}Fe_{0.09}Ni_{0.02})As_{2.87}S_{0.04}$ (Skutterudite)							
Formula based on $\Sigma Co+Ni+Fe_{atoms}=1$							
CALCULATED FORMULA: $(Co_{0.43}Fe_{0.55}Ni_{0.02})As_{1.58}S_{0.08}$ (Safflorite)							
Formula based on $\Sigma Co+Ni+Fe_{atoms}=1$							

Table 6.8 Summary of skutterudite data.

MINERAL NAME:Skutterudite IDEAL FORMULA:$(Co,Ni,Fe)As_{3-x}$ LOCALITY:Unknown,E1003

CRYSTAL SYSTEM:Cubic,isotropic X-RAY ANALYSIS (Skutterudite):Co=18.91wt% As=78.20wt% Fe=1.90wt% Ni=0.53wt% S=0.49

REAL FORMULA (Skutterudite):$Co_{0.88}Ni_{0.02}Fe_{0.09}As_{2.87}S_{0.04}$ X-RAY ANALYSIS (Safflorite):Co=14.47wt% As=67.06wt%

Fe=17.48wt% Ni=0.51wt% S=1.59wt% REAL FORMULA (Safflorite):$(Co_{0.43}Ni_{0.02}Fe_{0.55})As_{1.38}S_{0.08}$

OPTICAL DATA:
Standard:WTiC

	Reflectance %								
λ nm	ELL Air	MP Air	MP Oil	ELL n	MP n	ELL k	MP k	ELL ε_1	ELL ε_2
320	55.17			2.38		3.13		-4.14	14.94
340	55.33			2.56		3.20		-3.69	16.40
360	55.61			2.70		3.26		-3.33	17.65
380	56.08			2.91		3.34		-2.76	19.46
400	56.45	55.34	41.92	3.13	2.45	3.42	3.17	-1.92	21.38
420	56.76	56.02	42.64	3.38	2.55	3.48	3.25	-0.69	23.46
440	56.81	56.44	42.70	3.65	3.08	3.49	3.41	1.11	25.45
460	56.64	56.59	42.55	3.91	3.66	3.46	3.46	3.33	27.06
480	56.34	56.39	42.26	4.16	3.92	3.39	3.43	5.82	28.20
500	55.92	56.09	41.77	4.38	4.38	3.29	3.31	8.37	28.79
520	55.47	55.68	41.19	4.56	4.82	3.17	3.10	10.70	28.89
540	55.08	55.28	40.73	4.71	4.92	3.06	2.99	12.81	28.78
560	54.74	54.98	40.35	4.84	5.15	2.95	2.82	14.72	28.50
580	54.46	54.68	40.01	4.96	5.25	2.84	2.70	16.59	28.14
600	54.18	54.42	39.75	5.07	5.24	2.73	2.66	18.23	27.62
620	53.90	54.12	39.41	5.16	5.29	2.61	2.56	19.87	26.95
640	53.68	53.81	39.04	5.24	5.42	2.51	2.39	21.16	26.32
660	53.43	53.46	38.66	5.30	5.38	2.42	2.36	22.25	25.61
680	53.18	53.11	38.23	5.36	5.60	2.31	2.05	23.34	24.08
700	53.01	52.71	37.79	5.39	5.58	2.24	1.97	24.03	24.21

OTHER DATA:Specimen contains small inclusions of calcite and chalcopyrite.

CIE Colour Co-ordinates			
	MP Air	MP Oil	ELL Air
Illuminant C			
x	0.3066	0.3038	0.3060
y	0.3139	0.3110	0.3126
z	0.3795	0.3852	0.3814
Luminance Y	55.06	40.49	54.86
Pe%	1.53	2.88	1.84
D_λ	482.6	479.9	478.9
Illuminant A			
x	0.4437	0.4412	
y	0.4074	0.4065	
z	0.1489	0.1523	
Luminance Y	54.83	40.21	
Pe%	0.92	1.55	
D_λ	494.5	492.1	
Illuminant D_{65}			
x	0.3092	0.3064	
y	0.3269	0.3240	
z	0.3639	0.3696	
Luminance Y	55.06	40.49	
Pe%	1.47	2.76	
D_λ	483.9	481.4	

6.7 Sphalerite

6.7.1 Introduction

A visual examination of the sphalerite specimen (E1004) reveals it to be dark brownish-yellow and semi-transparent with an adamantine lustre. Reflected light observations on the polished mineral surface show it to be isotropic (sphalerite has cubic symmetry), with deep yellow internal reflections visible in some areas. Apart from a few localised small surface fractures the mineral surface is devoid of any surface irregularities or mineral inclusions, fig. 6.17. When ellipsometric and microphotometric measurements were made care was taken to avoid areas where internal reflections and fractures were present.

The sphalerite specimen was ground and polished (section 3.5). Before measurements were made the sample was buffed using gamma-alumina. Sphalerite, apart from the formation of a thin, air-formed film which appears immediately after polishing, shows little visible tendency to tarnish. It is still advisable, however, to buff the sample before measurement to remove any surface contaminants.

6.7.2 Electron Probe Analysis

The sphalerite specimen was examined by electron probe microanalysis. The analysis of the mineral indicates that it is composed mostly of zinc and sulphur. Smaller concentrations of iron and traces of copper are also detected. Table 6.9 shows the analysis of the sphalerite specimen, together with the X-ray lines used in the determination and the formula of the mineral is also calculated from the data.

6.7.3 Reflectance, n, k, ε_1 and ε_2

The ellipsometric air reflectance curve is shown in fig. 6.18 together with the microphotometrically measured reflectance values for both air and oil environments. Fig. 6.19 shows the derived n and k values for both techniques. The ellipsometrically derived ε_1 and ε_2 curves are shown in fig. 6.20. A summary of the above data is to be found in table

6.10, together with the CIE colour coordinates for illuminants C, A and D_{65}.

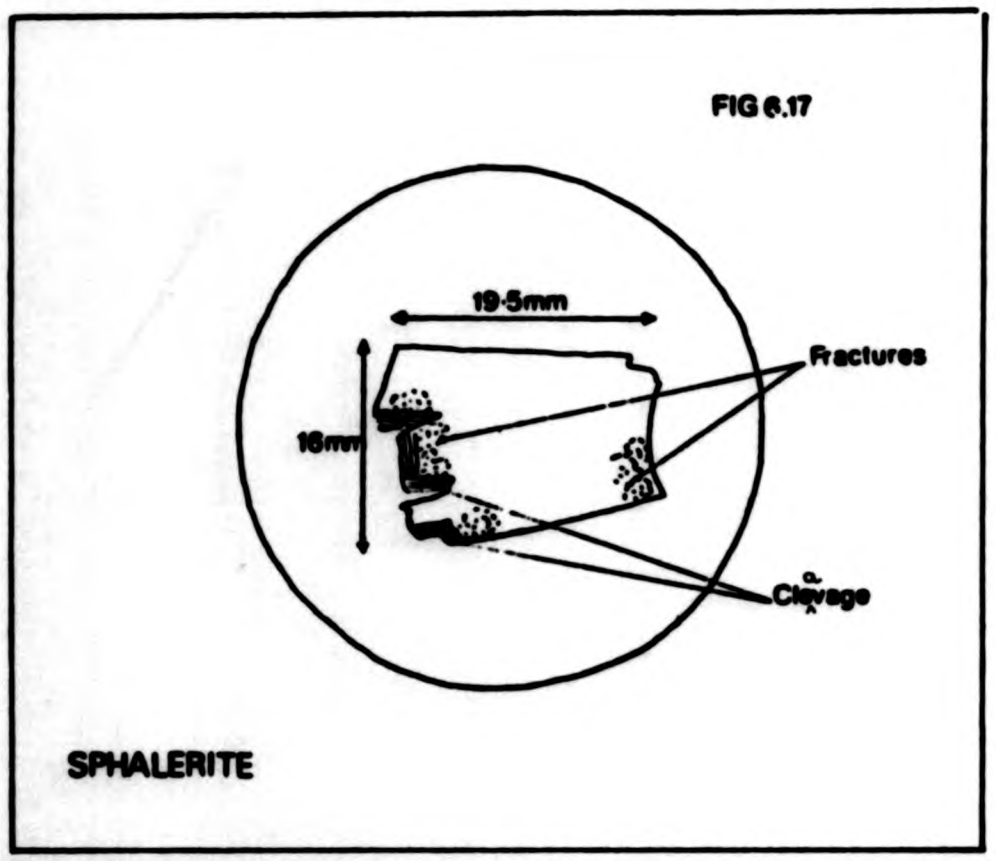

Fig 6.17 Sphalerite specimen directly after polishing.

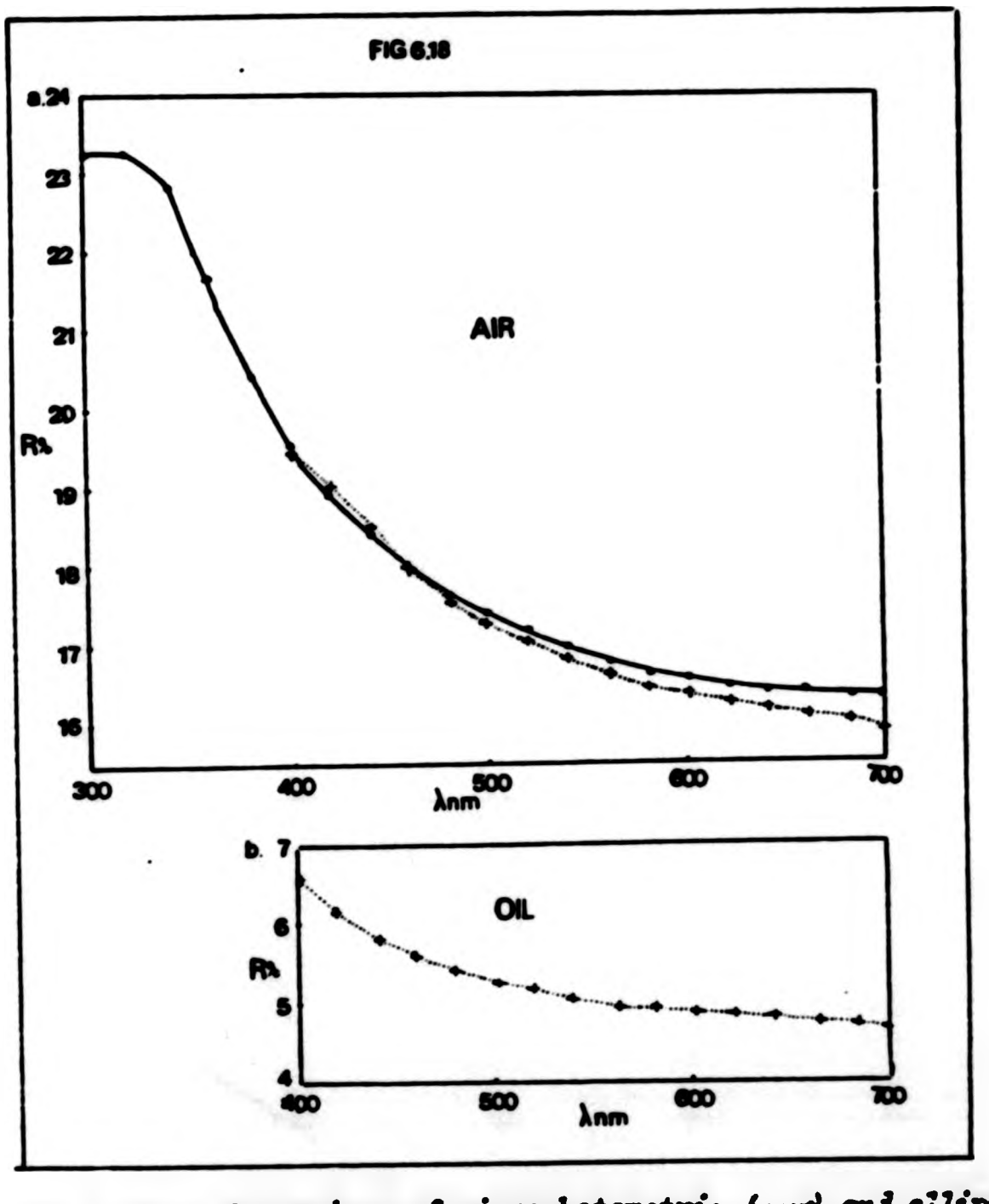

Fig 6.18 a, Comparison of microphotometric (·····) and ellipsometric (——) reflectance dispersion curves for sphalerite in in air.

b, Microphotometric reflectance dispersion curve for sphalerite in oil.

Fig 6.19 Comparison of microphotometric (·····) and ellipsometric (⟷) n and k values.

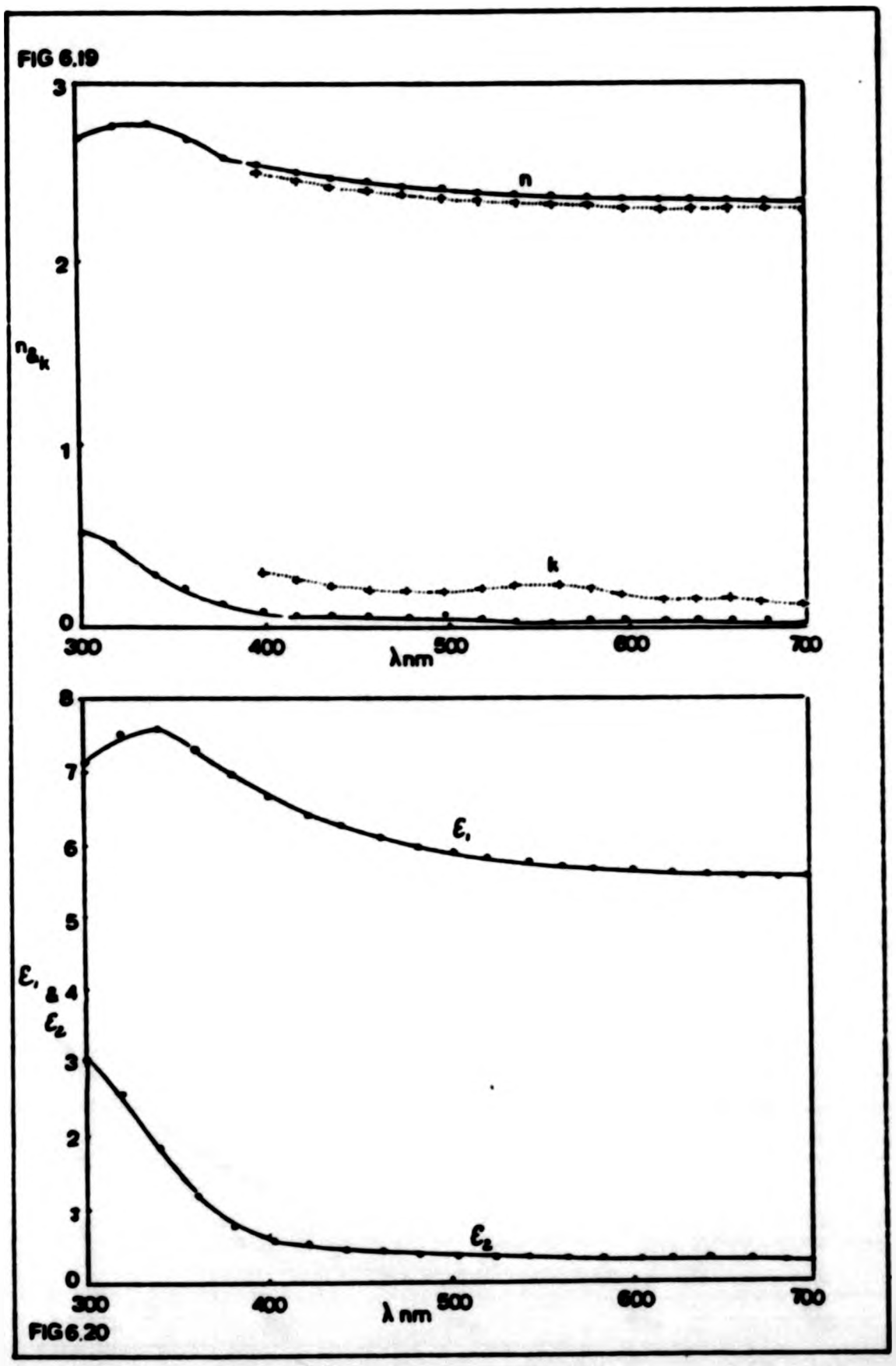

Fig 6.20 Ellipsometric ε_1 and ε_2 values for sphalerite.

Table 6.9 Electron Probe Analysis of Sphalerite

MINERAL NAME: Sphalerite			
ELEMENT	Wt%	ATOMIC RATIO'S	ELEMENT LINE
Zn	65.25	1.00	Zn Kα
Fe	2.61	0.05	Fe Kα
S	32.07	1.00	S Kα
Total	100.04		
CALCULATED FORMULA: $(Zn_{1.00}Fe_{0.05})S_{1.00}$			
Formula based on $\Sigma S_{atoms}=1$			
TRACE ELEMENTS: Cu=0.11wt%			

Table 6.10 Summary of sphalerite data.

MINERAL NAME:Sphalerite FORMULA:ZnS LOCALITY:Unknown,E1004 CRYSTAL SYSTEM:Cubic, isotropic.

X-RAY ANALYSIS:Zn=65.25wt%,S=32.07wt%,Fe=2.61wt%, trace copper. REAL FORMULA:$(Zn_{1.00}Fe_{0.05})S$.

OPTICAL DATA:

Standard:SiC

Reflectance %

λ nm	ELL Air	MP Air	MP Oil	ELL n	MP n	ELL k	MP k	ELL ϵ_1	ELL ϵ_2
300	23.21			2.72		0.58		7.06	3.13
320	23.16			2.76		0.48		7.39	2.65
340	22.75			2.77		0.35		7.57	1.95
360	21.65			2.72		0.23		7.32	1.26
380	20.50			2.64		0.16		6.96	0.86
400	19.61	19.51	6.59	2.58	2.52	0.13	0.35	6.65	0.66
420	18.93	18.96	6.24	2.54	2.50	0.11	0.29	6.42	0.54
440	18.40	18.41	5.92	2.50	2.47	0.09	0.27	6.23	0.48
460	18.00	17.98	5.68	2.47	2.44	0.08	0.26	6.09	0.42
480	17.65	17.60	5.47	2.45	2.41	0.08	0.25	5.98	0.38
500	17.39	17.28	5.30	2.43	2.39	0.07	0.24	5.89	0.35
520	17.14	17.00	5.20	2.41	2.36	0.07	0.29	5.81	0.33
540	16.94	16.79	5.08	2.40	2.35	0.06	0.27	5.74	0.30
560	16.78	16.59	4.97	2.39	2.35	0.06	0.26	5.69	0.29
580	16.64	16.45	4.89	2.38	2.33	0.06	0.25	5.64	0.29
600	16.55	16.34	4.81	2.37	2.33	0.06	0.21	5.61	0.29
620	16.47	16.23	4.76	2.36	2.33	0.06	0.21	5.58	0.29
640	16.38	16.16	4.73	2.36	2.32	0.06	0.21	5.56	0.28
660	16.32	16.06	4.68	2.35	2.31	0.06	0.21	5.54	0.28
680	16.32	15.97	4.64	2.35	2.31	0.06	0.21	5.54	0.28
700	16.32	15.90	4.60	2.35	2.30	0.06	0.21	5.54	0.28

CIE Colour Co-ordinates

		MP Air	MP Oil	ELL Air
Illuminant C				
	x	0.3013	0.2950	0.3024
	y	0.3063	0.2991	0.3072
	z	0.3924	0.4059	0.3904
Luminance	Y	16.70	5.02	16.87
	Pe%	4.37	7.53	3.84
	D_λ	475.1	475.1	474.2
Illuminant A				
	x	0.4397	0.4337	
	y	0.4043	0.4019	
	z	0.1560	0.1644	
Luminance	Y	16.57	4.95	
	Pe%	2.03	3.54	
	D_λ	487.8	487.8	
Illuminant D_{65}				
	x	0.3040	0.2977	
	y	0.3194	0.3123	
	z	0.3766	0.3899	
Luminance	Y	16.70	5.02	
	Pe%	4.17	7.20	
	D_λ	476.5	476.5	

OTHER DATA:Specimen contains several small fractures.

6.8 Tetrahedrite

6.8.1 Introduction

The sample of tetrahedrite (BM; 1917, E1005) is from an unknown locality. An initial visual examination of the mineral reveals it to be silvery-grey-blue in appearance with a metallic lustre. In reflected light the polished surface of the mineral displays no detectable aniso tropy, reflecting its cubic symmetry. The surface of the tetrahedrite is cut by a number of fractures most of which are small and localised, fig. 6.21. However, one is large and runs the entire length of the specimen. A degree of porosity is also exhibited;this is displayed in the form of rows of tiny pores arranged in lines approximately parallel to each other. Some larger isolated pores are also visible within the tetrahedrite matrix, as are several isolated inclusions of chalcopyrite, bornite and covelline. Areas of specimen do, however, exist where there are no perceivable surface irregularities or inclusions and it was upon these areas that the microphotometric and ellipsometric measurements were made.

The tetrahedrite specimen was ground and polished in the manner described in section 3.5 and gently buffed before making ellipsometric and microphotometric measurements. Like most copper sulphosalts, the tetrahedrite specimen showed visible tarnishing after a few weeks. This was exhibited by a general dulling of the mineral's lustre and by the formation of isolated dark blue spots flanked by brown rims, which indicated that in these areas the film had reached a sufficient thickness to cause light interference effects. The formation of such a tarnish film emphasises the need for adequate buffing of the specimen before making measurements. The mineral inclusions also exhibited tarnish films.

6.8.2 Electron Probe Analysis

An initial examination of the mineral reveals that it lies at the tetrahedrite end of the tetrahedrite-tennantite solid soution series. Quantitative analyse were carried out on several regions of the specimen. The analyses of the various areas of the mineral revealed that it was relatively homogeneous, with only slight detectable fluctuations in the major element concentrations.

The analysis of the tetrahedrite specimen is shown in Table 6.11 accompanied by the element lines used in the determination, and the calculated formula based on the premise of seventeen anions per formula unit.

6.8.3 Reflectance, n, k, ε_1 and ε_2

Fig. 6.22 displays the ellipsometric and microphotometric reflectance curves, in the latter case for both air and oil environments. The derived n and k values for both techniques are shown in fig. 6.23. Fig. 6.24 displays the ellipsometric ε_1 and ε_2 values. the data above are displayed with the CIE colour coordinates in table 6.12.

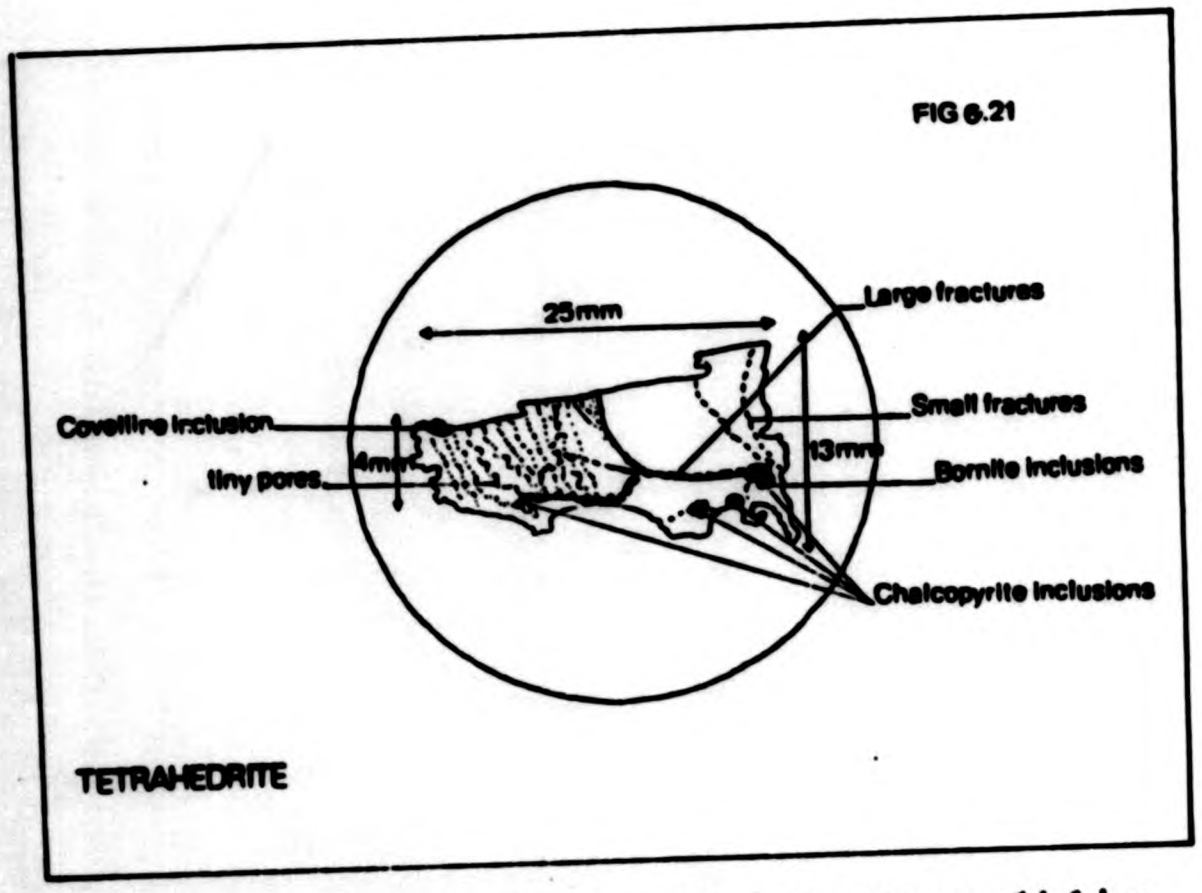

Fig 6.21 Tetrahedrite specimen directly after polishing.

FIG 6.22

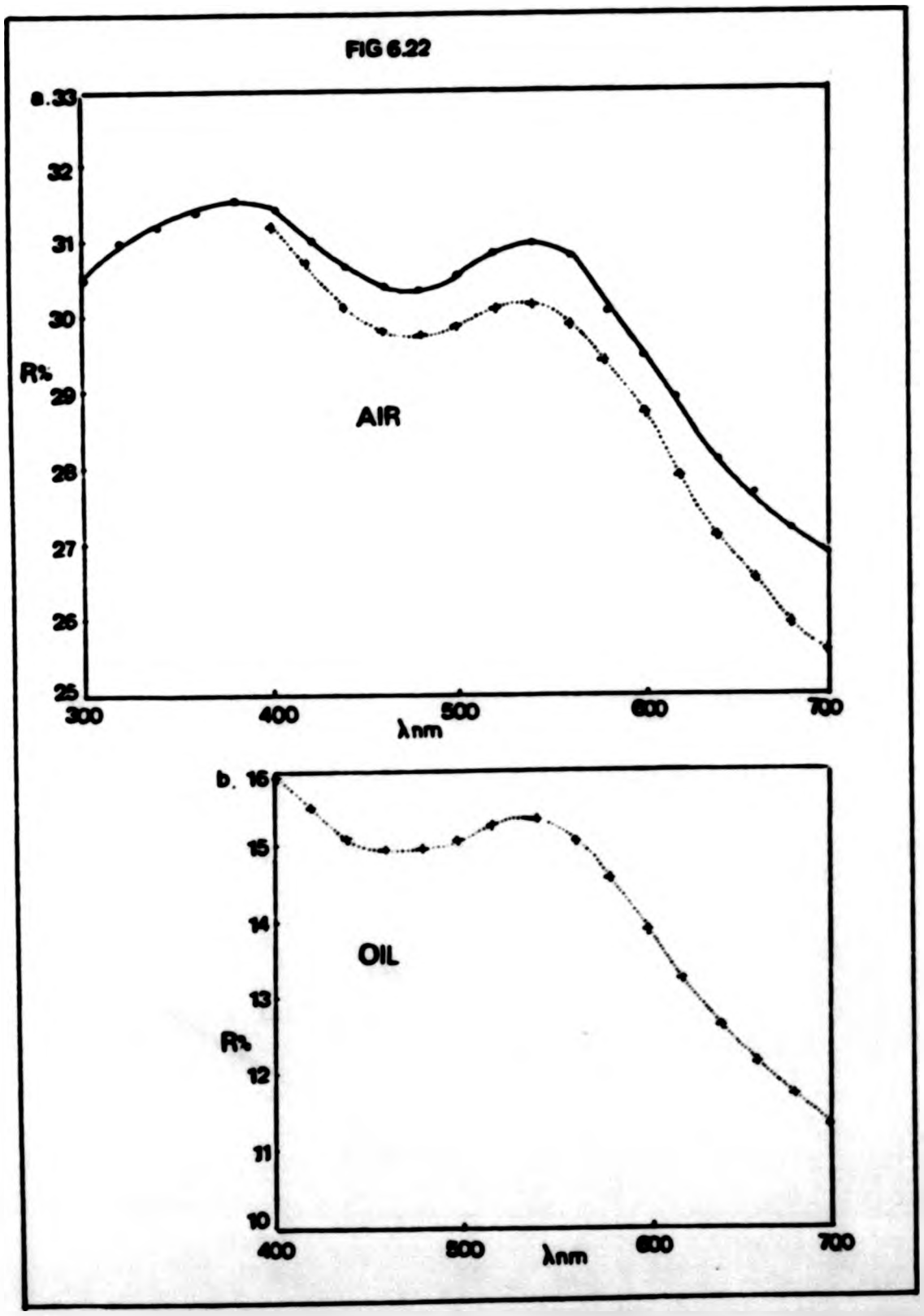

Fig 6.22 a, Comparison of microphotometric (·····) and ellipsometric (——) reflectance dispersion curves for tetrahedrite in air.

b, Microphotometric reflectance dispersion curve for tetrahedrite in oil.

Fig 6.23 Comparison of microphotometric (·····) and ellipsometric (——) n and k values.

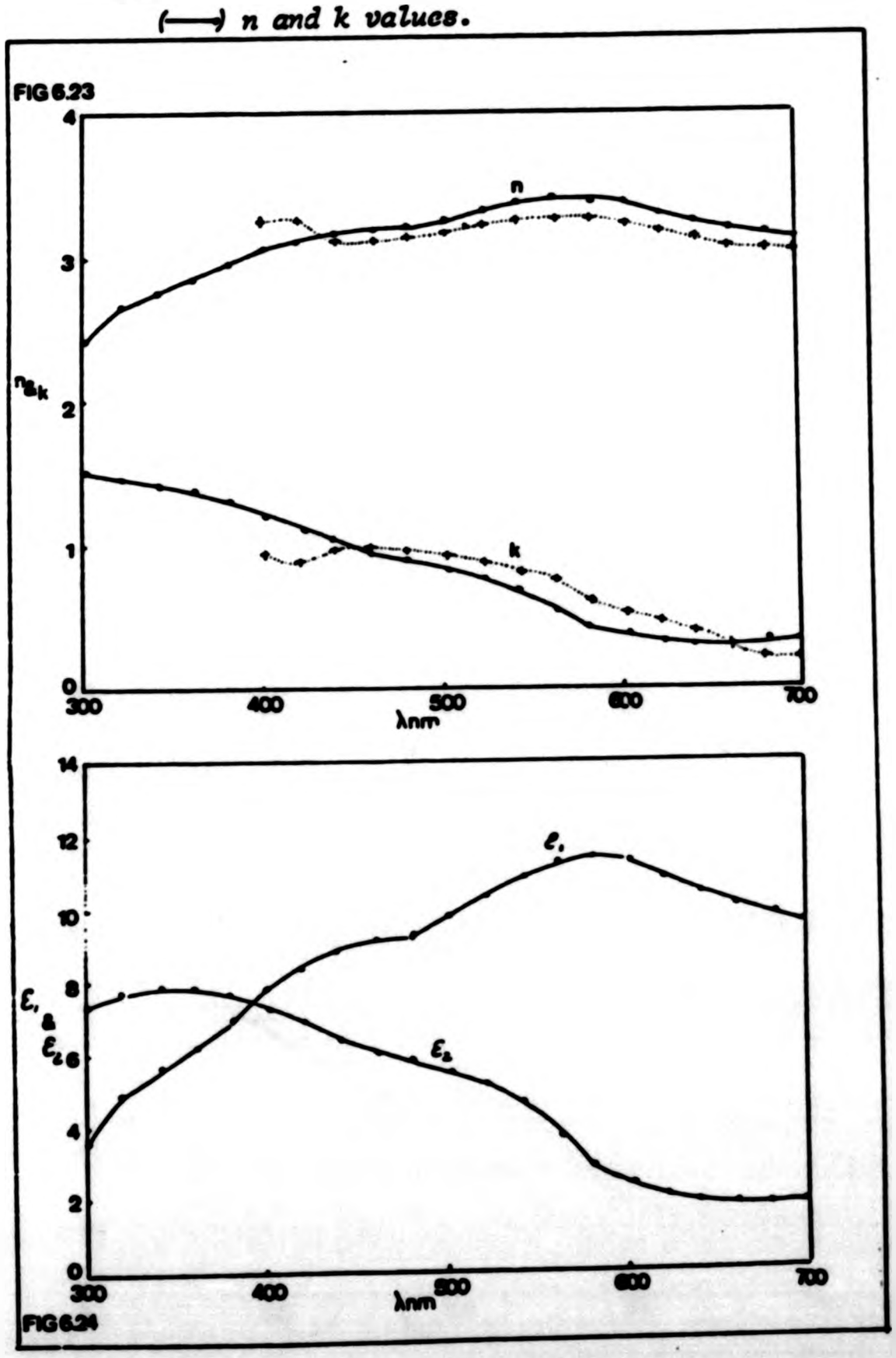

Fig 6.24 Ellipsometric ε_1 and ε_2 values for tetrahedrite.

Table 6.11 Electron Probe Analysis of Tetrahedrite

MINERAL NAME:Tetrahedrite				
ELEMENT	Wt%	ATOMIC RATIO'S	ELEMENT LINE	
Cu	39.88	10.18	Cu Kα	
Ag	1.89	0.28	Ag Lα	
Zn	7.69	1.91	Zn Kα	
Fe	0.51	0.14	Fe Kα	
As	5.49	1.19	As Kα	
Sb	22.16	2.95	Sb Lα	
S	25.40	12.86	S Kα	
Total	102.25			
CALCULATED FORMULA: $(Cu_{10.18}Ag_{0.28})(Zn_{1.91}Fe_{0.14})(As_{1.19}Sb_{2.95})S_{12.86}$				
Formula based on $\Sigma As+Sb+S_{atoms}=17$				

Table 6.12 Summary of tetrahedrite data.

MINERAL NAME:Tetrahedrite IDEAL FORMULA:$(Cu,Ag)_{10}(Cu,Fe,Zn)_2(Sb,As)_4S_{13}$ LOCALITY:Unknown,BM.1917,E1005

CRYSTAL SYSTEM:Cubic,isotropic X-RAY ANALYSIS:Cu=39.88wt% Ag=1.89wt% Zn=7.69wt% Fe=0.51wt% As=5.49wt% Sb=22.16wt% S=25.40wt%

REAL FORMULA:$(Cu_{10.12}Ag_{0.28})(Zn_{1.91}Fe_{0.14})(As_{1.19}Sb_{2.95})S_{12.84}$

OPTICAL DATA:

Standard:WTiC

	Reflectance%								
λ nm	ELL Air	MP Air	MP Oil	ELL n	MP n	ELL k	MP k	ELL t_1	ELL t_2
300	30.44			2.40		1.50		3.51	7.18
320	31.02			2.62		1.44		4.78	7.57
340	31.24			2.73		1.40		5.47	7.66
360	31.36			2.81		1.37		6.01	7.67
380	31.54			2.92		1.30		6.86	7.59
400	31.46	31.28	15.97	3.03	3.23	1.20	0.95	7.72	7.28
420	31.10	30.79	15.58	3.08	3.23	1.11	0.88	8.29	6.83
440	30.75	30.19	15.23	3.12	3.12	1.02	0.95	8.71	6.37
460	30.49	29.90	15.02	3.15	3.12	0.95	0.92	9.01	6.00
480	30.41	29.80	14.98	3.16	3.12	0.93	0.90	9.12	5.86
500	30.62	29.93	15.11	3.23	3.14	0.85	0.88	9.71	5.51
520	30.88	30.14	15.29	3.30	3.19	0.79	0.85	10.25	5.18
540	31.02	30.21	15.34	3.36	3.22	0.69	0.81	10.79	4.66
560	30.90	29.97	15.12	3.41	3.23	0.55	0.74	11.30	3.76
580	30.24	29.45	14.63	3.38	3.25	0.43	0.61	11.27	2.90
600	29.93	28.71	13.98	3.37	3.22	0.38	0.51	11.22	2.53
620	29.00	27.88	13.29	3.30	3.16	0.32	0.46	10.78	2.12
640	28.23	27.15	12.68	3.23	3.13	0.30	0.37	10.38	1.96
660	27.78	26.55	12.18	3.20	3.09	0.30	0.30	10.14	1.92
680	27.33	26.04	11.77	3.16	3.06	0.30	0.24	9.89	1.91
700	27.00	25.60	11.43	3.13	3.03	0.32	0.23	9.68	1.98

OTHER DATA:Specimen contains inclusions of covelline, chalcopyrite and bornite.

CIE Colour Co-ordinates	MP Air	MP Oil	ELL Air
Illuminant C			
x	0.3044	0.3033	0.3060
y	0.3160	0.3162	0.3168
z	0.3796	0.3865	0.3772
Luminance Y	29.55	14.75	30.44
Pe%	2.14	3.63	1.44
D_λ	490.2	490.9	492.6
Illuminant A			
x	0.4397	0.4340	
y	0.4106	0.4130	
z	0.1497	0.1530	
Luminance Y	29.28	14.51	
Pe%	1.79	3.07	
D_λ	501.8	502.0	
Illuminant D_{65}			
x	0.3070	0.3028	
y	0.3290	0.3295	
z	0.3640	0.3677	
Luminance Y	29.56	14.76	
Pe%	2.09	3.56	
D_λ	491.6	492.2	

6.9 Cassiterite

6.9.1 Introduction

The sample of cassiterite (E1006) in this investigation orginates from Slavkov in Bohemia. Visual examination of the mineral reveals it to be semi-transparent, dark reddish-brown in colour with an adamantine lustre, and showing distinct twinning, fig. 6.25. For reflected light studies an isotropic section of the mineral was cut at NHM (Cassiterite is tetragonal). Rotation of the specimen on the microscope stage revealed no significant change in the readings on the DVM. Thus the specimen surface could be effectively regarded as isotropic and treated as such.

During the course of microphotometric and ellipsometric measurements, care was taken to select areas free from surface imperfections, internal reflections and twin planes.

The mineral was ground and polished (section 3.5), and before measurements were made gently buffed with gamma-alumina. The specimen surface appears to be pure cassiterite, and is devoid of any mineral inclusions. The surface seems to be relatively inert, showing no appreciable tarnishing behaviour even after prolonged exposure to the atmosphere.

6.9.2 Electron Probe Analyses

Several areas of the cassiterite specimen were scanned using the electron probe microanalyser. The specimen appeared to be homogeneous and was composed mainly of tin and oxygen, with trace amounts of copper and titanium. No iron was detected.

The results of the analysis are displayed in table 6.13 together with details of the element lines used in the determination and the formula of the mineral calculated from the data.

6.9.3 Reflectance, n, k, ε_1 and ε_2

The air and oil reflectance curves for cassiterite using

ellipsometric and microphotometric techniques are displayed in fig. 6.26. The derived n and k values are shown in fig. 6.27, and the ellipsometric ε_1 and ε_2 curves in fig. 6.28. The above data together with CIE colour coordinates for illuminants C, A and D_{65} are displayed in table 6.14.

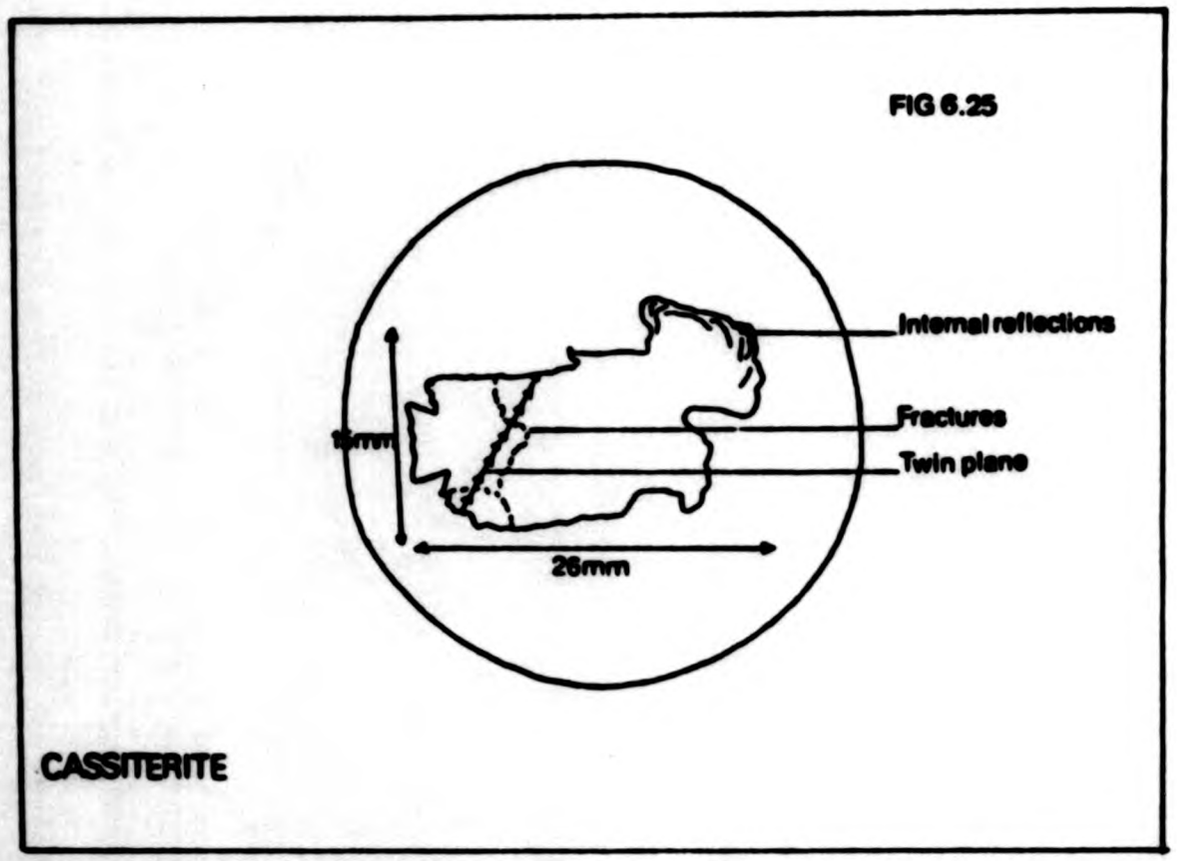

Fig 6.25 cassiterite specimen directly after polishing.

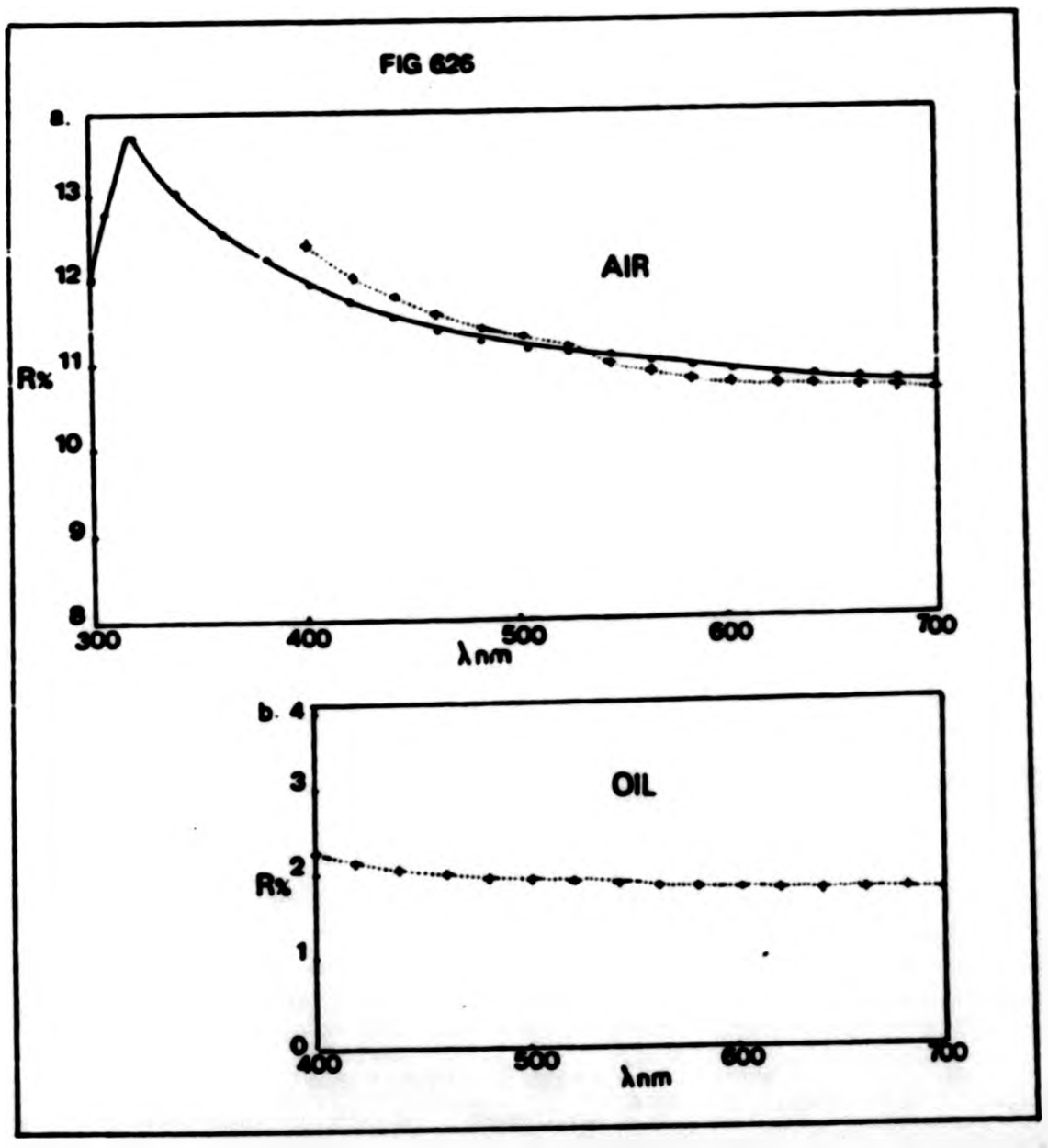

Fig 6.26 a, Comparison of microphotometric (·····) and ellipsometric (——) reflectance dispersion curves for cassiterite in air.

b, Microphotometric reflectance dispersion curve for cassiterite in oil.

Fig 6.27 Comparison of microphotometric (·····) and ellipsometric (——) n and k values.

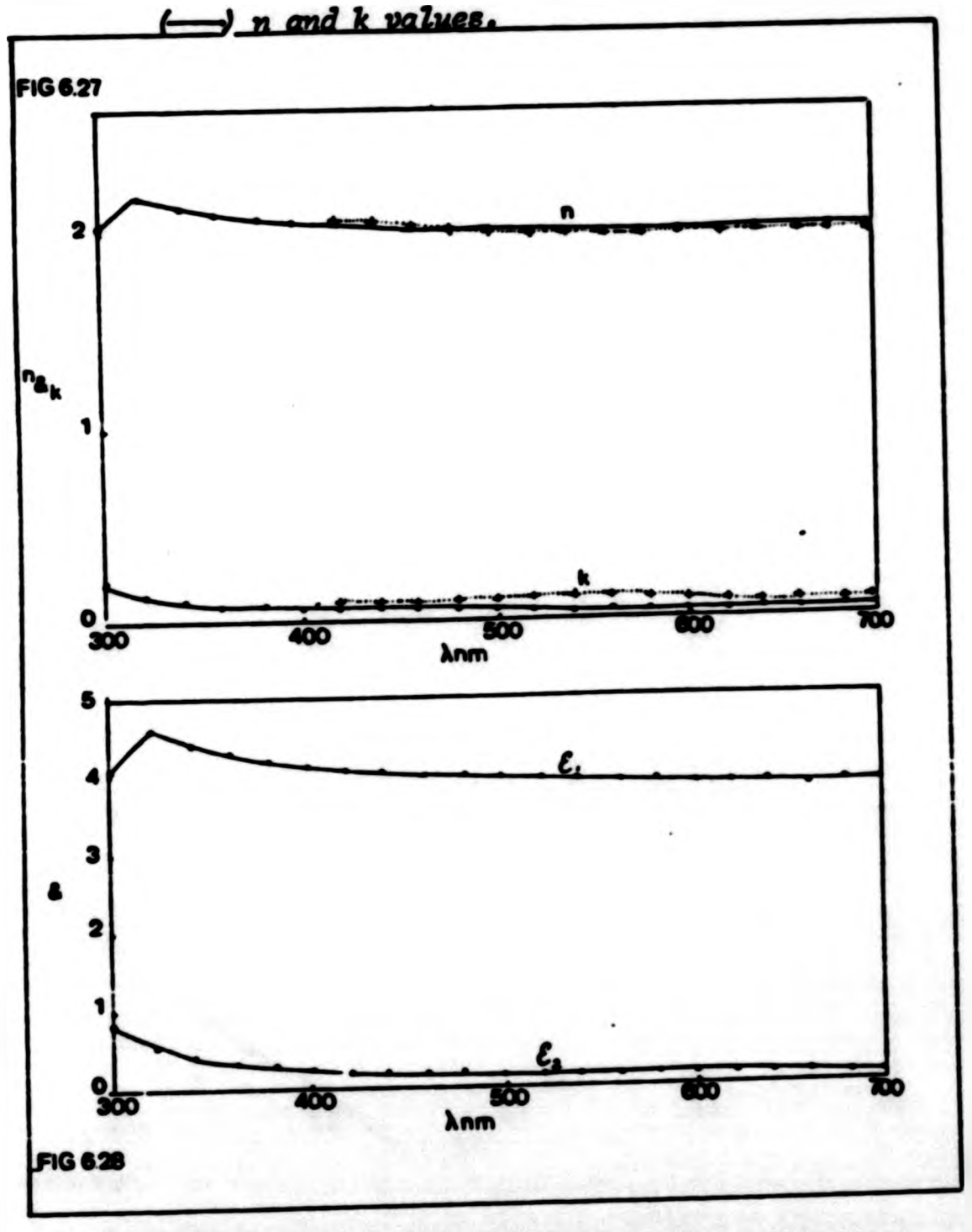

Fig 6.28 Ellipsometric ε_1 and ε_2 values for cassiterite.

Table 6.13 Electron Probe Analysis of Cassiterite

MINERAL NAME: Cassiterite			
ELEMENT	Wt%	ATOMIC RATIO'S	ELEMENT LINE
Sn	78.30	0.99	Sn La
O	21.37	2.00	By difference
Total	100.00		
CALCULATED FORMULA: $Sn_{0.99}O_{2.00}$			
Formula based on $\Sigma O_{atoms}=2$			
TRACE ELEMENTS: Ti=0.25wt%			
Cu=0.08wt%			

Table 6.14 Summary of cassiterite data

MINERAL NAME:Cassiterite IDEAL FORMULA:SnO_2 LOCALITY:Slavkov,Bohemia,E1006 CRYSTAL SYSTEM:Tetragonal, no detectable anisotropy

X-RAY ANALYSIS:Sn=78.3wt% O=21.37wt% trace copper and titanium REAL FORMULA:$Sn_{0.99}O_2$

OPTICAL DATA:
Standard:SiC

Reflectance%

λ nm	ELL Air	MP Air	MP Oil	ELL n	MP n	ELL k	MP k	ELL ε_1	ELL ε_2
300	11.96			2.02		0.23		4.04	0.92
320	13.69			2.16		0.15		4.65	0.66
340	13.06			2.12		0.12		4.49	0.51
360	12.63			2.10		0.10		4.38	0.43
380	12.29			2.07		0.09		4.29	0.39
400	12.02	12.39	2.27	2.06	*	0.08	*	4.22	0.33
420	11.78	12.08	2.20	2.04	2.06	0.07	0.08	4.16	0.30
440	11.60	11.82	2.11	2.03	2.04	0.07	0.08	4.12	0.27
460	11.44	11.64	2.06	2.02	2.03	0.06	0.09	4.08	0.24
480	11.31	11.43	1.99	2.01	2.01	0.06	0.10	4.04	0.23
500	11.19	11.26	1.94	2.00	2.00	0.05	0.11	4.01	0.22
520	11.10	11.11	1.91	2.00	1.99	0.05	0.12	3.99	0.21
540	11.02	10.99	1.88	1.99	1.98	0.05	0.13	3.97	0.20
560	10.99	10.90	1.85	1.99	1.97	0.05	0.14	3.96	0.21
580	10.95	10.84	1.83	1.99	1.97	0.05	0.13	3.94	0.21
600	10.89	10.81	1.82	1.98	1.97	0.05	0.12	3.93	0.21
620	10.84	10.79	1.80	1.98	1.97	0.05	0.10	3.92	0.21
640	10.82	10.76	1.80	1.98	1.97	0.05	0.11	3.91	0.21
660	10.78	10.71	1.80	1.98	1.96	0.05	0.11	3.90	0.21
680	10.77	10.70	1.79	1.97	1.96	0.05	0.11	3.90	0.21
700	10.77	10.65	1.78	1.98	1.96	0.05	0.11	3.90	0.21

* denotes imaginary solutions

OTHER DATA:Specimen shows two distinct twin planes.

CIE Colour Co-ordinates

		MP Air	MP Oil	ELL Air
Illuminant C				
	x	0.3036	0.2992	0.3055
	y	0.3084	0.3030	0.3108
	z	0.3880	0.3978	0.3837
Luminance	Y	10.97	1.87	11.01
	Pe%	3.30	5.57	2.28
	D_λ	473.6	473.5	473.7
Illuminant A				
	x	0.4419	0.4380	
	y	0.4048	0.4028	
	z	0.1533	0.1592	
Luminance	Y	10.91	1.85	
	Pe%	1.49	2.49	
	D_λ	486.7	486.1	
Illuminant D_{65}				
	x	0.3063	0.3019	
	y	0.3214	0.3161	
	z	0.3723	0.3820	
Luminance	Y	10.96	1.87	
	Pe%	3.14	5.31	
	D_λ	475.2	474.9	

6.10 Cuprite

6.10.1 Introduction

The sample of cuprite comes from near Windhoek, Namibia, (BM 1974, 411; E1007). An initial examination of the mineral reveals that its outer edges are coated with fine grains of malachite fig. 6.29. The cuprite itself is silvery-blue in appearance, and has a metallic lustre, and is semi-transparent appearing red in transmission. When the polished mineral surface was examined in reflected light a slight anisotropy was detectable. Measurements were therefore made at the two positions where a maximum and a minimum were registered on the DVM at 560 nm. The detected anisotropy is very small and is barely visible under crossed polars. Reflected light observations also revealed deep red internal reflections in some areas of the specimen. These areas along with others where surface imperfections were present were carefully avoided when making microphotometric and ellipsometric measurements.

The cuprite was ground and polished (section 3.5), and buffed gently with gamma-alumina. Apart from the malachite rim, the sample appears free from any mineral inclusions. The surface is, however, cut by several fine fractures.

The surface does not show any appreciable tarnishing, and measurements made immediately after and six weeks after polishing do not show any appreciable differences. It thus seems likely that a thin stable surface-film appears instantaneously after polishing and that further tarnishing only becomes apparent if the sample has been left undisturbed for a very long time, or if it has been left in a warm moist environment (which is condusive to rapid tarnishing).

6.10.2 Electron Probe Analyses

The electron probe analysis revealed that the mineral was pure cuprite and was free from any trace of impurities. Table 6.15 displays the cuprite analysis together with the X-ray element lines used in the determination. The formula of the mineral is calculated from the data.

6.10.3 Reflectance, n, k, ε_1 and ε_2

The microphotometric air and oil reflectance curves are displayed in fig. 6.30 together with the ellipsometric air values. Fig. 6.31 shows the derived values of n and k for both techniques, and fig. 6.32 displays the ellipsometric ε_1 and ε_2 values. The above data together with the CIE colour coordinates for illuminants C, A and D_{65} are shown in table 6.16.

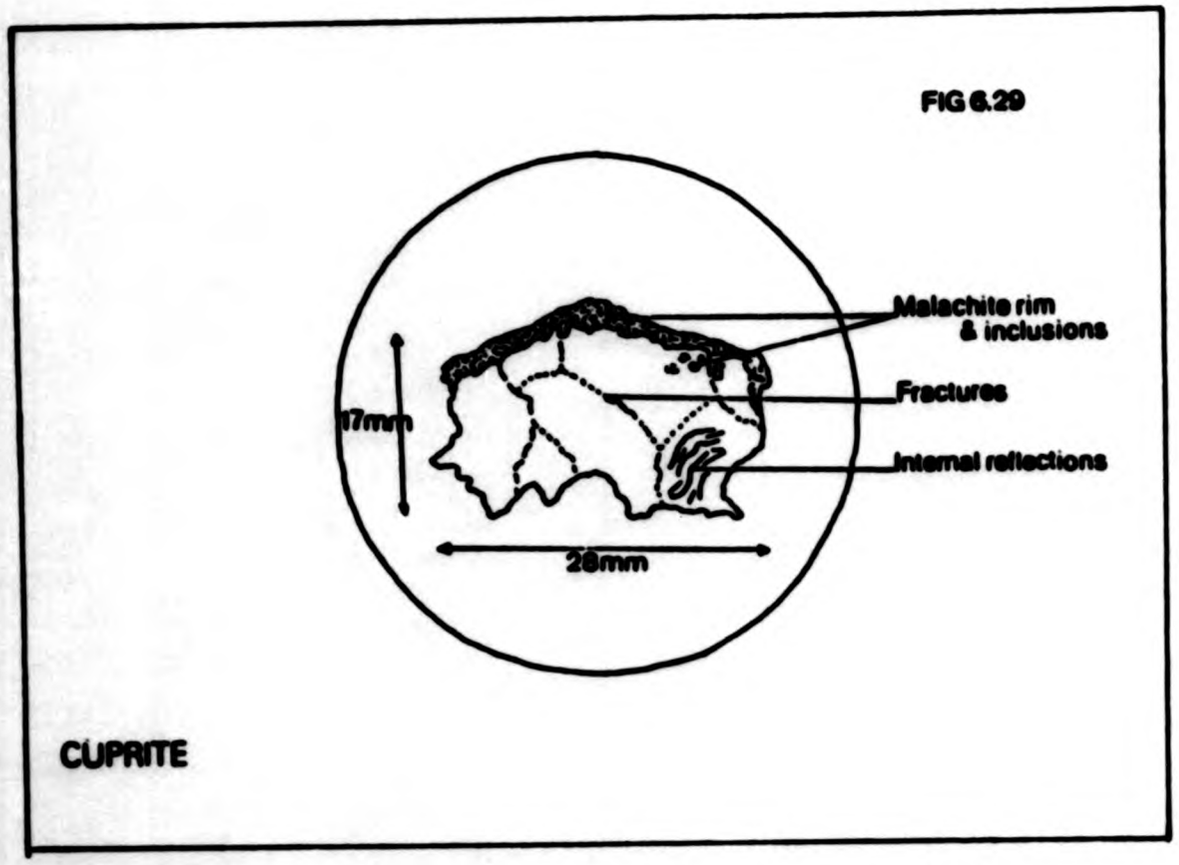

Fig 6.29 Cuprite specimen directly after polishing.

FIG 6.30

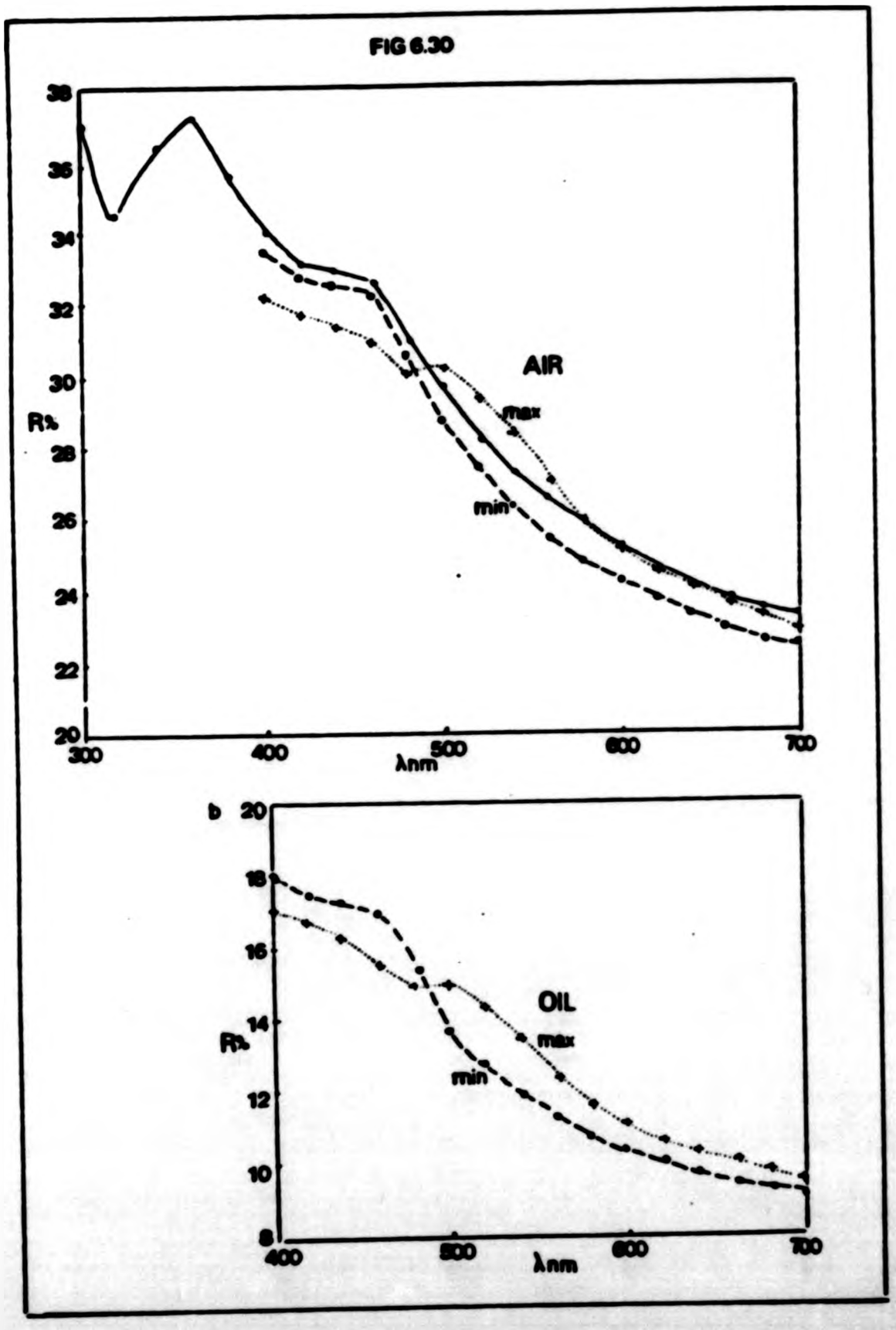

Fig 6.30 a, Comparison of microphotometric maximum (·····), minimum (– – –) and ellipsometric (——) reflectance dispersion curves for cuprite in air.
b, Microphotometric maximum (·····) and minimum (– – –) reflectance dispersion curves for cuprite in oil.

Fig 6.31 Comparison of microphotometric maximum (·····) ,minimum (- -) and ellipsometric (——) n and k values for cuprite.

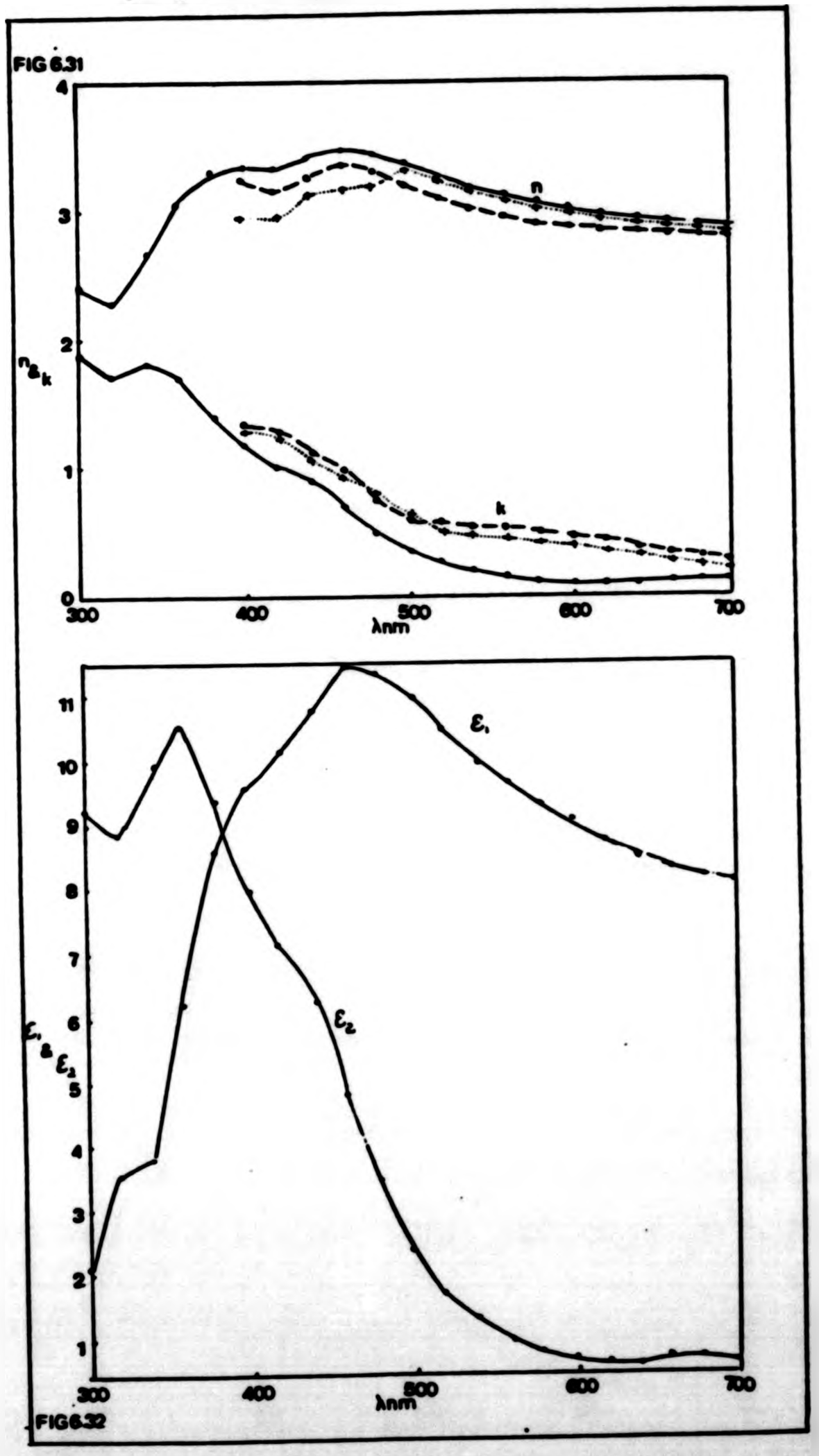

Fig 6.32 Ellipsometric ε_1 and ε_2 values for cuprite.

Table 6.15 Electron Probe Analysis of Cuprite

MINERAL NAME: Cuprite			
ELEMENT	Wt%	ATOMIC RATIO'S	ELEMENT LINE
Cu	88.04	1.85	Cu Kα
O	11.96	1.00	By difference
Total	100.00		
CALCULATED FORMULA: $Cu_{1.85}O_{1.00}$			
Formula based on $\Sigma O_{atoms}=1$			
TRACE ELEMENTS: None detected			

Table 6.16 Summary of cuprite data

MINERAL NAME:Cuprite IDEAL FORMULA:Cu_2S LOCALITY:Windhock,SW Africa CRYSTAL SYSTEM:Cubic,specimen shows slight anisotropy.

X-RAY ANALYSIS:Cu=88.04wt% O=11.96wt%,no other elements detected REAL FORMULA:$Cu_{1.85}O$

OPTICAL DATA:
Standard:WTiC

	Reflectance %													CIE Colour Co-ordinates				
λ	ELL	MP max	MP min	MP max	MP min	ELL	MP max	MP min	ELL	MP max	MP min			MP max	MP max	MP min	MP max	ELL
nm	Air	Air	Air	Oil	Oil	n	n	n	k	k	k	c_1	c_2	Air	Oil	Air	Oil	Air
300	37.06					2.41			1.92			2.14	9.27					
320	34.51					2.54			1.73			3.49	8.78					
340	36.31					2.67			1.82			3.82	9.70					
360	37.24					3.06			1.74			6.33	10.64					
380	35.60					3.27			1.44			8.58	9.44					
400	34.02	32.14	33.47	17.22	18.08	3.32	2.97	3.25	1.21	1.32	1.21	9.57	8.03					
420	33.06	31.71	32.66	16.88	17.56	3.34	2.97	3.12	1.06	1.28	1.25	10.04	7.07					
440	32.94	31.37	32.56	16.37	17.35	3.42	3.12	3.25	0.93	1.10	1.11	10.82	6.36					
460	32.33	30.85	32.26	15.84	17.03	3.48	3.18	3.30	0.71	0.96	0.99	11.59	4.95					
480	30.87	30.08	30.52	15.15	15.44	3.42	3.18	3.27	0.51	0.84	0.77	11.42	3.47					
500	29.56	30.05	28.71	15.04	13.89	3.33	3.27	3.18	0.38	0.69	0.62	10.98	2.54					
520	28.30	29.33	27.38	14.39	12.81	3.25	3.26	3.08	0.28	0.54	0.56	10.47	1.80					
540	27.34	28.19	26.33	13.46	12.01	3.18	3.17	2.99	0.22	0.51	0.55	10.03	1.40					
560	26.64	26.89	25.44	12.44	11.34	3.12	3.07	2.92	0.16	0.49	0.54	9.73	1.01					
580	25.80	25.90	24.72	11.66	10.79	3.06	3.00	2.88	0.13	0.45	0.50	9.33	0.81					
600	25.13	25.19	24.17	11.11	10.38	3.00	2.95	2.84	0.13	0.43	0.47	9.01	0.78					
620	24.52	24.58	23.71	10.64	10.01	2.96	2.91	2.83	0.12	0.38	0.42	8.72	0.73					
640	24.10	24.08	23.31	10.26	9.71	2.92	2.88	2.81	0.12	0.35	0.39	8.52	0.75					
660	23.74	23.69	22.97	9.95	9.45	2.89	2.86	2.79	0.13	0.30	0.36	8.36	0.76					
680	23.44	23.30	22.66	9.65	9.20	2.87	2.84	2.78	0.14	0.25	0.30	8.22	0.78					
700	23.33	22.93	22.35	9.39	8.99	2.86	2.81	2.76	0.14	0.26	0.30	8.17	0.80					
Illuminant C																		
	x													0.2910	0.2774	0.2864	0.2702	0.288
	y													0.3030	0.2915	0.2911	0.2721	0.29
	z													0.4061	0.4311	0.4225	0.4577	0.41
Luminance	Y													27.23	12.74	25.93	11.73	26.8
	Pe%													8.41	14.63	11.53	19.69	10.2
	D_λ													482.2	481.3	476.6	475.7	477.
Illuminant A																		
	x													0.4276	0.4126	0.4251	0.4081	
	y													0.4057	0.4026	0.3986	0.3900	
	z													0.1667	0.1848	0.1763	0.2019	
Luminance	Y													26.59	12.22	25.31	11.24	
	Pe%													4.81	8.47	5.73	10.16	
	D_λ													493.2	492.5	487.8	487.1	
Illuminant D_{65}																		
	x													0.2935	0.2799	0.2891	0.2730	
	y													0.3164	0.3054	0.3044	0.2855	
	z													0.3900	0.4147	0.4064	0.4415	
Luminance	Y													27.26	12.76	25.93	11.73	
	Pe%													8.13	14.16	11.11	19.01	
	D_λ													483.2	482.6	477.8	476.9	

OTHER DATA:Malachite rim around edge of specimen.

6.11 Iridium and Platinum Iridium Alloys

6.11.1 Introduction

The reason for investigating the optical properties of iridium and platinum-iridium alloys was to assess their suitability as temporary high reflectance standards. Originally we had hoped to obtain either some osmi-iridium or some platinum-arsenide (sperrylite) but due to the toxicity of osmium and the commercial non-viability of platinum-arsenide this was not possible. Unfortunately, the softness of iridium and the platinum-iridium alloys precludes their usefulness as standards. However, with careful handling it was felt that they could be used, temporarily, until the development of harder high reflectance standards.

As all the reflectivity standards currently in use in the Western world were either directly calibrated at the National Physical Laboratory (NPL), or else calibrated from an NPL standard, it was decided to approach NPL with a view to their calibrating one of our samples. This aim was accomplished with both ultra-violet, visible, reflectance and ellipsometric measurements being made on the platinum-iridium alloy, with an iridium content of 25 wt per cent.

6.11.2 Surface Preparation

The surface preparation of the iridium, and platinum-iridium alloys was slightly different from that described in section 3.5. This was due to the high cost of the iridium and platinum, and thus, grinding and mechanical polishing of the alloys was carried out by Johnson-Matthey Ltd.

6.11.3 Results

Four specimens were prepared and polished by Johnson-Matthey, these were:

i) Specimen 1. Pure iridium

ii) Specimen 2. Platinum-iridium with an iridium content of 25 wt%.

iii) Specimen 3. Platinum-iridium with an iridium content of 20 wt%.

iv) Specimen 4. Platinum-iridium with an iridium content of 10 wt%.

Fig. 6.33 shows a comparison of the reflectance dispersion curves for specimens 1, 2 and 4. As the reflectance curve for specimen 3 coincides with that of specimen 2 over a large wavelength range for reasons of clarity it was excluded from this study.

A comparison of the reflectance data for specimen 2 using a variety of measurement techniques can be found in fig. 6.34, namely;

i) Microscope photometry over a wavelength range of 400 - 700 nm inclusive (NHM),

ii) Ellipsometry over a range of wavelengths from 300 - 700 nm inclusive (CLP), with $\theta = 75°$,

iii) Ellipsometry at a single wavelength of 546 nm, $\theta = 65°$ (NPL),

iv) Visible and ultra-violet reflectometry over a wavelength range 400 - 700 nm (NPL) $\theta = 10°$.

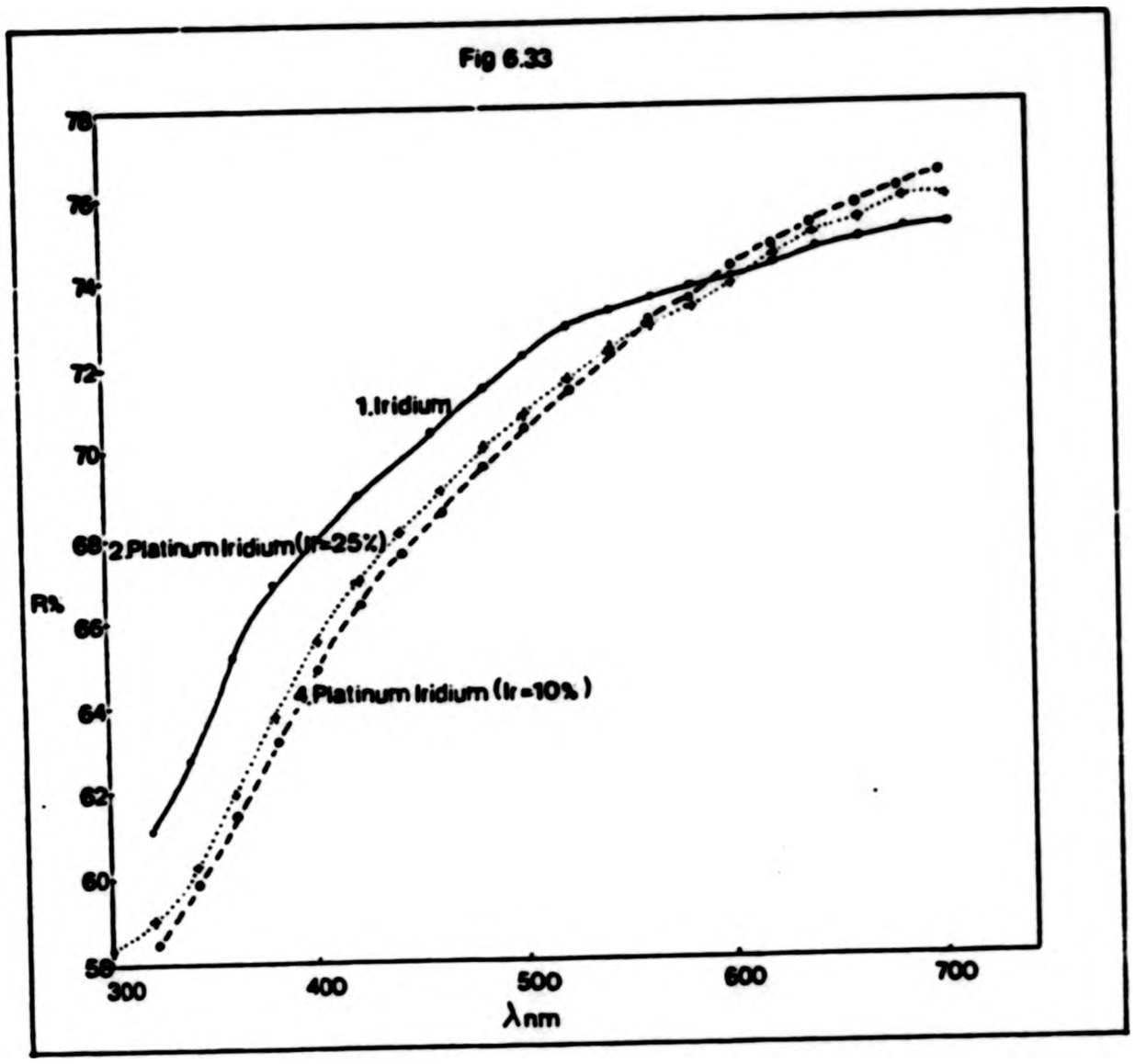

Fig 6.33 Reflectance dispersion curves for :

(——) 1.Pure iridium
(·····) 2.Platinum-iridium (Ir content - 25wt%)
(- - -) 4.Platinum-iridium (Ir content - 10wt%)

FIG 6.34

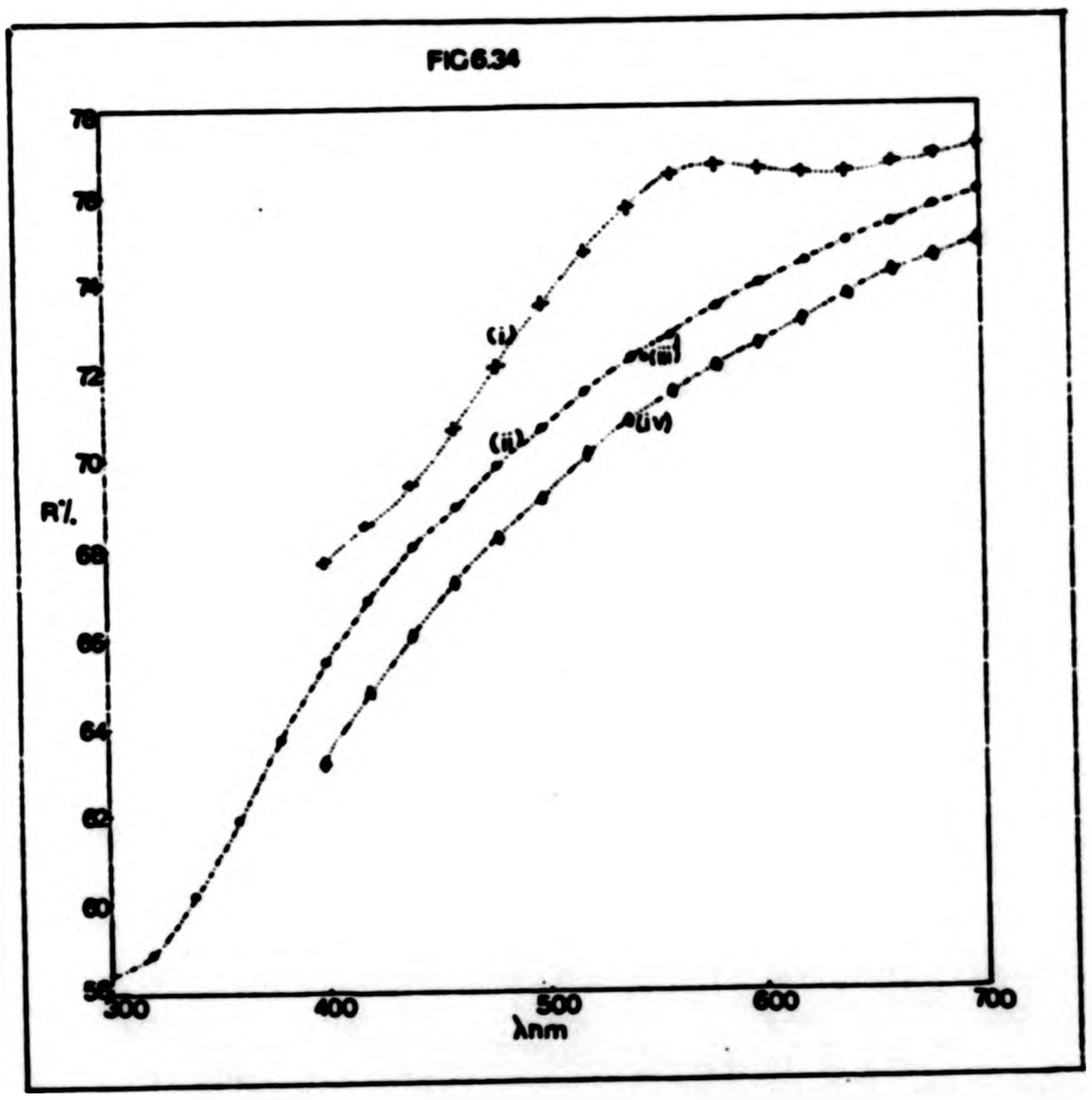

Fig 6.34 Reflectance dispersion curves for platinum-iridium (Ir content - 25wt%) measured by:

i), Microphotometry at N.E.N. (400-700 nm)

ii), Ellipsometry at C.L.P. (350-700 nm)

iii), Ellipsometry at N.P.L. (546 nm)

iv), Visible-ultra-violet reflectometry N.P.L. (400-700 nm)

CHAPTER SEVEN
DISCUSSION

7.1 Introduction

The previous chapter contains the results for the group of minerals used in this study. In this chapter these results are analysed and the differences between the ellipsometric and microphotometric data discussed. Comparison of the measured data is also made with the published results of other workers. The reflectance, n, k, ε_1 and ε_2 dispersion curves are analysed and where possible peaks are assigned to electronic, excitonic, defect and foreign-ion phenomena, using crystal-field, molecular-orbital, band and group theories.

7.2 Comparison of Microphotometric and Ellipsometric Measurement Techniques

7.2.1 Size of Measured Area and Angle of Incidence

Before proceeding to a discussion of the results it is necessary to emphasise the major differences between the two measurement techniques. The design and construction of the ellipsometer means that fairly large areas of surface must be measured, this is because of the size of the light spot on the specimen surface. The size of this spot is governed by two factors:

i) The angle of incidence, which is usually set to 75°. Reducing the angle of incidence does reduce the size of the light spot, however, angles less than 65° are unattainable unless major adjustments and realignments are made to the instrument. Moreover the equipment was designed and aligned to operate most accurately and efficiently at 75°.

ii) The size of the light spot can be reduced by reducing the aperture of the iris. Closing down the iris too far, however, has a detrimental effect on the accuracy of the readings as it makes primary alignment of the specimen virtually impossible and severely limits the amount of light reaching the photomultiplier.

Thus for practical purposes a mineral with a minimum homogeneous surface area of 1 cm^2 is desirable. The microscope-photometer, however can measure smaller areas down to a 10 μm diameter spot. One of the differences between the two techniques is the angle of the light incident upon the specimen surface. Most ellipsometric measurements (as mentioned previously) are made at oblique incidence ($\theta = 75°$), whereas microphotometric data are gathered at near-normal incidence.

7.2.2 Derivation of Reflectance and Other Optical Parameters

Another distinction between the two techniques arises from the differences in the measured quantities. The microphotometric data is obtained by comparing the light intensity reaching the photomultiplier from the specimen, with that arriving from a precalibrated standard, the ratio of which when multiplied by the standard's reflectance gives the reflectivity of the specimen. The basis for the ellipsometric measurements, however, is the relative displacements of the analyser and polariser prisms from pre-set fiducials. Thus the measured quantity is an angular displacement rather than light intensity. From this the relative phase shifts and amplitude changes and subsequently ε_1, ε_2, n, k and reflectivity can be calculated without using a standard.

The fact that two different quantities are being measured, highlights another important difference between the two techniques. In microscope-photometry, reflectance is the measured parameter, whereas in ellipsometry it is the last quantity to be derived. Thus while microphotometric n and k values are derived from measured reflectances, the ellipsometric reflectance value is calculated from previously derived n and k values (section 2.2.5).

7.2.3 Sensitivity Range Across the Spectrum

When looking at both the ellipsometric and microphotometric data it is important to remember that the accuracy of the readings is not constant across the spectrum. Above 600 nm the efficiency of the water modulating cores on the ellipsometer is dramatically reduced (section 3.4.2). Readings made on the ellipsometer between 600 - 700 nm

should therefore be regarded as suspect. Thus the maximum sensitivity and consequently the most reliable and reproducible data can be found in the wavelength range 350 - 550 nm.

With the microscope photometer the case is somewhat different, as both the sensitivity range of the instrument and the necessity of making all measurements at the same Digital Voltmeter (DVM) setting have to be taken into account. The latter ensures the intensity measurements are comparable. The optimum DVM setting is obtained by driving the system to its most sensitive spectral region (560 nm), then adjusting the amplifier gain until the DVM reads between 1700 and 1800 (arbitrary units), for the higher reflecting material (specimen or standard). As reflectance values are derived from a comparison of the reflected light intensities, the most accurate measurements will be achieved when comparing two four-significant-figure numbers. When it is only possible for two, two-significant-figure numbers to be compared the accuracy of the measurements will be decreased correspondingly. Thus the accuracy of the reflectance values depends on the sensitivity range of the photodetector (S20). In this case the maximum sensitivity is to be found in the middle of the spectrum. This fact can be demonstrated by examining the reflectivity of aluminium using a tungsten titanium carbide standard (table 7.1). Here a change of 1 in the DVM reading at 400 nm can cause the reflectivity to vary by more than 1%. At 560 nm, however, a change of 2 in the DVM response caused only a 0.1% variation in reflectivity. It should also be noted that microphotometric measurements carried out at 420 nm were suspect because of a pin hole in the interference filter.

7.3 Chalcosine

7.3.1 Introduction

Electron probe microanalysis of the mineral, specimen number BM; 1964R, 385, section number E720, described as chalcosine reveals the bulk of the specimen to be composed entirely of copper and sulphur, with traces of arsenic detectable around the rim. The analysis gives the formula $Cu_{1.9658}$ and as this lies within the narrow chalcosine solid solution field, it seems likely that the mineral is chalcosine.

Table 7.1. Microphotometric measurements on a deposited aluminium film using a WTiC standard. This shows the effects of a small change in the spectral response of the DVM on the measured reflectivity for a series of measurements on various parts of the specimen and standard.

λ	DVM reading		Calc.	DVM reading		Calc.	DVM reading		Calc.	Calibrated values of WTiC standard.
nm	Al	WTiC	R%	Al	WTiC	R%	Al	WTiC	R%	
400	0082	0041	90.00	0079	0041	86.70	0081	0041	88.90	45.00
420	0281	0140	90.78	0276	0139	89.91	0278	0139	90.46	45.23
440	0519	0257	91.89	0517	0256	91.89	0515	0256	91.53	45.50
460	0772	0384	92.24	0769	0382	92.36	0766	0382	92.00	45.88
480	1027	0512	92.85	1022	0508	93.13	1019	0509	92.67	46.29
500	1311	0656	93.37	1305	0651	93.66	1301	0653	93.08	46.72
520	1574	0793	93.67	1566	0788	93.78	1563	0788	93.60	47.19
540	1758	0894	93.76	1750	0887	94.07	1745	0888	93.70	47.68
560	1755	0904	93.59	1745	0898	93.68	1743	0898	93.57	48.21
580	1634	0855	93.28	1626	0850	93.37	1622	0849	93.25	48.81
600	1375	0734	92.71	1372	0731	92.89	1366	0730	92.61	49.49
620	1128	0613	92.37	1122	0608	92.64	1115	0609	91.91	50.20
640	0903	0503	91.38	0902	0500	91.82	0897	0500	91.31	50.90
660	0723	0412	90.53	0722	0408	91.29	0717	0409	90.44	51.59
680	0624	0367	88.94	0623	0360	90.52	0619	0360	89.94	52.31
700	0603	0357	89.52	0602	0354	90.13	0599	0354	89.48	53.00

7.3.2 Comparison of Microphotometric and Ellipsometric Data

In Fig. 6.2 the reflectance profiles for chalcosine measured microphotometrically in air and oil and ellipsometrically in air are given. Comparison of the ellipsometric and microphotometric results reveals that except for the readings at 400 and 420 nm the two sets of data are in remarkably good agreement. The disparities between the data at 400 nm and 420 nm are expected as the microscope photometer is known to give erroneous results at these wavelengths. It is interesting to note that at these two wavelengths the dispersion of the oil immersion data bears a closer resemblance to the ellipsometric reflectance profile than the microphotometric air data.

As chalcosine has a reflectance only slightly lower than that of the standard, (tungsten-titanium-carbide) the effects of the SSRDP (section 5.2) will be negligible in comparison to experimental error, and so need not be considered.

The disparities between the ellipsometric and microphotometric n and k values can be explained by their different methods of calculation. The ellipsometric values are derived from the angular displacements of the analyser and polariser prisms, the measurement of which defines the accuracy of the derived parameters and shows very little variation across most of the visible range. The limitations of deriving n and k values from microphotometrically measured air and oil reflectances are described in section 2.2.4. Figure 2.6 shows that under some experimental conditions, slight inaccuracies in determining the reflectance of standard and/or specimen in air and/or oil can dramatically alter the derived n and k values, especially when k is close to zero. As the experimental accuracy of the technique is limited to $\pm$ 0.5% such changes are often sufficient to account for unexpected dips in the n and k dispersions such as those seen in Figure 6.3.

The microphotometric n values are higher throughout the spectrum than the ellipsometric ones. The reverse is true for k where the microphotometric values are correspondingly lower in value than the ellipsometric ones. This effect can also be explained by the method of calculation which

uses a pair of simultaneous equations if the value of n is too high the value of k will correspondingly be too low.

7.3.3 Comparison of Data with Literature Results

The complexity of the structure of chalcosine and the number of nearby copper sulphide phases in this region of the Cu-S phase diagram mean there are very few consistent data in the literature relating to the optical properties of the mineral. The data displayed in table 7.2 come from the IMA.COM data file and the work of Bowie, Simpson and Auld (1978).

There are small differences between the results presented here and those for chalcosine listed in the data file. This could be due in part to compositional differences as the data file specimen apparently contains traces of silver, aluminium, silicon, titanium, magnesium and calcium, but could also be related to the apparent differences in anisotropy between the specimens.

7.3.4 Electronic and Optical Properties

Very little is known about the band structures of chalcosine, this again is probably due to the mineral's crystallographic complexity. It is known, however, that natural chalcosines consistently display p-type semi-conductor behaviour, the mechanism for which appears to be via copper vacancies acting as acceptor defects. Chalcosine is thought to have an indirect absorption edge because an electronic transistion from the valence band into the conduction band necessitates a change in the value of the wavevector $\vec{K}$. The magnitude of the band gap is estimated as between 1.1 and 1.4 eV by Mulder (1973) and is dependent on the plane of polarisation of the incident light.

Eisenmann (1952) and Abdullaev *et al.*: (1968) have noticed strong optical absorptions in the visible spectrum of chalcosine, which they attribute to interband electronic transitions. They have found that these transitions begin at 689 nm (1.8 eV) and increase rapidly with increasing photon energy upto at least 413 nm (3 eV) and are essentially independent of the polarisation state of the incident light. Examination

Table 7.2. Comparison of reflectance data from this study for chalcosine with literature values.

λ nm	Reflectance in air						Reflectance in oil				
	1	2	3Ra	3Rb	3Rc	4	2	3Ra	3Rb	3Rc	4
400	34.67	36.83	37.00	36.90	36.80	29.80	20.76	22.05	21.85	21.80	12.80
420	35.30	36.41	37.75	37.57	37.45	29.40	21.06	22.30	22.20	22.15	11.60
440	35.41	36.07	37.67	37.57	37.57	28.60	20.67	22.15	22.15	22.30	10.70
460	35.06	35.60	37.05	37.07	37.20	27.60	20.12	21.60	21.60	21.75	10.10
480	34.44	34.85	36.15	36.15	36.15	26.60	19.39	20.85	20.85	20.90	9.60
500	33.65	33.94	35.55	35.55	35.40	25.50	18.51	20.05	20.00	19.95	9.10
520	32.77	32.91	34.70	34.70	34.40	24.40	17.58	19.20	19.15	19.00	8.60
540	31.91	31.88	33.70	33.70	33.50	23.40	16.70	18.50	18.30	18.10	7.90
560	30.97	30.98	32.82	32.85	32.50	22.30	15.93	17.75	17.55	17.30	7.40
580	30.08	30.27	32.07	32.15	31.77	21.40	15.24	17.15	17.10	16.70	6.90
600	29.57	29.67	32.32	31.47	31.20	20.50	14.84	16.60	16.60	16.20	6.40
620	28.93	29.14	30.75	30.82	30.70	19.60	14.38	16.05	16.05	15.85	5.90
640	28.39	28.62	29.95	30.05	30.30	18.80	13.91	15.55	15.55	15.55	5.40
660	27.81	28.07	29.50	29.60	30.10	17.90	13.46	15.20	15.20	15.30	5.00
680	27.22	27.57	29.20	29.20	29.72	17.00	13.03	14.90	14.80	15.15	4.60
700	26.78	27.10	28.95	28.95	29.62	16.20	12.63	14.55	14.40	15.10	4.30

λnm	470	546	589	650
5	36.60-36.70	31.90	31.05-31.20	29.70-29.90

1. Ellipsometric measurements on chalcosine, this study
2. Microphotometric measurements on chalcosine, this study.
3. Reflectance measurements on chalcosine, COM,IMA data file using SiC standard P.R.Simpson.
4. Reflectance measurements on digenite, COM.IMA data file using SiC standard P.R.Simpson.
5. Reflectance measurements on chalcosine at selected wavelengths, Bowie, Simpson and Auld XI meeting IMA Novosibirsk.

of the reflectance profile of the chalcosine specimen in this study reveals essentially the same pattern, with reflectance rising rapidly from 700 to 400 nm after which it declines with equal rapidity into the ultra-violet. A similar feature is observed in the dispersions of k (fig. 6.3) and ε_2 (fig. 6.4), while n (fig. 6.3) and ε_1 (fig. 6.4) rise very slowly from 700 - 540 nm after which they decline rapidly.

7.4 Galena

7.4.1 Introduction

Electron probe microanalysis of the galena specimen, section number E1004, used in this study shows it has the formula $Pb_{1.04}S$ which agrees well with that for pure galena of PbS. The analysis also reveals traces of copper and bismuth which appear to be homogeneously distributed throughout the specimen.

7.4.2 Comparison of Microphotometric and Ellipsometric Data

Examination of fig. 6.6 shows that the ellipsometric and microphotometric reflectance data are in very good agreement throughout most of the spectrum. As the reflectivity of galena is very close to that of the standard tungsten-titanium-carbide (especially in the middle of the spectrum) the effects of the SSRDP (section 5.2) will be negligible and so need not be taken into account. At the blue end of the spectrum the ellipsometric and microphotometric measurements show a difference of approximately 0.15%, the latter having the higher magnitude. At the red end, although the microphotometric data are still higher, the difference has increased to 0.3%.

Even though these differences lie within the range of experimental error, for both techniques $\pm$0.5%, it should be remembered that the ellipsometric measurements between 600 and 700 nm are unreliable (section 7.2.3). This effect is not so marked for galena as for some other minerals as the analyser and polariser are not required to undergo large azimuthal changes.

The microphotometrically derived n values (fig. 6.7) are approximately 0.4 lower than the ellipsometric ones whereas the k values (fig. 6.7) are 0.3 higher. These disparities serve to illustrate what can happen when tiny errors are present in R and ^{im}R. Such errors may arise from the presence of tiny surface scratches (galena is a very soft mineral) the light scattering effects of which have been shown by Piller and Von Gehlen (1964) to exert a more irregular influence on measurements made in oil than on those made in air. The lumpy appearance of the microphotometric dispersion curves is probably due to the different scratch-induced light-scatter effects in air and oil and the ill conditioning of the equations used in the derivation of the n and k values section 7.3.2.

7.4.3 Comparison of Data with Literature Results

During the course of the last two and a half decades galena and the isostructural lead chalcogenides clausthalite (PbSe) and altaite PbTe, have been extensively studied. This is primarily because of their technological importance as detectors and emitters of infra-red and visible radiation. The vast majority of these studies were undertaken in the late 1950s and early 1960s before the lead chalcogenides were superseded by more modern materials. The somewhat unusual properties and the ready synthesis of galena, clausthalite and altaite, however, have meant that they still retain the academic interest of many workers. In fig. 7.1 and table 7.3 some of these results, on synthetic and natural galenas, are displayed, and compared with the results obtained in this study.

Cardonna and Greenaway (1964) studied the surface reflectivity of cleaved single crystals of galena over a wide spectral range (1-25 eV). The results they obtained are somewhat at odds with those of this study, especially at the red end of the spectrum. Several hypotheses can be advanced as to why this is so: Firstly their specimen was synthetic and presumably pure, whereas that used in this study is natural and contains trace impurities. Secondly they measured a cleaved not a polished surface which could have had serious mosaic defects. Thirdly, and most importantly, their measurements were made over twenty years ago when instrumental measurement techniques lacked much of the sophistication present today, especially over large wavelength ranges.

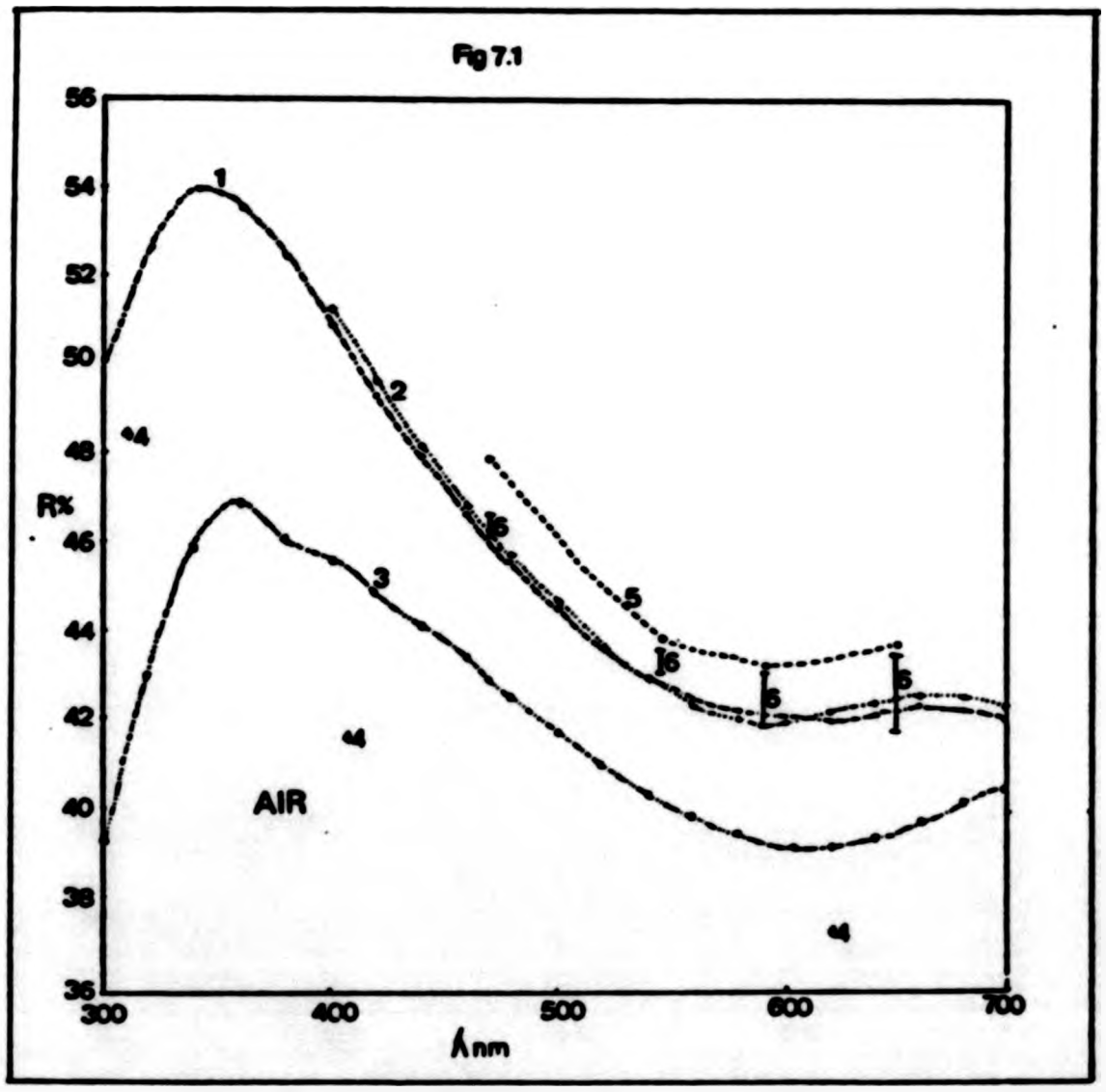

Fig. 7.1 Comparison of ellipsometric and microphotometric reflectance data for galena with literature results.

1. *Ellipsometric results this study.*
2. *Microphotometric results this study.*
3. *Results of Vendrell-Saz et al. (1978).*
4. *Results of Cardonna and Greenaway (1964)*
5. *Results of Utenbogaart and Burke (1971).*
6. *Results of Bowie, Simpson and Auld (1978).*

Table 7.3. Comparison of reflectance data from this study for galena with literature values.

λ	Reflectance in air					
nm	1	2	3	4	5	6
248				39.49		
260			29.12			
280			35.00			
300	49.89		39.20			
309				48.61		
320	52.58		42.96			
340	53.86		45.63			
360	53.60		46.77			
380	52.51		46.07			
400	50.91	51.20	45.58			
413				41.77		
420	49.38	49.67	44.91			
440	47.96	48.17	44.19			
460	46.71	46.90	43.39			
470			42.99		47.90	46.20-46.60
480	45.61	45.76	42.59			
500	44.60	44.69	41.78			
520	43.66	43.72	41.02			
540	43.03	42.98	40.38			
546					43.80	43.10-43.60
560	42.56	42.43	39.87			
580	42.29	42.13	39.48			
589					43.10	41.90-43.00
600	42.14	42.03	39.23			
620	42.04	42.18	39.17	36.46		
640	42.18	42.35	39.36			
650			39.52		43.70	41.80-43.50
660	42.38	42.53	39.70			
680	42.25	42.55	40.20			
700	42.04	42.33	40.46			

1. Ellipsometric measurements on galena, this study.
2. Microphotometric measurements on galena, this study.
3. Results of Vendrell-Saz et al.(1978) for galena.
4. Results of Cardonna & Greenaway (1964) for a cleaved surface of synthetic galena.
5. Results of Uytenbogaart & Burke (1971) for galena.
6. Results of Bowie, Simpson & Auld (1978) for galena.

The results of Vendrell-Saz et al. (1978) are also lower in magnitude than those of this study but, as they point out, their results are also lower than most of those published. They attribute this fact to a scratched specimen surface and/or compositional differences. Apart from these results the data presented here are in very good agreement with those of other authors and lie well within the reflectance ranges of Bowie, Simpson and Rudd (1978).

7.4.4 Electronic and Optical Properties

Galena has a very narrow band gap 0.37 eV and can exhibit both n and p-type semi-conductor behaviour. As p-type galenas have a higher resistivity than n-types (Shuey, 1975) and as the electron and positive hole mobilities are approximately equal it must be assumed that the n-type galenas have a higher carrier concentration than the p-types and consequently a higher reflectivity. Thus the galena specimen in this study, by virtue of its slight cation excess, would tentatively be expected to lie somewhere between the middle and the higher end of the Bowie - Simpson (1978) reflectance range, which in fact it does.

Problems, primarily due to the large spin-orbit-coupling of lead, have made the determination of the band structure of galena very difficult, and early calculations bore little resemblance to the experimental data. This problem seems to have been resolved by Overhof and Rossler (1970) who have produced a structure which is consistent with the published results. There seems to be a general consensus that the features observed in the visible spectrum arise from transitions between states of largely 3p non-bonding character and the conduction-band, such transitions are designated E_2 and E_1 in fig. 1.8.

The most common substituents in galena are antimony, bismuth and silver, the former two acting as donors and the latter as an acceptor. Other ions have been suggested, but careful analysis has shown them to be the result of mineral inclusions and not actually in solid solution with the galena itself. Werrick (1960) has implied that the concentration of silver ions will tend to equal the sum of the concentrations of bismuth and antimony ions, and that when the carrier concentration is determined by these impurities it will be equal to the difference between the

concentration of donors and acceptors. It should be pointed out that Werrick's study deals with high impurity ion concentrations and so is probably not applicable to the tiny amounts of bismuth found in our specimen.

The onset of the absorption edge in galena is in the far infra-red at 0.37 eV (3351 nm) and consequently lies well beyond the measurement range of either of the techniques used in this study. Higher energy transitions are, however, detectable, and arise from electronic transitions between the predominantly 3p non-bonding band and the conduction band. They are marked by a large maximum at 350 nm and a smaller one at 670 nm.

The reflectivity of galena increases rapidly from 600 to 350 nm where it reaches a maximum. A similar increase is also observed in the dispersion of k (fig. 6.7) and ε_2 (fig. 6.8), although in the latter it does not occur with the same rapidity. The dispersions of n (fig. 6.7) and ε_1 (fig. 6.8) show a corresponding decrease.

7.5 Pyrite

7.5.1 Introduction

The pyrite specimen section number E1002 examined in this study contains traces of arsenic and cobalt and has the formula $Fe_{1.05}S_2$ which agrees reasonably well with that recognised for pyrite FeS_2.

7.5.2 Comparison of Microphotometric and Ellipsometric Data

A graphical representation of the ellipsometric and microphotometric reflectance data can be found in fig. 6.10 together with the oil immersion results of the latter. Comparison of the two reflectance profiles reveals some disparity between them both in magnitude and dispersion. The reflectivity of the pyrite specimen increases rapidly from 400 - 520 nm. Over this range the microphotometric data are consistently lower than those measured ellipsometrically. At 520 nm the ellipsometric and microphotometric reflectance curves cross, so that the microphotometric measurements are now higher than the ellipsometric ones and continue to be so up to 700 nm.

Over this region the reflectivity of the mineral continues to rise, but more slowly and two maxima are clearly visible in its dispersion. As the reasons for the observed disparities are not consistent throughout the spectrum, the following discussion will deal with each of them separately and so will be divided into three ranges:

i) 400 - 500 nm; In this region the microphotometric reflectance data range from being 1.26% lower at 440 nm to 0.3% lower than the ellipsometric values at 500 nm. The convergence of ellipsometric and microphotometric reflectance data parallels the slowing down of the rate of increase of reflectance with respect to wavelength $\frac{\delta.R}{\delta.\lambda}$, and gives a clue to the origin of the difference between the data. No one has yet created a perfect monochromator and thus all monochromators including those used in this study operate within the pass bandwidth. This is not important when the rate of change of reflectivity with respect to wavelength is small as the reflectivity at say 420 nm, is approximately the same as that at 423 nm. When, however, the reflectance is changing rapidly, meaningful data comparisons are difficult, especially bearing in mind that the measurements in this case were made on two different instruments using different monochromators with different bandwidths. Thus it is hardly surprising that the disparities such as those in fig. 6.10 are observed.

ii) 520 - 580 nm; Over this wavelength range the microphotometric data are on average 0.7% higher than those derived ellipsometrically. As the rise in reflectivity is much less rapid in this range than in the previous one, the 'monochromator effect' can be regarded as negligible. The factor dominating in this spectral region is the SSRDP described in section 5.2. This effect is most pronounced between 520 - 580 nm, and for pyrite measured using a tungsten-titanium-carbide standard is of the order of + 0.3%. This effect together with the experimental error for both techniques of $\pm$ 0.5% accounts for the observed differences.

iii) 600 - 700 nm; In this spectral region the reflectance is still rising albeit slowly, and the microphotometric data is systematically 1.0% higher than that measured ellipsometrically. This difference is primarily caused by the loss of ellipsometer sensitivity in this spectral region (section 7.2.3).

Other factors such as the differences in size of the measured area may also be playing a part in the observed disparities, however, the point of the preceding discussion was to identify the major causes. Taking into account the above factors the curve displayed in fig. 7.2 has been plotted to try and rectify the observed errors.

Between 400 and 540 nm the ellipsometric and microphotometric n and k data are in fair agreement fig. 6.11, however, progressing into the red this comparison deteriorates and is at its worst between 600 and 700 nm. As this is the spectral region where the ellipsometric readings are unreliable, the derived n and k values would also be expected to be inaccurate. In addition due to the high reflectivity of the mineral the optical constants are being determined in a region where the n and k contours lie very close together (section 2.2.4.) and consequently any slight error in the microphotometric determination of R and ^{im}R will lead to erroneous values of n and k.

All the microphotometrically determined n values apart from those at 400 and 700 nm lie below the ellipsometric ones. The converse, however, is true for k where all the microphotometric values with the exception of those at 400, 420, 440 and 460 nm lie above those determined ellipsometrically. Some irregularities are discernible in the microphotometric n and k data and are due to the ill conditioning of the equations used in the microphotometric determination of n and k(section 7.3.2.)

7.5.3 Comparison of Data with Literature Results

Ever since the pyrite structure was first elucidated by Bragg (1913) the mineral has aroused the interest of many workers. This fact together with the natural abundance of large crystals of pyrite accounts for the large amount of data in the literature. In table 7.4 the results

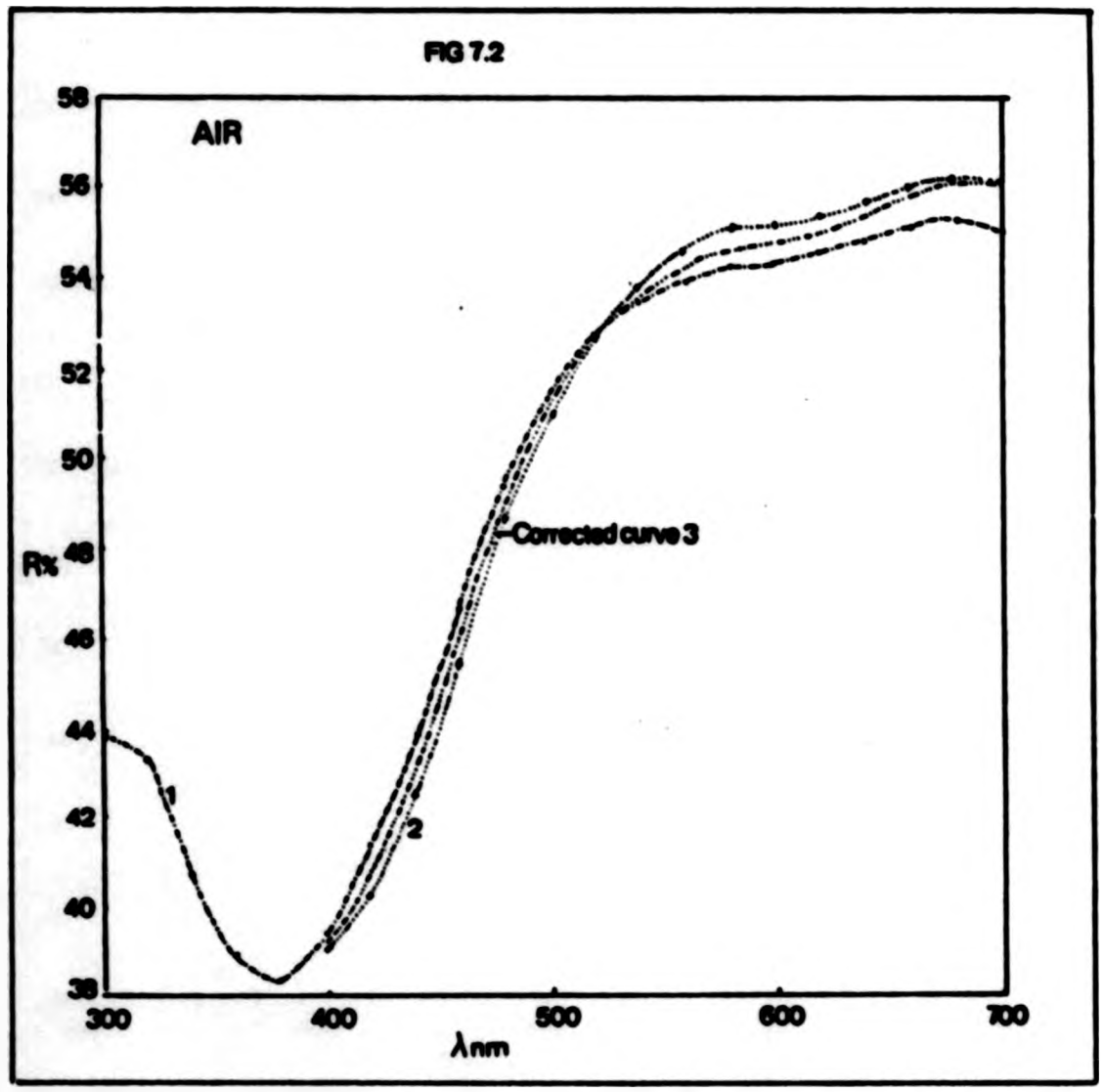

Fig 7.2 Correction of pyrite data for instumental errors.

1. *Ellipsometric results this study.*
2. *Microphotometric results this study.*
3. *Corrected values.*

Table 7.4. Comparison of reflectance data from this study for pyrite with literature values.

λ nm	Reflectance in air							
	1	2	3	4	5	6	7	8
275			45.81	35.58				
300	43.95				41.21			
310			49.09	37.09				
320	43.38							
340	40.58							
354			40.82	34.41				
360	38.96							
380	38.44							
400	39.40	39.04			36.74			
413			41.19	35.58				
420	41.39	40.31						
440	43.85	42.59						
460	46.71	45.54						
470						35.10	45.60	46.00
480	49.42	48.65						
496			52.17	46.05				
500	51.39	51.00			49.76			
520	52.69	52.68						
540	53.46	53.79						
546						36.20	51.70	52.80
560	54.00	54.57						
580	54.26	55.04						
589						41.50	53.50	55.00
600	54.42	55.23	58.33	51.51	55.35			
620	54.67	55.40						
640	54.93	55.65						
650						44.20	54.40	55.50
660	55.23	56.00						
680	55.29	56.22						
700	55.01	56.18			57.21			
827			61.94	49.53				

1. Ellipsometric measurements on pyrite, this study.
2. Microphotometric measurements on pyrite, this study.
3. Results of Bither et al. (1968) for pyrite.
4. Results of Schegal & Wachter (1976) for pyrite.
5. Results of Vendrell-Saz et al. (1978) for pyrite.
6. Results of Bowie, Simpson & Auld (1978) for nickelian pyrite.
7. Results of Bowie, Simpson & Auld (1978) for pyrite.
8. Results of Bowie, Simpson & Auld (1978) for pyrite (Elba)

of this study are compared with those of other workers and while some of the data are in reasonable agreement others display striking differences.

The magnitude and dispersion of the reflectance profile for the pyrite specimens discussed by Vendrell-Saz et al. (1978) and the IMA COM data file are in fair agreement with the data in this study. Discrepancies, however, occur when our data are compared with those of Bither et al. (1968) and Schlegal and Wachter (1976). The measurements of the latter are found to be systematically lower than our data while those of the former are systematically higher.

As Schlegal and Wachter (1976) give no indication of either the composition of their pyrite specimen, or the type of instrument used to determine its reflectivity, it is very difficult to account for the differences between their data and that presented here. The greater magnitude of the data obtained by Bither et al. (1968) may be due to the fact that they used an 'as grown' surface of synthetic 'pure' pyrite which could have a higher reflectivity than polished natural pyrite, and unless it was buffed before measurement will certainly have a tarnish film.

7.5.4 Electronic and Optical Properties

Pyrite has a narrow band gap of 0.9 eV $\pm$ 0.1 eV (Bither et al. 1968) and can exhibit either n or p type semi-conduction. Shuey (1975) claims both n-and p-type within the same mineralogical specimen, although he suggests that this may be due to mineral inclusions or surface deformation. The features observed in the visible spectrum arise from two types of electronic transitions, namely those between the non-bonding t_{2g} levels and the anti-bonding e_g^* band, and those between the bonding valence band and the anti-bonding e_g^* band (fig. 7.3). For reasons of increased energy separation the latter occurs at higher energies than the former.

Careful observation of the reflectance spectrum of the pyrite specimen used in this study reveals that the main peaks are split. This phenomenon is not peculiar to our specimen and has been noticed by other

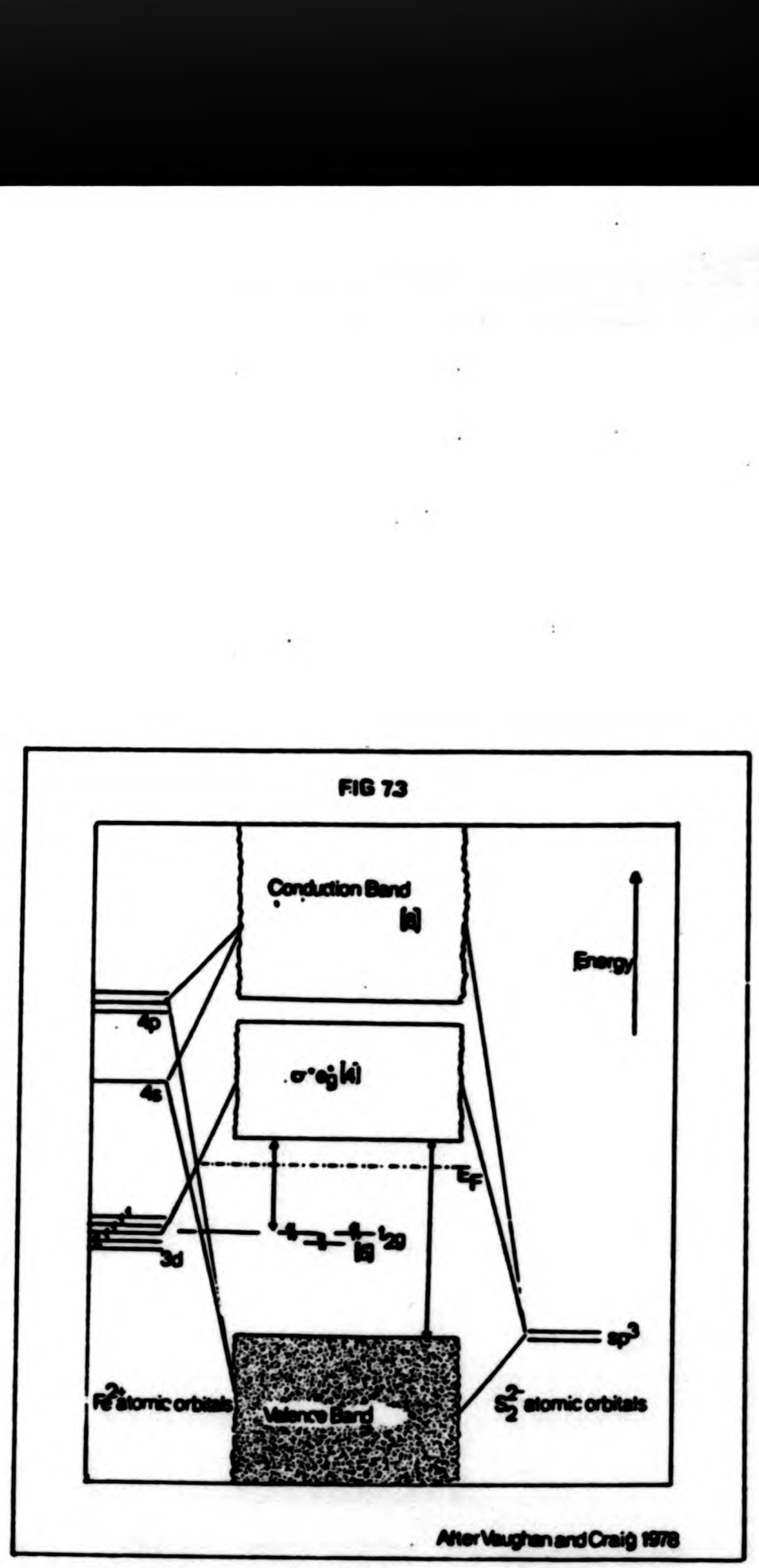

Fig 7.3 Simple band structure for pyrite.

workers (Schlegal and Wachter, 1976; Bither et al. 1968). The reason for this splitting lies in the fact the iron cation does not lie within a perfect octahedral environment, but one which is trigonally distorted, thus reducing the site symmetry to S_6. Such distortion lifts the degeneracy of the t_{2g} and the e_g levels, increasing the number of possible transitions. In the room temperature reflectance spectrum only the effects of e_g^* non-degeneracy are observed, those of t_{2g} are not apparent, as being non-bonding they are not split to the same extent. At liquid nitrogen and helium temperatures, however, where thermal-vibration effects are reduced one would expect to see t_{2g} splitting effects in addition to those of e_g^*.

Cobalt, nickel and arsenic are common substituents for the iron and sulphur in pyrite, and it has been amply demonstrated that the first two act as donors, while the last acts as an acceptor, (Favorov et al. 1972). High concentrations of cobalt and nickel will tend to decrease the reflectivity of the mineral. As they contribute electrons to the anti-bonding e_g^* band thus making it more localised, and thereby decreasing the mobility of the electrons within it, hence decreasing the conductivity and consequently the reflectivity. The presence of high arsenic concentrations will have the reverse effect. The greater polarisability of the arsenic ion (with respect to sulphur) will cause the covalent mixing of the anion and cation wave functions to be enhanced. This will lead to a greater degree of delocalisation in the e_g^* band and hence a higher reflectivity.

The pyrite specimen in this study contains trace quantities of arsenic and cobalt, the amounts of which are too small to have any significant effects on the reflectivity, especially when experimental error is taken into account. It should be noted that while in many minerals cations such as iron are thought to exist in an intermediate oxidation state, the iron in pyrite seems to be entirely diamagnetic low-spin Fe^{2+} (d^6). This supposition is supported by the available Mossbauer (Vaughan and Craig, 1978) and magnetic moment measurements (Bither et al. 1968).

Three maxima are observed in the visible reflectance spectrum of pyrite lying at 680, 580 and 300 nm. The first two of these are the

result of electronic transitions from the t_{2g} levels to the split e_g^* band, while the last is caused by transitions between the valence and e_g^* bands. Unfortunately as wavelengths shorter than 300 nm were unattainable by either measurement technique, the splitting of the high energy maximum at 300 nm was not observed but is confidently expected to occur in the near ultra-violet. For similar reasons the onset of the absorption edge in the near infra-red at 0.9 eV (1378 nm) was not observed. The presence of such an edge, however, is manifested by the slow and then rapid decrease in reflectivity from 700 - 400 nm. Below 400 nm the reflectivity begins to rise again indicating that the incident photons have sufficient energy to initiate higher energy electronic transitions. Similar features can also be observed in the n, k (fig. 6.11), ε_1 and ε_2 (fig. 6.12) spectra, although the decrease in ε_2 and particularly in k is not as marked as that of n and ε_1. The relatively high values of k and ε_2 in pyrite with respect to other first row transition metal sulphides accounts for the mineral's opacity and high conductivity.

7.6 Skutterudite

7.6.1 Introduction

Electron probe microanalysis of the 'skutterudite' specimen section number E1003 reveals that while a small area is composed of homogeneous skutterudite (this is the region which was measured and is discussed below), the rest is made up of a fine intergrowth of skutterudite and safflorite. Unfortunately the small grain size of the safflorite precluded microphotometric or ellipsometric measurements.

The formula calculated for the skutterudite phase is $(Co_{0.89}Ni_{0.02}Fe_{0.09})As_{2.87}S_{0.04}$ which is in reasonable agreement with that of (Co, Ni, Fe)As_{3-x} generally accepted for Skutterrudite, where x denotes the arsenic deficiency. The formula derived for the safflorite is $(Co_{0.43}Ni_{0.02}Fe_{0.55})As_{1.58}S_{0.08}$ which again agrees fairly well with that generally recognised for the mineral of (Co, Ni, Fe)As_2. When comparisons are made between the cationic distributions in skutterudite and in safflorite it is interesting to note that the cobalt seems to be concentrated in the skutterudite

lattice while in safflorite iron is the major cationic species. The concentration of nickel, however, changes very little from one mineral to the other. Safflorite also seems to have a greater ability to getter sulphur from the matrix, but in doing so becomes proportionally more deficient in arsenic.

7.6.2 Comparison of Microphotometric and Ellipsometric Data

In fig. 6.14 the ellipsometric and microphotometric reflectance curves are displayed together with a graphical representation of the latter's oil immersion data. The two sets of results agree fairly well, especially when the SSRDP (section 5.2) is taken into account. As skutterudite has a higher reflectance than the standard, tungsten titanium carbide, the effect of the SSRDP will tend to make the measured values slightly too high.

Examination of the microphotometric air and oil data between 600 and 700 nm reveals the start of a rapid decline in reflectivity. The same feature, however, is not nearly so clearly defined in the ellipsometric dispersion. This is because of the ellipsometer's sluggish response to large azimuthal changes in this spectral region (section 7.2.3). As has been mentioned previously (section 7.2.3) the microphotometric readings at 400 and 420 nm are also subject to small errors, a fact which accounts for the observed discrepancies between the ellipsometric and the microphotometric measurements at these wavelengths.

The crowding of the n and k contours at high reflectivities (section 2.2.4) accounts for the irregularities in the microphotometrically derived n and k values (fig. 6.15). Taking this factor and the effect of the SSRDP into account the agreement between the microphotometric and ellipsometric n and k values is rather good. The microphotometric n values are higher than the ellipsometric ones over most of the spectrum, and the ellipsometric k values higher than the microphotometric ones for all but a few wavelengths.

7.6.3 Comparison of Data with Literature Results

Minerals lying within the skutterudite solid solution field

have received very little attention and consequently the amount of published data relating to their optical properties is limited. As the relative concentrations of cobalt, nickel and iron, and the extent of the deficiency in arsenic, are likely to have a profound effect on the reflectivity, comparisons between different sets of data are difficult without a full compositional analysis.

Comparison of the data in this study with those of Simpson in the IMA COM data file, table 7.5, reveals that the data presented here, for both air and oil environments, are higher in magnitude. Although these differences are no doubt influenced by such factors as the SSRDP and the use of different standards and polishing procedures, the most important factor is likely to be due to compositional differences. Even though the data file gives only a semiquantitative analyses of the specimens examined by Simpson, from the arsenic to cobalt ratios it is clear that the specimen in this study lies much closer to the pure end member $CoAs_3$ than either of Simpson's specimens. This compositional factor could account for the higher reflectivity.

7.6.4 Electronic and Optical Properties

The fact that skutterudite has a small band gap is shown by its high reflectivity. Studies to determine the magnitude of this energy gap have, however, come to different conclusions. Hulliger (1959) reported a value of 0.2 eV, but actually believed the true value to be greater than 0.5 eV, the value of isostructural $CoSb_3$, while Pleass and Heyding (1962) gave a value of 0.12 eV. Unfortunately more modern techniques have yet to be applied to skutterudite and the results of Pleass and Heyding (1962), are the most recent in the literature.

The arsenic deficiency of many natural skutterudites would be expected to have a donor effect via arsenic vacancies. This hypothesis has yet to be confirmed by experiment. Pleass and Heyding (1962) have shown that nickel acts as a donor in $CoAs_3$, while iron in high concentrations acts as an acceptor. In addition Radcliffe (1968) has shown that some of the nickel and iron in natural skutterudites substitutes for arsenic rather than cobalt.

Table 7.5. Comparison of reflectance data from this study for skutterudite with literature values.

λ	Reflectance in air					
nm	1	2	3	4	5	6
320	56.17					
340	55.33					
360	55.61					
380	56.08					
400	56.45	55.34	58.00	55.60		
420	56.76	56.02	57.30	55.50		
440	56.81	56.44	56.70	55.40		
460	56.64	56.59	56.20	55.30		
470					53.80	55.20-56.00
480	56.34	56.39	55.90	55.10		
500	55.92	56.09	55.40	54.80		
520	55.47	55.68	55.00	54.50		
540	55.08	55.28	54.60	54.10		
546					53.40	54.00-54.40
560	54.74	54.98	54.20	53.80		
580	54.46	54.68	54.00	53.60		
589					53.00	53.50-53.80
600	54.18	54.43	53.60	53.30		
620	53.90	54.12	53.30	53.20		
640	53.68	53.81	53.00	52.90		
650					52.90	52.70
660	53.43	53.46	52.50	52.60		
680	53.18	53.11	52.20	52.40		
700	53.01	52.71	51.90	51.60		

1. Ellipsometric measurements on skutterudite, this study.
2. Microphotometric measurements on skutterudite, this study.
3. IMA,COM results for skutterudite from Bon Azzer Morocco As:Co=6:1, Co:Ni=3:1 P.R.Simpson
4. IMA,COM results for skutterudite from Offenbanga, As:Co=4:1 minor Fe trace Ni.
5. Results of Uytenbogaardt & Burke (1971) for skutterudite.
6. Results of Bowie, Simpson & Auld (1978) for skutterudite.

The hypothesis advanced by Nickel (1970) that the nickel in skutterudite is quadrivalent to preserve the d^6 low spin configuration seems somewhat improbable. Especially given that the few compounds reported to contain the highly oxidising Ni(IV) ion, also contain rather exotic highly electronegative species, viz., the heteropolymolybdate anion $[NiMo_9O_{32}]^{6-}$, the heteropolyniobate complex $[NiNb_{12}O_{38}]^{12-}$, the periodates $Na(K)NiIO_6.nH_2O$ and K_2NiF_6 (Cotton and Wilkinson, 1972). It thus seems highly unlikely that the square planar groupings of arsenic anions, in skutterudite, will be sufficiently electronegative to stabilise the Ni(IV) species, solely to enable it to retain a d^6 configuration. As it seems that nickel cannot exist in a quadrivalent state in skutterudite, the most likely oxidation state for it to adopt is Ni(II)(d^8). This will lead to an increase in the number of electrons in the 3d e_g levels, which because of the Jahn-Teller effect will be non-degenerate. Thus maxima in the spectra of nickel rich skutterudites, which are attributable to transitions from, or to, the e_g levels, should display some splitting. Such splitting is not observed in our skutterudite specimen, because the concentration of nickel is low with respect to that of cobalt and iron. As neither a full energy level diagram nor a band structure have been calculated for skutterudite the effects of ion substitution cannot be fully appreciated, although it is possible that a reflectivity decrease similar to that observed in substituted pyrites will occur. It is also likely that the arsenic deficiency is due to a process of charge neutralisation between anions and cations when Ni^{2+} and Fe^{2+} substitute for Co^{3+}.

The reflectance profile of skutterudite displays a pronounced broad peak, and a smaller satellite peak, with maxima at 430 and 630 nm respectively. These peaks are due to electronic transitions between the cobalt (III)(d^6) singlet $^1A_{1g}$ ground state and the singlet states $^1T_{1g}$ and $^1T_{2g}$. The reason why the higher energy transition (to $^1T_{2g}$) is more intense is uncertain but could be due to the splitting of the $^1T_{1g}$ level, caused by a reduction in cationic site symmetry due to crystallographic distortions.

From 700 to 400 nm the values of reflectance, k (fig. 6.15) and ε_2 (fig. 6.16) rise to a maximum, after which they slowly decline into the ultra-violet. The values of n (fig. 6.15) and ε_1 (fig. 6.16), however,

fall throughout the spectrum from infra-red to ultra-violet.

7.7 Sphalerite

7.7.1 Introduction

An examination of the electron probe microanalysis of the sphalerite specimen section number E1004 shows that it contains traces of copper and has the formula $(Zn_{1.00}Fe_{0.05})S$ which agrees well with that recognised for sphalerite. The presence of iron in the mineral had already been intimated by its colour, a dark yellowish-brown. The formula also reveals that the mineral has a slight excess of cations with respect to anions.

7.7.2 Comparison of Microphotometric and Ellipsometric Data

In Fig 6.18 the microphotometric and ellipsometric reflectance data are compared, and found to be in reasonably good agreement. As the reflectance of sphalerite is very close to that of the standard, silicon carbide, the effects of the SSRDP (section 5.2) can be regarded as negligible. The difference between the two sets of measurements ranges from 0.01% in the blue to 0.4% in the red. While these differences lie within the range of experimental error, it seems likely that the disparities at the red end are caused by the decreased sensitivity of the ellipsometer at wavelengths exceeding 600 nm (section 7.2.3).

A comparison of the calculated ellipsometric n and k values (Fig. 6.19) with those derived from the microphotometric readings shows them to be in fairly good agreement. The microphotometric results are up to 0.21 higher than those derived ellipsometrically, and in particular the values of k appear to be too high, this is probably caused by the difficulty in achieving accurate k values when k is very small (Section 2.2.4).

7.7.3 Comparison of Data with Literature Results

From Table 7.6 and Figs. 7.4 and 7.5 it is clear that the ellipsometric and microphotometric reflectance data are in fair agreement with the results of other workers, especially when the differences in composition are taken into account. The sphalerite specimen described by Velasco, Pesquera and Autefage (1981) is very close, compositionally, to that used in this study, and given that it was polished and microphotometrically measured under similar conditions comparisons can be made.

From 420 - 500 nm Velasco, Pesquera and Autefage's specimen (hereafter referred to as specimen 3, see Fig. 7.4) is consistently lower in reflectivity than the specimen used in this study. Over the remaining portion of the spectrum, however, it lies between the ellipsometric and microphotometric results. As has already been pointed out the ellipsometric data between 600 and 700 are suspect. This conclusion is further substantiated by the fact that the specimen 3 data mimic the microphotometric results in both magnitude and dispersion over this wavelength range.

Comparison of the sphalerite in this study with that described by Cervelle, Levy and Pinet (1975) is difficult because they do not give a full compositional analysis of their specimen. It can, however, be deduced that the concentrations of impurity ions will be small as the specimen is described as clear and transparent. Consequently the reflectivity of this specimen will be lower than that of the ferrian sphalerites.

The reflectance data derived by Cervelle, Levy and Pinet (1975) using the prism method seem reasonably close in value to the ellipsometric and microphotometric results (Fig. 7.5). This is somewhat surprising, as their specimen is colourless and transparent and so would be expected to have a lower reflectivity than the specimen used in this study (Section 1.7.3). However, Cervelle *et al*. found that the reflectances derived from the prism method were systematically higher than those for polished sections, and therefore concluded that the polishing procedure was responsible for a decrease in reflectance. This is probably a result of the proliferation of surface defects induced by the abrasion of the

Table 7.6. Comparison of reflectance data from this study for sphalerite with literature values.

λ	Reflectance in air						Reflectance in oil				
nm.	1	2	3	4	5a&b	6	2	4	5a	5b	6
300	23.21										
320	23.16										
340	22.75										
360	21.65										
380	20.50										
400	19.61	19.50		19.15	19.00	19.00	6.59	6.21	6.10	6.40	6.10
420	18.93	18.96	18.80	18.67	18.60	18.40	6.24	5.98	5.80	6.10	5.80
440	18.40	18.41	18.10				5.92				
460	18.00	17.98	17.90	17.86	17.70	17.50	5.68	5.52	5.30	5.60	5.20
480	17.65	17.60	17.50	17.50	17.40	17.20	5.47	5.35	5.20	5.40	5.10
500	17.39	17.28	17.20	17.30	17.20	17.00	5.30	5.22	5.10	5.20	4.90
520	17.14	17.00	17.00	17.10			5.20				
540	16.94	16.79	16.90	16.91	16.80	16.50	5.08	5.02	4.90	5.00	4.70
560	16.78	16.59	16.70				4.97				
570				16.68	16.50	16.30		4.90	4.80	4.90	4.80
580	16.64	16.45	16.50				4.89				
600	16.55	16.34	16.40	16.50	16.30	16.20	4.81	4.81	4.70	4.80	4.50
620	16.47	16.23	16.30				4.76				
640	16.38	16.16	16.30	16.29	16.20	16.00	4.73	4.73	4.60	4.70	4.50
660	16.32	16.06	16.20				4.68				
680	16.32	15.97	16.10	16.19	16.10	15.90	4.64	4.70	4.60	4.60	4.50
700	16.32	15.90					4.60				

1. Ellipsometric measurements on sphalerite, this study.
2. Microphotometric measurements on sphalerite, this study.
3. Results of Velasco, Pesquera & Autefage (1981) for natural sphalerite
4. Results of Cervelle, Levy & Pinet (1975) on a clear sphalerite from Spain, measured using the prism method ie. R & ^{1m}R calculated from measured n values, assuming k=0.
5. Results of Cervelle, Levy & Pinet (1975) on 2 cleaved surfaces a & b (from the same sample as 4).
6. Results of Cervelle, Levy & Pinet on a polished shalerite specimen (from the same sample as 4).

FIG 7.4

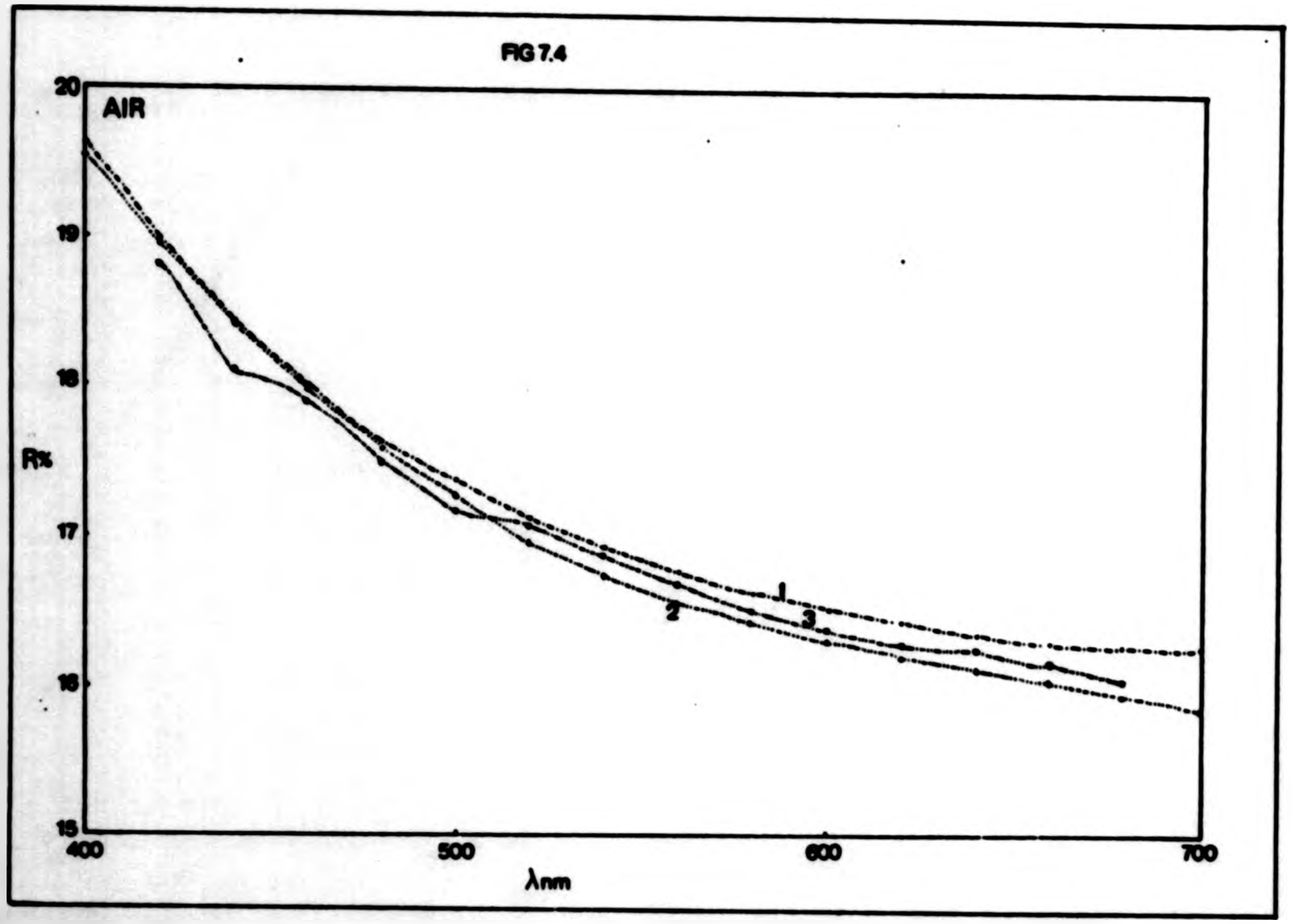

Fig 7.4 Comparison of ellipsometric (curve 1-·-·-)and microphotometric (curve 2·····)reflectance data for sphalerite with the results of Velasco, Pesquera and Autefage (1981) (curve.3-----).

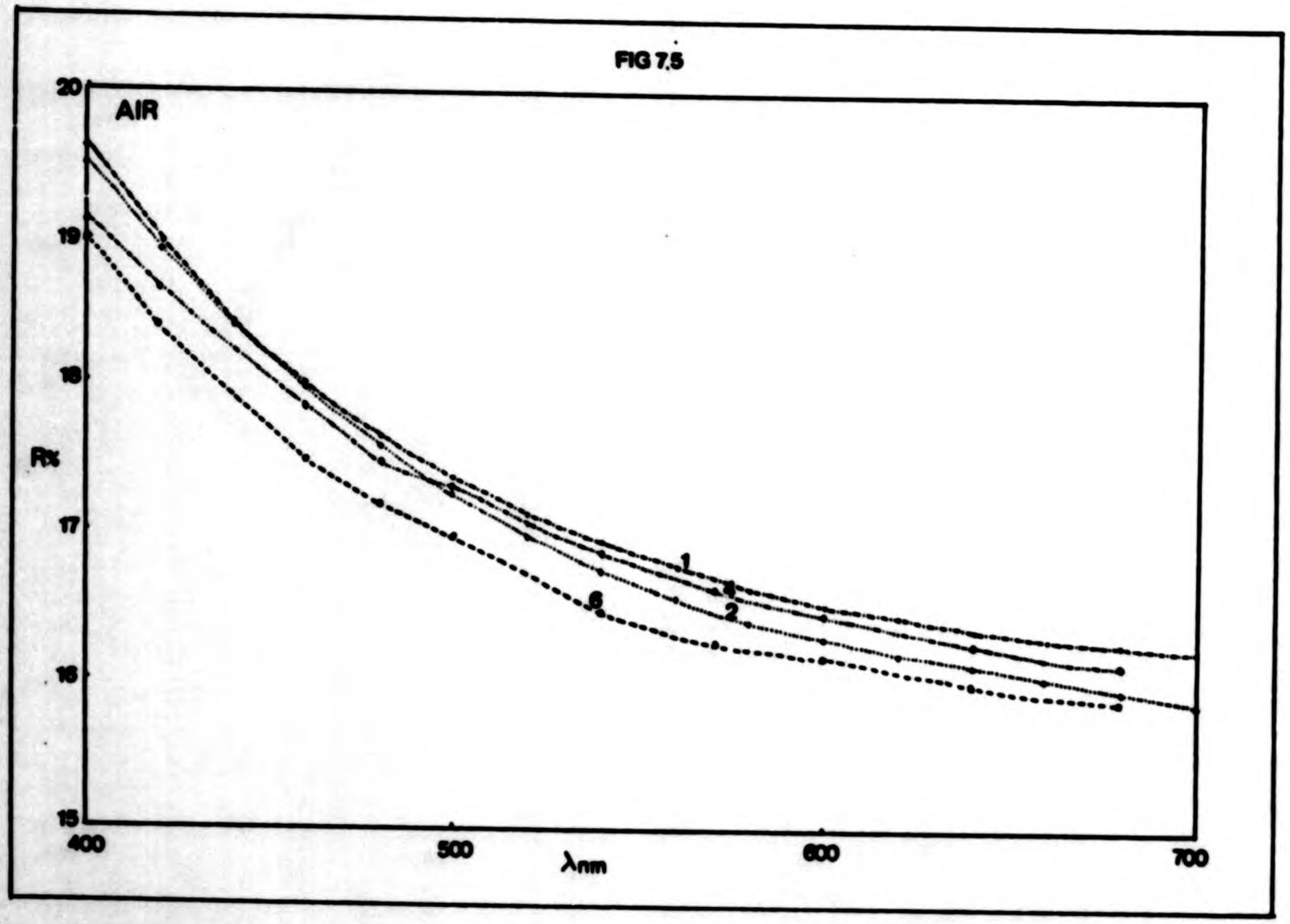

Fig 7.5 Comparison of ellipsometric (curve 1-·-·-·)and microphotometric (curve 2·····)reflectance data for sphalerite with the results of Cervelle, Levy and Pinet (1975) (curve 4 using the prism method----) (curve 5 on a polished section---)

surface. If the reflectance results of this study are compared with the polished section data of Cervelle et al.the expected difference due to composition is observed.

An investigation of the literature reveals that the refractive index of sphalerite has been measured or calculated by many workers des Cloizeaux, 1867; Horn, 1898; Brun, 1930; Bond, 1965; Cervelle, Levy and Pinet, 1975; Butterill and Nickel, 1967, using a variety of techniques (microscope reflectometry, Brewster angle, prism method etc.). Some workers have measured n over a wide spectral range while others have concentrated on one or two fixed wavelengths. In some cases pure transparent synthetic sphalerites were used so as to avoid the necessity of involving the absorption coefficient k in the calculations. This was also the reason for making measurments in the visible red where k is a minimum. Most of the published data especially in the green and red regions of the spectrum lie between the ellipsometric and microphotometric values, Table 7.7. As the majority of these results are for transparent sphalerites one can surmise that foreign ion impurities have a greater effect on the absorption coefficient and the position of the absorption edge than on the refractive index.

7.7.4 Electronic and Optical Properties

The importance to the semi-conductor industry of chalcogenide materials with the general formula NX (where N = Zn, Cd, Hg and X = S, Se and Te) of which sphalerite is a member has been established in recent years, and has stimulated extensive research into their optical and electronic properties. Pure sphalerite is a transparent material with a band gap of approximately 3.6 eV, a fact that has led some authors to describe it as a dielectric rather than a semiconductor. The great importance of sphalerite, however, lies in its ability to accommodate a wide range of foreign ions within its structure. Some of these substituents are found in naturally occuring sphalerites, the more exotic are, however, the product of the research laboratory.

In the case of the sphalerite used in this study there are two impurity ions present, iron and copper with weight percents of 2.61 and 0.11 respectively. There is some controversy in the literature about the

Table 7.7. Comparison of *n* values from this study for sphalerite with literature values.

λ	*n* values										
nm	1	2	4	5a	5b	6	7	8	9	10	11
300	2.72										
320	2.76										
340	2.77										
360	2.72										
380	2.64										
400	2.58	2.52	2.56	2.45	2.56	2.55					
420	2.54	2.50	2.52	2.43	2.56	2.52					
430							2.53				
440	2.50	2.47									
460	2.47	2.44	2.46	2.40	2.49	2.46					
480	2.45	2.41	2.44	2.40	2.46	2.44					
486							2.47				
500	2.43	2.39	2.43	2.39	2.44	2.42					
509								2.41			
520	2.41	2.36									
540	2.40	2.35	2.40	2.38	2.40	2.37					
560	2.39	2.34									
570			2.38		2.37	2.38					
580	2.28	2.33									
590								2.37	2.37		
600	2.37	2.33	2.37		2.36	2.37				2.35	2.36
620	2.36	2.33									
640	2.36	2.32	2.35		2.36	2.36					
660	2.35	2.31	2.35		2.35	2.36					
680	2.35	2.31									
700	2.35	2.30									

1. Ellipsometric values for sphalerite, this study
2. Microphotometric values for sphalerite, this study.
4. Results of Cervelle, Levy & Pinet (1975) on a clear sphalerite from Spain, *n* measured using prism method.
5. Results of Cervelle, Levy & Pinet for *n* calculated from R and ^{im}R for two cleaved surfaces of sphalerite a and b (from the same sample as 4).
6. Results of Cervelle, Levy & Pinet for *n* calculated from R and ^{im}R for a polished sphalerite surface (from the same sample as 4).
7. Results of Horn (1898) for sphalerite.
8. Results of Brun (1930) for sphalerite.
9. Results of Des-Cloizeaux (1867) for sphalerite.
10. Results of Butterill & Nickel (1967) for sphalerite.
11. Results of Bond (1965) for sphalerite.

oxidation state which should be ascribed to iron in sphalerites. $Fe^{2+}(d^6)$ is relatively unstable in tetrahedral sites whereas the higher oxidation state $Fe^{3+}(d^5)$ is stabilised by tetrahedral coordination. Manning (1967) claimed that both Fe^{2+} and Fe^{3+} were present in sphalerite, the former in tetrahedral sites and the latter in interstitial octahedral sites. Later Mossbauer data (Vaughan and Craig, 1978) does not substantiate this finding, and a knowledge of iron chemistry would indicate that if anything the reverse should be true. Rauber and Snider (1962) claim to have identified Fe^{3+} by electron paramagnetic resonance spectroscopy (EPR) and postulated that it is formed when Fe^{2+} 'traps' a positive hole. Similarly Holton et al. (1964) claim $Fe^{+}(d^7)$ is formed by the interaction of Fe^{2+} with an electron. Further studies using EPR are therefore warranted but are beyond the scope of the work in this study. A plausible explanation is that the iron in sphalerites, like that in tetrahedrites (see section 6.8.4) exists in an intermediate oxidation state, formed by the following disproportionation type mechanism:

$$2Fe^{2+}(d^6) \longrightarrow (Fe(d^5) + Fe(d^7))^{4+}$$

The small amount of copper present in sphalerite specimen in this study will act as a dopant promoting conduction via positive holes.

An appreciation of the electronic structure, and the effects of impurity ions upon it, is an aid to a fuller understanding of the observed optical phenomena. The onset of the absorption edge (ie, the start of electronic transitions from the valence band into the conduction band) in sphalerite is marked by a rapid increase in reflectivity, ε_2 (fig. 6.20) and k (fig. 6.19) which reaches a maximum at 310 nm. The sharpness of the edge is diminished by the effects of thermal broadening and impurity photoionization phenomena.

At the red end of the spectrum both k and ε_2 tend towards zero indicating that the mineral is transparent to red light. n (Fig. 6.19) and ε_1 (Fig. 5.20) decrease likewise from blue to red, although the drop is not as dramatic as that of k and ε_2. The energy at which electronic transitions occur is dependent on the composition of the mineral, unfortunately neither of the techniques used in this study extend far

enough into the infra-red for the iron $^5E_2 \longrightarrow {}^5T_2$ transition to be observed. The presence of iron and copper impurities, however, are manifested in more subtle ways e.g. by the increased reflectivity with respect to pure sphalerite, and by a slight shift to lower energies of the absorption peak, which is indicative of a smaller band gap and a higher conductivity.

7.8 Tetrahedrite

7.8.1 Introduction

A study of the electron probe analysis of the mineral reveals it to have the formula $(Cu_{10.19}Ag_{0.28})(Zn_{1.91}Fe_{0.14})(As_{1.19}Sb_{2.95})S_{12.86}$. This agrees reasonably well with the generally recognised formula for naturally occuring tennantites and tetrahedrites of $A_{10}B_2C_4D_{13}$ where A = Cu, Ag; B = Cu, Fe, Zn, Hg, Cd, Pb; C = As, Sb, Bi, Te, Pb; D = S, Se (Johan and Kvacek, 1971; Charlat and Levy, 1974; Sandecki and Amcoff, 1981; Basu *et al*. 1981; Johnson and Jeanloz, 1983).

7.8.2 Comparison of Microphotometric and Ellipsometric Data

A comparison of the ellipsometric and microphotometric reflectance data (Fig. 6.22) reveals that while the two curves have essentially the same dispersion, the ellipsometric data is some 0.5% to 1.5% higher in magnitude. This discrepancy between the measured values is probably caused by a number of factors.

In the microphotometric analysis the tetrahedrite specimen has a lower reflectivity than the tungsten-titanium-carbide standard. Thus the SSRDP described in section 5.2 will come into play causing a lowering of the observed values by about 0.1%. Clearly this does not account for anything approaching the observed differences, which means that other factors must be involved. The widest discrepancy between the measured values is between 600 and 700 nm, and is partly caused by the insensitivity of the ellipsometer in this spectral region (section 7.2.3). This problem is further compounded by the fact that the reflectance is changing rapidly with respect to wavelength and so the effect of the bandwidth of the monochromator is likely to be significant. It should also be remembered that the ellipsometer measures a much larger

area than the microscope photometer and as the available area of homogeneous material was small by ellipsometric standards this must be considered a contributory factor.

Over most of the spectrum the microphotometrically derived n values (fig. 6.23) are slightly lower than those obtained ellipsometrically, the reverse is, however, true for k where those values calculated from the microphotometric results are higher than the ellipsometric values. The microphotometrically derived n and k values display some irregularities reflecting the sensitivity of the derived optical constants to tiny fluctuations in R and ^{im}R (Section 2.2.4.).

7.8.3 Comparison of Data with Literature Results

Minerals in the tetrahedrite-tennantite solid solution series have a marked ability to accommodate 'foreign' ions in their lattices. This makes the interpretation and comparison of reflectance data difficult as subtle changes in the chemical composition can significantly alter both the magnitude and dispersion of the reflectance spectrum. In Fig. 7.6 and Table 7.8 the results for the tetrahedrite used in this study are compared with those of similar natural and synthetic tetrahedrites studied by other workers.

The reflectance curves shown in Fig. 7.6 can be divided into two categories. The first is composed of curves 3, 4 and 5 while the second comprises curves 1, 2 and 7. The difference between these two sets of curves is that although they have essentially the same shape the first set is displaced by some twenty nanometres towards the red end of the spectrum with respect to the second set. It is also interesting that this marked division between the data differentiates the synthetic tetrahedrites from those occurring naturally. Obviously as none of the tetrahedrites have exactly the same composition, comparisons must be broadly based and generalised. For example, the greater reflectivity and displacement of curves 3, 4 and 5 can be partially explained by their high antimony concentrations.

Hall, Cervelle and Levy (1974) have suggested that the presence of zinc and iron in synthetic tetrahedrites causes a displacement of

Fig 7.6 Comparison of ellipsometric and microphotometric reflectance data for tetrahedrite with the literature results for natural and synthetic tetrahedrites

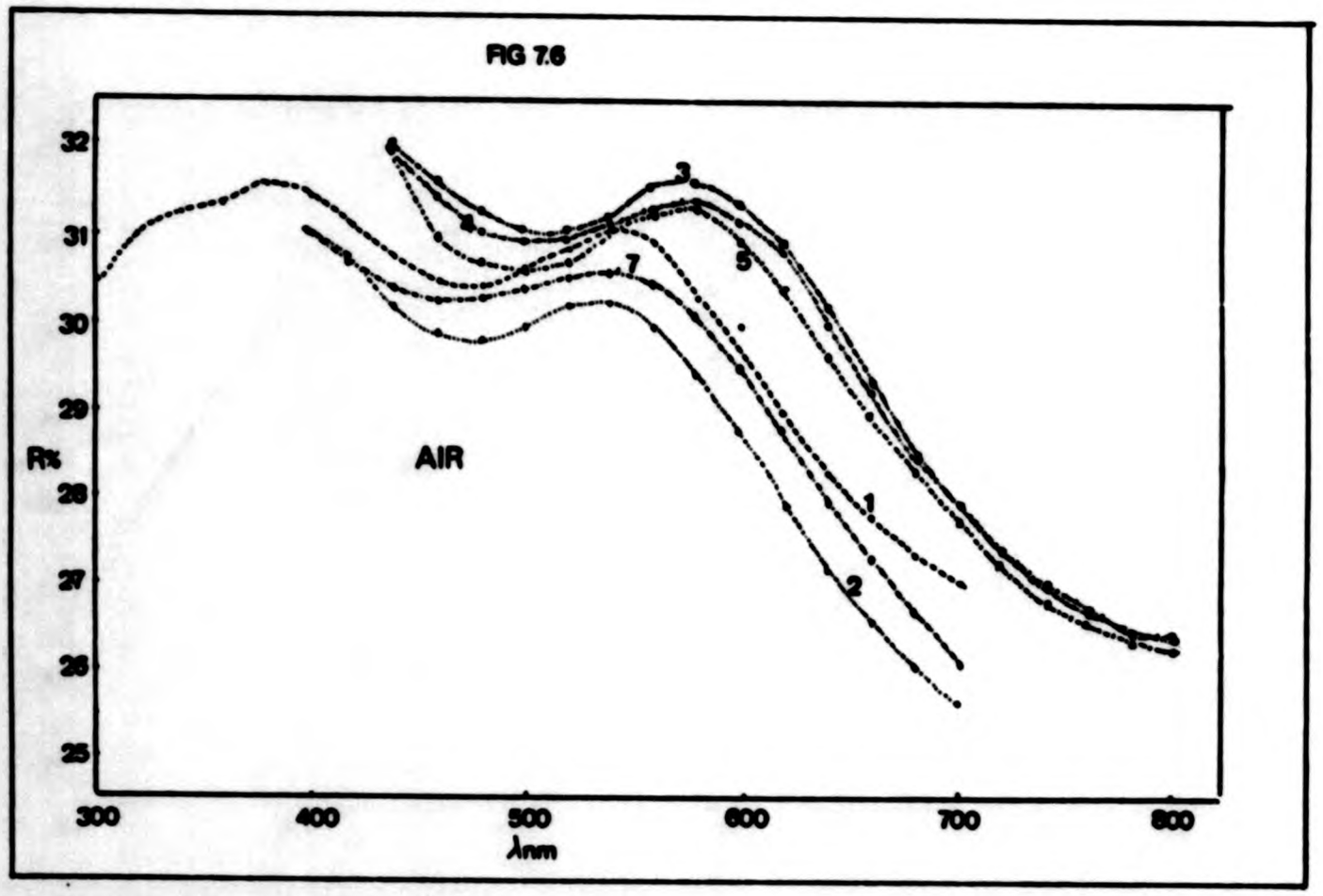

1. *Ellipsometric results this study*
2. *Microphotometric results this study*
3. *Synthetic tetrahedrite* $Cu_{10.15}Zn_{2.05}Sb_{4.15}S_{12.15}$ *Hall et al. (1974)*
4. *Synthetic tetrahedrite* $Cu_{9.95}Zn_{2.05}Sb_{4.15}S_{13.25}$ *Hall et al. (1974).*
5. *Synthetic tetrahedrite* $Cu_{10.06}Ag_{0.06}Zn_{1.62}Fe_{0.27}Sb_{3.40}As_{0.06}S_{12.70}$ *Charlat and Levy (1976).*
7. *Natural tetrahedrite* $Cu_{9.77}Ag_{0.07}Zn_{1.75}Fe_{0.38}Sb_{1.79}As_{2.07}S_{11.58}$ *Araya et al. (1978).*

Table 7.8. Comparison of reflectance data from this study for tetrahedrite with literature values.

λ nm	Reflectance in air								
	1	2	3	4	5	6	7	8	9
300	30.44								
320	31.02								
340	31.24								
360	31.36								
380	31.54								
400	31.46	31.28					31.10		
420	31.10	30.79					30.70	30.80	30.90
440	30.75	30.19	32.10	31.95	32.15	31.60	30.40	31.80	32.00
460	30.49	29.90	31.65	31.40	30.95	31.25	30.30	32.00	32.20
480	30.41	29.80	31.30	31.05	30.70	31.15	30.30	32.00	32.20
500	30.62	29.93	31.10	30.95	30.60	31.10	30.40	32.30	32.40
520	30.88	30.14	31.05	30.95	30.65	31.10	30.50	32.60	32.60
540	31.02	30.21	31.20	31.10	31.05	31.15	30.60	33.00	33.10
560	30.90	29.97	31.55	31.30	31.30	31.15	30.50	33.30	33.30
580	30.24	29.45	31.55	31.35	31.30	30.90	30.10	33.20	33.10
600	29.93	28.71	31.35	31.15	30.95	30.60	29.50	32.70	32.20
620	29.00	27.88	30.90	30.70	30.35	30.20	28.80	31.40	31.10
640	28.23	27.15	30.15	29.95	29.65	29.65	28.00	31.40	31.40
660	27.78	26.55	29.35	29.20	28.95	29.20	27.30		
680	27.33	26.04	28.60	28.50	28.35	28.80	26.70		
700	27.00	25.60	27.95	27.95	27.80	28.45	26.10		
720			27.40	27.40	27.30	28.10			
740			26.95	27.00	26.90	27.75			
760			26.65	26.70	26.60	27.35			
780			26.40	26.50	26.40	27.05			
800			26.30	26.25	26.20	26.80			

1. Ellipsometric measurements on tetrahedrite, this study
2. Microphotometric measurements on tetrahedrite, this study.
3. Results of Hall, Cervelle & Levy (1974) on synthetic tetrahedrite $Cu_{10.15}Zn_{1.85}Sb_{3.90}S_{12.65}$
4. Results of Hall, Cervelle & Levy (1974) on synthetic tetrahedrite $Cu_{9.95}Zn_{2.05}Sb_{4.15}S_{13.25}$
5. Results of Charlat & Levy (1976) on synthetic tetrahedrite $Cu_{10.06}Ag_{0.06}Zn_{1.62}Fe_{0.27}Sb_{3.40}As_{0.06}S_{12.70}$
6. Results of Charlat & Levy (1976) on synthetic tetrahedrite $Cu_{10.09}Ag_{0.03}Zn_{0.80}Fe_{0.63}Hg_{0.43}Sb_{2.93}As_{1.08}S_{13.30}$
7. Results of Araya, Bowles & Simpson (1978) on a natural tetrahedrite
8. $Cu_{9.77}Ag_{0.07}Zn_{1.75}Fe_{0.32}Sb_{1.79}As_{2.07}S_{11.58}$
8. IMA,COM results on a natural tetrahedrite $Cu_{10.18}Zn_{1.52}Fe_{0.33}Sb_{3.31}S_{13.66}$
9. IMA,COM results on a natural tetrahedrite $Cu_{10.98}Zn_{1.71}Fe_{0.69}Hg_{0.005}Sb_{3.56}As_{0.67}S_{11.31}$.

the spectral maxima towards the infra-red with respect to pure tetrahedrite. The results of this study and those of Araya, Bowles and Simpson (1978) on natural tetrahedrites seem to contradict this finding and it seems more likely that this apparent 'red-shift' is the result of a number of interacting factors, for example, high zinc and high antimony concentrations. The presence of zinc does, however, as suggested by Hall, Cervelle and Levy (1974), cause the spectral maxima to become more pronounced. In addition, Hall, Cervelle and Levy, (1974) and Charlat and Levy (1976) have shown that the incorporation of silver in the tetrahedrite lattice leads to a decrease in reflectivity and a general flattening of the curve. This phenomenon may account for the fact that curves 1 and 2 are slightly lower than expected, given their antimony to arsenic ratio.

7.8.4 Electronic and Optical Properties

The complexity both in composition and structure of minerals in the tetrahedrite-tennantite solid solution series has led to little being understood about their bonding and electronic structure. In the general sense tetrahedrite can be regarded as a semiconductor with a narrow band gap, the size of which can fluctuate depending on the elemental composition and the number of occupied d orbitals therein. At wavelengths longer than 600 nm the energy of the incoming light is insufficient to excite electrons from the valence band into the conduction band, and so the reflectivity is low and the absorption coefficient k correspondingly tends towards zero.

When zinc and iron substitute for copper in tetrahedrite they enter slightly distorted tetrahedral sites and become essentially sp^3 hybridised. $Fe^{2+}(d^6)$ is fairly unstable in tetrahedral sites whereas the higher oxidation state $Fe^{3+}(d^5)$ is stabilised by four-fold coordination, so it is probable that in tetrahedrites an intermediate iron composition is attained. Hall, Cervelle and Levy (1974) have suggested that the following disproportionation-type mechanism may occur for iron in tetrahedrites and tennantites.

$$2Fe^{2+}(d^6) \longrightarrow (Fe(d^5) + Fe(d^7))^{4+}$$

A similar mechanism is also postulated for copper.

Tetrahedrites are often economically important because of extensive silver substitution for copper in trigonal planar sites. As copper and silver have similar ground state configurations $3d^{10}4s^1$ and $4d^{10}5s^1$ respectively, the only constraint on such a substitution is the size of the Ag^+ ion. Incorporation of silver in the tetrahedrite structure leads to a drop and a flattening of the reflectivity profile, a decrease in hardness and an increase in the size of the unit cell. In addition there is a marked antipathy between silver and arsenic whereby the latter constricts the lattice inhibiting the entrance of the former.

The reflectance spectrum of the tetrahedrite specimen exhibits two maxima at 380 nm and 540 nm, in addition it also shows a rapid decrease in reflectivity at wavelengths greater than 600 nm. The onset of the absorption edge at 600 nm and continuing into the blue is marked by an increase in ε_2, Fig. 6.24 and a corresponding decrease in ε_1, Fig. 6.24. The ε_1 and ε_2 spectra like those of n, k and reflectance have a double humped appearance indicating that at least two excitation processes must be taking place. The value of k like ε_2 increases with decreasing wavelength and at the red end of the spectrum tends towards zero ie, the mineral is semi-transparent to red light. Although all tetrahedrites and tennantites exhibit this phenomenon the tendency is particularly marked in those which are rich in zinc. It is interesting to note that these are the tetrahedrites where the ion substituting for copper has a complete stable d^{10} configuration and therefore suggests that in other tetrahedrites low energy transitions promoted by partially occupied d-orbitals are taking place. The sharpening of the reflectance maxima which are also characteristic of zincian tetrahedrites may also a consequence of this effect ie. the spectrum is not smeared by transitions from d-levels.

7.9 Cassiterite

7.9.1 Introduction

Electron probe microanalysis of the cassiterite specimen,

section number E1006, used in this study showed it to contain trace quantities of copper and titanium and to have the formula $Sn_{0.99}O_2$ which is not significantly different from that for pure tin (IV) oxide SnO_2.

7.9.2 Comparison of Microphotometric and Ellipsometric Data

Cassiterite is a mineral of tetragonal symmetry, so for the purposes of this study an isotropic section was prepared. As the response of the DVM did not fluctuate upon rotation of the specimen on the specimen stage, the mineral section was treated as isotropic and measured in one orientation only. A graphical representation of the ellipsometric and microphotometric reflectance data can be found in Fig. 6.26 together with the oil immersion results of the latter. Over most of the spectrum the ellipsometric and microphotometric results are in extremely good agreement and lie well within the experimental error ranges for both techniques ($\pm$0.5%). (The SSRDP (section 5.2) accounts for the slight lowering of the magnitude of the microphotometric data between 500 and 600 nm). Slight discrepancies are also found at 400 and 420 nm, but as noted previously (section 7.2.3) the microphotometric results are suspect at these wavelengths.

The ellipsometric and microphotometric n and k values are in very good agreement, Fig. 6.27. This is because of the closeness both in magnitude and dispersion of the reflectance data. The microphotometric and ellipsometric n values are practically identical, the differences occurring for the most part in the second place of decimals, the ellipsometric data, however, have slightly higher values over most of the spectrum. The agreement between the k values is not quite so good with the microphotometric values being higher throughout the spectrum. This is because the mineral is practically transparent and so values are being derived in the proximity of the k = 0 contour (section 2.2.4.2), a fact that also accounts for the undulating nature of the microphotometric dispersion.

7.9.3 Comparison of Data with Literature Results

In the past most optical studies on cassiterite have used the

prism method to determine its refractive index, from which assuming k = 0 its reflectance has been calculated. Very few workers have measured reflectance directly although Cal as and Cottrant (1982) have examined the absorption spectra. In Table 7.9 the results from this study are compared with those from the IMA COM data file.

The range of values given in the data file are consistently higher than our results, but as no information relating to the type of mineral section or its orientation are given comparisons are difficult. This problem is further compounded by the fact that the data file gives only a semiquantitative analysis of the mineral and gives no indication as to its trace element concentrations. It is, however, possible to speculate upon the reasons for these differences. Most cassiterites for example contain traces of iron as an impurity while that used in this study does not. Thus it may be that increasing iron concentration leads to an increase in reflectivity as occurs in sphalerites.

7.9.4 Electronic and Optical Properties

Cassiterite is a mineral with a large band gap which is quoted at 3.54 eV for light vibrating parallel to the C axis and 3.93 eV for light vibrating perpendicular Cal as and Cottrant (1982). The difference in band gap with vibration direction is exhibited by the strong pleochroism of the mineral in ultra-violet light. This indicates that for certain crystallographic orientations less energy is required to initiate electronic transitions from the valence band to the conduction band than for others.

Naturally occurring cassiterites are uniquely n-type semiconductors. Attempts to produce p-type cassiterites by variously doping with zinc (Matthew and Kohnke, 1968) and gallium and indium (Morgan and Wright, 1966) have failed, although Wright (1968) claims that doping with chromium does produce a high resistivity p-type specimen. The n-type semiconductor behaviour (observed in cassiterite) seems to occur via doubly ionised oxygen vacancies, however, the full nature of the defect structure has yet to be satisfactorily elucidated.

Table 7.9. Comparison of reflectance data from this study for cassiterite with literature values.

λ	Reflectance in air		
nm.	1	2	3
300	11.96		
320	13.69		
340	13.06		
360	12.63		
380	12.29		
400	12.02	12.39	
420	11.78	12.08	
440	11.60	11.82	
460	11.44	11.64	
470			11.95-12.80
480	11.31	11.43	
500	11.19	11.26	
520	11.10	11.11	
540	11.02	10.99	
546			11.50-12.40
560	10.99	10.90	
580	10.95	10.84	
589			11.30-12.20
600	10.89	10.81	
620	10.84	10.79	
640	10.82	10.76	
650			11.20-12.20
660	10.78	10.71	
680	10.77	10.70	
700	10.77	10.65	

1. Ellipsometric values for cassiterite, this study.
2. Microphotometric values for cassiterite, this study.
3. IMA,COM results for cassiterite from Mwirasando mine, Uganda, using SiC standard.

Iron is the most common and most studied substituent in cassiterite and is thought to be responsible for the peak sometimes observed at 450 nm (Cal as and Cottrant, 1982). Iron is known to act as an acceptor, but its effects are more than compensated for by the presence of oxygen vacancies and donor ions such as niobium and tantalum. In our specimen, no iron was detected, however, the small quantities of copper would be expected to act as acceptors, while the presence of titanium ions may lead to a very slight increase in reflectivity.

The brownish red colours of natural cassiterites have been attributed by many authors to iron impurities. As the cassiterite specimen in this study is brown in colour but contains no detectable iron, it seems likely that the colouration is due to charge transfer processes between the electronic levels of the copper and titanium and the cassiterite lattice. Such processes appear to provide just as intense a colouration as those ascribed to iron.

The only feature worthy of note in the reflectance spectrum of the cassiterite specimen is the peak at 320 nm, which is indicative of electronic transitions between the valence band and the conduction band (absorption edge). Apart from this maximum the reflectance spectrum is remarkably flat varying by as little as 0.2% from 400 - 700 nm. There is no indication of the expected excitonic transitions superimposed on the absorption edge, but it is possible that these are too weak to be observed at room temperature.

As would be expected the dispersions of n, k, (Fig. 6.27), ε_1, and ε_2 (Fig. 6.28) have a similar shape to the reflectance profile being essentially flat between 700 - 400 nm after which they slowly rise to a maximum between 300 and 320 nm.

7.10 Cuprite

7.10.1 Introduction

Electron probe microanalysis of the cuprite specimen number BM 1974, 411, section E1007, revealed it to be composed entirely of copper and oxygen, having the formula $Cu_{1.85}O$, this agrees reasonably well with that generally recognised for cuprite Cu_2O. An examination of the formula reveals that the mineral is copper deficient, as are all cuprite specimens (Shuey, 1975). This fact accounts for the p-type semiconductor behaviour observed in cuprite, which occurs via copper vacancies which act as acceptors.

7.10.2 Comparison of Microphotometric and Ellipsometric Data

In Fig. 6.30 the microphotometric air and oil maximum and minimum reflectance curves are given together with the ellipsometric air measurements. Comparisons of these data are difficult because of the anisotropy of the mineral (Section 7.10.4.). The fact that the dispersion of the ellipsometric data is similar to the minimum microphotometric reflectance curve is probably pure chance, and caused by the fact that in order to avoid areas of internal reflections, the specimen was always orientated in the same direction so as to accommodate the ellipsometric beam. Despite this fact several points are worthy of note, firstly an examination of the ellipsometric reflectance curve between 600 and 700 nm reveals the machine's unreliability in this spectral range (section 7.2.3). Secondly because of the SSRDP, Section 5.2, the microphotometric data will be slightly below their true values especially in the middle of the spectrum.

The anisotropy of the cuprite specimen also makes comparisons between the ellipsometric and microphotometric n and k values difficult. There are, however, some general points which are worthy of discussion. Examination of Fig. 6.31 reveals that the ellipsometric n values are higher than the microphotometric ones, and that the dispersion of the ellipsometric n data bears a closer similarity to the microphotometric minimum curve, than it does to the maximum. In the case of the k values the distinctions between the microphotometric maximum and minimum curves are less clearly

defined, as over most of the spectrum the so called minimum curve is actually higher in magnitude than the maximum curve. The ellipsometric k values are lower than the microphotometric ones throughout the spectrum. The latter are, however, probably artificially high because they are being measured in a region where k tends towards zero (Section 2.24).

7.10.3 Comparison of Data with Literature Results

Ever since Groes and Karryev (1952) in Leningrad and Hayashi (1952) in Japan observed excitonic behaviour in the visible spectrum of cuprite, the mineral has attracted the attention of many workers. Some of these results are displayed in Table 7.10. Unfortunately all of these data relate to isotropic cuprite. Rastall (1980) has observed differences in reflectivity and in the positions of the excitonic peaks with changing crystallographic orientation but attributes these to the difficulties in polishing different cuprite crystal faces to the same standard. Throughout his discussion, Rastall maintains the isotropism of his specimen although his data would not seem to substantiate this claim.

Taking the anisotropy of the cuprite specimen used in this study, and compositional differences into account, the data agree reasonably well with the results of other workers. It is interesting to note the differences in the reflectance dispersion between the cuprite specimen used in this study and that measured by Rastall (1980), Table 7.10, especially when it is remembered that both were measured on the same ellipsometer although the latter specimen was chemically etched before measurement.

Fig. 7.7 displays the results of Brahms and Nikitine (1965) carried out on a single crystal of cuprite at 77 K between 200 and 500 nm. It is interesting to compare these results with those of this study. Thermal lattice vibrations and lattice imperfections will tend to broaden the spectral maxima and it is the reduction of the former in particular via low temperature measurements which accounts for the sharp narrow peaks in Brahms and Nikitine's dispersion. As a result of thermal broadening it is only the major peaks, E, F, H and J which are observed in our spectrum, the smaller peaks G and I are not detected as they lie within the envelope of the broadened peaks H and J. They do, however,

Table 7.10. Comparison of reflectance data from this study for cuprite with literature values.

λ	Reflectance in air							
nm.	1	2	3	4	5	6	7	8
300	37.06					35.20	34.98	
320	34.51							
340	36.31					35.51	35.03	
360	37.24							
380	35.60							
400	34.02	32.14	33.47	31.50	34.50	33.65	33.41	
420	33.06	31.71	32.66	31.60	33.60		32.44	
440	32.94	31.37	32.56	31.60	32.70	32.34	31.98	
460	32.33	30.85	32.26	31.60	31.85		31.50	
470						31.34	31.11	31.10-31.40
480	30.87	30.08	30.52	30.80	30.90		30.70	
500	29.56	30.05	28.71	29.60	29.70	30.26	29.96	
520	28.30	29.33	27.38	28.20	28.30		29.23	
540	27.34	28.19	26.33	27.00	27.00	28.20	28.19	
546								26.60-26.70
560	26.64	26.89	25.44	25.80	26.00		27.05	
580	25.80	25.90	24.72	25.00	26.30	26.19	26.05	
589								24.60-25.00
600	25.13	25.19	24.17	24.20	24.70	25.34	25.25	
620	24.52	24.58	23.71	23.60	24.20		24.62	
640	24.10	24.08	23.31	23.20	23.70		24.10	
650						23.97	23.88	23.00-23.50
660	23.74	23.69	22.97	22.80	23.30		23.60	
680	23.44	23.30	22.66	22.50	22.90		23.33	
700	23.33	22.93	22.35	22.20	22.60	23.16	23.04	

1. Ellipsometric values for cuprite, this study.
2. Maximum microphotometric values for cuprite, this study.
3. Minimum microphotometric values for cuprite, this study.
4. IMA,COM results for cuprite from Liskeard,Cornwall using a SiC standard, Simpson.
5. IMA,COM results for cuprite from Mindouli,Congo using a SiC standard, Caye & Pasdeloup.
6. Ellipsometric results of Roberts & Rastall (1978) for cuprite from Onganja,Namibia (BM.1974.411) .
7. Ellipsometric results of Roberts & Rastall (1978) for synthetic cuprite.
8. Results given by Bowie, Simpson & Auld (1978) for natural cuprites.

FIG 7.7

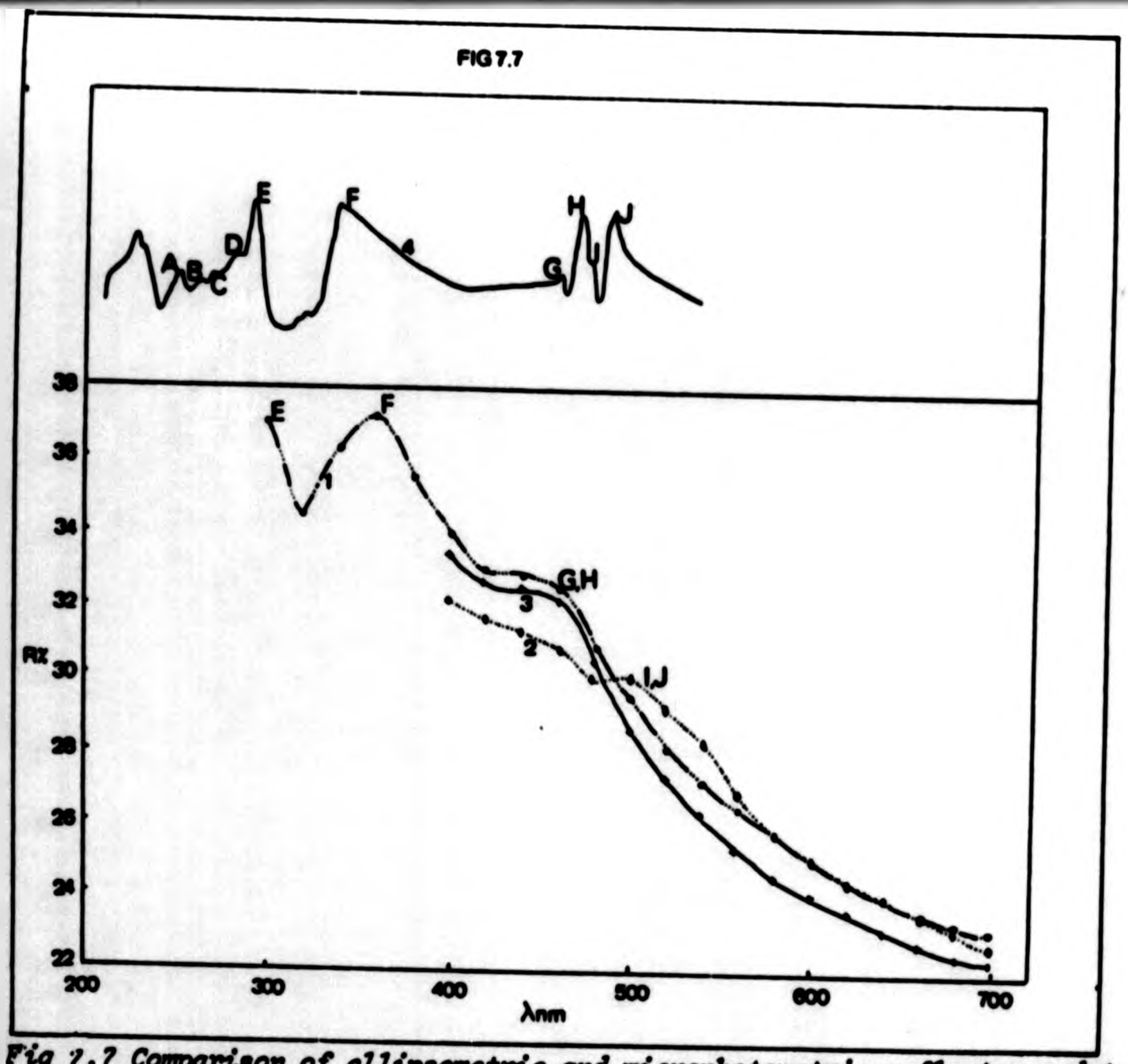

Fig 7.7 Comparison of ellipsometric and microphotometric reflectance data for cuprite with the results of Brahms and Nikitine (1965).

1. *Ellipsometric results this study.*
2. *Microphotometric results (maximum) this study.*
3. *Microphotometric results (minimum) this study.*
4. *Results of Brahms and Nikitine (1965).*

manifest their presence by slightly shifting the position of the maxima ie, what is seen is the weighted average of peaks and G and H, and I and J respectively.

7.10.4 Electronic and Optical Properties

Cuprite is a semiconductor with a band gap which has variously been reported as between 2.17 and 2.31 eV ie, allowed electronic transitions from the valence band into the conduction band begin at about 570 nm and continue into the ultra-violet. Superimposed on the absorption edge are peaks primarily derived from excitonic processes designated A-J by Brahms and Nikitine (1965). It has been established (Brahms and Nikitine, 1965) that peaks, H and J are particularly defect sensitive. The results of this study take this argument one stage further by appearing to suggest that peaks H and J are also orientation dependent. It thus seems likely that peaks H and J (and G and I) are derived from the same excitonic process and that this is initiated at lower energies when the specimen is in its 'maximum' orientation.

It is appropriate here to consider the origin of the observed anisotropy in our cuprite specimen. This anisotropy is weak, being scarcely detectable under crossed polars and only becomes readily apparent when observing the fluctuating response of the DVM upon rotation of the specimen stage. Its effect on the optical data, however, is quite dramatic. This is because of the orientation dependence of the excitonic processes responsible for the peaks H/J which subsequently leads to two very different dispersions. Whether this slight anisotropy is a surface or bulk effect is uncertain at the moment and because of its weakness would be very difficult to ascertain. Bearing in mind the results of Rastall this phenomenon does not seem to be unique to our specimen. In addition recent X-ray studies on chalcotrichite (fine hair-like crystals of cuprite) have shown slight departures from cubic symmetry.

Examination of Fig. 6.30 reveals that the reflectivity of cuprite rises rapidly after the onset of the absorption edge and continues to do so into the ultra-violet. The area of low reflectivity in the red and near infra-red is characterised by low values of ϵ_2 (Fig. 6.32) and k and higher values of ϵ_1 (Fig. 6.32) and n.

7.10.5 Surface Film Formation

The effects of surface films on cuprite have been examined by Rastall, Clarke and Roberts (1980), who suggested that the presence of an absorbing film of CuO on the surface of cuprite would account for their anomalously high k values. Interpretation of filmed systems by ellipsometry should always be undertaken with care as Smith (1983) has shown that a slightly scratched surface with a thin transparent film can mimic the properties of an unscratched surface with an absorbing film. Hence the need to reduce surface artefacts to a size below the wavelength of visible light. To see if a film was growing on our cuprite specimen, measurements were made:

i) immediately after buffing with an Al_2O_3-water slurry
ii) two days after buffing
iii) seven days after buffing
iv) twenty-eight days after buffing
v) fifty six days after buffing

The results, which showed no perceptible change in the optical parameters led us to the conclusion that either there is no surface film present or that a surface film forms instantaneously after buffing. Thus, provided that the mineral is kept in a dry, cool environment, this film will not show an increase in thickness with time. Of these two hypotheses the latter seems the most plausible as it has been postulated that most materials, with the possible exception of gold, form a thin physi-sorbed surface film immediately after polishing.

7.11 Iridium and Platinum Iridium

7.11.1 Introduction

In Fig. 6.33 the ellipsometric reflectance profiles for iridium, and the two platinum-iridium alloys with iridium contents of ten and twenty five percent are displayed. The effects on the reflectance dispersion when platinum is alloyed with iridium can thus be clearly demonstrated. In blue light the higher the iridium content of the alloy, the higher is its reflectance, the reverse however, is true in red light

where the alloy with the lowest iridium content has the highest reflectivity. These observations can be explained by recourse to the iridium reflectance profile which unlike that of platinum does not continue to rise rapidly in red light. Thus although iridium has the highest reflectivity at the blue end of the spectrum, the platinum alloy with the lowest iridium content (10%) has the highest reflectance at the red end of the spectrum.

7.11.2 Comparison of Reflectance Data Using Various Techniques

In Fig. 6.34 the reflectance profiles for a platinum iridium alloy with an iridium content of twenty five percent measured using various optical techniques are displayed. Examination of Fig. 6.34 shows that there is a great deal of disparity between the measurements. Although the SSRDP accounts for some of the observed differences between the microphotometric data and the other results, it can not be held entirely responsible for them all.

The clue to the observed disparities lies in the closeness of the ellipsometric measurments carried out at CLP and at NPL suggesting that the angle of incidence effects the measured results. Such a conclusion would mean that either a surface film is present or that the surface is damaged. As both platinum and iridium are noble metals it is unlikely that an alloy of them would form a surface film of sufficient thickness to affect the measured results so dramatically. It is, however, known that surface damage can mimic the optical characteristics of an absorbing film (Smith, 1983).

As the noble metal specimens were not prepared in the same manner as the mineralogical specimens, where very few sizeable discrepancies were observed, surface damage seems to be the most likely explanation. The cost of the iridium and the platinum-iridium alloys precluded any further polishing and so regrettably it was felt that they were unsuitable as even temporary microphotometric standards standards as their 'true' reflectivity was unknown.

7.12 Tarnish Films on Mineral Surfaces

The importance of pre-measurement buffing cannot be overstated

as has been amply demonstrated by the work of Criddle et al.(1983) on henryite, where contrary to expections the surface reflectivity after one month's exposure to the atmosphere was greater than that immediately after buffing. In addition the mineral surface after this period of time displayed little visible evidence of tarnish film formation. For this reason all the mineral surfaces examined in this study were buffed immediately prior to measurement.

This is not to say that the mineral specimens were completely film free, but as few measurements are carried out in vacuum, the air formed films on similar mineral specimens will be essentially the same world wide. It is therefore possible to compare the 'real' surface results of minerals, provided the pre-measurement buffing requirements are strictly adhered to.

CONCLUSIONS

Comparison of the ellipsometric and microphotometric results reveals that on the whole the data are in fairly good agreement and that where discrepancies do occur they can usually be rationalised. Discrepancies in the reflectance data are most likely to occur in regions where the rate of change of reflectance with respect to wavelength $\left(\frac{dR}{d\lambda}\right)$ is high. This is because in this spectral region any slight errors in determining either the microphotometric or ellipsometric reflectances will be magnified by the rapid changes required in the spectral response of the equipment. An example of this phenomenon is found in tetrahedrite where the reflectance decreases rapidly between 600 - 700 nm. As the ellipsometer is unable to react swiftly to large azimuthal changes in this spectral region the ellipsometric data appears artificially high. Similarly, slight differences in the monochromator pass bands used on the ellipsometer and microscope-photometer leads to the observed discrepancies in the data for pyrite between 400 - 500 nm.

The effects of the Standard-Specimen-Reflectance-Difference-Phenomenon (SSRDP) on the microphotometrically derived reflectance values only becomes important when the reflectivity of the specimen is significantly greater than that of the standard or vice-versa. These effects are predictable and can be corrected for by using the values listed in table 5.1. It is less easy to correct the microphotometric data for the effects of the pinholes in the interference filter at 420 nm and the loss of sensitivity at 400 nm. However, as long as such factors are born in mind when the data are analysed the credibility of the experiment remains intact.

The agreement between the derived n and k values for the two techniques is slightly less good, with irregularities being observed in the microphotometric data especially for the high-reflectance minerals. To some extent this problem can be reduced by using the 15 scan averaging technique of microphotometric measurement. Presumably this reduction is because the mean values of R and ^{im}R are statistically more likely to bear a resemblance to the true reflectance values than are single scan air and oil measurements. For most minerals the microphotometric k values

are higher than the ellipsometric ones especially when k tends towards zero. Conversely the microphotometric n values are usually lower than the ellipsometric ones. By virtue of the equations used to calculate the microphotometric n and k values if k is too high n will necessarily be too low in addition at higher reflectances small changes, in the measured values, can dramatically effect the derived optical constants. The presence of surface films and surface topography can also influence the optical parameters but will have a greater effect on those measured ellipsometrically than on those measured microphotometrically, by virtue of the different angles of incidence used in the two techniques.

One of the principal differences between ellipsometry and microscope photometry is the manner in which reflectance and the optical constants n and k are derived. In microscope photometry the measured quantity is the light intensity reaching a photodetector and reflectance is calculated from the ratio of light intensities, from a specimen and a precalibrated standard. The n and k values are then derived via a pair of simultaneous equations from the air and oil reflectance values. In ellipsometry reflectance is calculated from the n and k values and is the last quantity to be derived and so contains the product of any errors involved in any previous computations. The measured quantities in ellipsometry are the angular displacements of the analyser and polariser prisms from their pre-set fiducials so negating the need for a standard.

Standards are a major problem in microscope photometry as very few materials fulfil the necessary requirements for a good standard. The situation is particularly acute at high reflectances (>55%) where no adequate standards exist. In this study a calibrated evaporated aluminium film was used, to try to establish the cause of the SSRDP which was particularly apparent at high reflectances. Evaporated aluminium because of its fragility and tendency to oxidise, however, is unsuitable for normal microphotometric measurements. The most likely candidate for a high reflectance standard is sperrylite (PtAs) but at present no manufacturer can be persuaded to fabricate this material.

From the above it may seem that ellipsometers of the type used in this study have much to offer the mineralogist especially as they do not require standards and so provide an independent means of evaluating

the optical constants n and k. There are, however, some drawbacks, for example, a homogeneous surface area of not less than 1 cm^2 is required to accommodate the ellipsometer beam and in addition this area must be isotropic and as free from surface films and surface irregularities as possible. Such stringent conditions clearly limit the number of minerals available for study and hence systematic studies of groups of minerals are difficult and the examination of small mineral inclusions impossible. These problems are not insurmountable, a normal incidence ellipsometer would go some way to solving the problems of specimen size and anisotropy. At the present time, however, it is unlikely that standard ellipsometers, will ever replace microscope photometers in the study of minerals. They may, however, provide some mineral values with which microphotometric measurements may be compared.

BIBLIOGRAPHY

Abdullaev, G.B., Alizarova, Z.A, Zamanova, E.H., and Asadov, G.A. (1968) Phys. Stat. Sol. 26,65.

Adams, D.M. (1974) Inorganic Solids, Wiley.

Araya, R.A., Bowles, J.F.W. and Simpson, P.R. (1977) N. Jb. Miner. Mh. H. 10, 467.

Atanasov, V.A. (19 5) Min. Mag. 40 233.

Atkin, B.P. and Harvey P.D. (1979) Can. Mineral 17 639.

Atkins, (1977). Physical Chemistry, Oxford.

Barton, P.B. and Toulmin, P. (1963) Geological Society of America Annual Meeting, abstr. 1191, GSA, Boulder Colorado.

Basu, K., Bartnykov, N., Mookherjee, A., Mozgova, N. and Tsepin, A.I. (1981) N. Jb. Miner. Mh. 141 280.

Benoit, R. (1955) J. Chem. Phys. 52, 119.

Berek, M., (1936) Z. Instrumentenkunde 56, 1.

Bernard, J.H. (1958) Rozpr. teskosl. Akad. Ved. 68, 14.

Bishop, A.C., Criddle, A.J. and Clark A.M. (1977) Min. Mag. 41 59.

Bither, T.A., Bouchard, R.J., Cloud, W.H., Donahue, P.C. and Siemons, W.J. (1968) Inorg. Chem. 7 2208.

Bond, W.L. (1965) J. Appl. Phys. 36 1674.

Bowie, S.H.U., Simpson, P.R. and Auld, H. (1978) XI Meeting of IMA, Novosibirsk.

Bowie, S.H.U. and Simpson, P.R. (1977) Microscopy: Reflected Light. In "Physical Methods in Determinative Mineralogy" (J. Zussman, ed.) Academic Press, London.

Bragg, W.L. (1913) Proc. R. Soc. Lond. 89A, 468.

Brahms, S. (1965) Solid State Comm. 3, 209.

Brostigen, G. and Kjekshus, A. (1970) Acta. Chem. Scand. 24, 2993.

Brun, A. (1930) Bull. Soc. Fr. Miner. 53, 35.

Buerger, M.J. (1942) X-ray Crystallography, Wiley, 435.

Buerger, M.J. and Buerger, N.W. (1944) Am. Mineral. 29, 55.

Burns, R.G. and Vaughan, D.J. (1970) Am. Mineral. 55, 1576.

Butterill, J.D. and Nickel, E.H. (1967) Am. Mineral. 52, 1247.

Calas, G. and Cottrant, J.F. (1982) Bull. Soc. Fr. Miner. 105, 598.

Capdecomme, L. (1936) Comptes Rendus Acad. Sci. Paris, 202, 1842.

Capdecomme, L. (1938) Bull Soc. Fr. Miner. 61, 5.

Cardona, M. and Greenaway, D.L. (1964) Phys. Rev. 133 A 1685.

Cvech, F. and Hak, J. (1979) Casopis pro Mineralogii a geologii 24, 83.

Cervelle, B., Levy, C. and Pinet, M. (1975) Fortschr. Mineral 52, 539.

Charlat, M. and Levy, C. (1976) Bull. Soc. Fr. Mineral. Cristallogr. 99, 29.

Chen, T.T. and Petruk, W. (1978) CANMET Rep MRP/MSL 78 - 23 (IR) Dep. Energy, Mines and Resources, Ottawa.

Chen, T.T., Dutrizac, J.E., Owens, D.R. and Laflamme, J.H.G. (1980) Can. Mineral. 18, 173.

Chikhaoui, S. and Levy, C. (1982) Can. Mineral. 20, 101.

Clark, A.M. and Criddle, A.J. (1982) Min. Mag. 46, 371.

Clarke, F.J.J. (1972) J. Res. Natl. Bur. Stand. 76A, 375.

Clarke, K. Mc. (1980) CNAA PhD Thesis.

des Cloizeaux (1867) Mem. Acad. Sciences, Paris, 18, 515.

Commission an Ore Microscopy (1976) International Tables for the Microscopic Determination of Crystalline Substances Adsorbing in Visible Light.

Cook, W.R.Jr. (1972) Nat. Bur. St. 364, Sol. St. Chem. 703.

Cotton, F.A. and Wilkinson, G. (1972) Advanced Inorganic Chemistry, Interscienc

Criddle, A.J. (1983) Private communication.

Criddle, A.J., Stanley, C.J., Chisholm, J.E. and Fejer, E.E. (1983) Bull. Mineral. 106, 511.

Criddle, A.J. (1983) Private communication.

Dahl J.P. and Swittendick, A.C. (1966) J. Phys. Chem. Sol. 27, 931.

Dalven, R. (1969) Infrared Phys. 9, 141.

Djurle, S. (1958) Acta. Chem. Scand. 12, 1415.

Eisenmann, L. (1952) Ann. Physik 10, 129.

Elliot, E.J. (1961) Phys. Rev. 124, 340.

Embrey, P.G. and Criddle, A.J. (1978) Am. Mineral 63 853.

Embrey, P.G. (1984) Private communication.

Evans, H.T. (1979) Beits. fur Krist. 150, 299.

Evans, H.T. (1981) Am. Mineral. 66, 807.

Favarov, V.A., Krasnikov, V.I. and Sychugov, V.S. (1972) Akad. Nauk SSSR Geolog 11, 72.

Folmer, J.C.W. and Jellinek, F. (1980) J. Less Common Metals 76, 153.

Galopin, R. and Henry, N.F.M. (1972) Microscopic Study of Ore Minerals, Cambridge.

Gross, E.F. and Karryev, N.A. (1952) DAN SSSR. 84.2, 261.

Gross, E.F. and Karryev, N.A. (1952) DAN SSSR. 84.2, 471.

Gross, E.F. and Kuang-Yin, C. (1962) Sov. Phys. Doklady, 7 336.

Gross, E.F. (1962) Sov. Phys. Uspheki, 5.2, 195.

Guimaraes, D. (1934) Serv. Geol. Estado de Minas Geraes Bol. 2, 17.

Hall, A.J. (1972) Bull. Soc. Fr. Mineral. Cristallogr. 95, 583.

Hall, A.J., Cervelle, B. and Levy, C. (1974) Bull. Soc. Fr. Mineral. Cristallogr. 97, 18.

Hallimond, A.F. (1949) Nature 163, 729.

Hallimond, A.F. (1953) Manual of the Polarising Microscope Cooke Troughton and Simms, York 2nd Edition

Hallimond, A.F. (1957) Min. Mag. 31, 487.

Hallimond, A.F. (1970) The Polarising Microscope Vickers Instruments Ltd. York 3rd Edition

Ham, F.S. and Slack, G.A. (1971) Phys. Rev. 48, 777.

Hayashi, M. (1952) J. Fac. Sci. Hakkaido Univ. 4, 107.

Hoffmann, G.C. (1895) Am. J. Sci. ser. 3, 50, 274.

Holl, (1963). Report no. RF-TR-63-4, Vol 1, Redstone Arsenal, Alabama.

Holton, W.C., Schneider, J. and Estle, T.L. (1964) Phys. Rev. A133, 1638.

Holton, W.C., DeWit, M., Watts, R.K., Estle, T.L. and Schneider, J. (1969) J. Phys. Chem. Solids, 30, 963,

Horn, G. (1893) N. Jb. Miner. Beit. Bd. 12, 269.

Hulliger, F. (1959) Helv. Phys. Acta 32, 615.

Hunt, R. (1984) CNAA. PhD Thesis.

Janosi, A. (1964) Acta Crystallogr. 17, 311.

Jarzebski, Z.M and Marton, J.P. (1976) J. Electrochem. Soc. 123, 299C.

Jarzebski, Z.M. and Marton, J.P. (1976) J. Electrochem. Soc. 123, 333C.

Johan, Z. and Kvacek, M. (1971) Bull Soc. fr. Mineral. Cristallogr. 94, 45.

Johnson, M.L. and Jeanloz, R. (1983) Am. Mineral. 68, 220.

Kalbskopf, R. (1971) Tschermaks Mineral. Petrog. Mitt. 16, 173.

Kalbskopf, R. (1972) Tschermaks Mineral. Petrog. Mitt. 18, 147.

Kjekshus, A. and Nicholson, D.G. (1971) Acta. Chem. Scand. 25, 866.

King, R.J. and Downs, M.J. (1969) Surface. Sci. 16, 288.

King, R.J. (1983) Private communication.

Koenigsberger, J. (1913) Annalen. Phys. 43, 1205.

Koto, K. and Morimoto, N. (1970) Acta. Crystallogr. 26B, 915.

Lebas, G. and Lebihan, M. Th. (1976) Bull. Soc. fr. Mineral. Crystallogr. 99, 351.

Low, W. and Weger, M. (1960) Phys. Rev. 118, 1130.

Lorentz, H.A. (1952) Theory of Electrons, Dover.

Machatschki, F. (1928) Norsk. Geol. Tiddokr. 10, 23.

Machatschki, F. (1928) Z. Kristallogr. 68, 204.

Manning, P.G. (1967) Can. Mineral. 9, 57.

Marfunin, A.S. Platonov, A.N. and Fedorov, V.E. (1968) Soviet Phys. Solid State 9, 2847.

Marshall, R. and Mitra, S.S. (1965) J. Appl. Phys. 36, 3882.

Maske, S. and Skinner, B.J. (1971) Econ. Geol. 66, 901.

Matthew, H.E. and Kohnke, E.E. (1968) J. Phys. Chem. Solids, 29, 653.

Meadows, A. (1975) CNAA PhD Thesis.

Miller, J.W. and Craig, J.R. (1983) Am. Mineral. 68, 227.

Miyahara, S. and Teranishi, T. (1968) J. Appl. Phys. 39, 896.

Morgan, D.F. and Wright, D.A. (1966) J. Appl. Phys. 17, 337.

Morimoto, N. (1962) Mineral. J. (Tokyo) 3, 338.

Morimoto, N. and Gyobu, A. (1971) Am. Mineral. 56, 1889.

Mowat, J.R. and Muller, R.H. (1966) Report no. UCRL 11813, University of California, Radiation Laboratory, Berkley, California.

Mulder, B.J. (1973) Phys. Stat. Sol. 18A, 633.

Muller, R.H. (1969) Surface Sci. 16, 14.

Naora, H. (1952) Science 115, 240.

Nash, J.T. (1975) Econ. Geol. 70, 1038.

Nickel, E.H. (1965) Mines Branch Information Circular IC 170 Ottawa.

Nickel, E.H. (1970) Chem. Geol. 5, 233.

Nikitine, S. (1966) Proc. Int. Conf. on Luminescence 1501.

Onlidahl, I. (1974) Surface Science 45 91.

Overhof, H. and Rossler, V. (1970) Phys. Stat. Sol. 37, 691.

Pattrick, R.A.D. (1978) Min. Mag. 42, 286.

Pauling, L. and Neuman, E.W. (1934) Zeits fur Kristallogr. 88, 54.

Petrova, I.V., Kuznetsov, A.I. Besokoneva, E.L., Symonov, M.A., Pobedimskaya, E.A. and Belov, N.V. (1978) Dokl. Acad. Nauk. USSR. 242, No. 2, 337.

Petruk, W. (1971) Can. Mineral. 11, part 1.

Piller, H. (1964) Mineral. Depos. 1 175.

Piller, H. (1974) J. Microscopy 100, 35.

Piller, H. (1977) Microscope Photometry, Springer-Verlag.

Piller, H. and Von Gehlen, K. (1964) Am. Mineral. 49, 867.

Platanov, A.N. and Marfunin, A.S. (1968) Geochem. Internat. 5, 245.

Pleass, C.M. and Heyding, R.D. (1962) Can. J. Chem. 40, 590.

Potter, R.W. (1977) Econ. Geol. 72, 1524.

Radcliffe, D. (1968) Can. Mineral. 9, 559.

Rahlfs, P. (1936) Z. Phys. Chem. 31B, 157.

Rastall, P. and Roberts, E.F.I. (1978) Min. Mag. 42, 505.

Rastall, P., Clarke, Mc.K. and Roberts, E.F.I. (1980) Min. Mag. 43, 633.

Rastall, P. (1980), CNAA PhD Thesis.

Rauber, A. and Schneider, J. (1962) Z. Naturforsch. 17A, 26.

Riley, J.F. (1974) Min. Dep., 9, 117.

Roberts, E.F.I., and Meadows, A. (1974), J. Phys. E7, 379.

Roseboom, E.H., Jr. (1962) Am. Mineral. 47, 310.

Roseboom, E.H., Jr. (1962) Am. Mineral. 47, 1181.

Roseboom, E.H., Jr. (1966) Econ. Geol. 61, 641.

Sandecki, J. and Amcoff, O. (1981) N. Jb. Miner. Abh. 141, 324.

Schlegal, A. and Wachter, P. (1976) J. Phys. C. 9, 3363.

Schoolar, R.B. and Dixon, J.R. (1965) Phys. Rev. 137, A667.

Shestatskii, S.N. and Sobolev, V.V. (1968) Phys. Stat. Solidi. 28, K131.

Shestatskii, S.N. and Sobolev, V.V. (1969) Phys. Stat. Solidi. 32, K109.

Shuey, R.T. (1975) Semiconducting Ore Minerals, Developments in Economic Geology No. 4 Elsevier.

Springer, G. (1969) N. Jb. Miner. Mh. 24.

Smith, F.H. (1964) Min. Mag. 33, 725.

Smith, T. (1983) J. Electroanal. Chem. 150, 277.

Stanley, C.J. (1983) Private communication.

Thorpe, R.I., Pringle, G.J. and Plant, A.G. (1976) Geol. Surv. Can. Pap. 76-1A, 311.

Tossell, J.A., Vaughan, D.J. and Burdett, J.K. (1981) Phys. Chem. Minerals. 7, 77.

Tossell, J.A. (1983) Phys. Chem. Minerals 9, 115.

Uytenbogaart, W. and Burke, E.A.J. (1971) Tables for the Microscopic Identification of Ore Minerals, Elsevier.

Vaughan, D.J. (1971) D. Phil. Thesis University of Oxford.

Vaughan, D.J. (1978) Bull. Mineral. 101, 484.

Vaughan, D.J. and Craig, J.R. (1978) Mineral Chemistry of Metal Sulphides, Cambridge.

Vaughan, D.J. and Tossell, J.A. (1980) Science 179, 375.

Vaughan, D.J. and Tossell, J.A. (1983) Phys. Chem. Minerals, 9, 253.

Velasco, F., Pesquera, A. and Autefage, F. (1981) Can. Mineral. 19, 593.

Vendrell-Saz, M. Karup-Moler, S. and Lopez-Soler, A. (1978) XI Meeting of IMA, Novosibirsk.

Wells, A.F. (1964) Structural Inorganic Chemistry, Oxford University press.

Werrick, J.H. (1960) Am. Mineral. 45, 591.

Wright, D.A. (1968) Proc. Ceram. Soc. 10, 103.

Wright, F.E. (1920) Proc. Amer. Phil. Soc. 58, 401.

Wuensch, B.J. (1964) Zeits fur Krist. 119. S.437.

Zhilich, A.G. and Makarov, V.P. (1960) Sov. Phys. Solid. State 2, 1587.